Predictions of F-111 TACT Aircraft Buffet Response and Correlations of Fluctuating Pressures Measured on Aluminum and Steel Models and the Aircraft

Charles F. Coe and Atlee M. Cunningham, Jr.

NASA

NASA Contractor Report 4069

Predictions of F-111 TACT Aircraft Buffet Response and Correlations of Fluctuating Pressures Measured on Aluminum and Steel Models and the Aircraft

Charles F. Coe
Coe Engineering, Inc.
Los Altos, California

Atlee M. Cunningham, Jr.
General Dynamics Corporation
Forth Worth, Texas

NASA
National Aeronautics
and Space Administration

Scientific and Technical
Information Branch

1987

TABLE OF CONTENTS

INTRODUCTION

Buffeting and the related flow phenomena that cause buffeting strongly affect the maneuver characteristics of aircraft. Because of the complexity of the aerodynamic excitation and aerostructrual interaction, the ability to predict buffet characteristics has been severely limited. A good review of the general principles of the aerostructural buffet problem including the basic features of the fluctuating aerodynamic pressures and the elastically responding aircraft structure is given by Jones in Ref. 1.

The effects of buffeting and other transonic phenomena on maneuvering combat aircraft were the subject of a study of an AGARD Working Group (sponsored by the Flight Mechanics Panel) which was reported in Ref. 2. This study, also summarized by Lamar (the Working Group Chairman) in Ref. 3, documented the comprehensive review of the state-of-the-art of buffet test techniques and prediction methods that was carried out by the Working Group. Lamar's paper, which emphasizes the correlation of data from wind tunnel and flight tests, points out the many gaps and ambiguities in available buffet information. Important factors which may affect the correlation of wind-tunnel and flight- test buffet data are listed in Figure 1 (adapted from Ref. 2).

The list in Figure 1 shows that wind tunnel measurements of buffet excitation or response involve the same classic problems for proper flow-field simulation as any steady-state force or pressure tests. Important common problems that affect wind-tunnel data are Reynolds number, wall interference, flow turbulence, transition fixing, boundary-layer thickness distribution, and static elasticity. All of these items may affect the occurence, boundaries, and characteristics of separated flow fields that cause buffeting. Additionally, buffet excitation measurements may be influenced by dynamic motions, so data obtained from nondynamically-scaled models can be critically influenced.

Flight-test measurements of buffet excitation or response also have been subject to many uncertainties that are obstacles to successful correlation of data (Figure 1). The main problems with flight data relate to limitations in measurement accuracies. It is difficult to measure flight parameters accurately, but the nonstationarity of data has also been a more serious problem affecting buffet measurements. The nonstationarity is due to the fact that most aircraft cannot hold steady conditions in a high-g maneuver. Statistical accuracy is critically affected by the usual short duration of the data samples. Also, flight tests are expensive, sensor installations are complex, and airborne data systems have limited versatility. These facts have generally caused flight data to be sparse, often incomplete, and lacking in one-to-one sensor locations. In addition, there are usually no boundary-layer measurements or flow visulations to enhance the data analysis.

References 2 and 3 contain very complete bibliographies on buffeting. Of all the referenced authors, Mabey (Refs. 4 and 5) has probably contributed more information on the basics of buffeting and practical empirical methods of predicting buffet boundaries and beyond than any other researcher. Among the many references, a pertinent one is by John (Ref. 6), who contributed a comprehensive review of methods for buffet prediction. He generally concluded that empirical methods were good for prediction of buffet boundaries and he recommended that Mabey methods be applied in early design phases of an aircraft. He concluded that wind-tunnel tests of dynamically scaled models should

yield the most accuate prediction of full-scale buffeting, but the technique is expensive and probably not practical during an early phase of aircraft design.

In addition to the extremes of empirical tests that do not yield the often desired buffet response of various structual modes and aeroelastic tests, there are two other test techniques of interest. One method, which has received considerable attention involves the measurements of the fluctuating pressures on a nominally rigid model; the measurements are then used to calculate the response of the elastic aircraft. The other method, originally suggested by Jones (Ref. 7) and implemented by Butler and Spavins (Ref. 8), uses measurements of the buffet response of a nominally rigid model of a wing to calculate the aerodynamic excitation and damping; the measurements are then used to calculate the response of the corresponding full-scale wing.

Each of the experimental approaches for obtaining buffet intensity information has its unique technical and cost advantages and disadvantages. From a cost point of view, the dynamically scaled models are the most expensive; and simple solid metals models with only strain-gage and accelerometer instrumentation are clearly the least expensive. Pressure models are complex and costly due to the instrumentation requirements, but they offer an advantage of also revealing local flow-field information that is beneficial to buffet research.

From a technical point of view, elastically scaled models should yield the most accurate predictions of buffet intensities. The only technical drawback of elastically scaled models is that they are static-strength limited and consequently compromises are required on the upper limits of test angles-of-attack and/or Reynolds number.

Good examples of buffet predictions from an elastically scaled model are illustrated in Figure 2 taken from Hanson (Ref. 9). Figure 2 shows comparisons of F-111A aeroelastic model and aircraft response spectra. These data are for a wing-sweep angle (Λ) of 26° and Mach number (M) of 0.81. The angle of attack (α) was only about 8.5° which was the maximum angle allowed by the static load limit at M = 0.8. Figure 2(a) shows excellent correlation of the normalized bending moments at the first wing bending mode. This result supports the expectation of good buffet intensity prediction by this method. However, correlations in Figure 2(b), which shows the normalized spectra of accelerations at the center of gravity for modes other than first wing bending, are not so encouraging. If the normalization factor is accounted for, some of the differences in corresponding spectral peaks would be greater than a factor of 10.

Several previous investigations of the prediction of buffet intensity from fluctuating-pressure measurements have been conducted prior to this research. Good examples of the investigations are reported in Refs. 10, 11 and 12.

Mullens and Lemley (Ref. 10) were amoung the first to correlate predicted buffet intensities from fluctuating-pressure measurements with the measured buffeting of an aircraft. An illustration of their correlations of accelerations of an F-4 wingtip is shown in Figure 3. These results, which are somewhat typical of early attempts to predict buffet intensities, proved to be disappointing. The differences between predictions and measurements of spectral peaks for the various noted vibration modes varied from a factor of 5 for wing bending modes to more than a factor of 10 for torsion modes. It was this generally poor success of buffet intensity predictions that prompted NASA-Ames Research Center

to embark on a research program that included the investigations by Hwang and Pi (Ref. 11), and Cunningham, et al, (Ref. 12).

The investigation by Hwang and Pi used pressure fluctuations measured on the F-5A aircraft to predict the buffeting of the same aircraft. Examples of the results are shown in Figure 4. which include power spectra of wingtip accelerations during four different segments of time in a wind-up turn at a Mach number of 0.925. As in the previous example, the comparison of analytical and experimental power spectra is disappointing. Generally it appears that the differences in spectral peaks for the labeled vibration modes varied from a factor of 5 to greater than a factor of 10. Hwang and Pi attributed the poor correlation to the nonstationarity and short duration of the data. These are factors which are critical to the statistical accuracy of the spectral analysis. Figure 5 illustrates these factors by showing the variation of wingtip acceleration response of the F-5A aircraft with time and angle of attack. The figure shows the four time segments analyzed for the spectra in Figure 4. It can be seen that the time segments were only slightly longer than 2 seconds. Angles of attack varied from 2° to 4° during the four time segments.

The investigation by Cunningham, et al, (Ref. 12) used pressure fluctuations measured on a 1/6-scale steel semispan model of the F-111A aircraft. Examples of the comparisons of predicted and measured wingtip acceleration response for a wing sweep angle of 26° and Mach number of 0.8 are shown in Figure 6. These data are of special interest because the model scale was large to minimize Reynolds number effects, and it contained the largest number of dynamic pressure tranducers used for any buffet tests. There were 97 tranducers on the upper and lower surfaces of the wing at 5 spanwise stations. Power and cross-power spectral densities of all 97 pressures were used to construct the complex pressure distributions and ultimately the buffet predictions in Figure 6. The results show that this extensive effort on the aerodynamics may have yielded some improvement in the predictions of spectral peaks for some modes of interest, but generally the results were not encourging. Unfortunately, as with the F-5A, the flight data were nonstationary and the data samples were of short duration. For the data in Figures 6(a) and 6(b) the time span of the data was only 2-seconds long for each case. The angles of attack varied from 6.80° to 7.12° during the time of flight data analyzed in Figure 6(a) and from 10.35° to 12.90° during the time of data analyzed in Figure 6(b).

The other method of interest, presented by Butler and Spavins in Ref. (8), uses solid metal models to predict the single degree-of-freedom buffet response of aircraft. The method is simpler and less costly than the pressure-fluctuation method. The first application of the method to predictions of buffeting of the Gnat aircraft yielded very encouraging results. The predictions for the first bending mode only were generally better than the previous predictions by the pressure-fluctuation method. Because of this initial success, the research in the UK was extended to include predictions of the F-111 TACT aircraft buffeting as part of a collaborative program on buffet research with the US. The results of the UK research involving the TACT aircraft, reported in Refs. 13 and 14, further confirmed that the method could yield good buffet predictions. The UK TACT buffet investigation was conducted concurrently with the NASA research reported herein.

The F-111 TACT Program provided a timely opportunity to investigate many aspects of the buffet problem, and particularly, nearly all the factors that affect

3

wind-tunnel and flight-test data (Fig. 1). NASA-Ames Research Center partici-pated in the buffet research aspects of the TACT Program with objectives of: (1) to verify the applicability of buffet excitation measurements obtained on nominally rigid wind-tunnel models to the full-scale elastic aircraft, (2) to investigate effects of Reynolds number and static and dynamic elasticity, and (3) to correlate predictions of buffet response with flight-test measurements.

At Ames Research Center two 1/6-scale semispan models of the TACT aircraft were tested in the 11- by 11-Foot Transonic Wind Tunnel. One model was of solid steel and the other of solid aluminum. Both models were instrumented identi-cally for steady-state and fluctuating-pressure measurements and for buffet response measurements.

The TACT aircraft was more completely instrumented for buffet testing than any previous research aircraft. In addition to the thorough instrumentation for steady-state measurements, there were 25 dynamic-pressure transducers on the wing at locations which corresponded to locations on the two 1/6-scale models. The TACT aircraft was also instrumented with strain gages and accelerometers for buffet response measurements. In addition to the advantages of the abundance of instrumentation on the TACT aircraft, major improvements were made in the statistical accuracy of the flight-test buffet excitation and response data.

This report presents the results of the buffet research conducted as part of the F-111 TACT Research Program. It presents separately: (1) the correlation of wind-tunnel and flight measurements of buffet excitation, and (2) a method for prediction of buffet response based on fluctuating-pressure measurements and correlation of predicted and measured buffeting of the F-111 TACT aircraft.

NOTATION

a_T	total root-mean-square normal acceleration
AR	aspect ratio
b	semispan length
C_p	pressure coefficient
c	chord length
$\bar{c}$	mean aerodynamic chord
E	buffet excitation coefficient
f	frequency
G	power spectral density of pressure
h	altitude
K	damping parameter
LE	leading edge
i	incidence angle (referred to model centerline)
M	Mach number
p	pressure
q	dynamic pressure

Q	generalized force
R	Reynolds number
rms	root mean square
S	wing area
T	total time of record included in analysis
TR	taper ratio
t	thickness
V	velocity
x	chordwise position from LE
α	angle of attack (referred to chordline at wing pivot)
ζ	damping ratio
Γ	dihedral angle
γ	coherence function
η	ratio of span station to semispan
Λ	sweep angle
ρ	free-stream density
σ_T	total root-mean-square bending moment acceleration

Abbreviations:

A/C	aircraft
AL	aluminum model
BD	bending
CG	center of gravity
CGA	acceleration at center of gravity
FVB	1st fuselage vertical bending
GVT	ground vibration test
LWT	1st left wing torsion
PSD	power spectral density
RMS	root mean square
RWA	acceleration at right wing tip
RWT	1st right wing torsion
SC	scale
ST	steel model
TORS	torsion
WASB	1st wing antisymmetrical bending
WAST	1st wing antisymmetrical torsion
WSB	1st wing symmetrical bending

2WSB   2nd wing symmetrical bending

WST   1st wing symmetrical torsion

W/T   wing tip

WIND-TUNNEL MODELS AND AIRCRAFT

The 1/6-scale semispan model of the F-111 TACT is shown installed in the Ames 11- by 11-Foot Transonic Wind Tunnel in Figure 7 along with some pertinent dimensions. The model was mounted on a subfloor strain-gage balance. All slots in the tunnel floor were sealed.

Two wings which could be positioned at selected sweep angles were tested. To give a variation of static deformation under load, one wing was made of solid aluminum. The 1/6-scale semispan configuration was chosen for the TACT buffet investigation to be consistent with a previously tested 1/6-scale F-111A model (Ref. 12). As with the F-111A model, it was desirable to use the largest model that would not exceed reasonable blockage constraints in the 11-foot tunnel. The benefits of the large solid metal models were large volume for instrumentation and high strength and rigidity for high angle-of-attack and high dynamic-pressure testing; they also made it possible to obtain maximum test Reynolds number. Both the steel and aluminum wings had 0.0032-m (1/8-in.) wide transition strips of 0.00016-m (0.0064-in.) diameter edge. All of the buffet tests were conducted with a solid steel horizontal tail at -4° incidence. The primary natural frequencies of the wings are given in Table 1 for $\Lambda = 26°$ and 35°. The frequencies, mode shapes and node lines were determined by vibration tests of the model installed in the wind tunnel.

The TACT aircraft (Figure 8) is described in detail in Ref. 13. The main features of the geometry are the variable sweep and supercritical airfoil section. Of special advantage to the buffet tests are the dry wing, the ability to achieve adequate lateral and directional control with empennage controls (wing spoilers were not used while fluctuating pressures were measured), and sufficient thrust to hold reasonably steady conditions at high angles of attack. The primary natural frequencies of concern to the buffet excitation investigations and the response predictions are given Table 2. Details of the natural frequencies and mode shapes of the aircraft as determined by ground vibration tests are given in Ref. 15. A complete discussion of the structural dynamic analysis employed for the buffet prediction part of the present investigation is given a following section of the report.

INSTRUMENTATION

A main feature of the TACT models and aircraft is the abundance of steady and fluctuating pressure instrumentation at matching locations. This section describes the fluctuating pressure instrumentation and some related buffet response instrumentation. The steady pressure instrumentation is described by Kinsey and by Pyle (Ref. 13).

The location of the fluctuating pressure instrumentation in the models and aircraft are shown in Figure 9.

6

Models

The steel and aluminum semispan-wing models are left-wing panels. Each of the model wing panels had 50 dynamic-pressure transducers and the model horizontal tail had six dynamic-pressure transducers installed by the technique described for the third-phase tests of the F-111A model (Ref. 12). The transducers that were in the chordwise rows were aligned with the free-stream flow at $\Lambda = 26°$. The transducers are small differential-pressure units (Kulite model XCQL-7-093-4D); they are cylindrical in shape with an outside diameter of 0.00236 m (0.093 in.) and a length of 0.00952 m (0.375 in.). The transducers were installed in the models in removable blocks which were secured in slots cut into the wing and tail surface. The axes of each transducer was parallel to and slightly beneath the model surface, and the pressure sensing diaphragm was in the small cavity formed by a (0.00127-m (0.050-in.) diameter static-pressure orifice and the tip of a 0.00236-m (0.093-in.) diameter drilled hole. It was determined by test that the submerged configuration had a usable pressure-fluctuation range from zero to at least 7000 Hz. Some attenuation of the signals above 7000 Hz was present due to the orifice and cavity.

Two accelerometers were installed at the tips of each model wing, and semi-conductor strain gages were installed at the wing roots to measure fluctuating bending and torsional moments. The fluctuating pressure, acceleration and moment signals were amplified, high-pass filtered at 5 Hz to remove the steady-state components of the signals and then recorded on magnetic tape. The tape recording system used was an 80-channel FM-multiplex system with a useable useable frequency range from zero to 16,000 Hz.

The steel wing contained oil supply tubes and orifices along the 5% and 70% chordlines on the upper surface and 5% chordline on the lower surface to provide for fluorescent-oil studies of the flow. The orifices were drilled into the supply tubes with a spacing of 0.024 $\bar{c}$ to give an even dispersion of the oil on the wing surfaces.

Aircraft

There were twenty-five dynamic pressure transducers in the right wing of the aircraft. The same model of Kulite transducer was used in the aircraft as in the 1/6-scale wings; however, there was an important modification. An extremely thin, but opaque, aluminum coating was vapor deposited onto the silicon pressure sensitive diaphragm of the transducers that were installed on the upper surface of the wing. This was deemed necessary after initial flights in which it was found that extraneous fluctuating pressure signals could be caused by the light sensitivity of the transducers. Tests showed that very small changes in orientation of the tranducer diaphragm to direct radiation of sunlight would cause outputs equivalent to pressures greater than 3,447 N/m² (0.5 lb/in.²). In the aircraft, the transducers were installed in removable fixtures with the diaphragms parallel to the surface and submerged about 0.00076 m (0.030 in.) behind 0.0013-m (0.050-in.) orifices.

Strain gages and accelerometers were installed in the aircraft at several locations. For flights on which buffet excitation was investigated, outputs from right-wing and left-wing root bending-moment gages, a right-wing-tip accelerometer, and an accelerometer at the c.g. were recorded. The aircraft fluctuating pressure, acceleration, and moment signals were high-pass filtered

7

at about 3 Hz to remove steady-state or short-period-motion induced components of the signals, then amplified and recorded by an on-board tape recorder. The 29 channels of unsteady data plus an angle-of-attack signal were recorded on five of the available tape tracks by a constant-bandwidth FM-multiplex system.

TEST TECHNIQUE

Models

The wind-tunnel tests were conducted in two phases. The first phase was for surface-flow visualization using the steel wing prior to the installation of the pressure instrumentation. The second phase included the tests of the fully instrumented steel and aluminum wings to measure the fluctuating pressures and model responses. For both phases, tests were conducted at Mach numbers from 0.7 to 0.95 at Reynolds numbers of 7×10^6, 10.5×10^6, and 14×10^6 based on $\bar{c}$ and with wing-sweep angles at 26°, 35°.

Flourescent oil was used for the flow visualization, and photographic records were made at each test condition with still and motion picture cameras. Angle of attack was varied from -5° to +25° for the oil-flow tests. Prior to taking each set of photographic data, oil was momentarily ejected onto the wing and the flow allowed to stabilize. Oil-flow control valves were off during the picture-taking sequences.

Pressure fluctuations were measured at most of the above mentioned test conditions at angles of attack from 7° to 15°. Model strength limitations, however, restricted the maximum angle of attack in some cases. The dynamic pressure transducers were calibrated before each wind-tunnel start. Recordings of 1-minute length were made for each test condition after amplifiers automatically adjusted gains to obtain maximum amplitudes allowed by the tape recorder.

Aircraft

Fluctuating pressures and the corresponding buffet response were measured on the TACT aircraft at wing sweep angles of 26° and 35°, Mach numbers of 0.8 and 0.9, and at dynamic pressures of about 14,364, 21,546, and 28,728 N/m² (300, and 450, and 600 lbs/ft²). Data were obtained in continuous turn maneuvers at various constant mean angles of attack within the range from 7° to 13°. Some data were also obtained at cruise conditions.

In order to maximize the statistical accuracy of the data, pilots were requested to record data for 60 seconds while holding angle of attack, Mach number, and altitude as steady as possible. Target boundaries of maximum allowable deviation about the mean conditions were specified for α at ±0.5°, for M at ±0.01, and for q at ±10%. For many conditions, 60 seconds or more of continuous data were recorded within the specified boundaries. When flight conditions within the boundaries could not be sustained for 60 seconds, the conditions were usually repeated until a total of 60 seconds of data was recorded. Figure 10 shows some typical time histories of M, q, and α which illustrate the skillfulness of the pilots in holding steady conditions with the TACT aircraft. At $\alpha = 9°$, which was near buffet onset for $\Lambda = 35°$ and M = 0.80, a continuous recording of data for 120 seconds was obtained with α variations not over ±0.1°. For $\alpha = 10°$ and 11.9°, when buffet intensities were high, conditions were still

held within the specified boundaries for relatively long periods.

The dynamic-pressure transducers were calibrated before or after each TACT flight which was conducted to measure the buffet excitation. Transducers were powered by a 28-V supply for some flights and by a 12-V supply for some flights. Thus a variation of transducer sensitivities was obtained for different ranges of angle of attack without changing fixed gain resistors in the signal conditioning system. Angles of attack of 10° or less were scheduled when the 28-V supply was used and angles of attack of 10° and more were scheduled when the 12-V supply was used. The fixed gain resistors were selected to give the highest possible signal amplitudes for tape recordings without exceeding limits of the recorder. The selection of sensitivities for each transducer location was based on the previously obtained 1/6-scale model data.

DATA REDUCTION

Mean and fluctuating static pressures on the 1/6-scale models and aircraft were reduced to mean static pressure cofficients (C_p) and fluctuating pressure coefficients ($C_{p_{rms}}$). The fluctuating pressure signals were band-pass filtered prior to processing by the multichannel rms system. The frequency range between 3 dB points was 5 Hz to 16,000 Hz for the scale-model data for 2.5 Hz to 2500 Hz for the aircraft data. Power and cross-spectral densities of the pressure fluctuations at selected conditions were obtained using a hybrid analog-digital analysis process described in Ref. 16.

Test conditions in the wind tunnel are steady and, therefore, any time segments of the tape recordings for a given condition were acceptable for data analysis. For the flight tests, segments of the tape recordings suitable for analysis had to be carefully selected by studying digital printouts (at a rate of 1/sec) of important flight parameters and analog strip charts of the pressure-fluctuation time histories. The criteria for selecting the time segments for data analysis was that conditions remained with the tolerance previously specified for α, M, and q. After the time segments were selected, the arithmetical means of α, M, and q were computed from the digital printout.

CORRELATION OF WIND TUNNEL AND FLIGHT
MEASUREMENTS OF BUFFET EXCITATION

The correlation of wind-tunnel and flight measurements of buffet excitation was one of the main objectives of the Ames Research Center participation in the TACT program. Procedures for scaling pressure fluctuations had been well established, but some references including Riddle (Ref. 17) and Coe and Riddle (Ref. 18) have shown that for some test conditions pressure fluctuations tended to couple with model wing torsion and second-bending mode vibrations. Consequently, there was still some uncertainty whether pressure fluctuations on non-dynamically scaled models truly represent the pressure fluctuations on elastic aircraft. In question are the effects of static and dynamic elasticity and effects of Reynolds number.

Root-Mean-Square Pressure Fluctuations

Correlation of wind-tunnel and flight data.- Pressure fluctuations measured at corresponding locations on the upper wing surfaces of the 1/6-scale models and aircraft are presented in Figure 11. The data show the variation of $C_{p_{rms}}$ with α for test conditions that yielded the closest matching of Reynolds numbers in the wind tunnel and flight. For M = 0.80, the model data are from the steel wing at $R_{\bar{c}} = 14 \times 10^6$ (Figs. 11(a) and (c)). Model strength limits restricted the maximum Reynolds number to $R_{\bar{c}} = 10.5 \times 10^6$ at M ▫ 0.90; so the data from the aluminum wing were arbitrarily selected for presentation at these conditions (Figs. 11(b) and (d)). The dashed lines connecting some data points indicates an author judgement of the probable variations of $C_{p_{rms}}$ with α.

The data in Figure 11 generally show excellent correlation of the pressure-fluctuation measurements on the models and aircraft except in regions of shock waves and separation boundaries. This judgement of excellence is based on the authors' knowledge of the state of the art of random pressure-fluctuation measurements, on the relatively meager previous wind-tunnel-to-flight correlations and on the authors' experience with model-to-model correlations. The data show some significant differences in angle of attack of the model and aircraft where the pressure fluctuations suddenly increase due to the occurrence of a shock wave or separation boundary at a measurement location. These differences are due to some combination of effects of the various wind-tunnel factors listed in Figure 1 that can affect the correlation of data. It is expected that Reynolds number simulation and static-elastic effects are the most important effects, but the separation of these effects is not apparent due to inconsistencies of the data. The main problem is that in some cases the rise in $C_{p_{rms}}$ occurred at lower α on the aircraft than on the model (Figs. 11(a) and (d)) and in other cases at lower α on the model than on the aircraft (Figs. 11(b) and (c)). Static elasticity should have a larger effect on the data at $\eta = 0.910$ than at $\eta = 0.744$ or $\eta = 0.578$. Such a trend in data can be noted, but additional analyses including computations of the deformed shapes of the models and aircraft under load would be needed to further account for effects of Reynolds number and static elasticity.

Reynolds number and static elastic effects.- Reynolds number and static elasticity have been mentioned in the foregoing presentation of data as causes of discrepancies in the correlation of the pressure fluctuations measured on the models and aircraft. The separate effects of Reynolds number and elasticity could not be distinguished because both Reynolds number and wing shape varied in the correlations. The data from the steel- and aluminum-wing models almost circumvent this problem. The steel wing at $R_{\bar{c}} = 14 \times 10^6$ deformed under load to two-thirds the deflection of the aluminum model at $R_{\bar{c}} = 7 \times 10^6$ so that the shapes of the wings were similar. When the wings were tested at $R_{\bar{c}} = 10.5 \times 10^6$, the aluminum-wing deflection was three times the deflection of the steel wing. Figure 12 shows the Reynolds number effects and Figure 13 the static elastic effects on the pressure fluctuations at three span stations for $\Lambda = 26°$ and M = 0.80.

Figure 12 shows some definite trends resulting from Reynolds number effects. The shock wave and separation boundary occurred at x/c = 0.06 at approximately 1° lower angle of attack at $R_{\bar{c}} = 14 \times 10^6$ than at $R_{\bar{c}} = 7 \times 10^6$. This trend is consistent with the observed movement of the shock wave to x/c = 0.06 at lower

angle of attack on the aircraft than on the model. The pressure fluctuations were relatively unaffected by Reynolds number within the region of separated flow downstream of $x/c = 0.45$ and $\eta = 0.910$ and $\eta = 0.744$ at all angles of attack and at $\eta = 0.578$ at angles of attack less than 12°. At $\eta = 0.578$ for $\alpha > 12°$, there was a large effect of Reynolds number on $C_{p_{rms}}$. The pressure fluctuations appear to become independent of dynamic pressure, possibly due to the influence of a leading-edge vortex.

With respect to effects of static elasticity, Figure 13 shows that the shock wave and separation boundary occurred at $x/c = 0.06$ at a lower angle of attack on the steel wing than on the aluminum wing. The data at $\eta = 0.910$ indicate that the section angle of attack near the wing tip was about 1° less on the aluminum wing than on the steel wing. The data at other span stations show less effect of elasticity as expected. As with the Reynolds number effects, the pressure fluctuations were relatively uneffected by static elasticity within the separated flow downstream of $x/c = 0.45$. Some significant differences in the pressure fluctuations on the steel and aluminum wings occurred at $\eta = 0.578$ at $\alpha > 11°$. However, the differences are not so large as the previously noted Reynolds number effects at $\eta = 0.578$ at high angle of attack.

A comparison of the pressure-fluctuation measurements at $x/c = 0.06$ in Figures 12 and 13 shows the counteracting influences of Reynolds number and static elasticity on the position of the shock wave. The shock wave has moved upstream with increasing Reynolds number and downstream due to increasing elasticity. Therefore, this compensating effect probably improved the correlation between the model and aircraft pressure-fluctuation measurements (Fig. 11).

As previously mentioned, the TACT program is providng more complete information for the wind-tunnel/flight correlation of buffet excitation data than any previous program. A major asset of the analysis of the data is the static mean pressure distributions obtained on the models and aircraft and the flow visualizations on the steel-wing model. Examples of some steady and fluctuating pressure distributions and corresponding photographs of fluorescent oil are shown in Figure 14 for $\Lambda = 26°$ and $M = 0.80$. The steady pressure distributions on the model and aircraft are distinguished by solid and dashed lines. The fluctuating pressures on the model are presented by solid lines where the data follows reasonable trends and by dashed lines between measured values the steady pressure distributions and photographs indicate the probability of high pressure fluctuations due to the shock waves. The fluctuating pressures measured on the aircraft are indicated by the symbols. When the locations of shock waves are defined, as in Figure 14, and the probable steep gradients in the chordwise distributions of $C_{p_{rms}}$ are considered, the overall excellent correlation between the wind tunnel and flight fluctuating pressures is as good as the correlation of wind tunnel and flight steady pressures. Additional correlations of wind tunnel and flight measurements of steady pressures are presented by Kinsey (Ref. 13).

Effects of dynamic pressure on flight data.- The previous correlations of pressure-fluctuation data (Figs. 11 and 14) compared $C_{p_{rms}}$ from the models at the highest test Reynolds numbers, to 14×10^6, with $C_{p_{rms}}$ from the aircraft at a Reynolds number of about 25×10^6. Both Reynolds-number values are based on $\bar{c}$. Some flight data were also obtained, however, at different altitudes to determine the combined effects of static elasticity and Reynolds number over a range

11

of flight Reynolds numbers. An example of the pressure-fluctuations measured at dynamic pressures of 14,364 to 28,728 N/m^2 (300 to 600 lbs/ft^2) and corresponding Reynolds numbers of 25 x 10^6 to 40 x 10^6 is given in Figure 15 for Λ = 26°, M = 0.80, and η = 0.744. These data show very little effect of dynamic pressure on $C_{p_{rms}}$. Only the data at x/c = 0.63 and x/c = 0.90 indicate an α shift of 0.1° to 0.3°, possibly due to the greater washout of the wing at high dynamic pressures. The $C_{p_{rms}}$ values measured at x/c = 0.45 do not show evidence of such an α shift, however. It is interesting to note the extreme sensitivity of the fluctuating pressures to angle of attack at x/c = 0.06 and 0.20 near α = 10°. It can be seen that the shock wave on the TACT supercritial wing moved from x/c = 0.20 to 0.06 with an angle-of-attack variation of less than a few tenths degree.

Pressure fluctuations on lower surface of aircraft wing.- Typical pressure-fluctuation measurements on the lower surface of the aircraft wing are illustrated in Figure 16. These data show that the pressure fluctuations on the lower surface of the wing increase significantly at the same angles of attack associated with increasing buffet excitation on the upper surface of the wing. Below α = 10°, the $C_{p_{rms}}$ values were about 0.006, which is the generally expected value for subsonic attached-turbulent boundary layers (Refs. 19, 20). At α > 10° the lower surface pressure fluctuations increased with α to maximum $C_{p_{rms}}$ values between 0.015 and 0.025 which were 15% to 20% of the corresponding measurements on the upper surface. The variation of q, which affects Reynolds number and wing distortion, did not affect the lower surface pressure fluctuations.

Pressure fluctuations were also measured on the lower surfaces of the 1/6-scale model wings. These data are not presented and correlated with the flight data because of the dominating effects of wind-tunnel environmental turbulence and noise.

PSDs of Pressure Fluctuations

Typical PSDs of pressure fluctuations on aircraft.- PSDs of the pressure fluctuations on the aircraft, which are typical of the broad range of data examined, are shown in Figure 17. These PSDs are presented for angles of attack of approximately 10° and 12°; this was done to illustrate the differences between upper- and lower-surface measurements, the general shapes of the PSDs, and some effects of dynamic motions of the wing on the data. The frequencies of important wing vibration modes are noted in the figure. Torsional modes are indicated by a band of frequencies since there are several modes involving torsional motion near the same frequency.

One of the reasons for looking at the PSDs of the lower surface pressure fluctuations was the expectation that the increase in $C_{p_{rms}}$ on the lower surface with α (Fig. 16) was due to increasing dynamic motion of the wing as the upper-surface buffet excitation increased. The data in Figure 17 indicate that this expectation was not correct and that the increase in $C_{p_{rms}}$ on the lower surface was due to an increase in the spectral level at all frequencies. The lower surface pressures tended to couple with torsional motion, although in some cases, like the Λ = 35° M = 0.80 case shown in Figure 17, such motion dependency of the pressures was negligible.

The PSD levels of the pressure fluctuations on the wing upper surface were generally from 1 to 2 decades higher than the corresponding levels on the lower surface. Coupling of the pressure fluctuations on the upper surface with dynamic motions was in evidence in less than 5% of the approximately 500 PSDs examined. In most cases, when coupling occurred, torsion and/or second bending motions were involved. Coupling effects were most pronounced at angles of attack near buffet onset and were usually negligible when the pressure fluctuations were large. However, exceptions are shown in Figure 17 for $\Lambda = 26°$, $M = 0.80$, $x/c = 0.90$, and for $\Lambda = 35°$, $M = 0.90$ at $\alpha = 12°$. These PSDs show coupling with torsion and second antisymmetric-bending modes in one case and coupling with the torsion modes in the second case. No significant coupling of first bendng modes and pressure fluctuations has been noted in the data. The extent of such coupling is important to this investigation since the wind-tunnel models were nominally rigid. If coupling effects were to dominate the pressure fluctuations, then the use of such models for prediction of the aircraft buffet excitation would be inappropriate.

Wind-tunnel-to-flight correlation of PSDs.- Samples of the correlations of PSDs of the pressure fluctuations on the 1/6-scale models and aicraft are in Figure 18. On the basis of the overall frequency range of the data the correlations of the PSDs are considered to be excellent. However, it should be kept in mind that the important vibration modes of the aircraft buffeting are within a relatively small range of nondimensional frequencis from about 0.03 to 0.3. Figures 18(a) shows one of the excellent correlations of PSDs to illustrate the output of the hybrid analog/digital spectral analyzer used at Ames (Ref. 16). The figure is at large scale to show the computer plotted output of the correlation, wherein separately analyzed files of the model and aircraft data were called and plotted with the application of appropriate nondimensionalizing variables. In Figure 18(a) each symbol ("A" for model and "B" for aircraft) represent a fixed bandwidth in the stepped-frequency PSD analysis. In the remainder of Figure 18 the PSD correlations have been traced to more clearly distinguish the model and aircraft PSDs.

Figure 18(b) shows the correlation of PSDs of pressure fluctuations at three span stations for $\Lambda = 26°$, $M = 0.80$, and $\alpha \simeq 9°$, a condition of relatively low buffet excitation (see Fig. 11(a)). For this condition, effects of aircraft dynamic motions and wind-tunnel environmental noise are clearly seen. The aircraft torsional modes have the most pronounced effect at $\eta = 0.910$, particularly at $x/c = 0.64$. The prominent peaks in the model at $fc/V = 1.2$, 4.5, and 9.0 have been identified to be due to compressor-blades crossing the stator blades and to the transonic test-section slots (Ref. 21). The origin of the peaks in both model and aircraft data at $fc/V = 0.6$ may be aerodynamic resonance due to upstream propagating pressure waves as discussed in Ref. 22.

Figures 18(c), (d) and (e) show the correlation of PSDs of pressure fluctuations for conditions when the buffet excitation was medium and high relative to the range of measurements (see Fig. 11). The data in Figure 18(c) are for $\Lambda = 26°$, $M = 0.80$, and $\alpha = 11.1°$. The data in Figure 18(d) are for $\Lambda = 35°$, $M = 0.80$, and $\alpha = 10°$, and in Figure 18(e) for $\Lambda = 35°$, $M = 0.90$, and $\alpha = 12°$. These data show that the correlations of PSDs generally improved with increasing pressure fluctuations. It is quite clear from the correlations that the reduced frequency parameter, fc/V, and the nondimensionalization of the PSDs by GV/q^2c are valid. Figure 18(c) shows that for $\Lambda = 26°$ PSD correlations were

13

better to excellent for spanwise stations inboard of η = 0.910. For Λ = 35° PSD correllations were also good to excellent at η = 0.910 (Figure 18(d) and (e)). In Figure 18(e) it is of interest to note corresponding peaks in the model and aircraft PSDs near fc/V = 0.18. The peaks in the aircraft PSDs coincide with the torsional modes, whereas the peaks in the model PSDs occur between the second bending and torsion modes.

Coherence and Phase Angle of Pressure Fluctuations

A typical analysis of the spatial correlation of the pressure fluctuations on the models and aircraft is given in Figure 19. Shown is the coherence and phase angle (θ) between fluctuations at x/c = 0.45 and x/c = 0.63 at η = 0.744 for M = 0.80 and α = 12° for Λ = 26° and Λ = 35°. Generally, the trends of these data are the same with the exception that the results for Λ = 26° show a strong coherence of pressures on the aircraft wing at a frequency corresponding to torsional vibrations. The excellent agreement of the phase angles confirms the acceptability of the nondimensional-frequency parameter for scaling the buffet excitation. Equal phase angles for a given nondimensional frequency mean that the dominant boundary-layer turbulence causing the pressure fluctuations is convecting between x/c = 0.45 and x/c = 0.63 at the same velocity-to-free-stream velocity ratio on the model and aircraft.

Concluding Remarks on Correlation of Wind Tunnel and Flight Measurements of Buffet Excitation

Generally, there was relatively good agreement between measurements of the pressure fluctuations on the models and aircraft in regions of separated flow. At the shock-wave boundaries of the separated flow, good correlation cannot be expected due to Reynolds number and static-elastic effects that displace the boundaries. Reynolds number and static-elastic effects on the position of the shock wave tend to be compensating. The PSD analysis of the pressure fluctuations show evidence of dynamic-elastic effects in both the aircraft and model data. At certain test conditions, the fluctuating pressures may interact with torsional and/or second-bending natural vibration modes of the aircraft and model wings. Generally this coupling of the pressures with the vibratory motion was small or negligible when the buffet excitation pressures were high.

PREDICTION OF F-111 TACT AIRCRAFT BUFFET RESPONSE

It was pointed out in the Introduction that buffet predictions prior to the work of Butler and Spavins (Ref. 8) and the TACT Program (Ref. 13) generally have been disappointing. Correlations of predicted buffet response spectra with flight measurements typically have shown factors of 5 to 10 or even larger differences in spectral peaks for important modes. There are several possible reasons for the poor correlations. The most important reasons are:

1. The nonstationarity and short time durations of flight data, which can affect the correlations for any method of buffet prediction.

2. The assumption required for non-elastically scaled models that modal aerodynamics are separable (buffet pressures are unaffected by model motions).

3. The use of potential-flow unsteady aerodynamic analysis to estimate aerodynamic damping.

4. Insufficient pressure measurements for the fluctuating-pressure method and simplifications of spatial correlations.

5. Reynolds number effects.

6. Static and dynamic aeroelastic differences.

7. Possible pitch rate effects.

The disappointing history of buffet predictions is what prompted this research to be included as part of the TACT Program. As previously mentioned, the TACT aircraft provided a large improvement in the statistical accuracy of buffet flight-test data. Also, it was proposed to evaluate a simpler more direct approach for predicting the generalized buffet forces on the aircraft from fluctuating-pressure measurements obtained from a wind-tunnel model. Aerodynamic damping also would be predicted from model damping measurements.

Overview of Method

There are two significant differences between the present method and previous fluctuating-pressure methods. First, for the present method, the measured fluctuating-pressure time histories were summed on a real-time basis to yield the generalized aerodynamic forces for selected modes. This approach is much simpler and more direct than the approaches of Refs. 11 and 12 which required the analyses of a large number of cross spectra to represent the complex spanwise and chordwise buffet excitation. Second, experimental measurements of aerodynamic damping for limited pivotal modes that are clearly distinguishable in the model response were used in conjunction with a similarity analysis of damping to predict the total damping of the aircraft for all of the selected modes.

The various functions involved in the method and their relationships to the prediction of buffeting are shown in Figure 20. The three major elements of the buffet prediction are the model tests, aircraft structural dynamic analysis and the calculation of the aircraft forced response.

The data from the model tests include fluctuating-pressure and buffet response time histories. The fluctuating pressures must be measured at sufficient locations on the model for accurate integration to the overall buffet excitation.

15

For the F-111 TACT model tests there were 62 fluctuating pressure transducers on the 1/6-scale semispan wing and tail surfaces (Figure 9). The buffet response time histories are used for damping measurements.

Because fluctuating-pressure models are not dynamically scaled in order to measure motion independent buffet excitations, the model and model support should be as rigid as practical. However, some compromise on the wing construction material is necessary to allow sufficient wing responses relative to support elastic and joint motions so that aerodynamic damping can be evaluated at least for the fundamental bending and torsion modes. It is important that structural damping is as small as possible relative to the total damping. For this investigation both aluminum and steel semispan wings were tested and it was found that the aluminum wing yielded better damping measurments. As part of the model tests it is necessary to determine the generalized masses, natural frequencies and structural damping for the modes that yield total damping measurements. This information is applied to the damping measurements to determine the aerodynamic damping parameter, K_p, for each of the pivotal modes. K_p thus accounts for the model structure and wind tunnel test conditions. K is the same damping parameter defined by Butler and Spavins (Ref. 8).

$$K_p = \frac{M_p \omega_p V_{WT} \zeta_{ap}}{q_{WT} S} \tag{1}$$

$$\zeta_{ap} = \zeta_{tp} - \zeta_{sp} \tag{2}$$

where M_p = generalized mass of pivotal mode

ω_p = natural frequency of pivotal mode

V_{WT} = freestream velocity in wind tunnel

ζ_{ap} = aerodynamic damping ratio for pivotal mode

ζ_{tp} = measured total damping ratio for pivotal mode

ζ_{sp} = measured structural damping ratio for pivotal mode

q_{WT} = freestream dynamic pressure in wind tunnel

S = area of model wing

For each mode desired in the buffet response prediction the aircraft structural dynamic analysis provides normalized modal displacements at the centroids of panels over which the pressures from each pressure transducer are assumed to be uniform. The normalized modal displacements $[h_i]$ for the ith mode are then combined with the aircraft panel areas $[A]$ and model pressures $\{p\}$ to yield the total generalized aerodynamic force Q_{ti} for the ith mode.

$$Q_{ti} = [h_i][A]\{p\} \tag{3}$$

For this investigation, because the pressure fluctuations were measured on a half-span model, it was assumed that the pressures on the right-and left-hand lifting surfaces were symmetrical and uncorrelated. Therefore,

$$Q_{ti} = (Q_{tiR}^2 + Q_{tiL}^2)^{\frac{1}{2}},$$

16

where Q_{tiR} and Q_{tiL} are the right- and left-hand total generalized aerodynamic forces for the ith mode. Then, to take into account the right- and left-hand modal deflections on the aircraft and the fact that pressures were measured on a semispan model,

$$Q_{ti} = [[h_{iR}]^2 + [h_{iL}]^2]^{\frac{1}{2}} [A_{AS}] [v_{MS}] [k] \qquad (4)$$

where $[h_{iR}]$ and $[h_{iL}]$ are the right- and left-hand normalized modal displacements at the centroids of the panel areas, $[A_{AS}]$ are the panel areas on the aircraft semispan, $[v_{MS}]$ are the voltage outputs from the pressure transducers on the model semispan and $[k]$ are the pressure transducer sensitivity factors.

The motion-independent generalized force, Q_{ii}, is determined from the power spectrum of Q_{ti} where

$$G_{Q_{ii}}(f) = G_{Q_{ti}}(f) - G_{Q_{di}}(f) \qquad (5)$$

and Q_{di} is the motion-dependent generalized force. (The estimation of $G_{Q_{di}}(f)$ will be discussed in a following paragraph). After $G_{Q_{ii}}(f)$ is determined it is is then reduced to the generalized aerodynamic force coefficient

$$E = \frac{G_{Q_{ii}} V_{WT}}{S_A^2 q_{WT}^2 \bar{c}_M} \qquad (6)$$

where $\quad G_{Q_{ii}} = G_{Q_{ii}}(f_n)$

f_n = resonant frequency of the aircraft i^{th} mode

S_A = aircraft wing area

V_{WT} = free stream velocity in wind tunnel

q_{WT} = free stream dynamic pressure in wind tunnel

$\bar{c}_M$ = mean aerodynamic chord of model wing

In addition to the modal displacements (Figure 20), the structural dynamic analysis also yields frequency dependent generalized masses and frequencies, including the effects of fuel weight, and normalized aerodynamic damping, including the effects of altitude, for all modes selected for analysis. The normalized damping for each mode is the theoretical aerodynamic damping for the mode divided by the theoretical aerodynamic damping for a pivotal mode (bending or torsion). The pivotal modes are the primary bending and torsion modes with similar mode shapes for the aircraft and model.

The aircraft structural dynamic analysis including the aerodynamic damping analyses is a multidegree-of-freedom analysis that accounts for modal coupling. The combination of the aerodynamic damping parameter, K_p, with the generalized masses, frequencies and normalized aerodynamic damping for the aircraft yield the damping for each of the aircraft modes and flight conditions selected for analysis,

$$\zeta_a(f,h) = \frac{K_p q_A S_A \zeta_{an}(f,h)}{M_A(w) \omega(f,w) V_A} \qquad (7)$$

17

$$\zeta_t(f,h) = \zeta_a(f,h) + \zeta_s \qquad\qquad (8)$$

where $\zeta_a(f,h)$ = aerodynamic damping as a function of frequency and altitude

$\quad\quad\;\; K_p$ = damping factor for pivotal mode (Eq. 1)

$\quad\quad\;\; q_A$ = dynamic pressure for aircraft flight condition

$\quad\quad\;\; S_A$ = area of aircraft wing

$\quad\quad\;\; \zeta_{an}(f,h)$ = normalized aerodynamic damping ratio as a function of frequency and altitude

$\quad\quad\;\; M_A(w)$ = generalized mass as a function of fuel weight

$\quad\quad\;\; \omega(f,w)$ = natural frequency as a function of frequency and fuel weight

$\quad\quad\;\; V_A$ = aircraft velocity

$\quad\quad\;\; \zeta_t(f,h)$ = total damping as a function of frequency and altitude

$\quad\quad\;\; \zeta_s$ = structural damping ratio

The final step in the buffet prediction method (Figure 20) is the calculation of the power spectral density of the forced response of the aircraft. The generalized aerodynamic force coefficients, generalized masses, frequencies and total damping are embodied in the PSD calculation for a range of frequencies that includes the selected modes. Details of the model tests, structural dynamics analyses and the TACT aircraft buffet predictions are given in following sections of the report. A preliminary evaluation of the method is also reported in Ref. 23 which describes in detail the prediction of the buffeting of the 1/6-scale TACT aluminum model.

Model Tests

Data processing.- Details of the 1/6-scale semispan model of the F-111 TACT aircraft, the instrumentation, test technique and general data reduction are given in previous sections of the report as they apply to the recording of the pressure fluctuations and model wing buffeting. All of the dynamic data were recorded at the time of the tests on a one-inch magnetic tape by an 80-channel FM-multiplex system. At a later date, when the modes to be included in the buffet predictions were selected and the normalized modal displacements [h_i] were tabulated, the magnetic tape was processed for each mode via an analog system shown in Figure 21 to yield the generalized force time history, Q_{ti}, (Eq. 4).

The flow chart in Figure 21 shows that the pressure-fluctuation time histories were high-pass filtered (3 dB at 1 Hz) and then attenuated by weighting factors that comprised the normalized products of $[[h_{iR}]^2 + [h_{iL}]^2]^{\frac{1}{2}}$, [A] and [k]. The attenuated time histories were then summed to yield the time histories of the separate upper- and lower-surface contributions to the generalized force; the lower-surface time history was then inverted and summed with the upper-surface time history to obtain and record a time history proportional to the total generalized force. For this investigation the wing and tail contributions to the generalized force were also recorded separately in order to study the effects of the wing and tail on the buffet excitation.

Mode shapes.- The mode shapes employed in the present analysis of the generalized aerodynamic forces were generated by General Dynamics Corp., Fort Worth Division, during the original structural dynamics analysis required for the TACT modification to the F-111 aircraft. Either numerically or experimentally determined mode shapes could have been used for the TACT analysis; however, the numerical mode shapes were used in this case to evaluate buffet predictions that could be made prior to aircraft manufacture. Six modes were selected to be included in the TACT aircraft buffet predictions. They are as follows:

1. 1st wing symmetrical bending, WSB

2. 1st fuselage vertical bending. FVB

3. 1st wing antisymmetrical bending, WASB

4. 1st right-wing torsion, RWT

5. 1st left-wing torsion, LWT

6. 1st wing symmetrical torsion, WST

The mode shapes for the selected modes and natural frequencies, which are in the range from 4.42 Hz to 17.14 Hz, are shown in Appendix A (Figure A1) and in Table 2. The modes were selected to provide a variety of mode shapes (wing bending vs fuselage bending vs wing torsion), and because they were expected to dominate the TACT aircraft buffeting. Also, the differences in the natural frequencies for the FVB and WASB modes and the RWT, LWT and WST modes are small; therefore, it was considered necessary to include all modes in the close-frequency groupings because of the possible influence of the forced response of each mode on the response of the neighboring modes.

Model paneling.- As previously mentioned the aircraft wing and tail were divided into panel areas, [A], over which the pressure fluctuations were assumed to be constant. Sketches showing the wing and tail panel areas, centroids and corresponding 62 locations of the pressure transducers on the 1/6-scale model are in Figure 22. It can be seen that the transducers were near the panel centroids for most of the panels with the exception of the panels bordering the wing and tail root chords. The normalized modal displacements, $[h_{iR}]$ and $[h_{iL}]$, at the centroids were determined by interpolation of the displacements at the modal-analysis grid points (Figure A1).

Generalized aerodynamic force.- Typical PSD's of predicted total generalized aerodynamic forces on the TACT aircraft are shown in Figure 23 for the WSB and WST modes (Modes 1 and 6). For all frequencies except near the model resonant frequencies, f_{nM}, the total generalized forces are unaffected by model motions and therefore $G_{Q_{ii}}(f) = G_{Q_{ti}}(f)$ at $f \neq f_{nM}$. At model resonant frequencies the effect of motion is to decrease the motion-dependent generalized force, $G_{Q_{di}}(f)$ in relation to the aerodynamic damping and amplitude near the modal resonant frequencies. Such an affect, which was discussed by Jones in Ref. 24, is shown in Figure 23 in the PSD for the WSB mode where a significant notch is apparent at 25 Hz. The notch is at the natural frequency of the 1st bending mode of the 1/6-scale aluminum wing. For this investigation $G_{Q_{ii}}(f)$ in the vicinity of f_n, was assumed to have a straight-line variation with frequency bridging the effects due to $G_{Q_{di}}$. Further, because $G_{Q_{ii}}(f)$ for all the selected aircraft modes appeared to be constant within a reasonable range of the aircraft resonant frequencies, $G_{Q_{ii}}$ has been evaluated only at the resonant frequencies.

Buffet excitation coefficients.- In order to conveniently account for the differences in the model and aircraft scale and wind-tunnel and flight conditions the generalized aerodynamic forces were reduced to buffet excitation coefficients, E, (Eq. 6). The buffet excitation coefficients obtained from the aluminum- and steel-wing models are shown in Figure 24 versus angle-of-attack for five of the modes selected for analysis. The aluminum-wing data were obtained at test Reynolds numbers of 10.5×10^6 and the steel-wing data were obtained at test Reynolds numbers of 14.0×10^6. Figure 24 shows that excitation coefficients evaluated from the aluminum- and steel-wing models were within a factor of 2 for all test points except for a few points at intermediate angles-of-attack at $\Lambda = 26°$ for the WASB mode (Figure 24(c)). This generally good agreement of E, which is on a mean-square scale, substantiates the repeatability of data and adds confidence to the excitation coefficients.

Effects of wing and tail.- The effects of the wing and tail on the buffet excitation obtained from the aluminum wing are shown in Figure 25. The results show that for the six modes selected for analysis the effects of the tail were negligible only for the WSB mode (Figure 25(a)) and for the WST mode (Figure 25(f)). For the other modes, FVB, WASB, RWT and LWT, the effects of the wing and tail varied with angle-of-attack (Figure 25(b) through 25(e)). The largest effects of the tail occurred for the FVB mode (Figure 25(b) and for the WASB Mode (Figure 25(c)). For these modes E due to the tail exceeded E due to the wing at the lower and higher test angles of attack. Consequently, these results show that the tail buffet excitation was a necessary part of this buffet response analysis. As would be expected, a relationship can be seen between the wing and tail excitation coefficients (Figure 25) and the modal displacements (Figure A1). The effects of the tail are insignificant for modes with small fuselage and empenage displacements, and they are more significant for the modes with large fuselage and empenage displacements.

Aerodynamic damping of pivotal modes.- As a necessary part of the model tests measurements were made of the total damping ratios of the 1st wing bending and 1st wing torsion modes of the 1/6-scale aluminum model. The data for these modes, which are referred to as pivotal modes, are shown in Figure 26. The data were obtained from the model buffet response time histories using the Randomdec system described in Ref. 25.

As previously mentioned the aluminum-wing model yielded more accurate aerodynamic damping information than the steel-wing model. This result was expected because the structural damping for the aluminum wing was less than the structural damping for the steel wing. The structural damping ratio of the aluminum model was 0.005, which was from 7- to 14-percent of the total damping ratio for the bending mode and 14- to 20-percent of the total damping ratio for the torsion mode. Also, in order to yield accurate damping measurements for the pivotal modes, it was important that the modes were clearly separable by bandpass filtering to allow the analysis of an apparent single-degree-of-freedom time history. Table 1 shows that the resonant frequencies of the primary vibration modes of the model were sufficiently different to allow the modal separation. Details of the model structural dynamic characteristics, buffet response and damping measurements are given in Ref. 23.

To apply the model total damping measurements (Figure 26) to the prediction of the aircraft aerodynamic damping, the model structure and wind-tunnel test

conditions are accounted for in the conversion of the aerodynamic damping, ζ_{ap}, to the aerodynamic damping parameter, K_p(Eq. 1). The variation of K_p with angle of attack for the (pivotal wing bending and torsion modes is shown in Figure 27. It is of interest to note that these data agree reasonably well with similar data obtained by Butler and Spavins using a 1/8-scale aluminum model of the F-111 TACT (Ref. 13).

Structural Dynamic Analysis

After the excitation forces of the selected modes and damping data for pivotal modes have been determined, the next step is to develop the appropriate equations of motion that describe aircraft buffet response. In addition, damping must be determined for all the selected modes including the pivotal modes that exist on the model in such a way that the real flow effects are accounted for as well as the modal coupling that exists for the full scale aircraft. Also, the miss-match between modes on the model and the aircraft must be considered in the damping analysis. All of these effects plus the effects of altitude and fuel weight must be accounted for in the modal frequencies, damping and generalized masses that are inserted into the equations of motion. The solution to these final equations produces the predicted aircraft buffet response. This section describes the problems and how they are solved.

Equations of Motion.-   The basic working tool for this section is the standard set of equations of motion for modeling dynamic response of a flexible aircraft. The matrices involved are generally diagonal in form with exception of those associated with the aerodynamic forces produced by the elastic response of the aircraft. With certain assumptions, however, it is possible to utilize eigenvalues of this equation that are obtained in routine flutter analyses to reduce all of the matrices to diagonal form. The diagonalized equations may be simply solved with techniques that are easily programmed on small personal computers. This subsection therefore describes the diagonalization process and also the implications of the assumptions that are necessary to accomplish the diagonalization of the matrices.

The equations of motion for an aircraft with flexible degrees of freedom (first wing symmetric bending, first wing symmetric torsion, etc.) can be expressed in a matrix equation for generalized coordinates which are the normal modes of vibration. The form is

$$([M_i(\omega^2 - \omega_i^2 - i2\omega\omega_i\zeta_{i_s})] + [Q_{ij}]) \{r_i\} = \{Q_{i_B}\} \qquad (9)$$

where

M_i = generalized mass of the ith mode

ω_{i_s} = undamped natural frequency of the ith mode

ω = exciting frequency

ζ_{i_s} = structural damping for the ith mode

Q_{ij} = generalized aerodynamic force for pressures due to the jth mode motion working on deflections of the ith mode

r_i = generalized coordinate response of the ith mode

Q_{i_B} = generalized aerodynamic force for the buffeting pressures working on deflections of the ith mode

21

For purposes of discussions, Equation 9 can be written in a more compact form:

$$[D - I]\{r_i\} = \left\{\frac{Q_{i_B}}{M_i \omega^2}\right\} \qquad (10)$$

where

$$[D] = \left[\frac{-\omega_i^2 - i2\omega\omega_i\zeta_{i_s}}{\omega^2}\right] + \left[\frac{Q_{ij}}{M_i\omega^2}\right]$$

I = identity matrix

This form leads directly to the eigenvalue/eigenvector problem from which the diagonalization is evolved. The purpose of the diagonalization is to produce a set of equations that are uncoupled mathematically but are effectively coupled through the eigenvalues obtained from solutions to the fully coupled equations.

The eigenvalue/eigenvector form of Equation 10 is

$$[D - I\lambda_i]\{\Phi_i\} = \{0\} \qquad (11)$$

where

λ_i = eigenvalue of the ith mode

Φ_i = eigenvector of the ith mode

The eigenvalue represents the frequency and damping values for the ith mode which, as a result of the frequency dependent aerodynamic forces in Q_{ij}, are a function of the excitation frequency, ω. The eigenvector, $\{\Phi_i\}$, is not to be confused with the normal mode shape but is a complex vector that recombines the undamped mode shapes into a complex form for the ith degree of freedom. To illustrate, let $\{h_i\}$ be the undamped mode shape function (deflections) for the ith mode. The damped mode shape, $\{h'_i\}$, is then expressed as

$$\{h'_i\} = \Phi_{i1}\{h_1\} + \Phi_{i2}\{h_2\} \quad \Phi_{i3}\{h_3\} \quad \cdots\cdots$$

Thus, if the Q_{ij} matrix is zero, then the aerodynamic forces are not available to alter the mode shape and

$$\Phi_{ik} = 0, \qquad i \neq k \qquad (12a)$$

$$\Phi_{ik} = 1, \qquad i = k \qquad (12b)$$

which leads to the trivial result

$$\{h'_i\} = 1\{h_i\}$$

For most flight conditions, except near flutter, Equations 12 are approximately true and the damped natural modes are very close to their undamped counterparts. Under these conditions, the aerodynamic terms, Q_{ij}, are small which leads to

$$\Phi_{ik} << \Phi_{ii} \qquad (13a)$$

$$\Phi_{ii} \approx 1 \qquad (13b)$$

This is the key equation needed for diagonalizing Equation 9.

Now, let Equation 11 be written in a more general form for all modes. Starting with

$$[D]\{\Phi_i\} = \lambda_i\{\Phi_i\} \qquad (14a)$$

The general form becomes

$$[D][\Phi] = [\lambda\Phi] \qquad (14b)$$

But from Equations 13, $[\Phi]$ is very nearly a diagonal unit matrix, hence

$$[\Phi] \approx [I] \qquad (15a)$$

and

$$[\lambda\Phi] \approx [\lambda] \qquad (15b)$$

Combining Equations 14 and 15 yields

$$[D][\Phi] \approx [D][I] = [D]$$

and finally

$$[D] \approx [\lambda] \qquad (16)$$

which is the desired diagonal form.

The eigenvalues are composed of a real part, frequency, and an imaginary part, damping, in the following form

$$\lambda_i = \frac{1}{\omega^2}(\widetilde{\omega}_i^2 + i2\omega\widetilde{\omega}_i\widetilde{\zeta}_i) \qquad (17)$$

where the $\widetilde{\omega}_i$ and $\widetilde{\zeta}_i$ are a function of frequency,

$$\widetilde{\omega}_i = \widetilde{\omega}_i(\omega)$$

$$\widetilde{\zeta}_i = \widetilde{\zeta}_i(\omega)$$

This dependency is a result of the Q_{ij} terms in the matrix which are a function of frequency, ω. These eigenvalues are readily available from routine flutter analyses and include all of the effects of aerodynamic coupling between modes. One drawback of using the flutter eigenvalues, however, is that the aerodynamic methods customarily used are based on linear theory and hence do not reflect the effects of separated or transonic flows. This point will be discussed later.

Substitution of Equations 16 and 17 into Equation 10 leads directly to the working form of the diagonalized equations of motion:

$$[M_i] [\omega^2 - \tilde{\omega}_i^2 - i2\omega\tilde{\omega}_i (\zeta_i + \zeta_{i_s})] \{r_i\} \approx \{Q_{i_B}\} \qquad (18)$$

The solution to Equation 18 is simply

$$\{r_i\} \approx \left[\frac{1}{M_i [\omega^2 - \tilde{\omega}_i^2 - i2\omega\tilde{\omega}_i (\tilde{\zeta}_i + \zeta_{i_s})]} \right] \{Q_{i_B}\}$$

If the squared amplitude of the transfer function is defined as

$$|H_i(\omega)|^2 = \frac{1}{M_i^2 [(\omega^2 - \tilde{\omega}_i^2)^2 + 4\omega^2 \tilde{\omega}_i^2 (\tilde{\zeta}_i + \zeta_{i_s})^2]} \qquad (19)$$

then, assuming no correlation between modes, the mean-square buffet response can be calculated. As an example, the response power spectrum for an accelerometer, a_n is given as

$$\Phi_{a_n}(\omega) \approx \omega^4 \sum_i h_{i_n}^2 |H_i(\omega)|^2 Q_{i_B}^2 \qquad (20a)$$

and the root-mean-square value, σ_{a_n}, is obtained from

$$\sigma_{a_n}^2 = \int_{\omega_1}^{\omega_2} \Phi_{a_n}(\omega) d\omega \qquad (20b)$$

for the frequency limits of ω_1, to ω_2.

Modal Frequency and Damping Analysis.- The magnitudes of the buffet-response spectral peaks are inversely proportional to the total damping squared as may be seen from Equation 19, where setting $\omega = \tilde{\omega}_i$, the transfer function becomes

$$|H_i(\tilde{\omega}_i)|^2 = \frac{1}{M_i^2 [4\tilde{\omega}_i^4 (\tilde{\zeta}_i + \zeta_{i_s})^2]}$$

Thus, it is clear that accurate determination of damping is mandatory for accurate prediction of response.

Aerodynamic damping is influenced by many effects which include transonic and separated flows as well as aerodynamic coupling between modes of vibration. Scaled wind-tunnel model damping data can provide the effects of transonic and separated flows on a limited number and type of modes that are available on the model as discussed in this report. Inherent in these effects are those of angle-of-attack. The influence of aerodynamic modal coupling on damping can be obtained from conventional flutter analyses as mentioned in the previous subsection. This influence is produced on realistic airplane modes but the aerodynamic methods are limited to attached linear theory techniques, thus a dilemma exists for determining accurate damping estimates. A technique was therefore contrived to deal with this dilemma.

The technique, which is discussed in detail in Appendix B, uses a hybrid approach which combines the scaled wind-tunnel model damping data with that

24

obtained for theoretical flutter analyses. The idea is to designate aircraft modes that are similar to the limited modes available on the model as "pivot modes". As an example, the first wing symmetric bending mode on the model and aircraft are usually very similar. Model damping data are then scaled to other similar modes on the aircraft using theoretical relationships for the damping of these modes. Likewise for the example, the first wing bending and first fuselage bending modes on a free-flying aircraft are very similar as far as the wing motion is concerned. Repeating this process for the next "pivot mode" and so on leads to a complete set of damping value functions, $\tilde{\zeta}_i(\omega)$, that have accounted for both the non-linear aerodynamic effects and intermodal coupling for the aircraft.

Also, discussed in Appendix B is the treatment of the modal frequency functions, $\tilde{\omega}_i(\omega)$, which are influenced by the unsteady aerodynamic forces. The values used are taken directly from the theoretical flutter analyses. Because the aerodynamic influence on mode frequencies is a second order effect, it was felt that ignoring separation and transonic flow contributions to this parameter was justified.

Composite Pivot Modes.-   The first wing symmetric bending mode for the F-111 TACT aircraft was very similar to that for the 1/6-scale aluminum wind-tunnel model. Thus, the first wing symmetric bending mode was a logical choice for the "pivot mode" that represented the family of modes involving fundamental wind-bending motion. The other aircraft modes included in this family were the first fuselage vertical bending and first wing antisymmetric bending modes. The similarity of wing motion is illustrated in Figures A1, A2 and A3 in Appendix A.

In the case of torsion modes, the choice of a "pivot mode" was not so simple. The model wing first torsion mode, for example, had an elastic axis and a torsion node line that was further aft than the elastic axes and corresponding node lines for the torsion modes on the airplane. The torsion modes on the F-111 TACT aircraft which are shown in Figures A4, A5, and A6, were not typical of pure torsion modes. The modes were actually a combination of first wing symmetric and antisymmetric torsion plus the second symmetric wing bending. This was a result of the distribution of the instrumentation mass which caused a mismatch between the right and left hand wings. The impossibility of matching one of the aircraft torsion modes with a model torsion mode significantly complicated the problem of scaling wind-tunnel model torsion mode aerodynamic damping data.

In order to remedy the problem of selecting an appropriate torsion pivot mode, a technique was developed for combining the airplane torsion modes to obtain a composite mode that was more like the model torsion mode. The technique is fully developed in Appendix C and is based on the assumptions that (1) the diagonalized equations of motion are valid and (2) separation and transonic effects scale similarily for similar mode shapes. The equations developed provide the generalized mass as well as damped and undamped natural frequencies for the composite mode. Equations are also developed for relating scaled aerodynamic damping values for the composite mode to those values of the "base modes" used to construct the composite mode.

The result of this effort for the F-111 TACT aircraft resulted in the composite mode shown in Figure 28. Also shown in Figure 28 is the first wing torsion mode

25

for the model. The comparison is very good and far superior to that which involved the original aircraft modes. The torsion modes shown in Figures A4, A5 and A6 were used as the base modes for this construction. Equations described in Appendix C solve for weighting numbers to be applied to the modes involved in the composite mode by satisfying deflection constraints imposed by the model torsion mode. These conditions were satisfied at two leading and trailing edge points (inboard near the pivot and the outboard near the wing tip) on both wings which resulted in eight equations. Since only three unknowns were desired, this led to a least squares solution. The weighting numbers obtained from the solution were

$$p_1 = 1.5272 \quad \text{(RWT)}$$
$$p_2 = 1.0284 \quad \text{(LWT)}$$
$$p_3 = -0.5865 \quad \text{(WST)}$$

with the generalized mass and undamped natural frequency

$$M_c = 1041.6 \text{ lbs}$$
$$f_c = 14.92 \text{ Hz}$$

for the composite mode. Although the eight boundary conditions were not exactly satisfied, this solution did produce a reasonable facsimile of the model torsion mode as shown in Figure 28.

Modal Frequency, Damping and Masses

The techniques described above were used to develop the frequency and damping data applied in the final response prediction equations. The generalized masses, which were determined as a function of aircraft fuel weight, were based on theoretical analysis. The mode shapes of the six vibration modes used in this study are in Figures A1 through A6.

The baseline generalized masses and undamped natural frequencies of the six modes are given in Table 1 for the empty aircraft. The factors used to account for aircraft fuel weight are shown in Figure 29. These factors are simple multipliers that are applied to the empty aircraft values given in Table 1. The eigenvalues used in the determination of the aerodynamic damping and frequencies were taken from the flutter solution velocity/damping curves given in Ref. 26.

The aerodynamic damping factors developed with the previously discussed techniques are shown in Figure 30 as functions of altitude and frequency. These factors represent those values that are multiplied by the scaled model data for the two "pivot" modes (the first wing symmetric bending mode and the composite torsion modes). It can be noted that the effects of altitude are not significant in these plots because the effects are already accounted for in the scaling of the model damping data. The influence of excitation frequency, f, is significant, however, particularly for the wing bending type modes, WSB, WASB and FVB, because frequency effects are a direct result of the flutter eigenvalue variations with frequency.

The influences of excitation frequency and altitide on mode frequencies are shown in Figure 31. In this case both altitude and frequency effects are very

pronounced. Figure 31 shows that the bending type mode frequencies tend to increase with density (decreasing altitude) as a result of the increasing aerodynamic stiffness. The frequencies of the first two torsion modes, RWT and LWT, exhibit the same trend with altitude, which is not typical of torsion modes, for which mode frequencies normally tend to decrease with increasing aerodynamic forces. This effect is attributed to the forward location of the node lines on the wing and to significant bending of the horizontal tails. The third torsion mode, WST, does exhibit the classical drop in mode frequency with the increasing aerodynamic foces associated with a decrease in altitiude. Although there is significant wing second bending motion in the WST mode, the node line is sufficiently aft to produce the expected mode-frequency variation.

Aircraft Buffet Prediction

The dynamic model developed in the previous sections was applied to predict the buffet response for the F-111 TACT aircraft at selected flight test conditions. This section presents and discusses the results of these predictions including correlations of predicted and measured damping. The correlation of predicted and measured buffeting are based on PDSs and integrated RMS values. The buffet response characteristics are correlated for the same range of angles of attack, altitude and wing sweep as the pressure-fluctuation correlations that were presented in a previous section of the report.

Flight Conditions for Correlations.-   Details of the flight test program are described in the "Test Techniques" section of the report. The nominal conditions for the buffet response correlations are summarized as follows:

MACH NUMBER	0.8 for all buffet response correlations		
ALTITUDE	3,700 m (12,000 ft)	6,100 m (20,000 ft)	8,500 m (28,000 ft)
DYNAMIC PRESSURE	28,700 N/m (600 psf)	21,500 N/m (450 psf)	14,400 N/m (300 psf)
ANGLES OF ATTACK	7° – 10°	7°– 12°	7° – 12°
WING SWEEP	26° & 35°	26° & 35°	26° & 35°

Correlation of Damping.-   As shown in a previous section on the development of the equations of motion the amplitude of predicted buffet response for any given vibration mode is inversely proportional to the total damping value for the mode. Because of this sensitivity, a significant effort was made to improve the accuracy of damping estimates. Therefore, the correlation of these estimates with measured flight test values of damping is a very important part of the buffet prediction investigation.

Comparisons of predicted and measured total damping ratios for the TACT aircraft WSB, FVB and RWT modes are shown in Figure 32. Total damping includes both aerodynamic and structural damping ratios. The total damping measurements, which were obtained with the Randomdec system (Ref. 25), could only be made for three of the six modes selected for the buffet predictions.

In Figure 32(a) total damping values for the WSB mode are compared for $M = 0.8$ with $\Lambda = 26°$ and $\Lambda = 35°$. Predicted and measured trends are shown for both altitude and angle of attack. Although there is scatter in the flight test data, the trends are generally the same with exception of the overall higher levels of

27

the predicted values. Results in Figure 32(b) for the FVB mode show a better correlation with magnitude but there is greater scatter in the flight test data in the critical onset range of $\alpha = 9.5°$ to $\alpha = 10.5°$. Better correlations are shown in Figure 32(c) for the RWT mode, with exception of usual scatter in the onset range.

In view of the expected difficulty of predicting and measuring aerodynamic damping values for aircraft operating in separated transonic flow fields, the above results are very encouraging.

Correlations of Power Spectral Densities.- Complete sets of figures that include the predicted and measured PSDs of the wing tip and CG accelerations are shown in Figure 33 for $\Lambda = 26°$ and Figure 34 for $\Lambda = 35°$ for all the flight conditions studied. In general the PSD predictions are considered to be quite good, thus confirming the method. The predictions for the bending type modes, WSB, FVB and WASB, were generally somewhat better than for the torsion modes, RWT, LWT and WST. This trend is inconsistent with the damping correlations (Figure 32), which showed better damping predictions for the RWT mode than for the WSB or FVB modes. Comparisons of the PSDs in Figures 33 and 34 show that the buffet predictions tend to be better for $\Lambda = 35°$ than for $\Lambda = 26°$.

With respect to the disappointing torsion mode correlations at $\Lambda = 26°$ in Figure 33, the PDSs show that the correlations of the spectral peaks in the wing-tip response of the RWT mode at about 14 Hz were significantly affected by altitude and the consequent q variation. For example, a comparison of the RWA PSDs in Figures 33(e), 33(k) and 33(o) shows that the correlations of the RWT mode spectral peaks improved with increasing q. The correlations of the CGA spectral peaks of the WST mode at about 17 Hz, on the other hand, were relatively good and unaffected by altitude, e.g. Figures 33(f) and 33(l). It is of interest that the PSDs show that the predicted response increased with q, as would be expected; but, for some reason, the measured RWA of the RWT mode remained about constant with the q variations.

It is significant that the predicted spectral peaks in the torsion group of modes (14 Hz - 17 Hz) in many cases correlate very well with corresponding measured spectral peaks. Yet because other torsion-mode spectral peaks occur in the measurements that are not predicted the RMS correlations covering the overall torsion-mode band of frequencies can be strongly affected. Examples of such spectral-peak correlations are in Figures 33(f) and 33(l).

Correlations of RMS Buffet Responses.- In order to correlate the RMS values of the predicted and measured buffeting, the PSDs were integrated over several different frequency ranges. The frequency limits of the integrations and grouping of modes were as follows:

MODES	PREDICTION LIMITS	FLIGHT TEST LIMITS
WSB	3.45 - 6.25 Hz	3.22 - 6.14 Hz
FVB and WASB	5.95 - 9.46 Hz	5.95 - 9.46 Hz
RWT, LWT and WST	11.9 - 19.0 Hz	12.0 - 19.0 Hz

The FVB and WASB modes and RWT, LWT and WST modes were combined because the

separate modes could not be isolated in flight test PSDs. A fourth integration was also preformed where all responses listed above were combined into a total RMS over the full frequency spectrum. As for the PSD comparisons, the RMS comparisons were made for both wing-tip and CG accelerations as a funcion of angle of attack, altitude and wing sweep at M = 0.8.

The integrated RMS results from all the PSDs contained in Figure 33 and 34 are shown in Figure 35. For the WSB mode, as shown in Figure 35(a) the predictions are very encouraging for the wing-tip accelerations at both wing sweeps. As might be expected because CG amplitudes are very small due to wing bending (see Figure A1), CGA predictions are not quite so good as the RWA predictions. Results for the FVB and WASB modes shown in Figure 35(b) show an improvement in correlation for the CG accelerations and excellent correlation for the wing-tip accelerations. It also can be noted that the buffet onset is fairly well predicted in both Figures 35(a) and 35(b).

Response predictions for the torsion mode family are not quite so good as the bending mode response predictions as was mentioned in the previous subsection on PSD correlations. The comparisons shown in Figure 35(c) indicate that torsion responses for $\Lambda = 26°$ are consistantly under predicted for angles-of-attack greater than about 9.5°. The predictions are quite good, however, for $\Lambda = 35°$, and the agreement is more consistent with that shown for the bending-type modes in Figures 35(a) and 35(b). For both wing sweeps, it should be noted that the acceleration responses are much higher for the torsion modes then for the bending modes. This is particularly true for $\Lambda = 26°$ where the maximum wing-tip acceleration at $\alpha = 12°$ for the torsion modes is about three times that for the WSB mode. As a result, the total RMS comparisons shown in Figure 35(d) are dominated by the torsion mode family characteristics and hence they closely resemble those shown in Figure 35(c).

A striking peculiarity that can be noted in the RMS data shown in Figure 35(c) is the absence of altitude effects on the measured torsion-mode family accelerations. This characteristic was restricted to $\Lambda = 26°$ and was most noticeable in the wing-tip acceleration. The expected affect of increasing altitude is a reduction of buffet response as shown by all of the other predictions and flight measurements summarized in this report. Thus, there must be another dominating factor that affects the buffeting at $\Lambda = 26°$.

Discussion of Factors that Influence the Correlations

The basic factors that affect the correlations of wind-tunnel and flight-test buffet data were discussed in the Introduction; and in the body of the report it was pointed out that the F-111 TACT program provided a significant improvement in the factors that affect the flight data. However, even with these improvements, the present correlations of predicted and measured buffeting still show some discrepancies. The questions arises then as to what factors were the most probable cause of the discrepancies.

Before discussing specific factors that influence the correlations, it should first be remembered that the buffet response data in Figure 33, 34 and 35 are presented in terms of accelerations. Acceleration data exaggerates the higher-frequency mode amplitude differences between predictions and measurements.

Selection of Modes for Analysis.-   The correlation of PSDs in Figures 33 and 34 generally show that the most disappointing results occurred at $\Lambda = 26°$ in the range of frequencies from 14 Hz to 17 Hz that includes the torsion modes. Three torsion modes were selected to be included in the analysis. The buffet response data, however, (Figure 33(e) show a group of four spectral peaks in the 14 Hz to 17 Hz frequency range.   It therefore now appears via hindsight and examination of GVT modes (Ref. 15) that a fourth mode should have been included in the analysis.   The additional mode which is identified as a complex mode involving mostly motion of the horizontal tail but also some antisymmetric pitch and torsion motion of the wing, occurs at a natural frequency of 15.04 Hz.   Unfortunately it is not possible to estimate the effects of this mode in the present correlations without substantial additional analysis of data including the determination of the generalized force for the mode. Originally the mode was not included because the wing tip and CG motions were expected to be small.

Aerodynamic damping.-   As has been previously discussed, aerodynamic damping plays a dominant role in the accurate determination of aircraft buffet response. Equations 19 and 20 show, for example, that the PSD of the response varies as $1/(\zeta_i + \zeta_{ij})^2$. The aerodynamic damping is very illusive because (1) it is very difficult to predict and (2) it is very difficult to measure.   Thus, when considering this difficulty, the comparisons of predicted and measured damping values shown in Figure 32 are believed to be quite satisfactory. As was discussed in connection with the presentation of the damping estimates, the damping predictions agree very well with the measurements for the FVB and the RWT modes but not so well for the WSB mode.

Based on the correlations of measured and predicted damping, it is believed that the technique used for scaling the wind-tunnel damping values to full scale for similar modes and the technique for extrapolating the results to other modes represents a satisfactory methodology for generating reasonable estimates of full-scale damping. The fact that damping correlations were good where buffet predictions were not so good suggests that other effects were responsible for differences in correlations between bending and torsion modes.

Generalized masses.-   As previously mentioned, these F-111 TACT buffet predictions were based on theoretical dynamic information that included the generalized masses for each of the six modes selected for analysis. This was done to illustrate the usefullness of the method for buffet estimates prior to the availability of a prototype aircraft.

The generalized mass affects both the damping estimate (Equation 7) and the response prediction (Equations 19 and 20). As can be seen from these equations, the effects of the generalized mass on the aerodynamic damping is somewhat compensating to the response prediction. Nevertheless, it is significant that the theoretical generalized masses for four of the six selected modes (WASB, RWT, LWT and WST) were substantially different than the GVT generalized masses (see Table 2). The fact that there are large differences in the theoretical and GVT generalized masses suggests that the theoretical modal deflections may also be substantially different than the GVT modal deflections.

Mode shapes.-   The accuracy of the mode-shape predictions is fundamental to the accurate predictions of the aircraft buffeting.   In addition to affecting the generalized masses, mode shapes affect the determination of the corresponding generalized forces (Equation 4) and also the displacement factors (Equation 20a)

involved in the final acceleration response prediction.

Errors in mode shape prediction can be expected to have a larger effect on the torsion modes than on the wing bending modes. For torsion modes, fluctuating pressures on the wing have opposite signs on each side of the node lines and distances from node lines to significant fluctuating pressures are less for torsion modes than for wing bending modes. Also, because the accelerometers are close to torsion node lines, the accurate resolution of the torsion-mode acceleration displacement factors is difficult. For this same reason the predictions of CG accelerations can be expected to be less accurate than wing tip accelerations for bending modes.

It is believed that the large differences between theoretical and GVT generalized masses (Table 2) stems primarily from the theoretical structural modeling and the resulting mode shapes. Therefore, the mode shapes are a key factor that has influenced the correlations in this investigation.

Reynolds number and static elasticity.-   One of the major objectives of the 1/6-scale TACT model test with aluminum and steel wings was the separation of Reynolds number and static aeroelastic effects. Discussions of these effects on the pressure fluctuations given earlier in this report (Figures 12 and 13) indicated that the effects were small except at the locations of the shock waves. This was particularly true for the range of angles-of-attack up to 12° included in the buffet response correlations. At the shock waves the effects of Reynolds number and static elasticity tended to cancel each other. Therefore, it is not expected that Reynolds number or static elasticity had a significant effect on the buffet response correlations, particularly for wing bending modes. However, for torsion modes, relatively small variations of the shock positions could have contributed somewhat to the differences in predicted and measured buffeting.

Pitch rate and maneuver time history.- One aspect of the flight dynamics of the aircraft, the effects of pitch rate on buffet response, was first discussed in Ref. 27 by Cunningham and Benepe. The idea was presented that a positive pitch rate would delay flow separation in the same manner that it can produce the well known dynamic overshoot of the maximum static lift. Likewise, a negative pitch rate would do the reverse and promote separation. Data from the F-111 TACT flight tests have also extended this idea to slower maneuvers which implies that maneuver time history likewise has a similar effect. This effect is illustrated in Figure 36, which shows a distinct hysteresis in the integrated RMS buffet response when the aircraft angle-of-attack was intentionally varied at a low pitch rate.

The data in Figure 36 are from the wing tip accelerometer. The symbols represent the RMS values obtained by the previously described TACT flight-test technique when the aircraft was held as close to steady conditions as possible for at least 20 to 60 seconds. The solid line is the RMS variation of RWA versus angle-of-attack connecting points that were measured at one-second intervals. Both data sets were recorded directly from flight data. The band-pass filter used to obtain the RMS values had a larger frequency band than the frequency integration limits of the RMS correlations, hence, the RMS levels in Figure 36 are higher than those seen in Figures 35. Nevertheless, a clear hysteresis loop is visible in the "non-steady" data which, because of the low pitch rate, is probably more indicative of a static hysteresis. In Figure 36,

31

it can be seen that the RMS wing-tip accelerations can vary by a factor of two at $\alpha = 10°$ depending upon which path of the maneuver that is being considered.

The above discussion has significant implications to the process of predicting the buffet characteristics of maneuvering fighter aircraft. With the rapid maneuvers that can be performed by current fighter aircraft, pitch rates up to 50° or 60° per second are possible. At such a postive pitch rate, buffet intensities would be expected to be far below those encountered during slow wind-up-turns at the same flow conditions. In fact, buffet onset angles-of-attack could be delayed by as much as 10° or 15° under the right conditions. With a similar negative pitch rate, however, the opposite effect would be true as is indicated by Figure 36. In this case high buffet intensities could persist to very low angles-of-attack, far below buffet onset. These aspects must be considered in future buffet research for any highly maneuverable fighter aircraft.

For the current study, careful attention was given to the flight test program to maintain steady conditions in order to minimize any dynamic or maneuver time-history effects in the buffet data. This presumption is justified by the results in Figure 36 which shows that the "static" symbols are at the apparent mean of "dynamic" hysteresis loop. Therefore, the effects of any maneuver transients are probably very small and they cannot be blamed for significant discrepancies between buffet predictions and flight measurements.

Coupling between wing modes and fluctuating pressures.- The possibility of any coupling between wing modes and fluctuating pressures on the aircraft could have a critical effect on the buffet correlations. Predictions of buffeting by the pressure-fluctuation method would be less than the measured buffeting because the models are not scaled to represent the structural dynamics of the aircraft.

For the F-111 TACT aircraft there were certain conditions when coupling may have affected the buffet response. These conditions were discussed with regard to correlations of pressure-fluctuation PSDs that were presented in Figures 17 and 18. These figures show that some flight-data PSDs exhibited peaks at the torsion-mode frequencies. This demonstration of possible coupling is important because it reveals another factor involved in the correlations; however, it does not explain the mechanism of the coupling. A proposed explanation of the coupling is therefore given in Appendix D.

Concluding Remarks on the Prediction of the F-111 TACT Buffet Response

A method has been presented for predicting buffet response from pressure-fluctuations on scale models in wind tunnels. The method embodies the following features:

1. The buffet forcing function is obtained by real time integration of pressure time histories with the natural modes.

2. Damping is obtained for pivot modes from model buffet response.

3. A hybrid method was developed and applied to extend the pivot-mode damping measurements to multiple modes by the use of theoretical damping data.

4. A technique was developed and demonstrated to form composite modes to obtain better one-to-one correspondence between model and aircraft modes to improve the scaling of damping.

32

5. Diagonalized equations of motion were derived and applied to simplify the multiple degree-of-freedom buffet response calculation.

The results presented have shown correlations of predicted and measured buffet response of the F-111 TACT aircraft at M = 0.8 with Λ = 26° and Λ = 35° for a range of angles-of-attack that includes buffet onset to high intensity buffeting. The correlations included comparisons of power spectral densities and integrated RMS results. Also included were comparisons of damping predictions with some flight-test measurements.

Generally the buffet predictions were considered to be quite good particularly in light of past buffet prediction experience. The most disappointing correlations of predictions and measurements were for the torsion modes at Λ = 26° at high buffet intensities. Generally the predictions were better at Λ = 35° than at Λ = 26°. Several factors could have affected the torsion-mode predic- tions. Factors such as damping predictions, generalized masses, mode shapes, Reynolds number, static elasticity, pitch rate, and coupling between torsional motions and fluctuating pressures were considered and discussed in detail.

REFERENCES

1. Jones, J. G.: Dynamic Response of Aircraft with Fluctuating Flow Fields, Von Karmon Institute For Fluid Dynamics Lecture Series 1981-4 on Unsteady Airloads and Aeroelastic Problems in Separated and Transonic Flow, March 9-13, 1981.

2. Effects of Buffeting and Other Transonic Phenomena on Maneuvering Combat Aircraft. AGARD Advisory Report No. 82, July 1975.

3. Lamar, W. E.: Effects of Buffeting and Other Transonic Phenomena. AGARD Conference Proceedings No. 187 on Flight/Ground Testing Facilities Correlation, April 1976.

4. Mabey, D. G.: Beyond the Buffet Boundary, Aeronautical Journal, Vol. 77, pp 201-215, April 1973.

5. Mabey, D. G.: Some Remarks on Buffeting, Von Karmon Institute for Fluid Dynamics Lecture Series 1981-4 entitled Unsteady Airloads and Aeroelastic Problems in Separated and Transonic Flow, March 9-13, 1981.

6. John, H.: Critical Review of the Methods to Predict the Buffet Capability of Aircraft, AGARD Report No. 623, September 1974.

7. Jones, J. G.: Modeling of systems with a high level of internal fluctuations, AGARD Conference Proceedings No. 172 on Aircraft State and Parameter Identification, November 1974.

8. Butler, G. F. and Spavins, G. R.: The Prediction of the Transonic Buffeting Response of the Gnat Aircraft in Flight from Wind-Tunnel Tests on Models of Conventional Construction, RAE TR 81075, June 1981.

9. Hanson, P. W.: Evaluation of an Aeroelastic Model Technique for Predicting Airplane Buffet Loads, NASA TN D-7066, February 1973.

10. Mullens, R. E. and Lemley, C. E.: Buffet Dynamic Loads During Transonic Maneuvers, AFFDL-TR-72-46, 1972.

11. Hwang, C. and Pi, W. S.: Investigation of Northrup F-5A Wing Buffet Intensity in Transonic Flight, NASA CR-2482, April 1974.

12. Cunningham, A. M., Jr., Benepe, D. B., Watts, D. and Waner, P. G.: A Method for Predicting Full Scale Buffet Response with Rigid Wind Tunnel Model Fluctuating Pressure Data, Volume I: Prediction Method Development and Assessment, NASA CR 3035, November 1978.

13. Symposium on Transonic Aircraft Technology (TACT), AFFDL-TR-78-100, August 1978.

14. Butler, G. F. and Jones, J. G.: Some Comparisons of Recent Flight and Tunnel Buffeting Measurements, Von Karmon Institute for Fluid Dynamics Lecture Series 1981-4 entitled Unsteady Airloads and Aeroelastic Problems in Separated and Transonic Flow, March 9-13, 1981.

15. Voelker, L. S.: Measurement of the Natural Frequencies and Mode Shapes of the TACT Aircraft. AFFDL-TM-74-42-FYS, July 1974.

16. Lim, R. S. and Cameron, W. D.: Power and Cross-Power Spectrum Analysis by Hybrid Computers. NASA TM X-1324, 1966.

17. Riddle, D. W.: Wind-Tunnel Investigation of Surface-Pressure Fluctuations Associated with Aircraft Buffet. AIAA Paper 75-67, January 1975.

18. Coe, C. F., Riddle, D. W. and Hwang, C.: Separated-Flow Unsteady Pressures and Forces on Elastically Responding Structures, Presented at the 44th Meeting of the AGARD Structures and Materials Panel on Unsteady Airloads in Separated and Transonic Flow, Lisbon, April 1977.

19. Willmarth, W. W. and Roos, F. W.: Resolution and Structure of the Wall Pressure Field Beneath a Turbulent Boundary Layer. J. of Fluid Mechanics, Vol. 22, Part 1, May 1965, pp. 81-94.

20. Bull, J. K., Wilby, J. F. and Blackman, D. R.: Wall Pressure Fluctuations in Boundary Layer Flow and Response of Simple Structures to Random Pressure Fields. University of Southampton, AASU Report 243, July 1963.

21. Dods, J. B., Jr. and Hanly, R. D.: Evaluation of Transonic and Supersonic Wind-Tunnel Background Noise and Effects on Surface Pressure Fluctuation Measurements. AIAA Paper 72-1004, Palo Alto, Calif., September 1972.

22. Roos, F. W. and Riddle, D. W.: Measurements of Surface-Pressure and Wake-Flow Fluctuations in the Flowfield of a Whitcomb Supercritical Airfoil. NASA TN D-8443, 1977.

23. Moore, J. W., Cronin, D. L. and Coe, C. F.: Predictions of Buffet Response of 1/6-Scale Models of F-111 TACT Wings. NASA TM 85858, October 1983.

24. Jones, J. G.: A Survey of the Dynamic Analysis of Buffeting and Related Phenomena. RAE TR 72197, February 1973.

25. Cole, H. A., Jr.: On-Line Failure Detection and Damping Measurement of Aerospace Structures by Random Decrement Signatures, NASA CR-2205, 1973.

26. Watts, D. and Haller, R. L.: F-111 TACT Final Flutter Analysis, Volume I, General Dynamics Corp., Fort Worth Division, FZS-595-021, October 1973.

27. Cunningham, A. M. Jr., Sheridan, A. E. and Freeman, T. K.: Update Structural Design Criteria, Design Proceedings and Requirements for Bomber/ Logistic Type Airplane Wing and Tail Loads, Volume I, AFWAL-TR-82-3084, December 1982.

28. Triebstein, H.: Steady and Unsteady Pressure Distributions on a NACA 0012 Profile in Separated Transonic Flow, ICAS Proceedings, Volume I, 1984, pp 483-493.

Table 1. Wind-off frequencies of primary vibration modes of
1/6-scale TACT wings

Vibration mode	$\Lambda = 26°$		$\Lambda = 35°$	
	Steel	Aluminum	Steel	Aluminum
1st wing bending	20.0	25.3	20.7	25.0
2nd wing bending	95.9	98.9	96.4	98.9
1st wing torsion	140.0	156.0	156.0	158.0
2nd wing torsion	256.0	---	270.0	303.0

Table 2. Generalized masses, frequencies and structural damping
for empty TACT aircraft

Vibration mode	Frequency, (Hz)		Mass, (lbs)		Structural damping ratio
	Theor.	GVT	Theor.	GVT	
WSB	4.418	4.54	1514.7	1317.3	0.022
FVB	7.296	8.20	4938.2	4428.6	0.024
WASB	7.684	7.13	456.0	973.8	0.017
RWT	14.093	14.17	871.3	565.9	0.026
LWT	15.204	15.48	268.5	704.8	0.026
WST	17.139	16.74	408.8	809.4	0.027

FACTORS THAT AFFECT WIND TUNNEL DATA

REYNOLDS NUMBER

WALL INTERFERENCE

FLOW TURBULENCE

TRANSITION FIXING

BOUNDARY-LAYER
THICKNESS DISTRIBUTION

STATIC ELASTICITY

DYNAMIC ELASTICITY

FACTORS THAT AFFECT FLIGHT DATA

FLIGHT PARAMETER ACCURACIES

NONSTATIONARITY OF DATA

SHORT DURATION OF DATA

INCOMPLETE MEASUREMENT

LACK OF ONE-TO-ONE SENSOR LOCATIONS

NO FLOW VISUALIZATION

Figure 1. Factors that affect the correlation of wind-tunnel
and flight-test data.
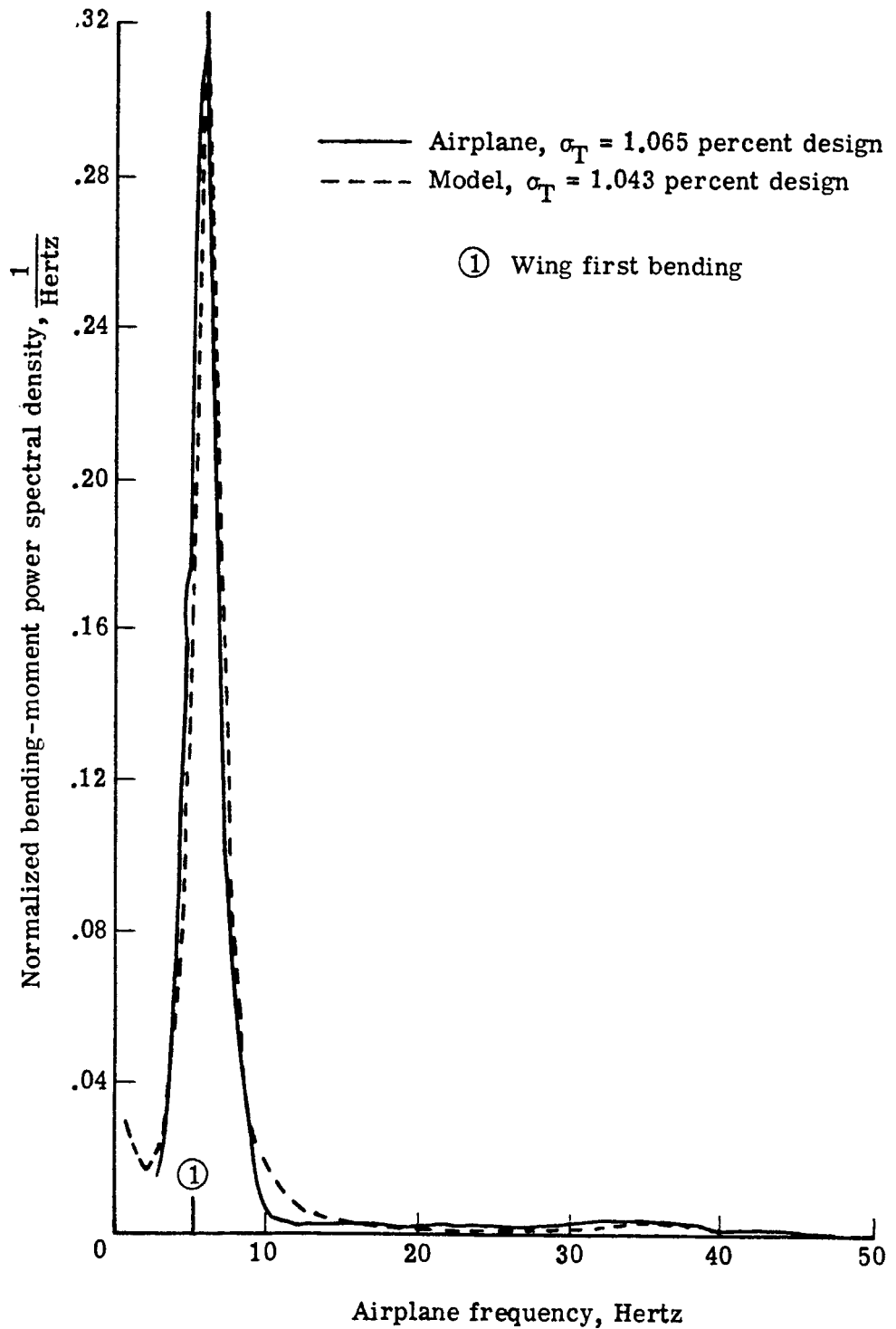
(a) Right wing bending moment.

Figure 2. Comparison of F-111A aeroelastic model and aircraft response spectra, $\Lambda = 26°$, $M = 0.81$, spectra normalized on rms level (Ref. 9).
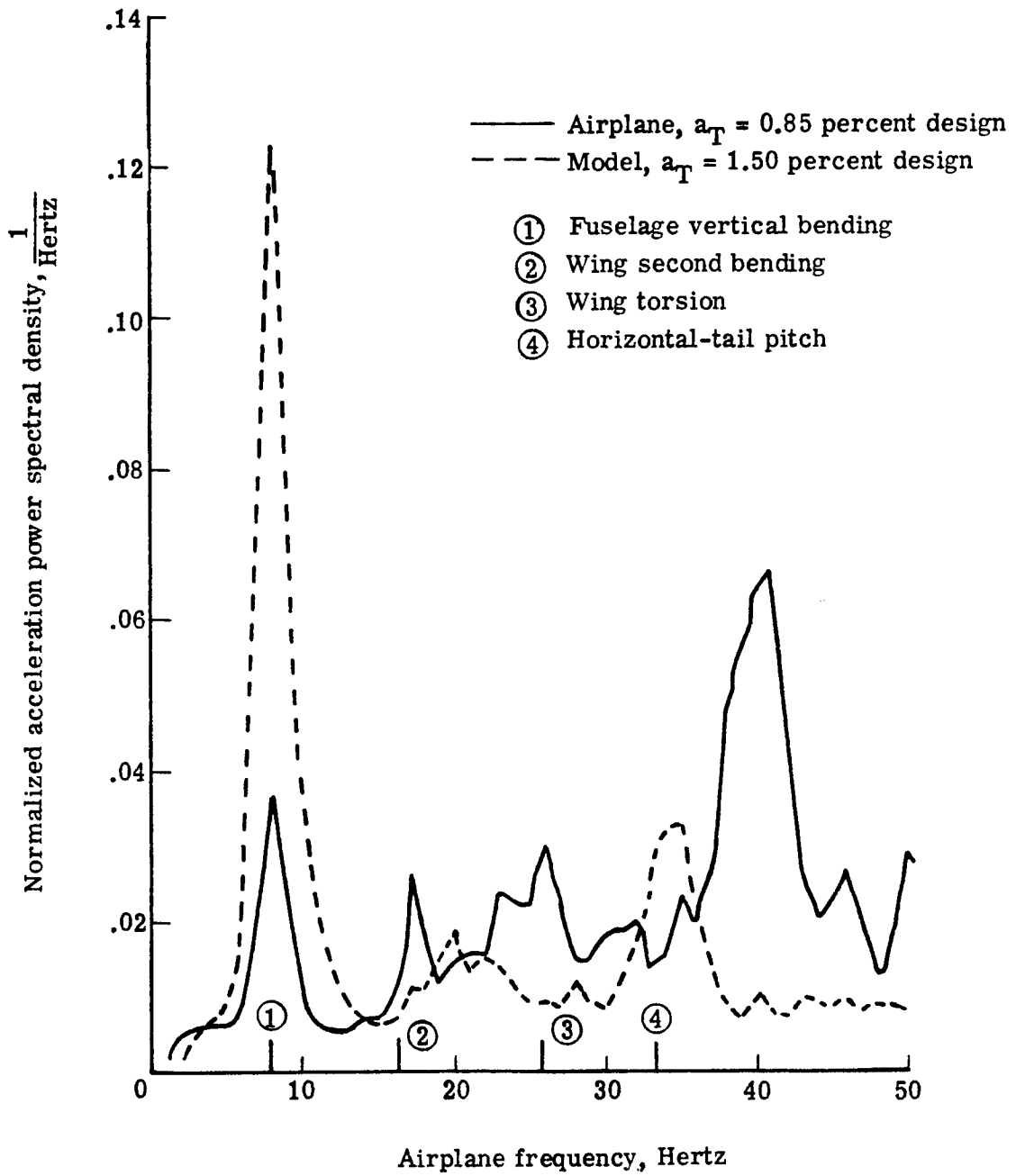
(b) Acceleration at center of gravity.

Figure 2. Concluded.
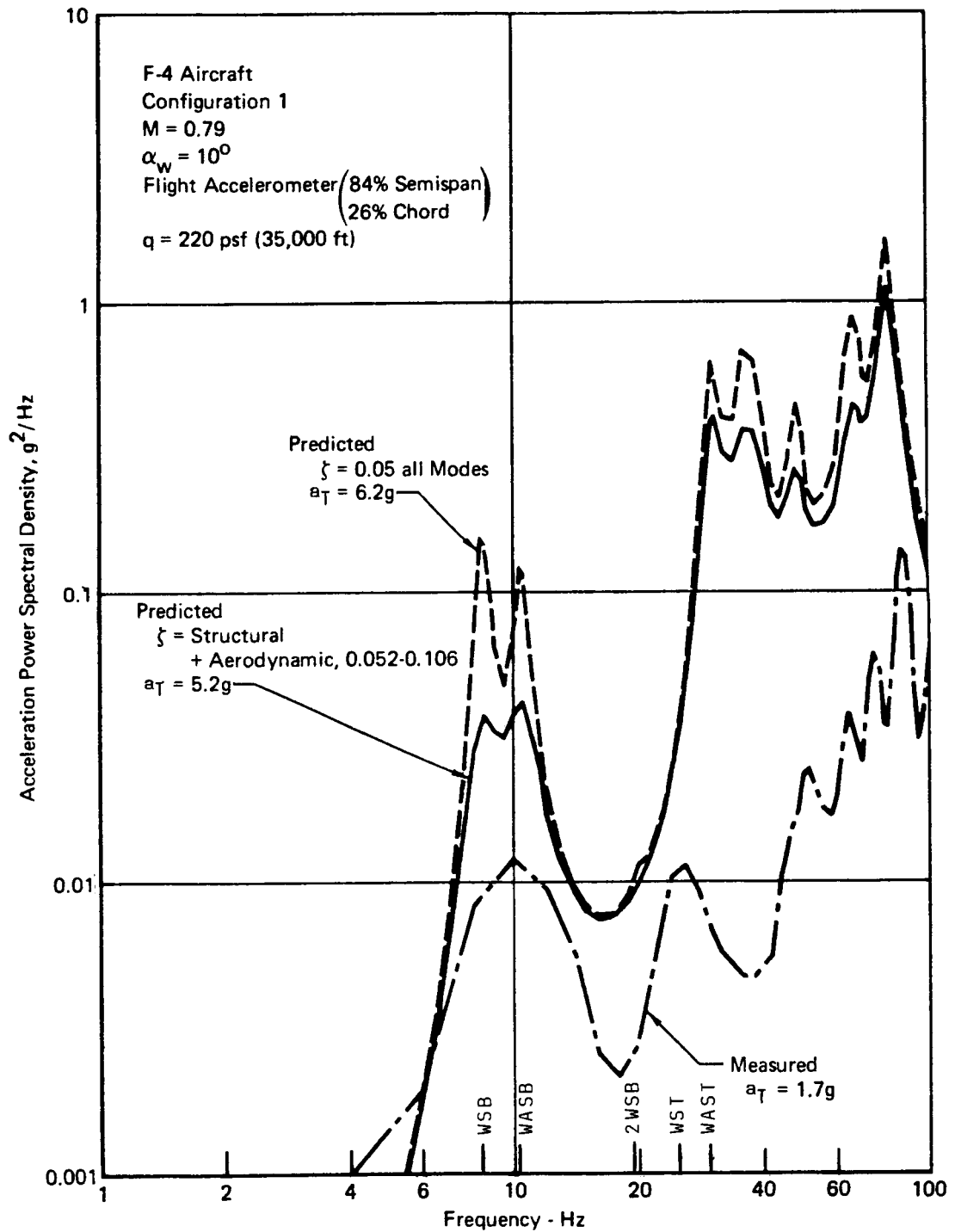
Figure 3. Comparison of predicted and measured acceleration
response of F-4 aircraft (Ref. 10).
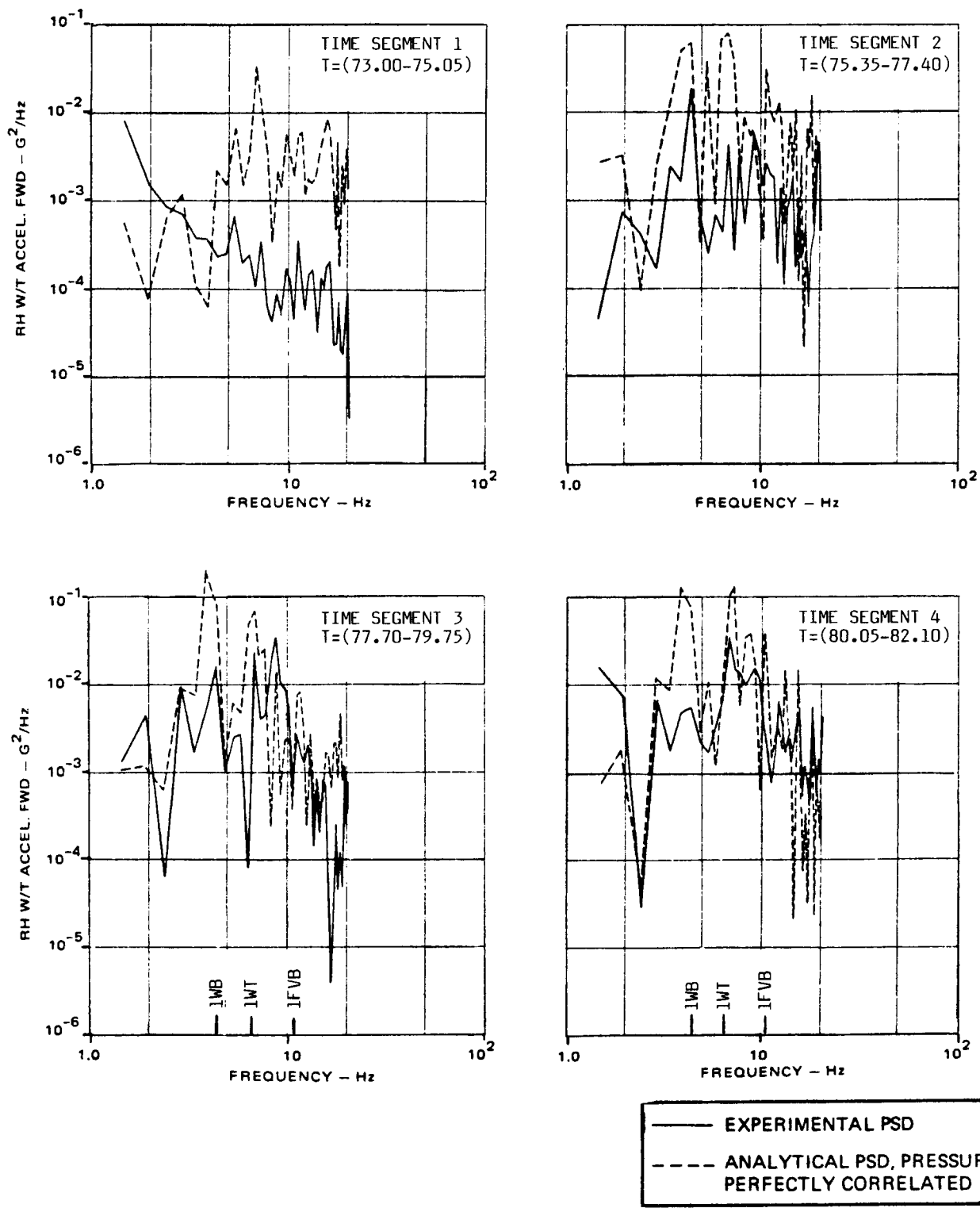
Figure 4. Comparison of analytical and experimental power spectra of wingtip accelerations on F-5A aircraft (Ref. 11).
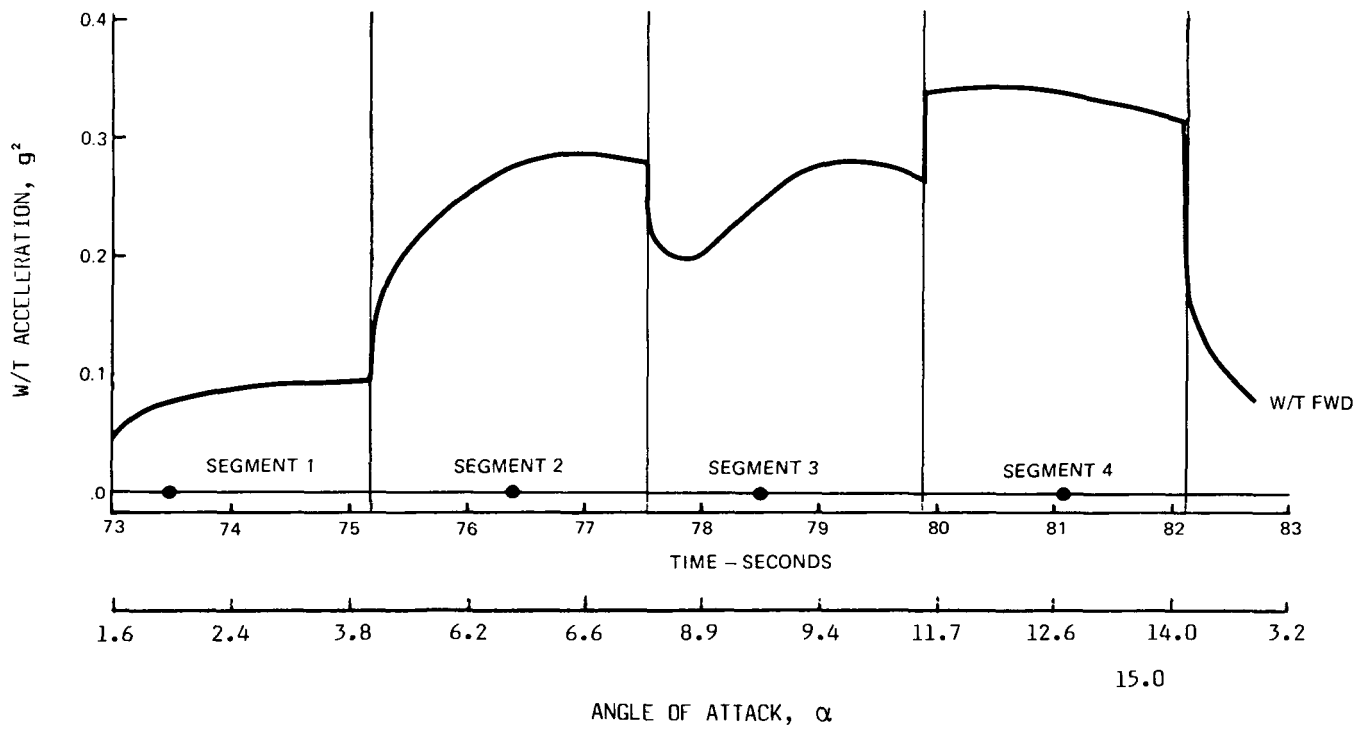
Figure 5. Variation of wingtip acceleration response of F-5A aircraft with time and angle of attack (Ref. 11).
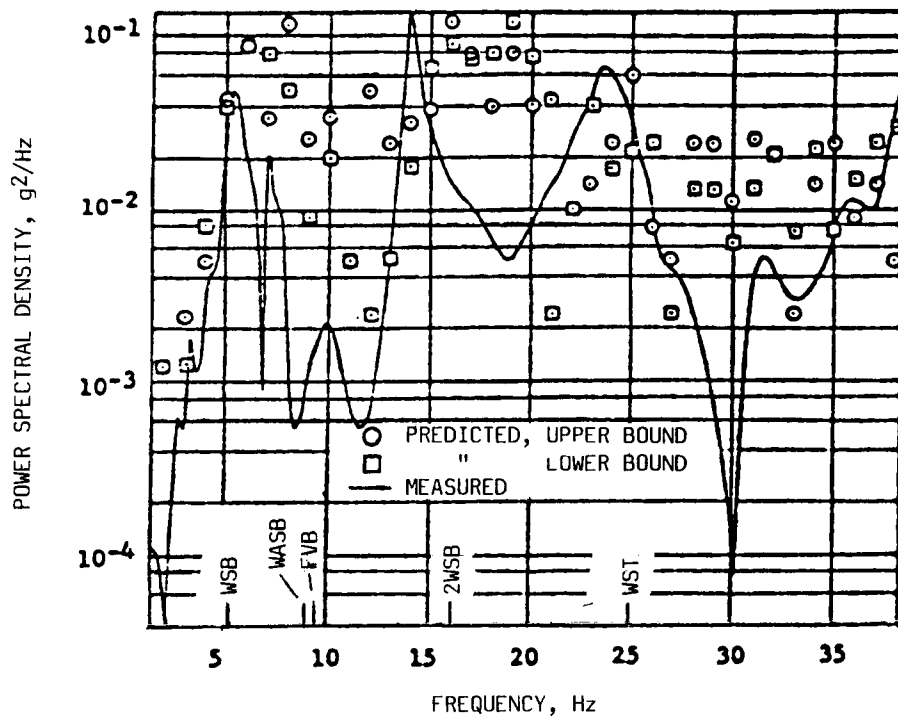
(a) $\alpha = 6.6°$
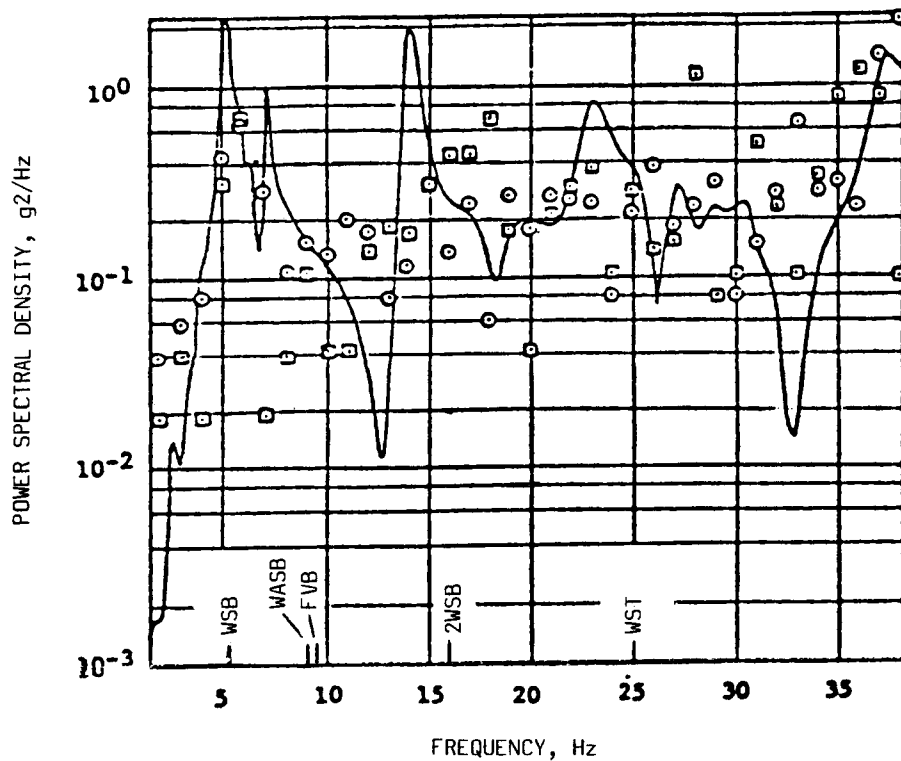
(b) $\alpha = 11.1°$

Figure 6.   Comparison of predicted and measured wingtip acceleration
response of F-111A aircraft, $\Lambda = 26°$, $M = 0.8$, spanwise and chord-
wise phasing of pressures, (Ref. 12).
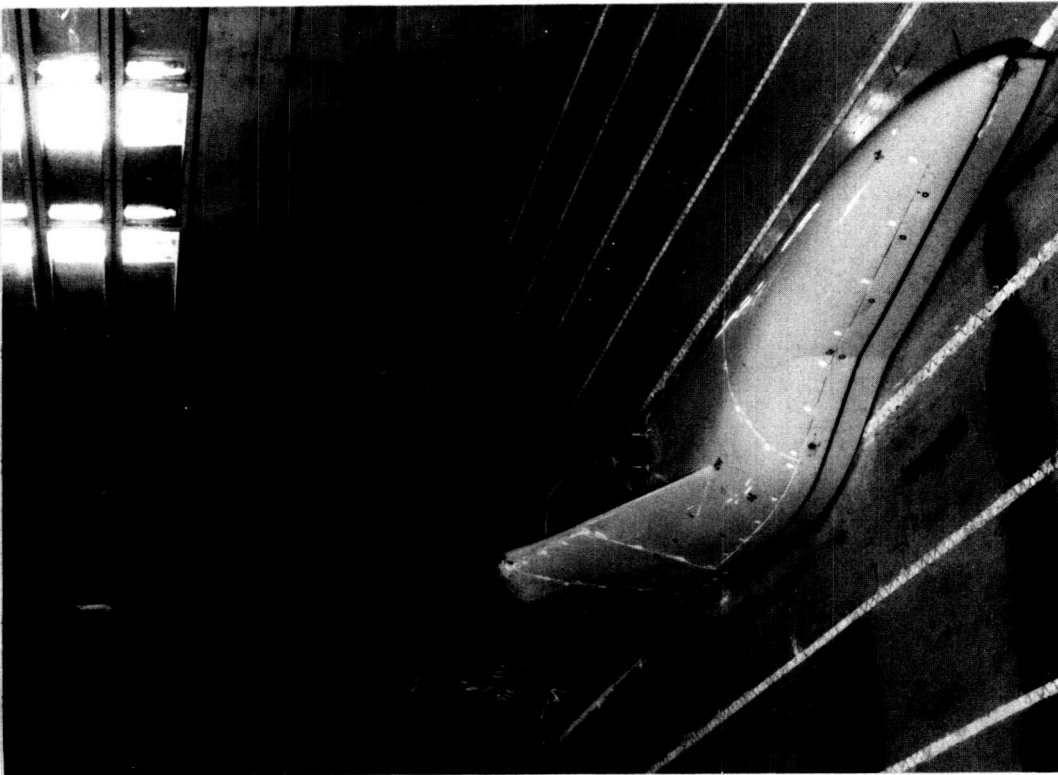
SEMISPAN GEOMETRY	WING		HORIZONTAL TAIL	
	PIVOT	TIP	ROOT	TIP
i	1.0°	-6.5°	0°	0°
t/c	10.2%	5.4%	4.0%	3.0%
AIRFOIL	SUPERCRITICAL		BICONVEX	
S	.78 m² (8.39 ft²)		.22m² (2.42ft²)	
b	1.51m (4.94ft)		.41m (1.36ft)	
c̄	0.53m (1.75ft)		.58m (1.91ft)	
AR	5.83		1.54	
TR	0.541		0.334	
Γ	0°		-1.0°	
Λ_{LE}	16° to 58°		57.5°	

Figure 7. 1/6-scale semispan model of the F-111 TACT aircraft installed in the Ames 11- by 11-Foot Transonic Wind Tunnel and pertinent dimensions.

44
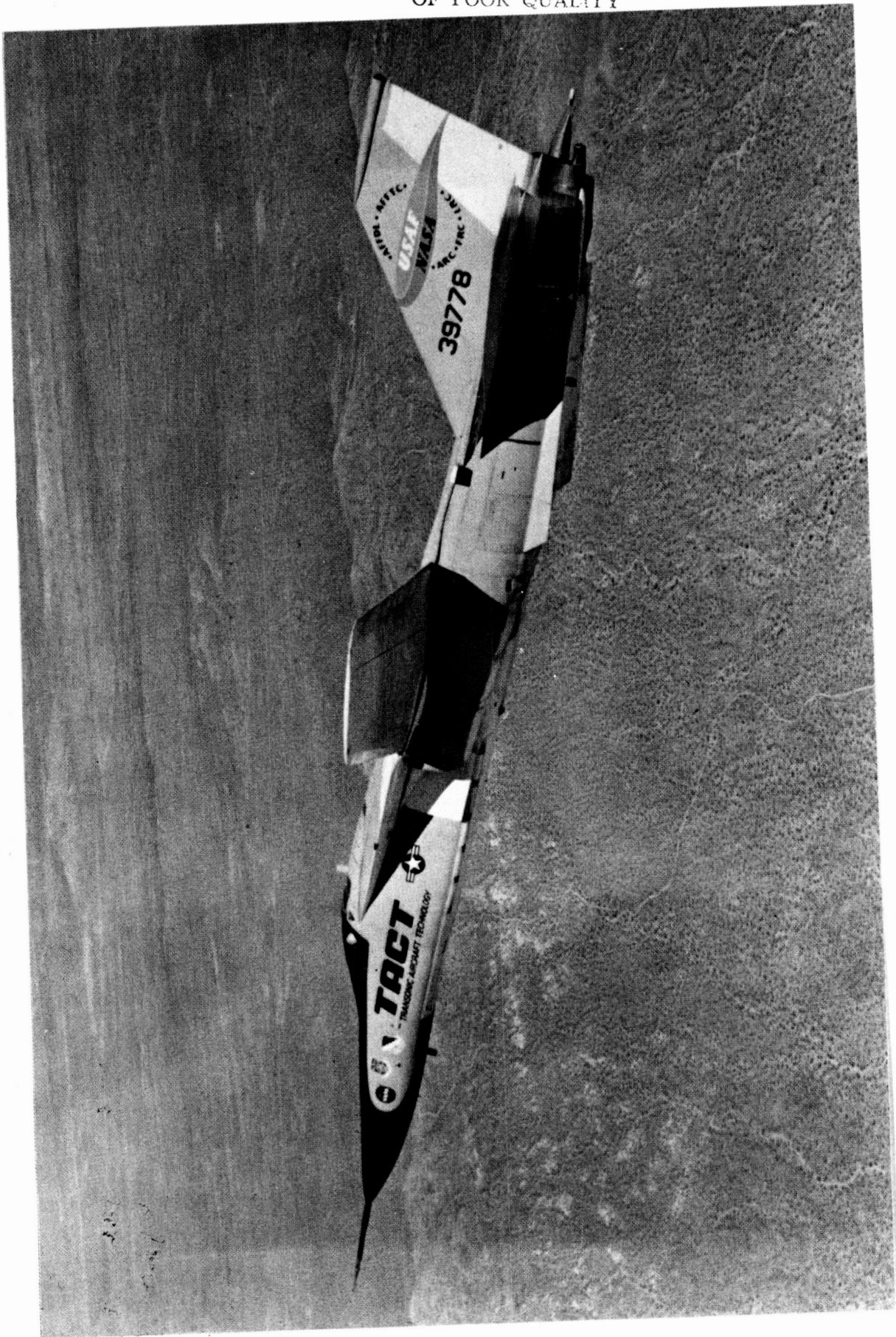
Figure 8. Photograph of F-111 TACT aircraft.

W. T. MODELS – LEFT WING PANEL
50 TRANSDUCERS
ALL SYMBOLS
– LEFT HORIZONTAL TAIL
12 TRANSDUCERS

AIRCRAFT – RIGHT WING PANEL
25 TRANSDUCERS
FILLED SYMBOLS

x/c
0.06
0.20
0.45
0.63
0.90

η = 0.307
0.413
0.578
0.744
0.910

○ UPPER SURFACE
◇ LOWER SURFACE

x/c
0.10
0.50
0.90
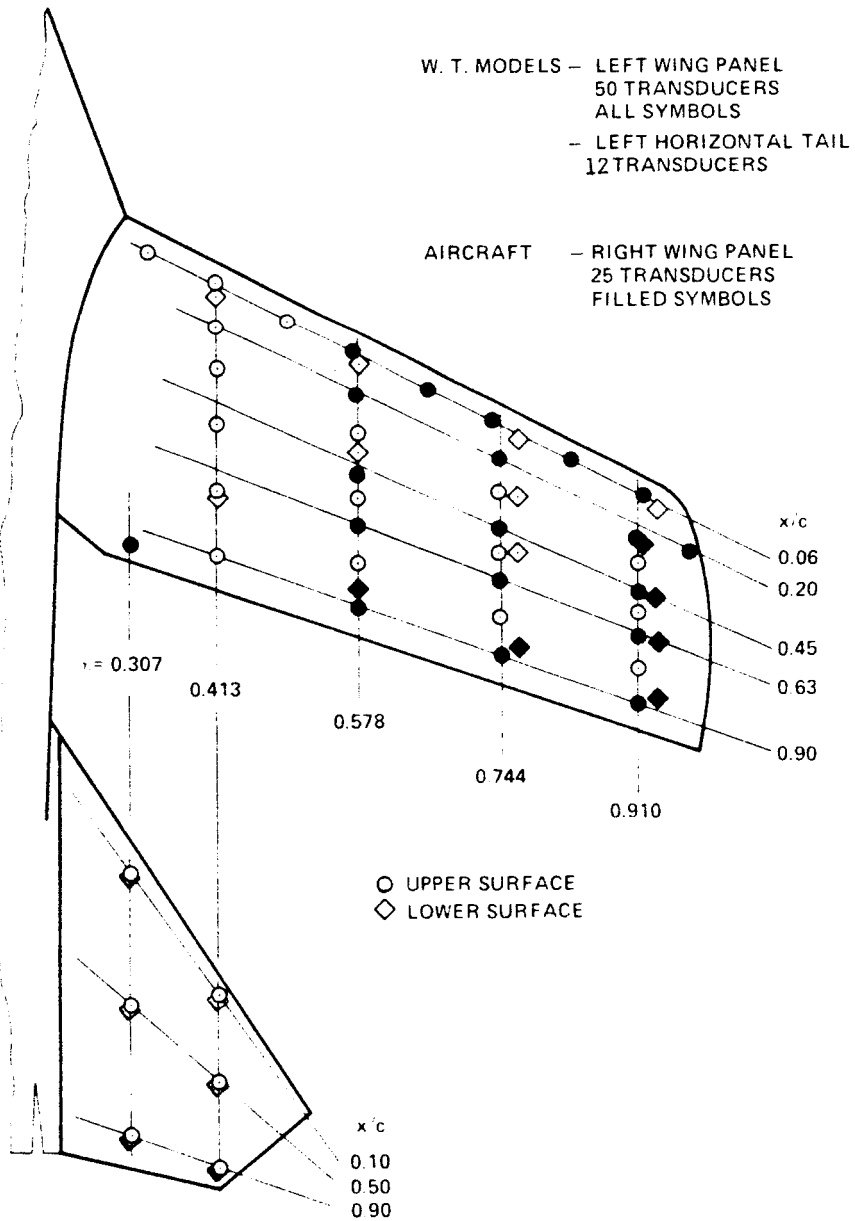
Figure 9. Locations of dynamic pressure transducers.

46

$\Lambda = 35.9°$, M = 0.80, q = 593 psf, $\alpha = 9.0°$

$\Lambda = 25.5°$, M = 0.80, q = 455 psf, $\alpha = 10.0°$

$\Lambda = 25.6°$, M = 0.80
q = 432 psf, $\alpha = 11.9°$
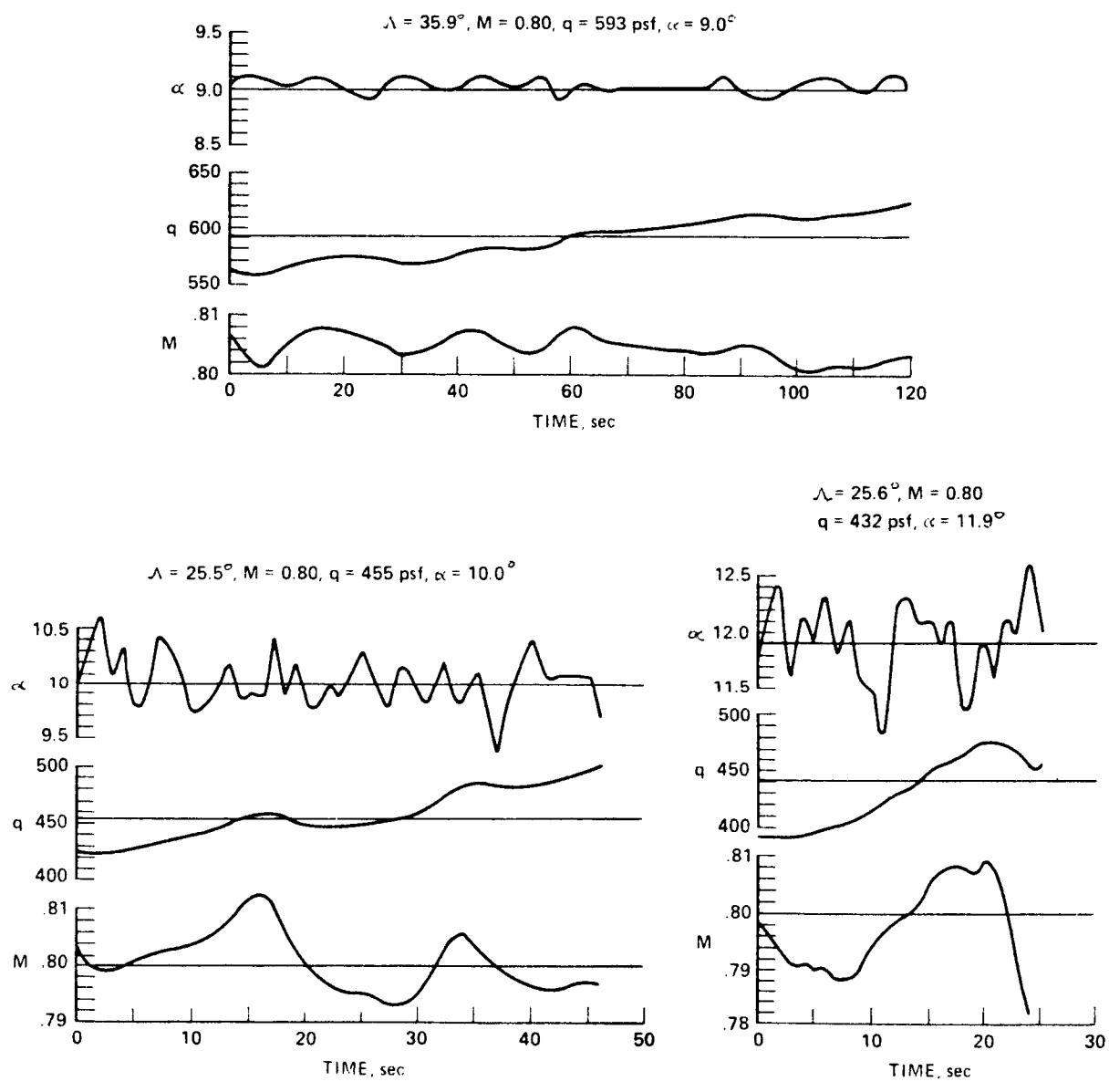
Figure 10. Time histories of flight conditions.
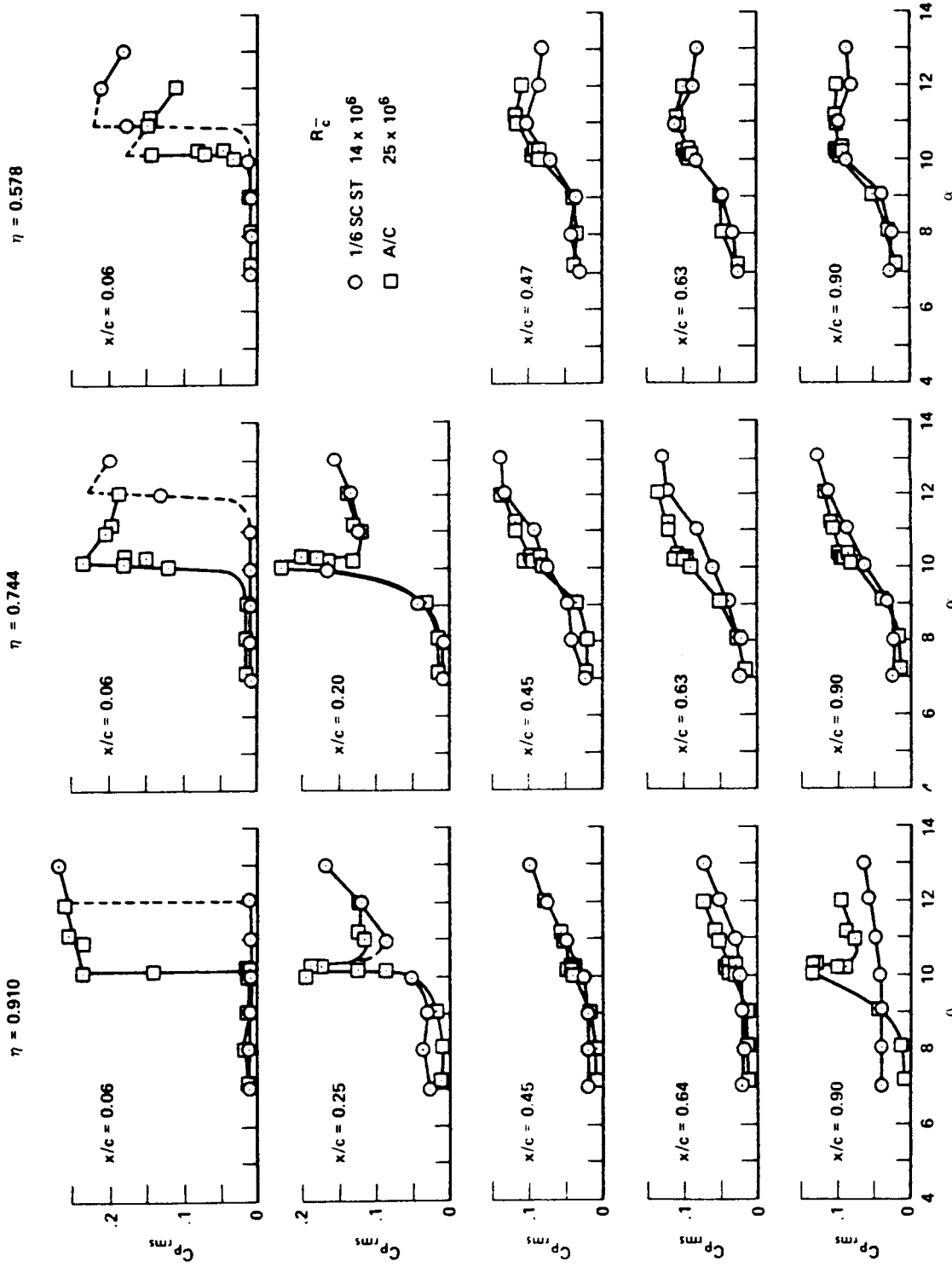
47

Figure 11. Correlation of pressure fluctuations on TACT 1/6-scale models and aircraft.

(a) $\Lambda = 26°$, $M = 0.80$.

48
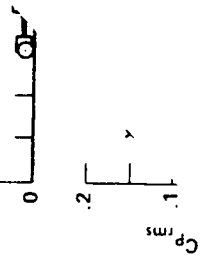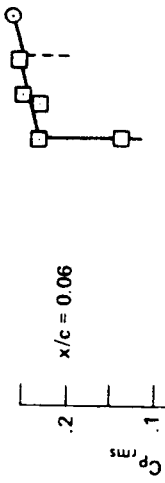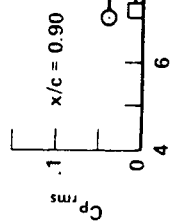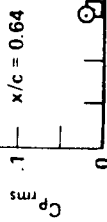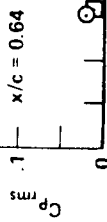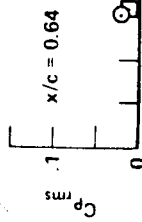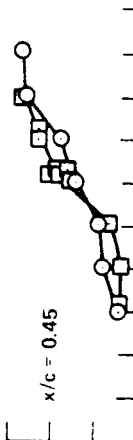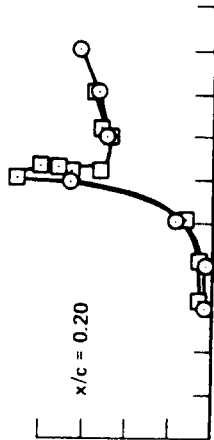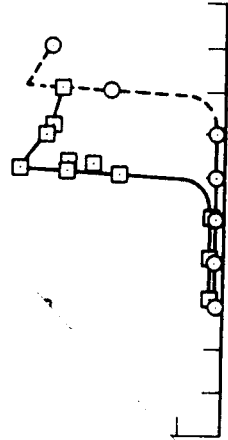
Figure 11. Correlation of pressure fluctuations on TACT 1/6-scale models and aircraft.
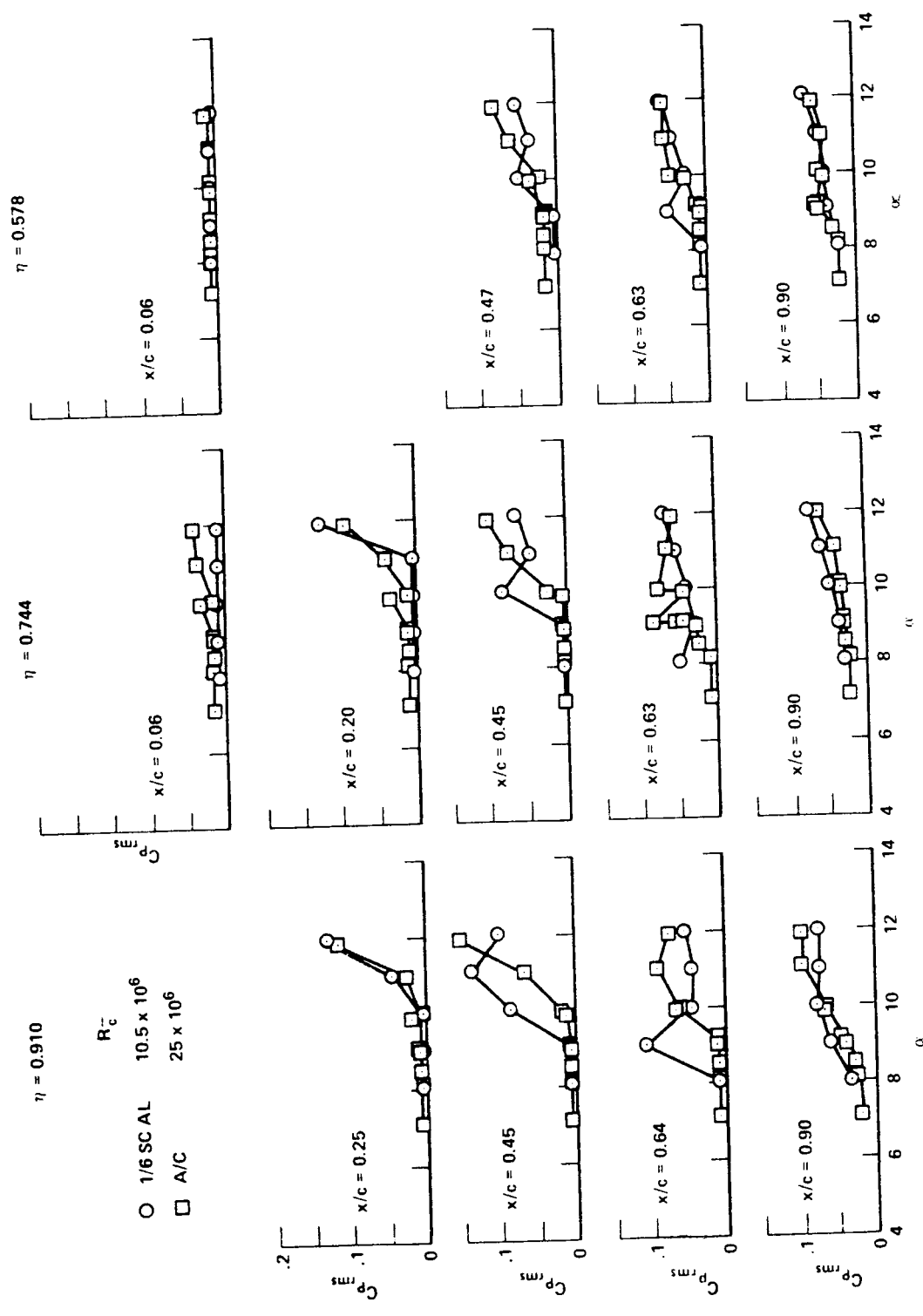
(a) $\Lambda = 26°$, M = 0.80.

(b) $\Lambda = 26°$, $M = 0.90$.

Figure 11. Continued.

50
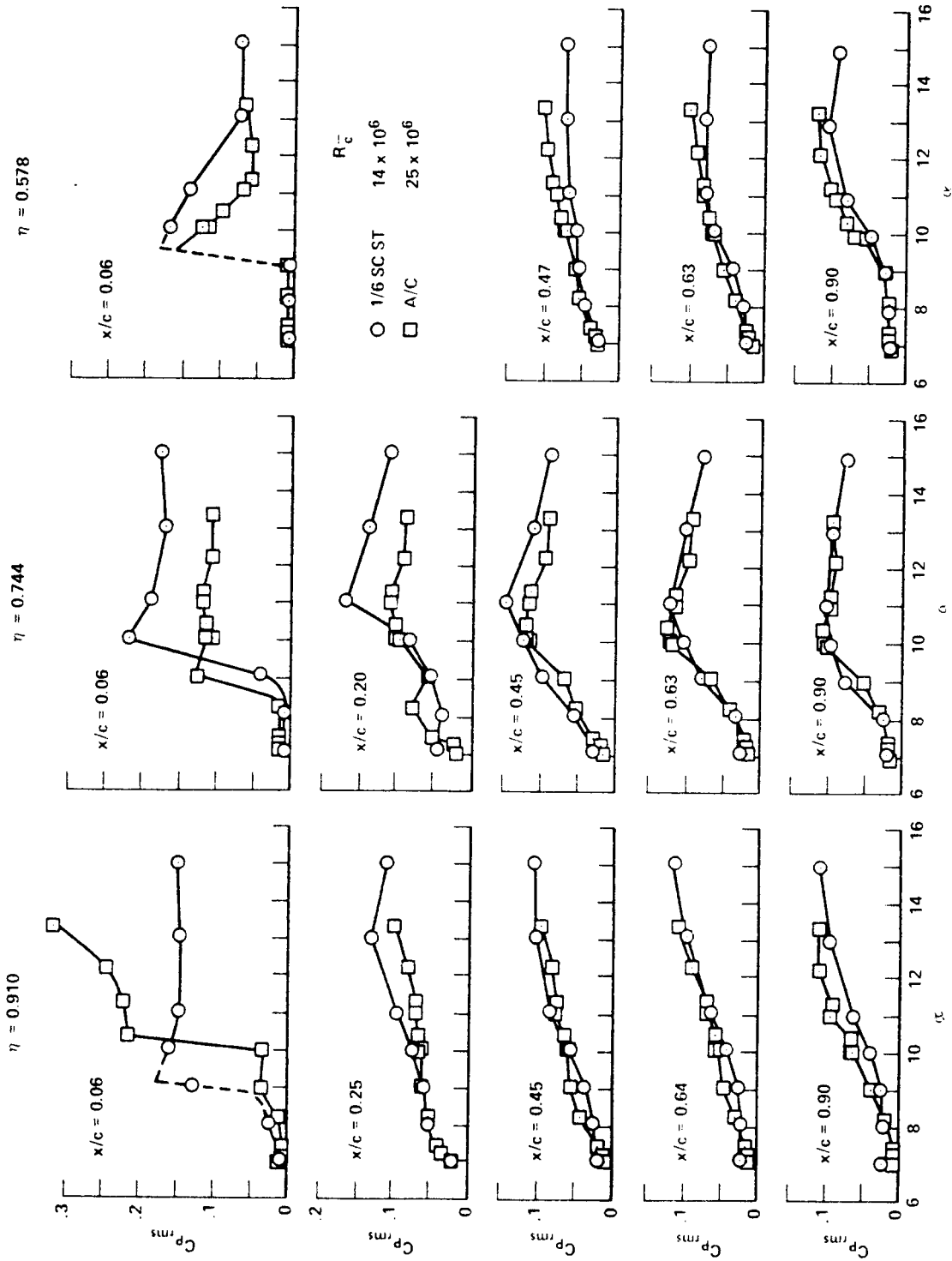
(c) $\Lambda = 35°$, $M = 0.80$.

Figure 11. Continued.

51
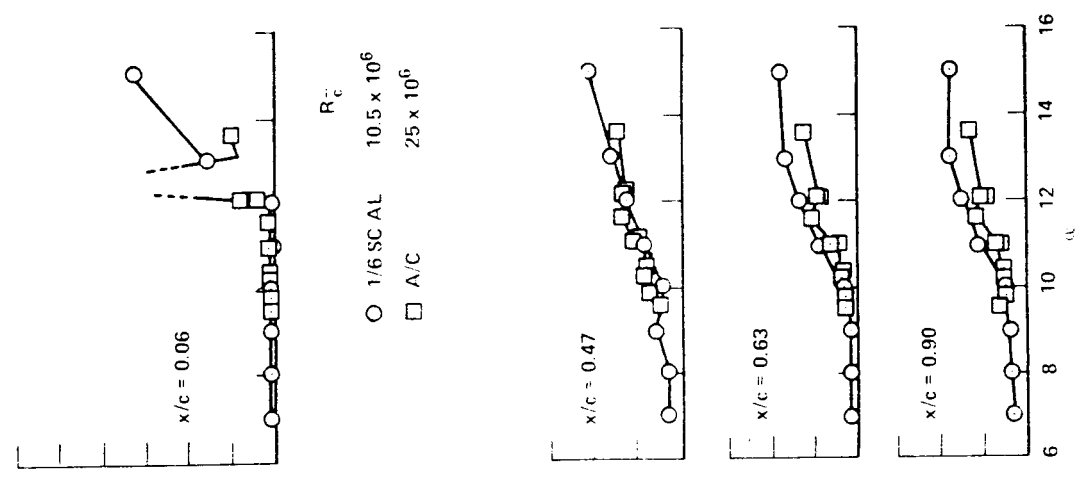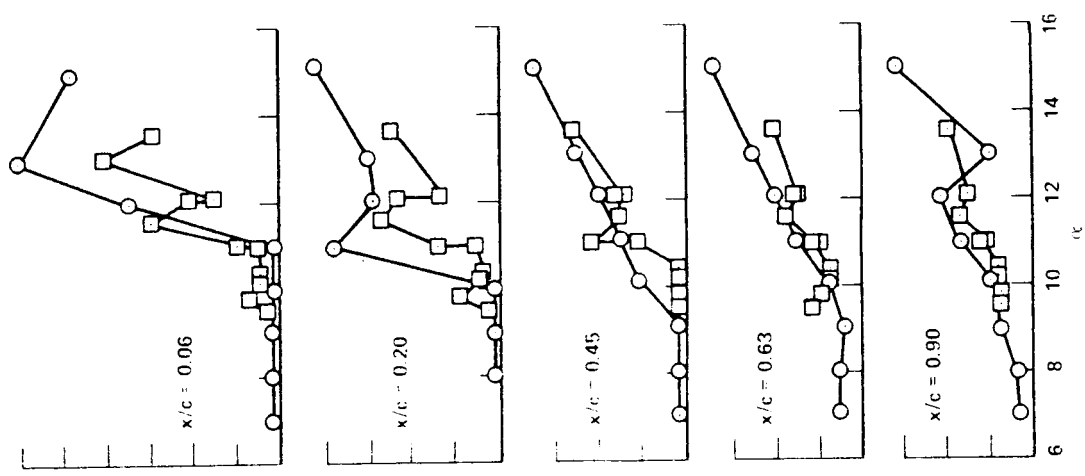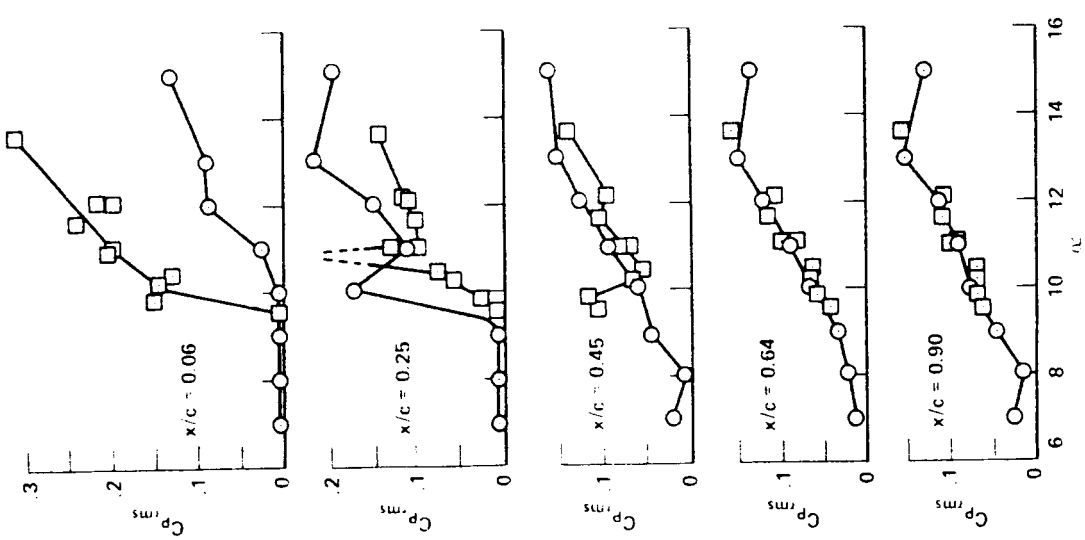
(d) $\Lambda = 35°$, $M = 0.90$.

Figure 11. Concluded.
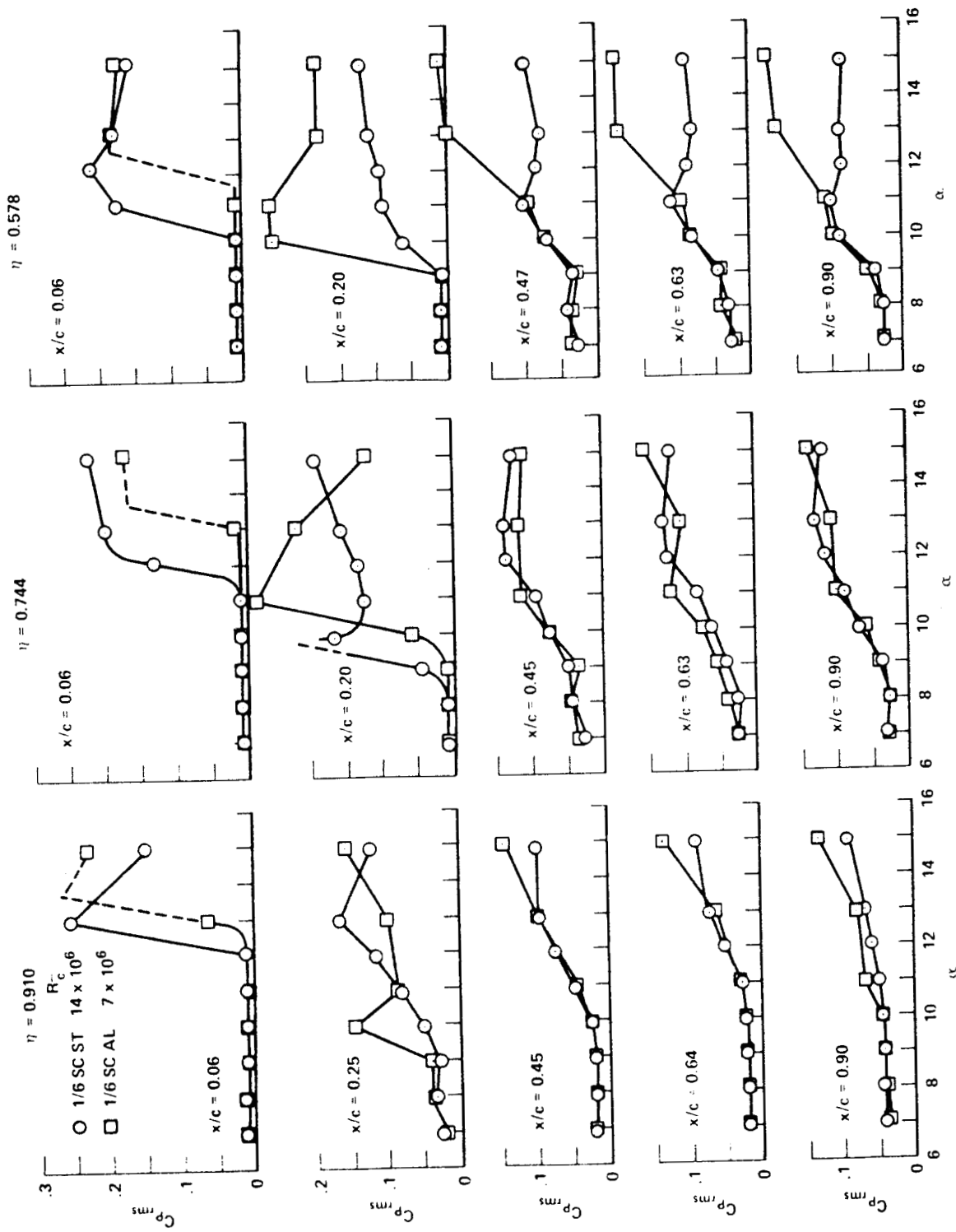
Figure 12. Reynolds number effects on pressure fluctuations on 1/6-scale TACT models, $\Lambda = 26°$, $M = 0.80$.

53
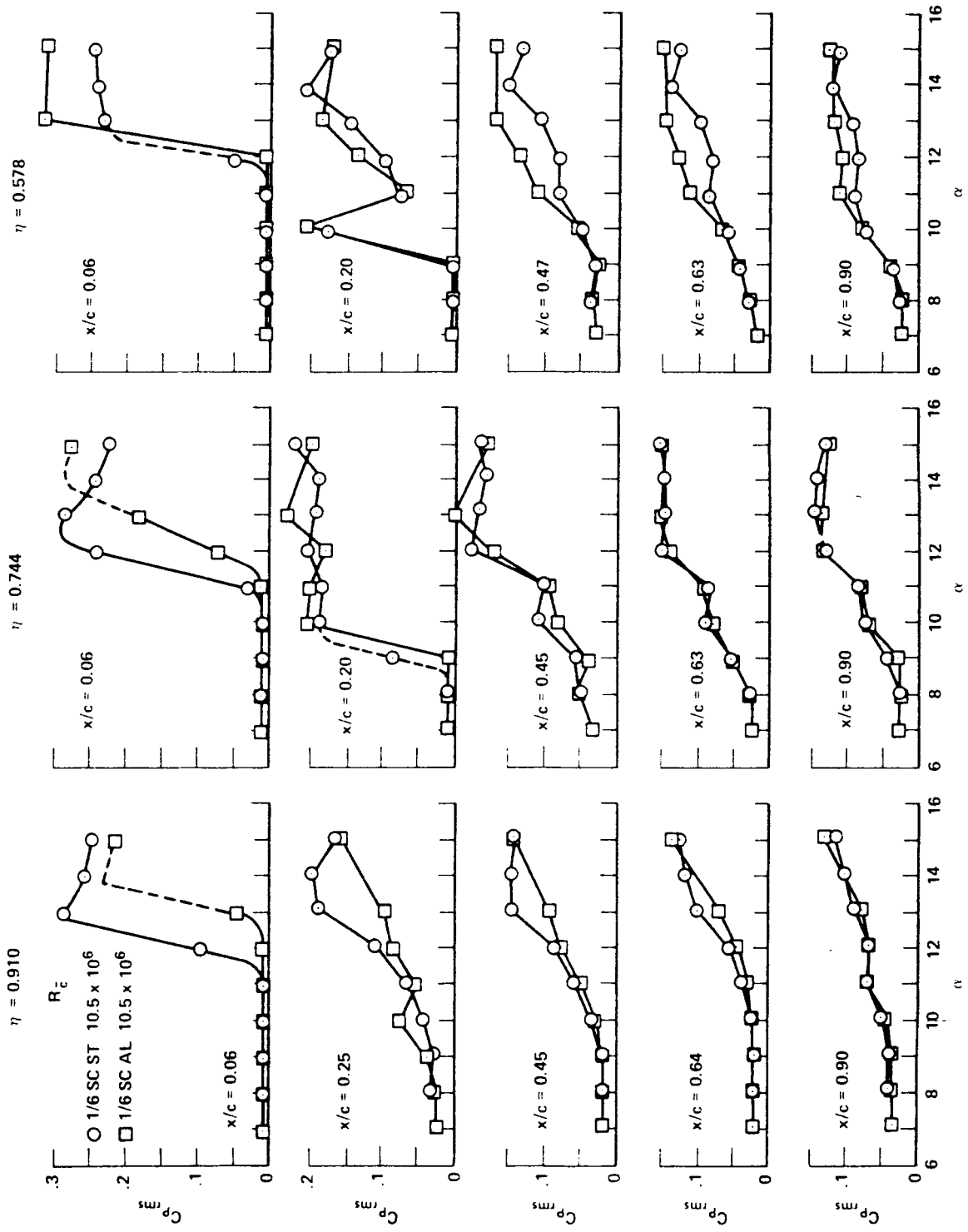
Figure 13. Effects of static elasticity on pressure fluctuations on 1/6-scale TACT models, $\Lambda = 26°$, $M = 0.80$.
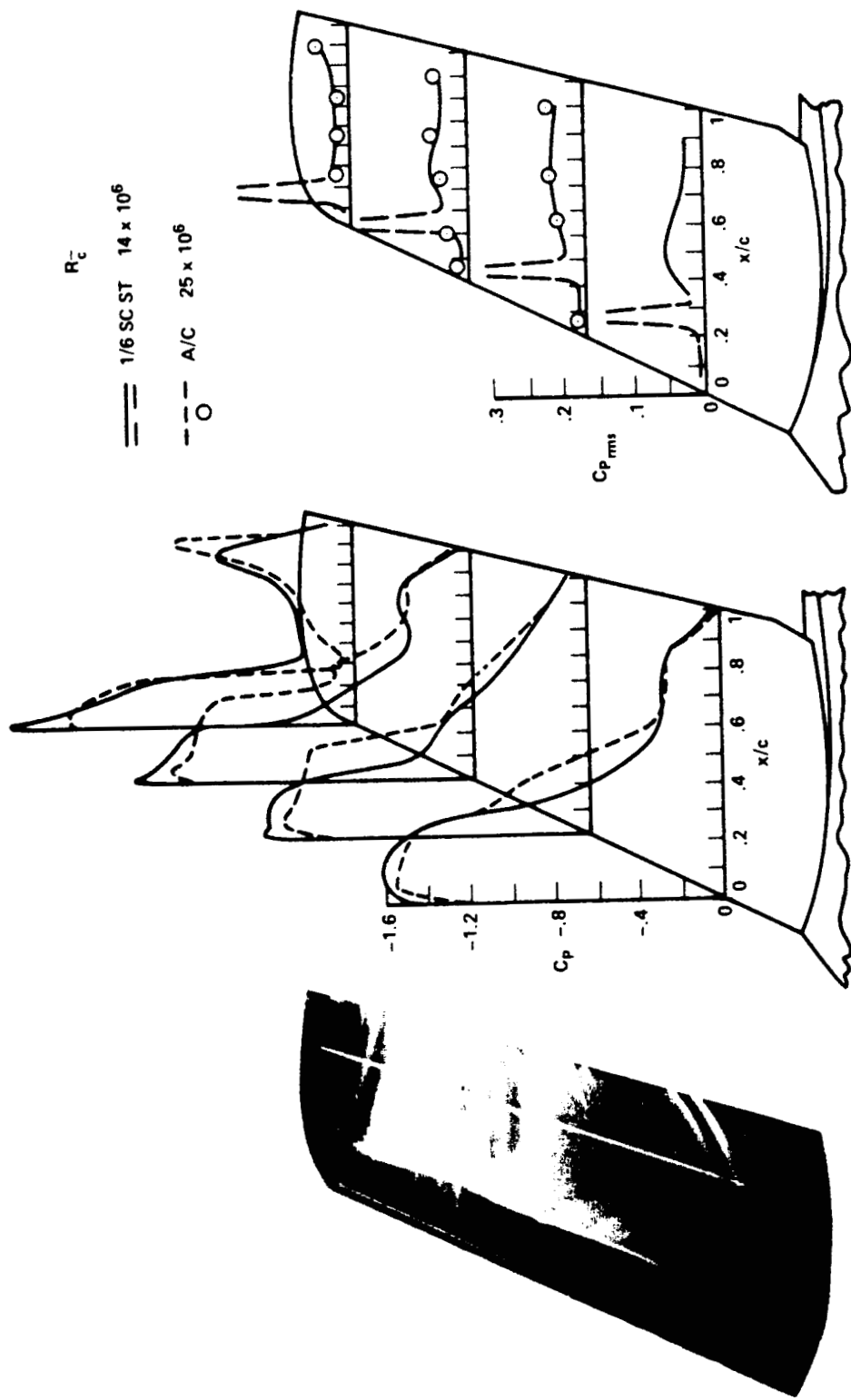
Figure 14. Correlation of steady- and fluctuating-pressure distributions on TACT 1/6-scale steel model and aircraft for $\Lambda = 26°$, $M = 0.80$.
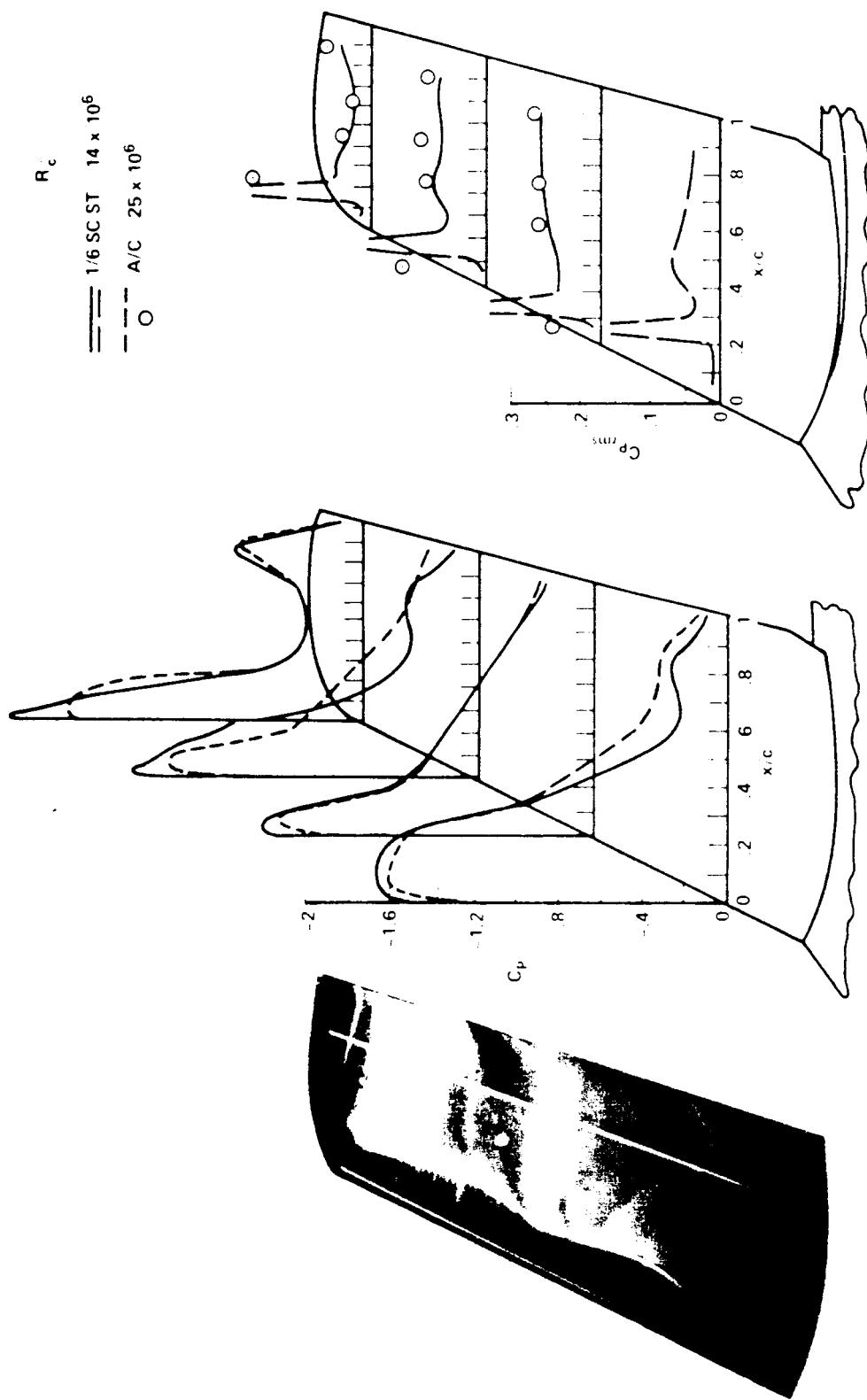
(a) $\alpha = 9.1°$.

(b) $\alpha = 10.0°$.

Figure 14. Continued.

R_c

———— 1/6 SC ST 14×10^6

– – – O A/C 25×10^6

$C_{p_{rms}}$

C_p

x.c

56

R_c

1/6 SC ST   14 x 10^6

A/C   25 x 10^6

$C_{p_{rms}}$

.3

.2

.1

0

0   .2   .4   .6   .8   1

x/c

C_p

-2

-1.6

-1.2

-.8

-.4

0

0   .2   .4   .6   .8   1

x/c

(c) α = 11.1°.

Figure 14. Continued.

57
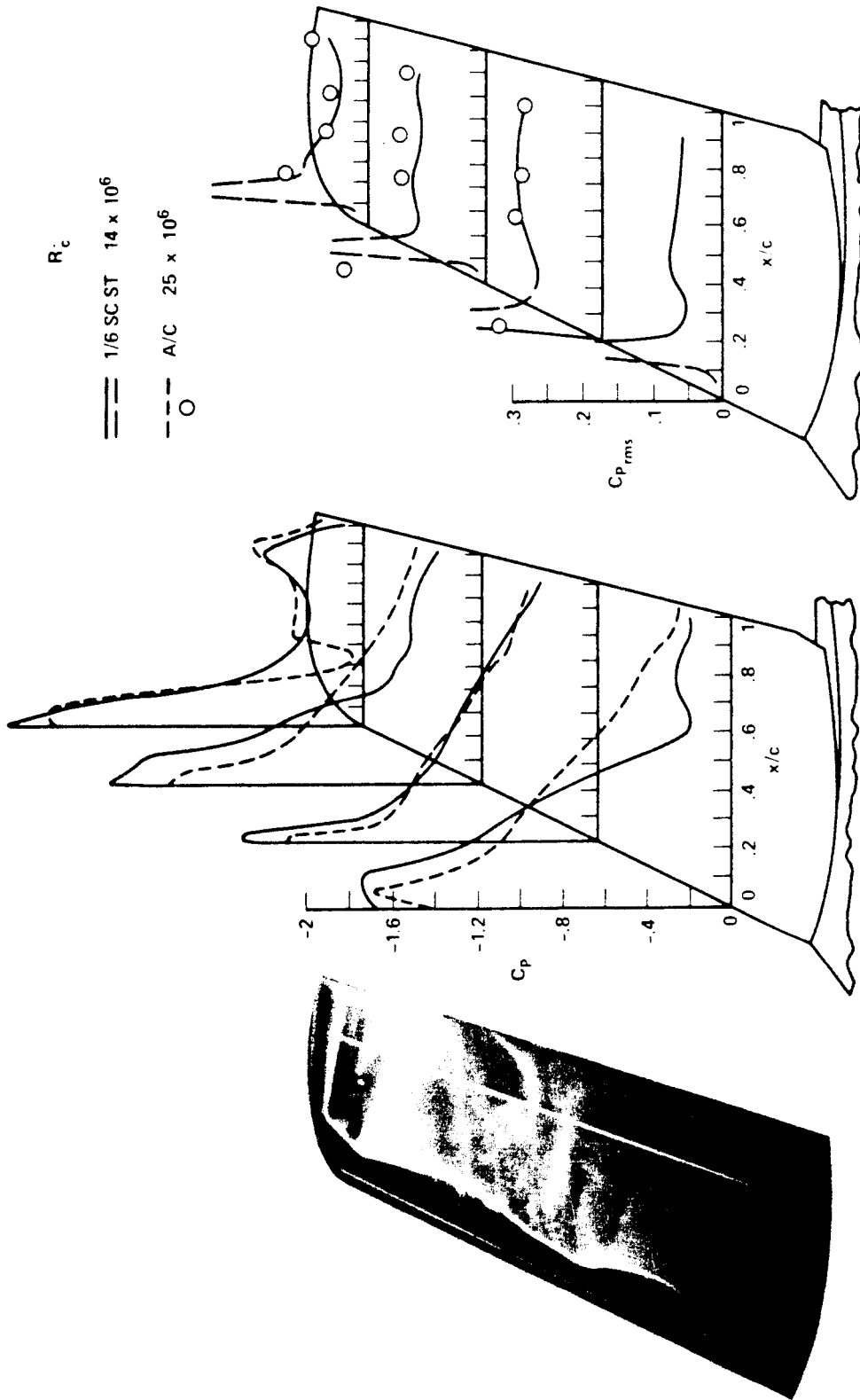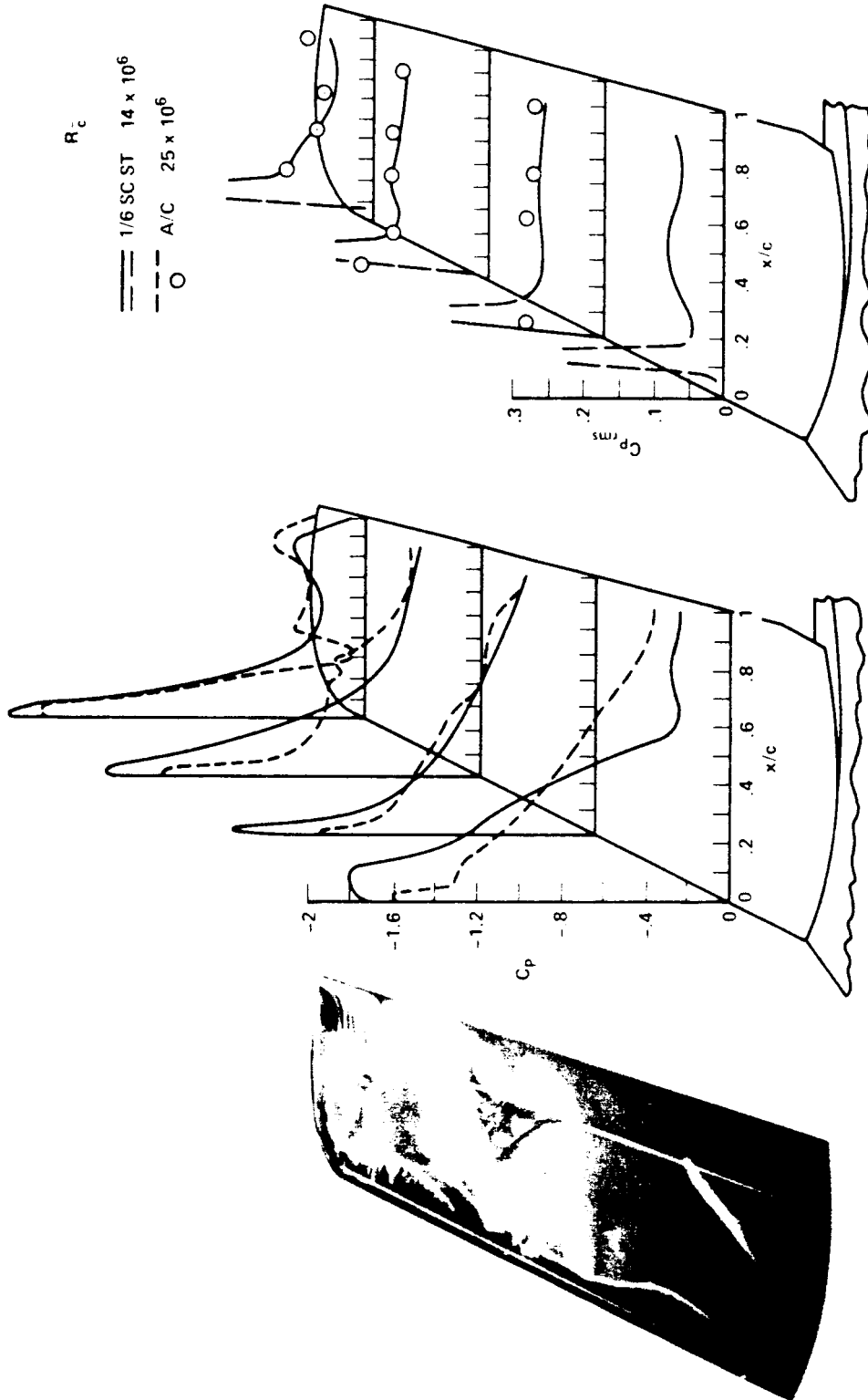
(d) $\alpha = 12.1°$.

Figure 14. Concluded.
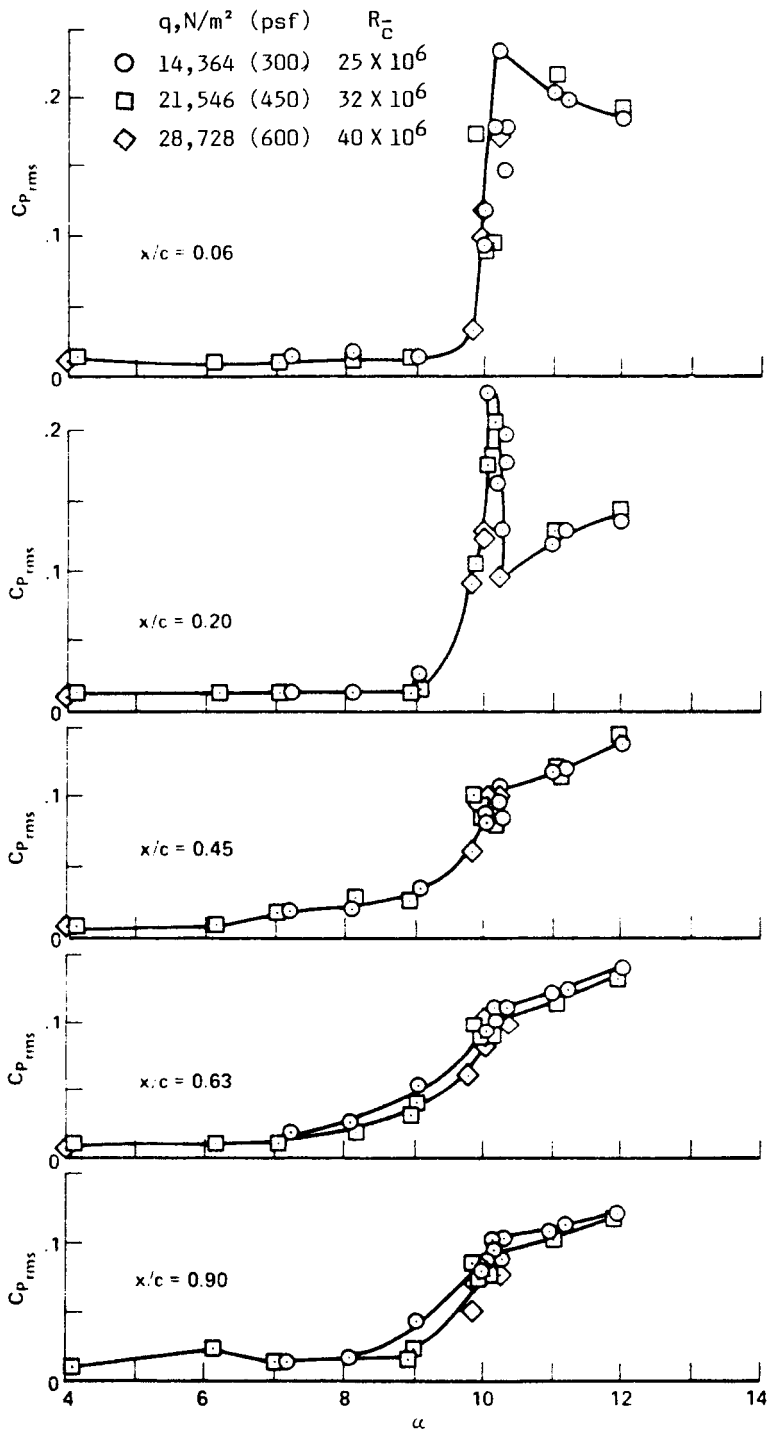
Figure 15. Effects of dynamic pressure on TACT aircraft pressure fluctuations, $\Lambda = 26°$, M = 0.80, r_i = 0.744.
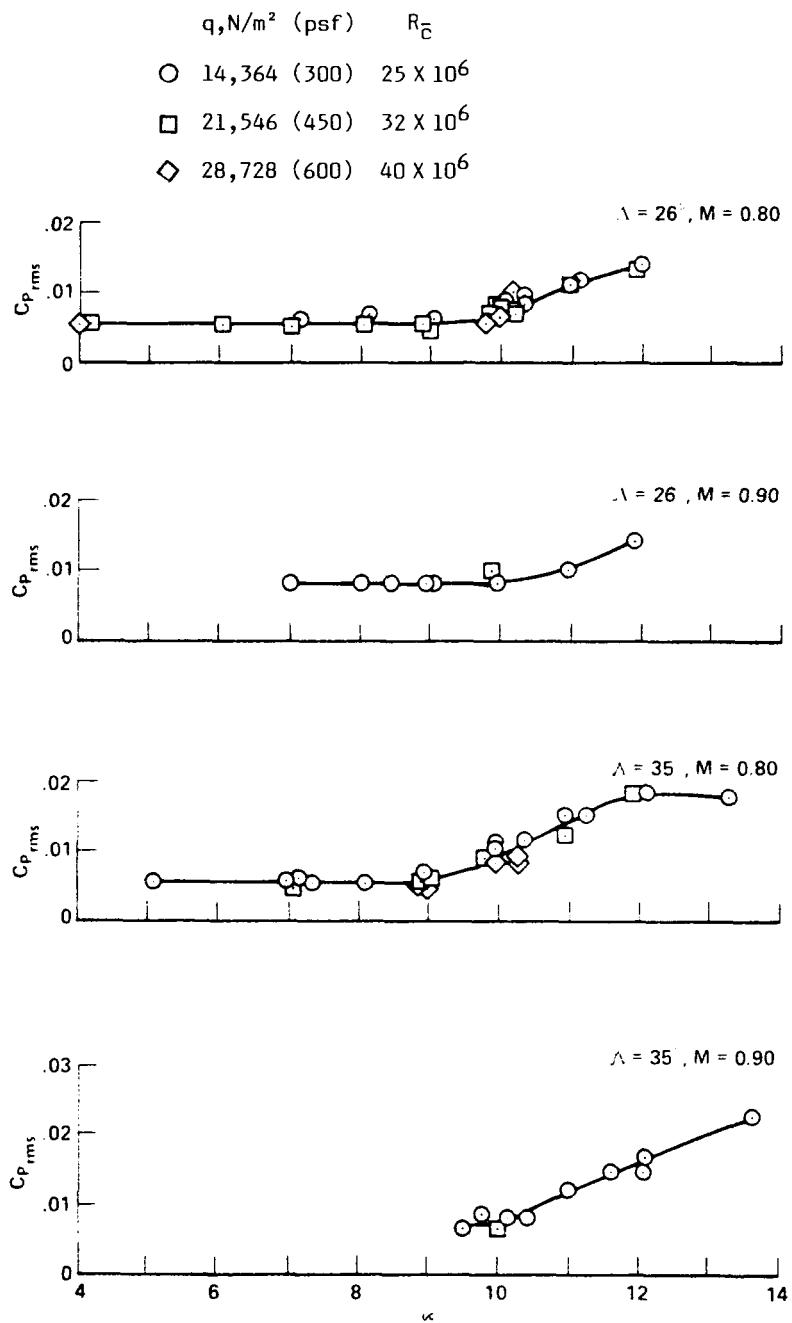
Figure 16. Pressure fluctuations on lower surface of TACT aircraft wing at $\eta = 0.744$, x/c = 0.85.
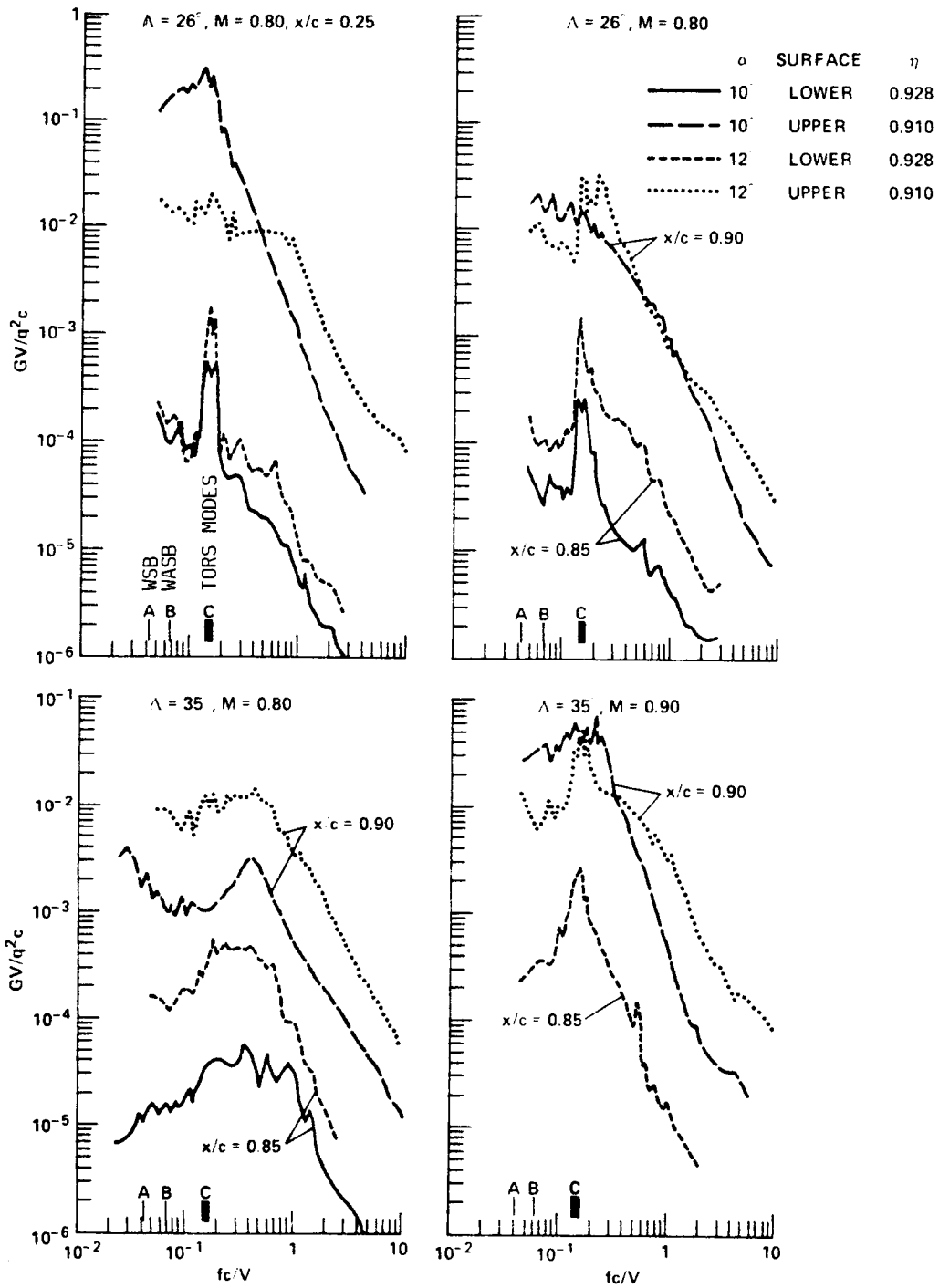
Figure 17. Typical power spectra of pressure fluctuations on TACT aircraft.

$\Lambda = 26°$, M = 0.80, $\alpha \approx 11.1°$, $\eta = 0.578$, x/c = 0.63
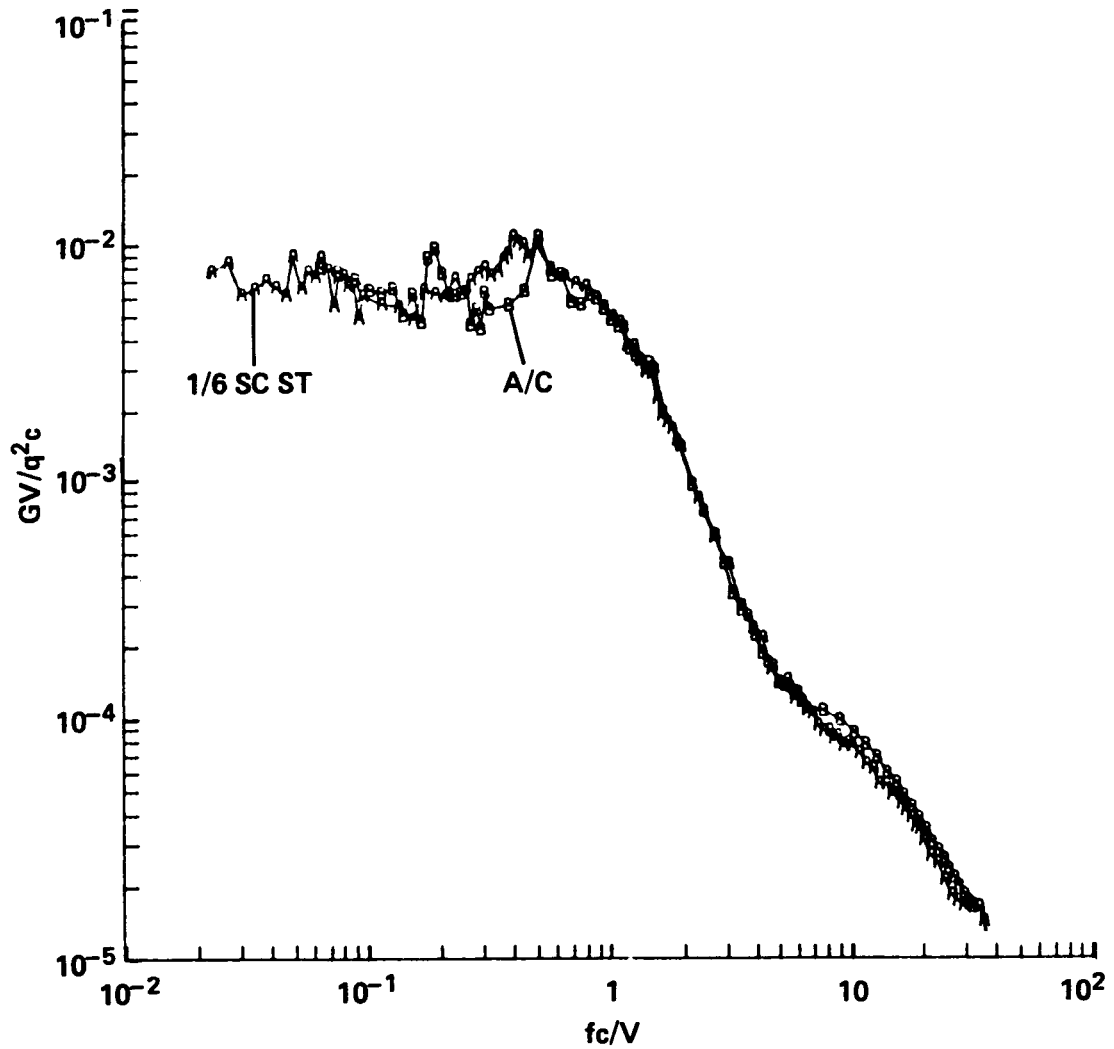
(a) $\Lambda = 26°$, M = 0.80, $\alpha_{ST} = 11.1°$, $\alpha_{A/C} = 11.0°$, $\eta = 0.578$, x/c = 0.63

Figure 18 (a). Correlation of power spectra of pressure fluctuations on TACT 1/6-scale models and aircraft.
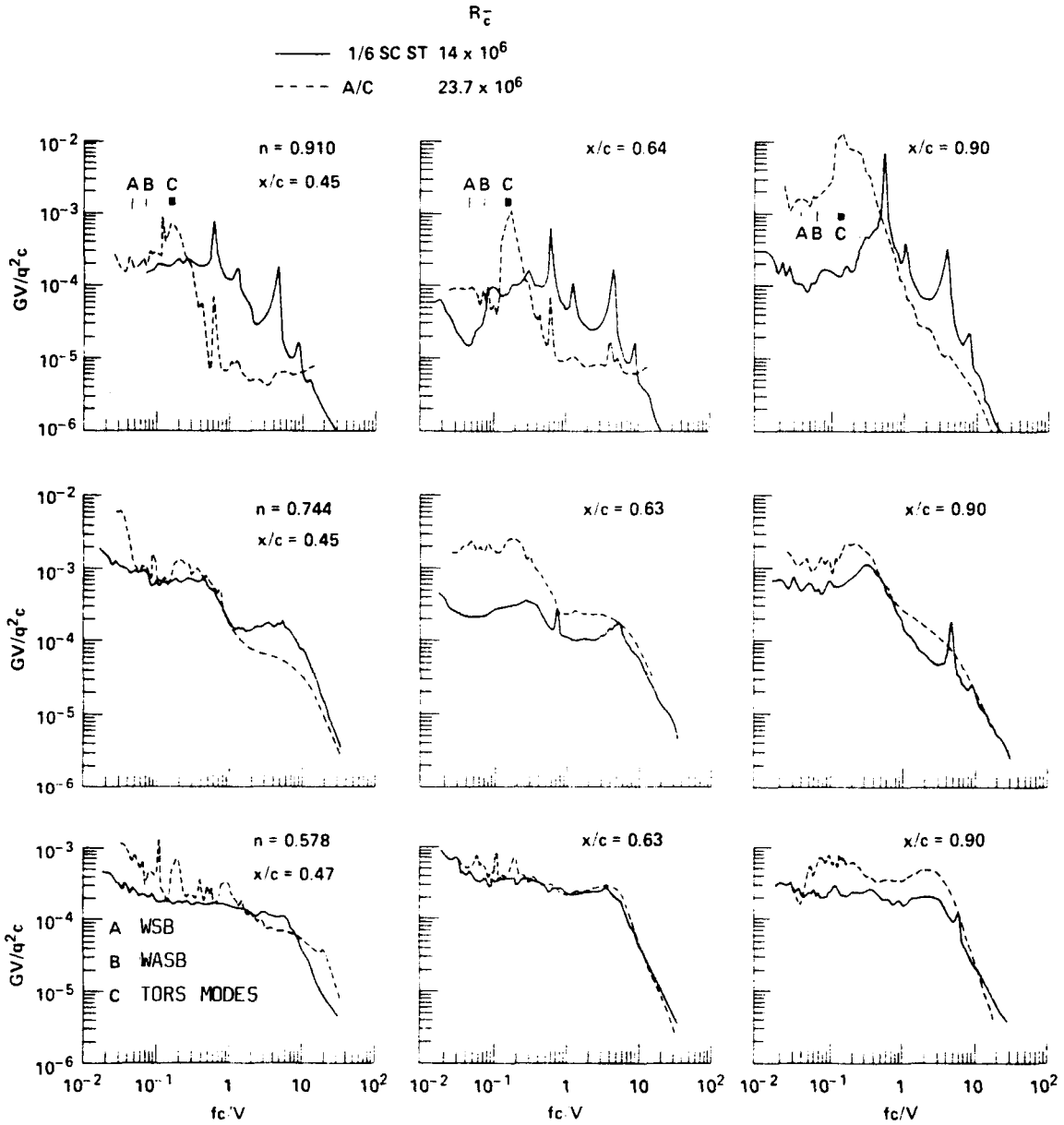
(b) $\Lambda = 26°$, $M = 0.80$, $\alpha_{ST} = 9.2°$, $\alpha_{A/C} = 9.0°$.

Figure 18.   Continued.

63
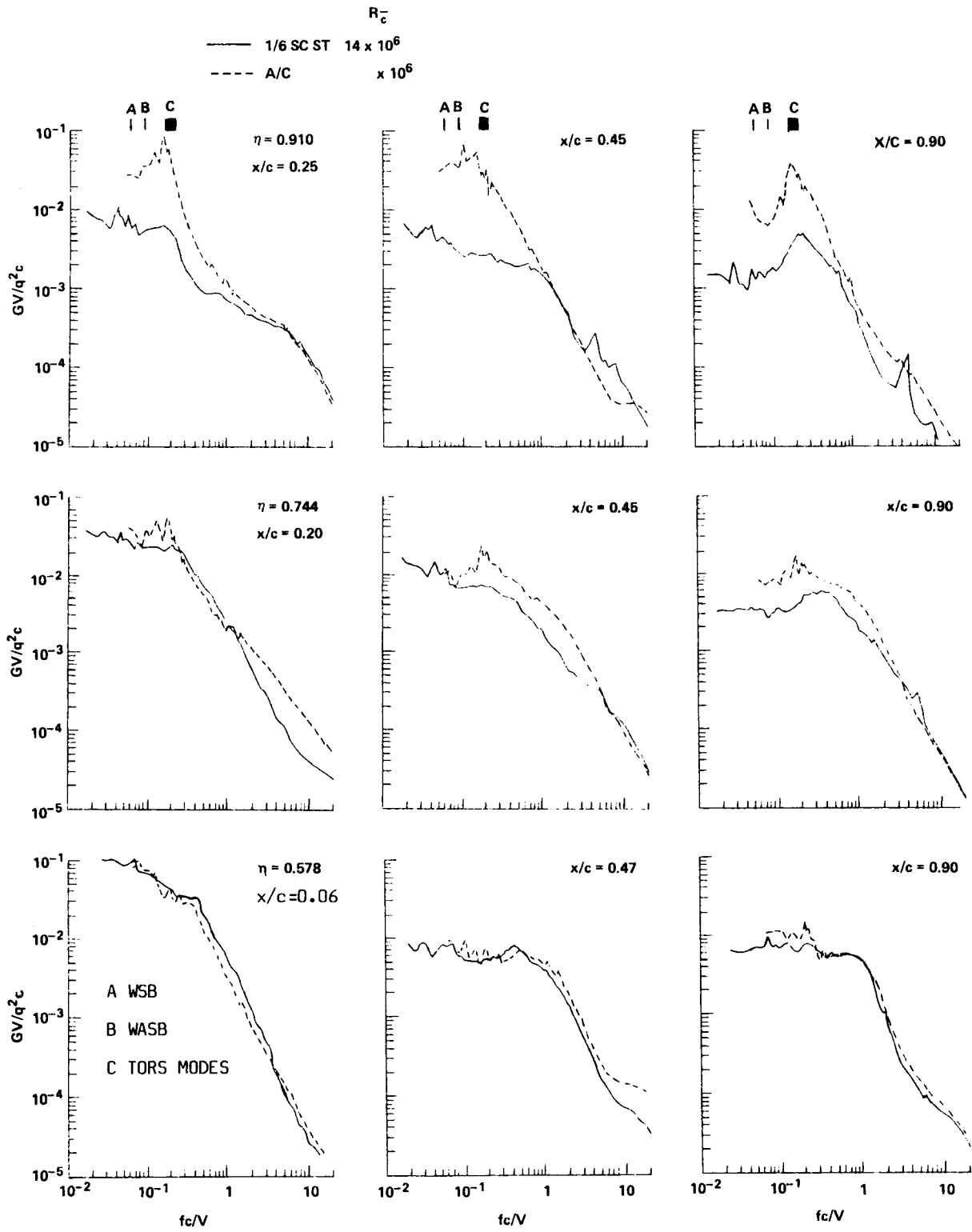
(c) $\Lambda = 26°$, $M = 0.80$, $\alpha_{ST} = 11.1°$, $\alpha_{A/C} = 11.0°$.

Figure 18. Continued.
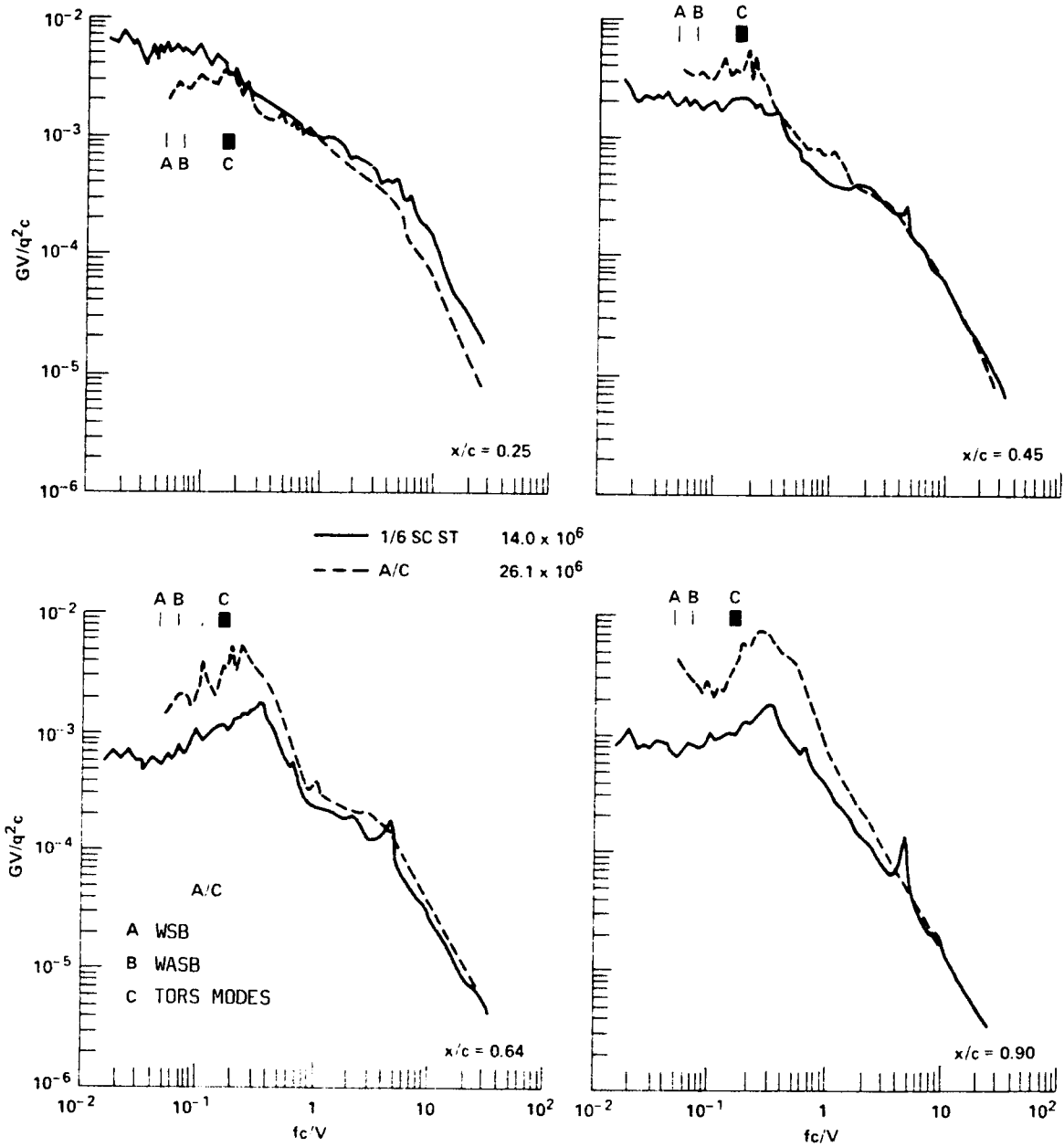
(d) $\Lambda = 35°$, $M = 0.80$, $\alpha_{ST} = 10.1°$, $\alpha_{A/C} = 10.0°$, $\eta = 0.910$.

Figure 18. Continued.

A B C
a b c

A B
a b c

10⁻¹
10⁻²
10⁻³
10⁻⁴
10⁻⁵

GV/q^2c

$R\bar{c}$
——— 1/6 SC AL   10.5 x 10⁶
- - - - A/C   22.8 x 10⁶

x/c = 0.25

a   b   c
A   B   C

x'c = 0.45

A B   C
a   b c

A/C
A   WSB
B   WASB
C   TORS MODES

x/c = 0.64

A B   C
a   b c

1 6 SC
a 1ST BD
b 2ND BD
c 1ST TORS

x'c = 0.90

GV/q^2c

fc/V

fc/V

10^{-2} 10^{-1} 1   10 10^2
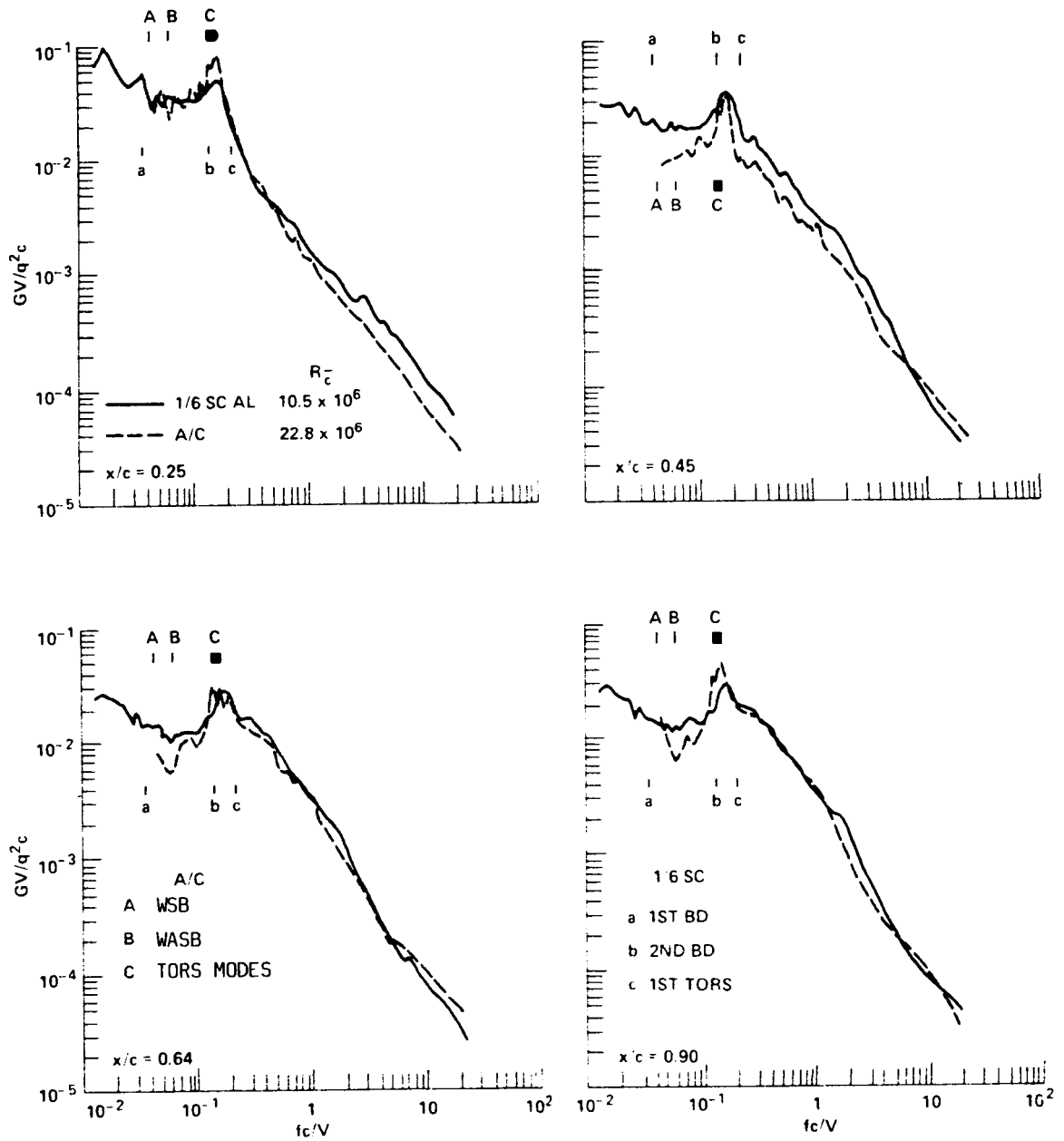
(e) $\Lambda = 35°$, M = 0.90, $\alpha = 12.1$, $\eta = 0.910$.

Figure 18.   Concluded.
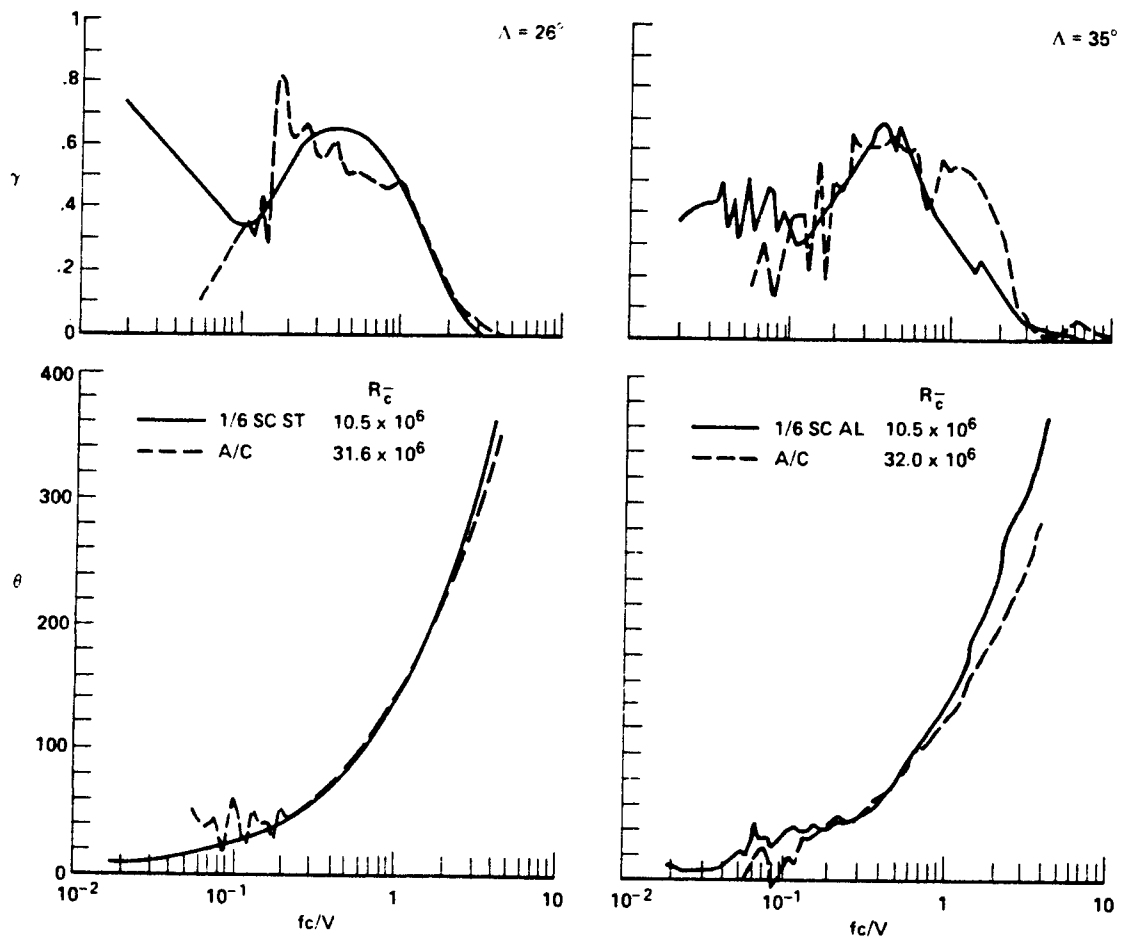
Figure 19. Coherence and phase angle between pressure fluctuations at x/c = 0.45 and x/c = 0.63, η = 0.744, M = 0.80, α = 12°.
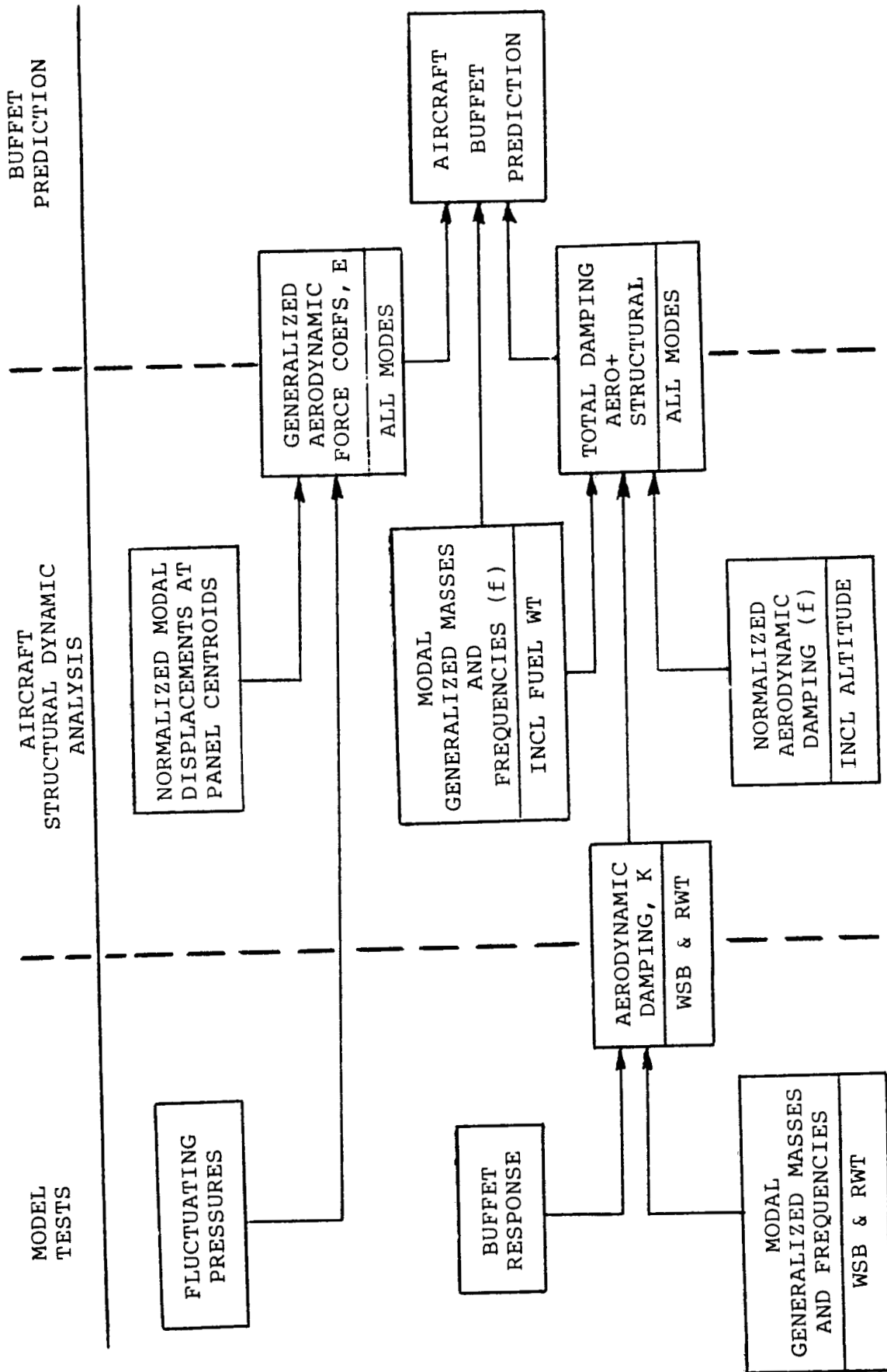
Figure 20. Buffet prediction method.
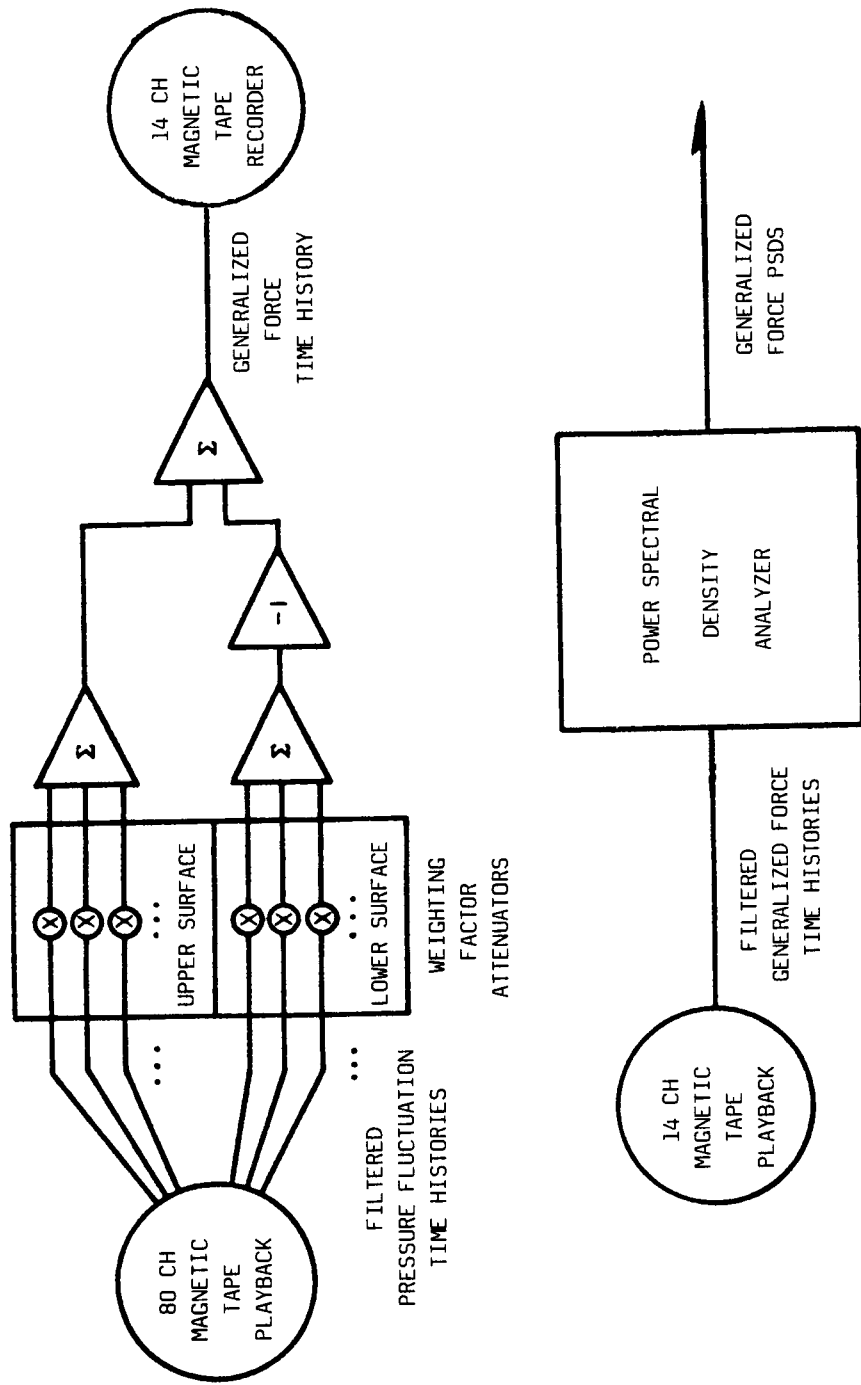
Figure 21. Flow charts for processing generalized force data.

CENTROIDS

PRESSURE TRANSDUCERS

0   .5   1.0   1.5 m
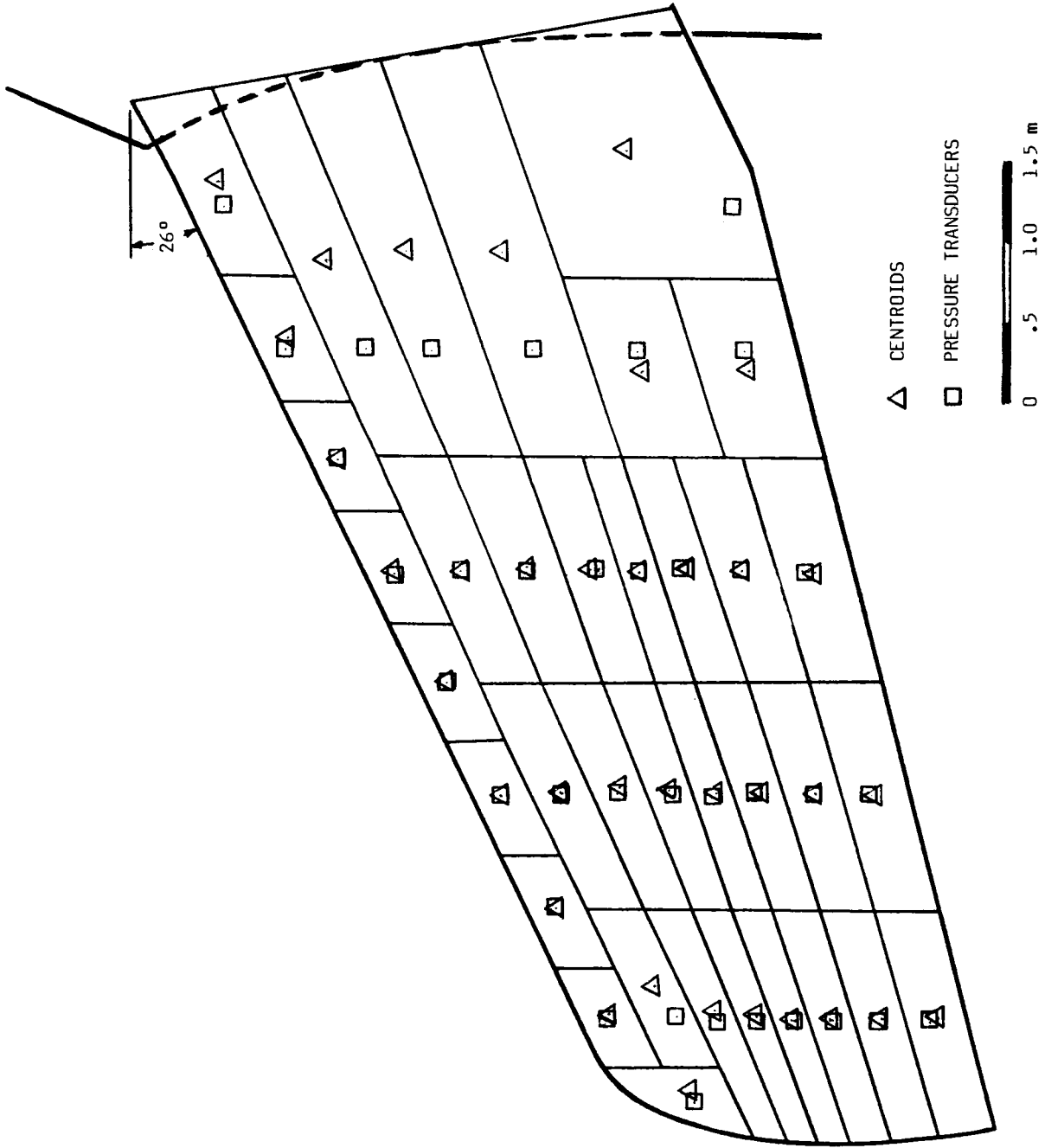
(a) Wing upper surface

Figure 22.   Sketches of TACT aircraft wing and horizontal tail showing panel areas, centroids and locations of pressure transducers.

CENTROIDS

PRESSURE TRANSDUCERS

0   .5   1.0   1.5 m

26°
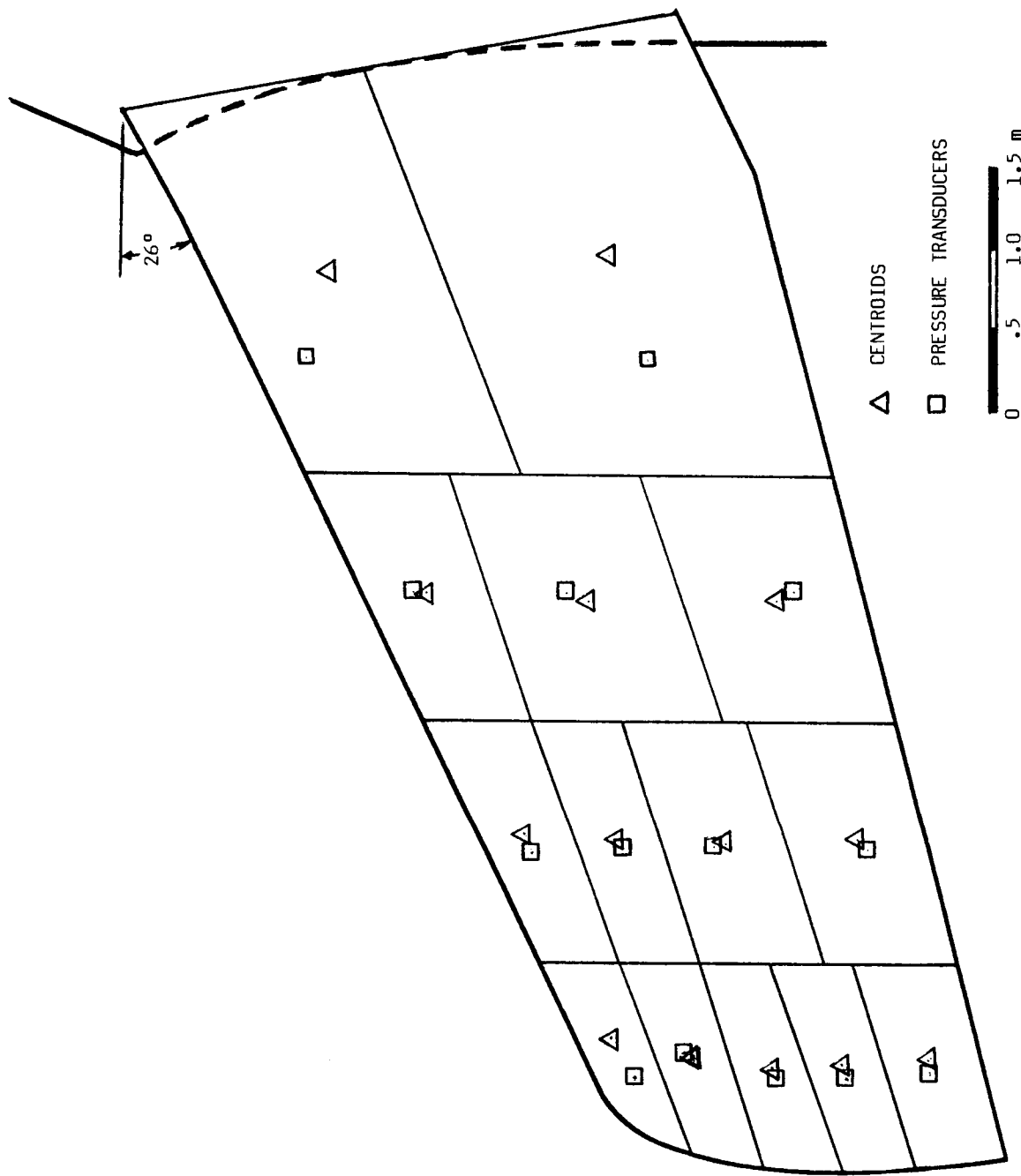
(b) Wing lower surface

Figure 22.   Continued.

71
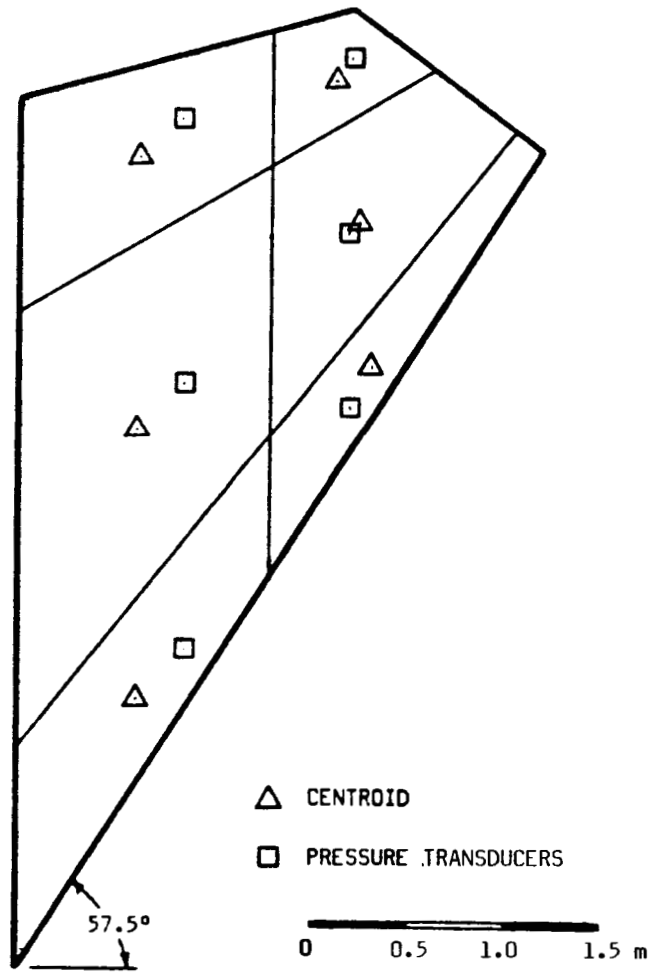
(c) Tail upper and lower surfaces

Figure 22.   Concluded.

WSB

WST

$G_{Qi1}(f)$

G_{Qi1}

G_{Qi6}

FREQUENCY, Hz

FREQUENCY, Hz

$GQ_{t1}(f)$, dB

$GQ_{t6}(f)$, dB
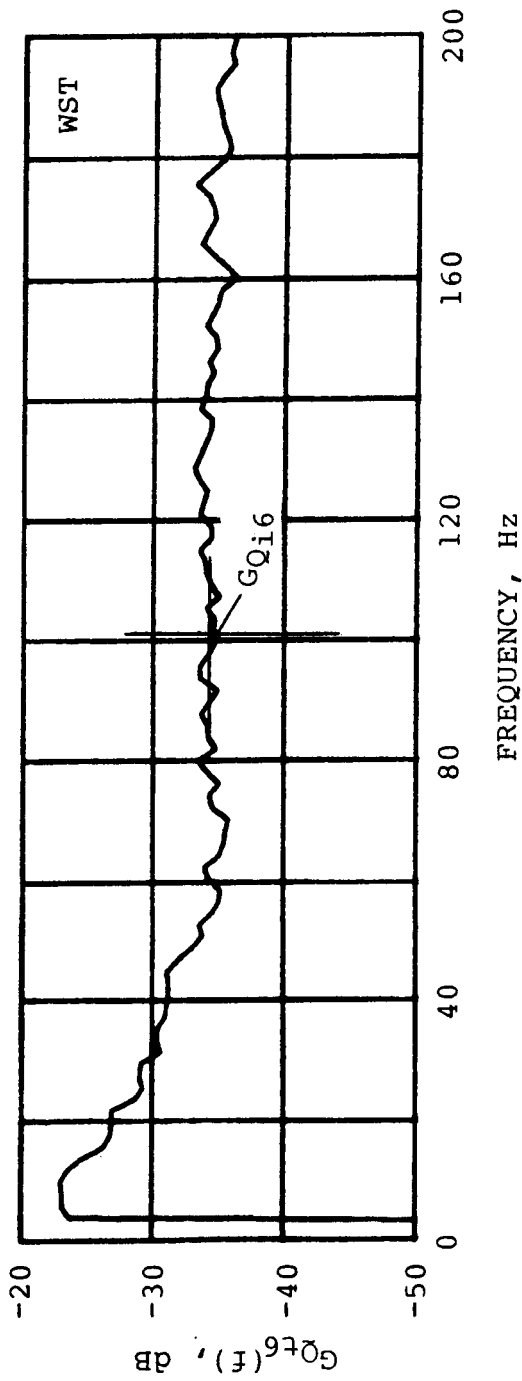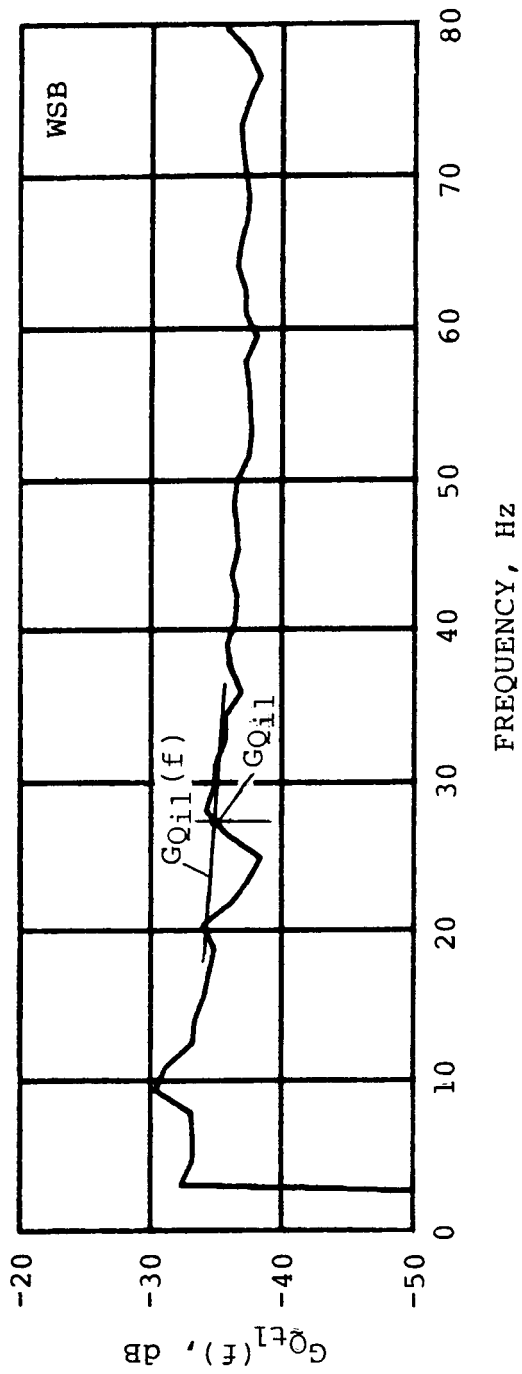
Figure 23. Typical PSDs of generalized forces on TACT aircraft.

$$E$$

O ALUMINUM WING, $R_{\overline{c}} = 10.5 \times 10^6$
* STEEL WING, $R_{\overline{c}} = 14.0 \times 10^6$
$\Lambda = 26°$

α

$\Lambda = 35°$
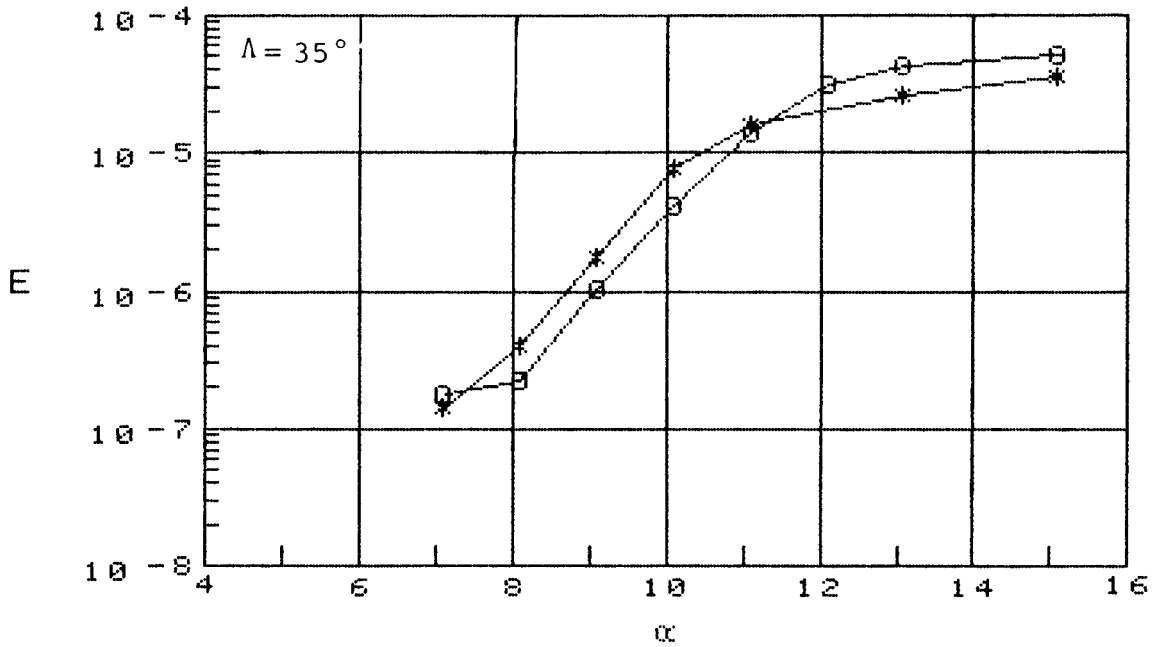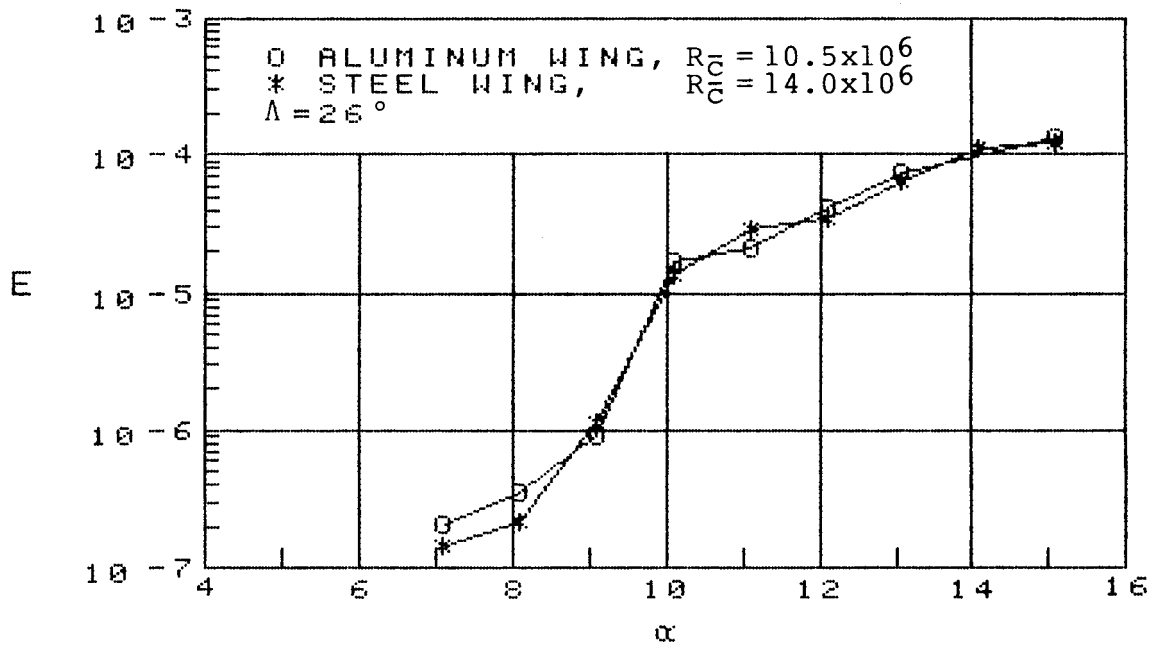
(a) Wing symmetrical bending mode, WSB

Figure 24. Comparison of buffet excitation coefficients obtained from 1/6-scale model with aluminum and steel wings, M = 0.80.
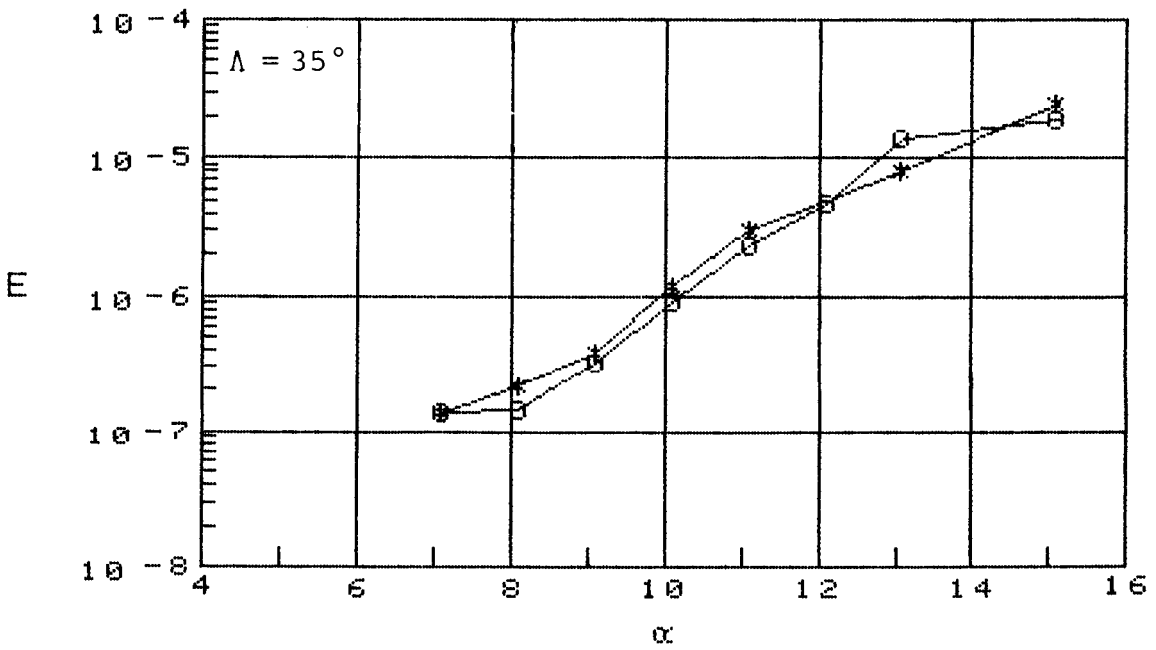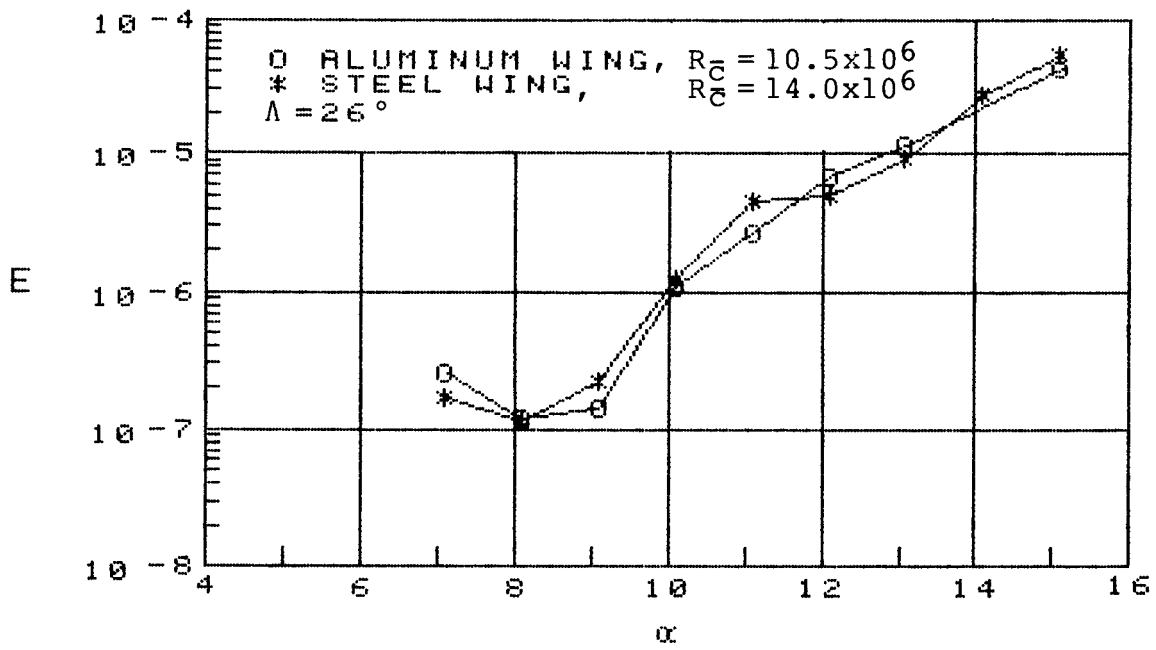
(b) Fuselage vertical bending mode, FVB

Figure 24. Continued.
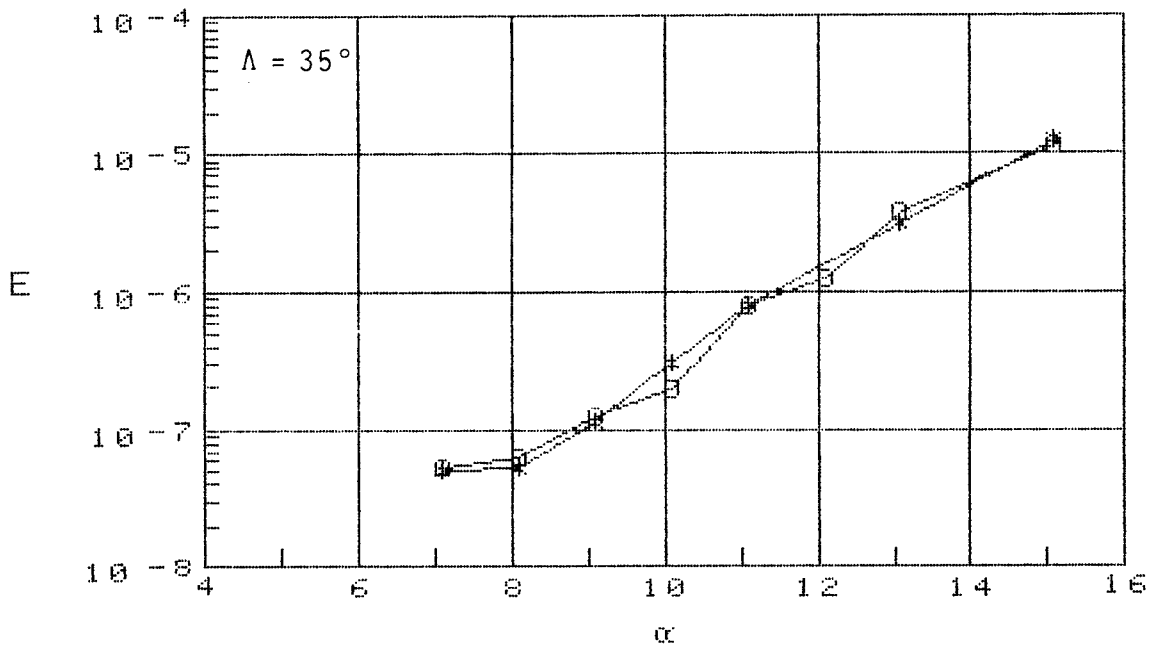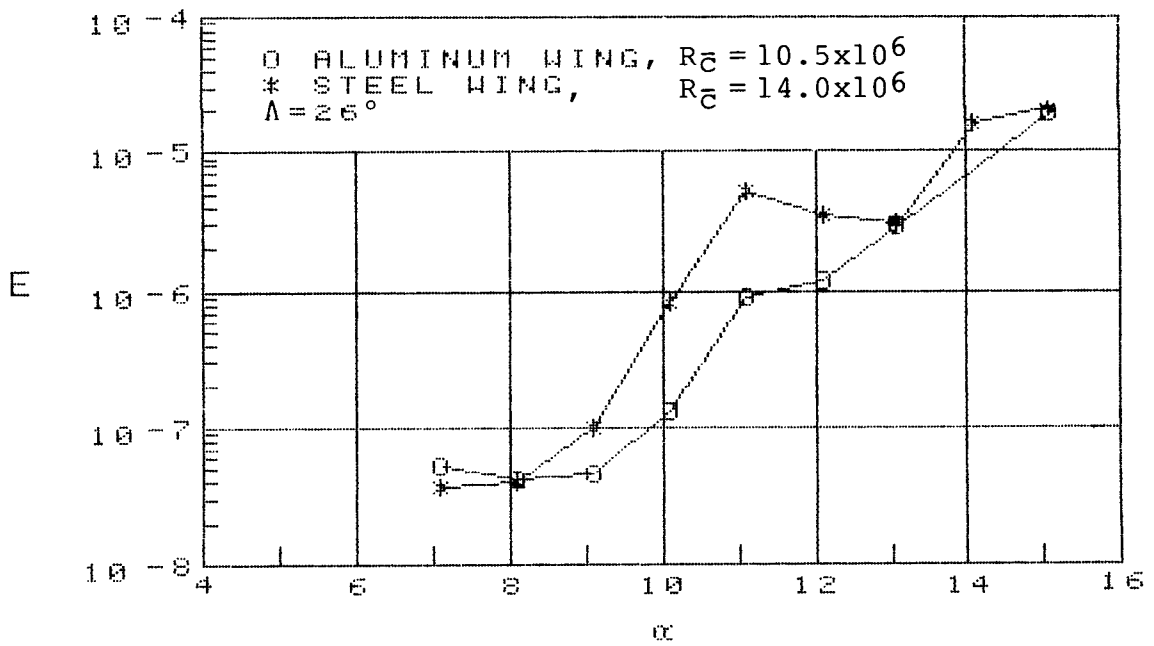
(c) Wing antisymmetrical bending mode, WASB

Figure 24.   Continued.
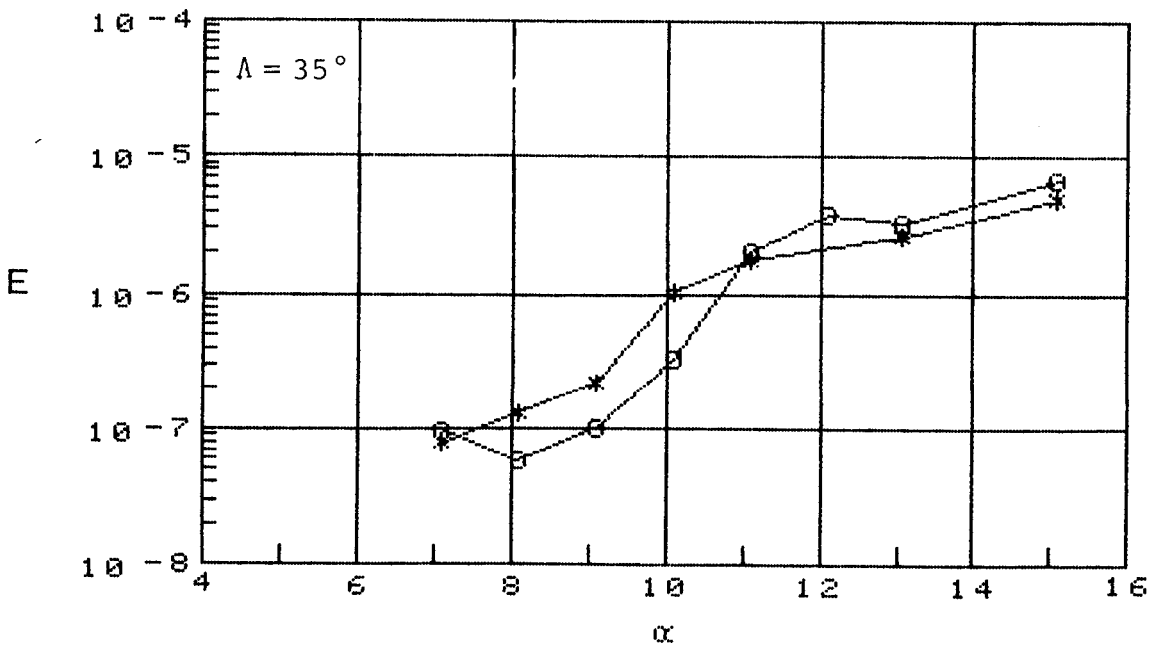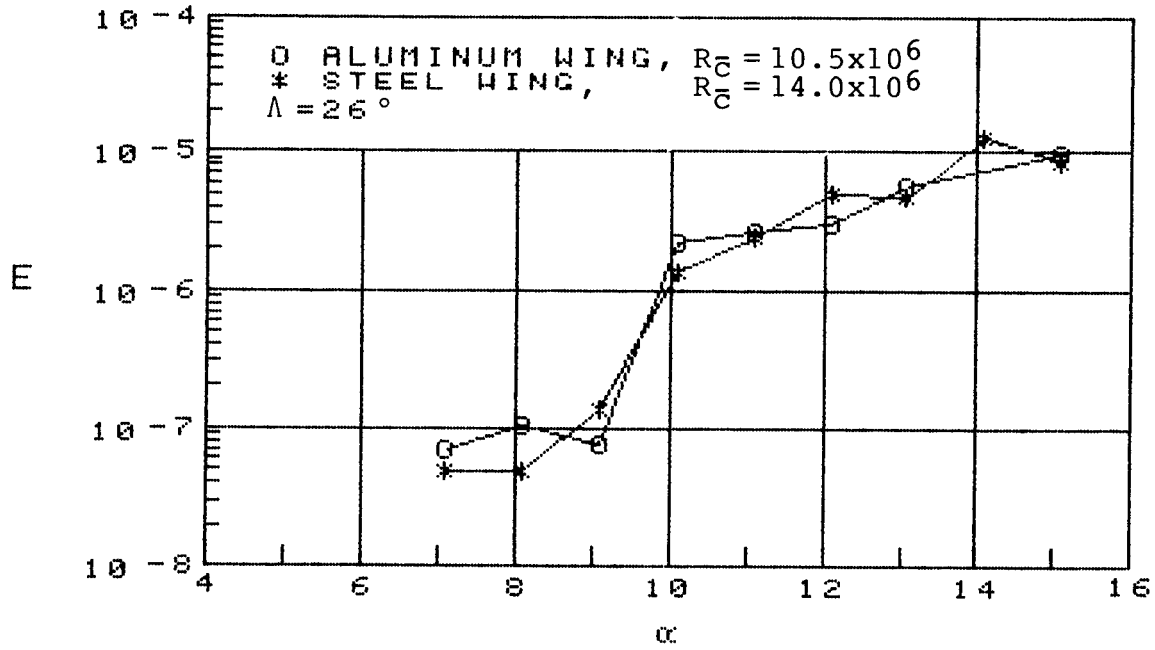
(d) Left wing torsion mode, LWT

Figure 24. Continued.

77
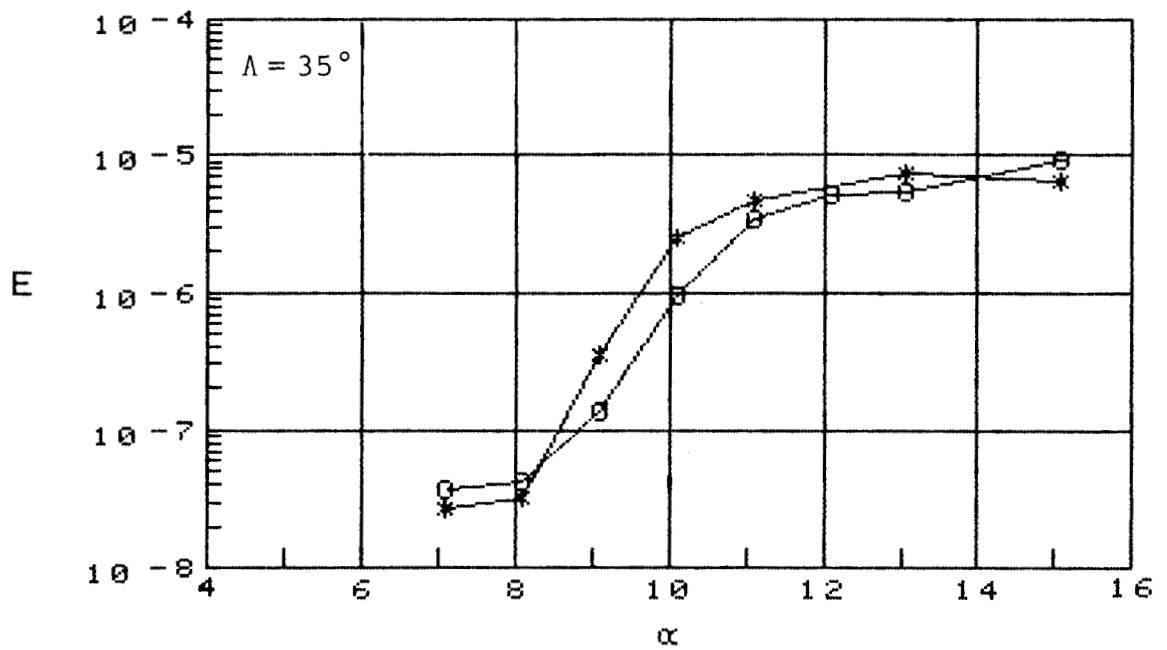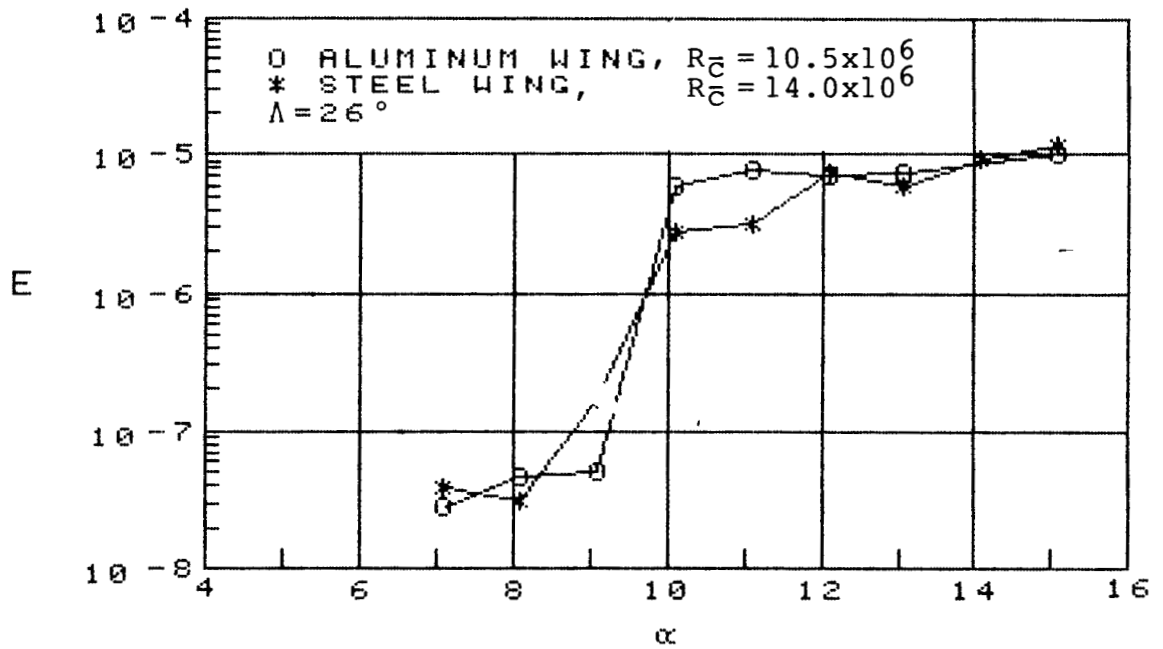
(e) Wing symmetrical torsion mode, WST

Figure 24. Concluded.
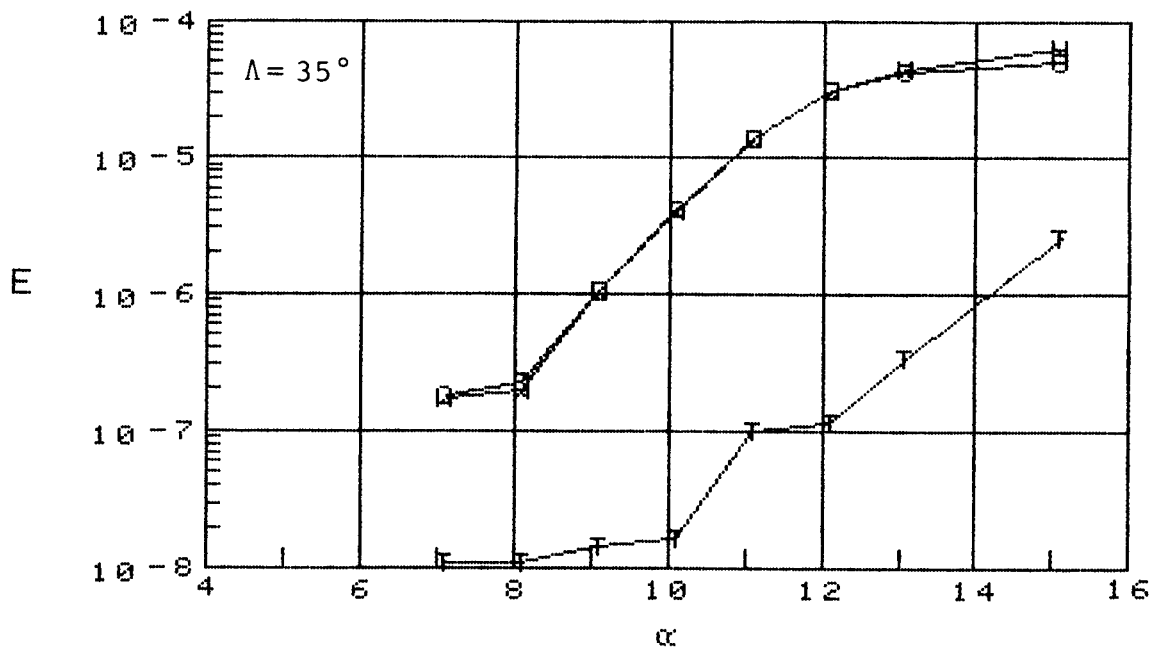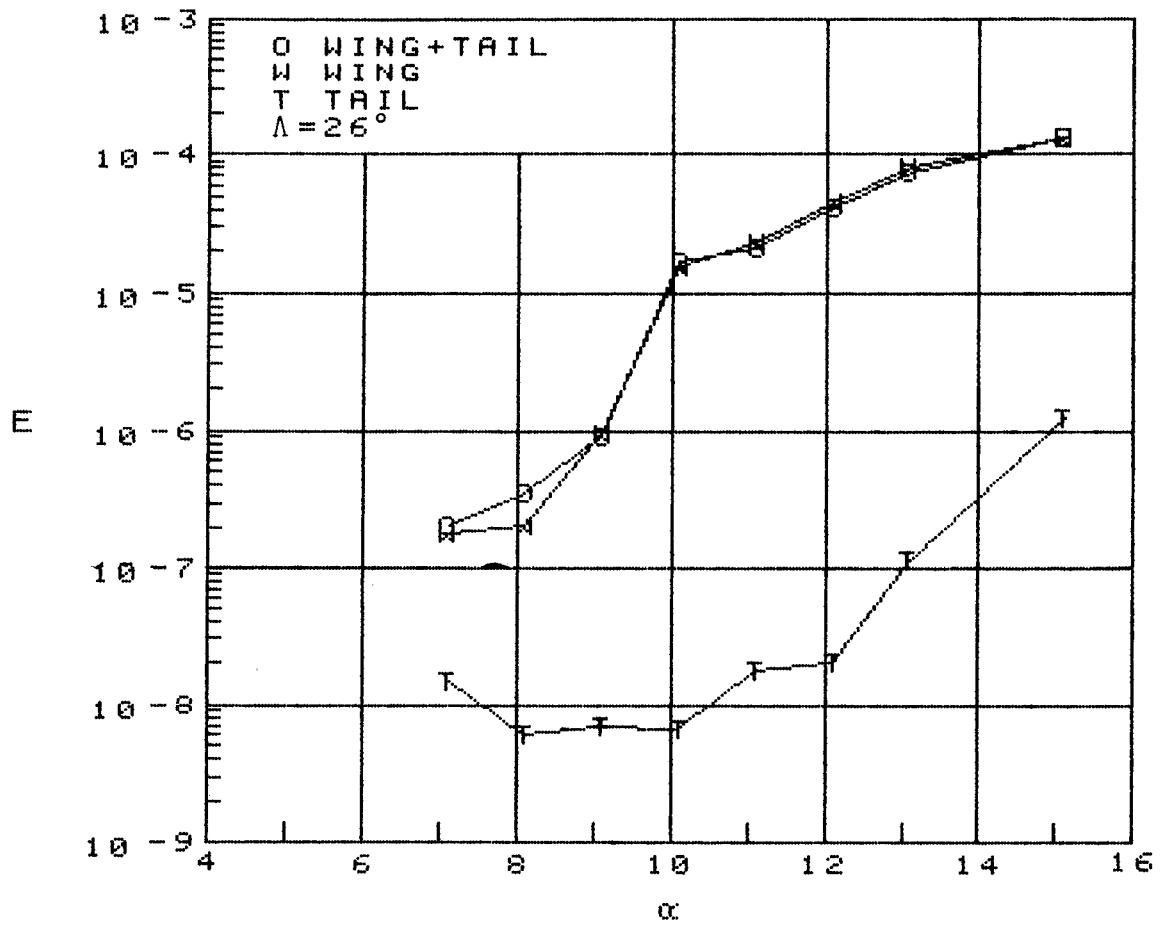
(a) Wing symmetrical bending mode, WSB

Figure 25. Comparison of buffet excitation coefficients due to wing and
tail loads on 1/6-scale model with aluminum wing, M = 0.80.
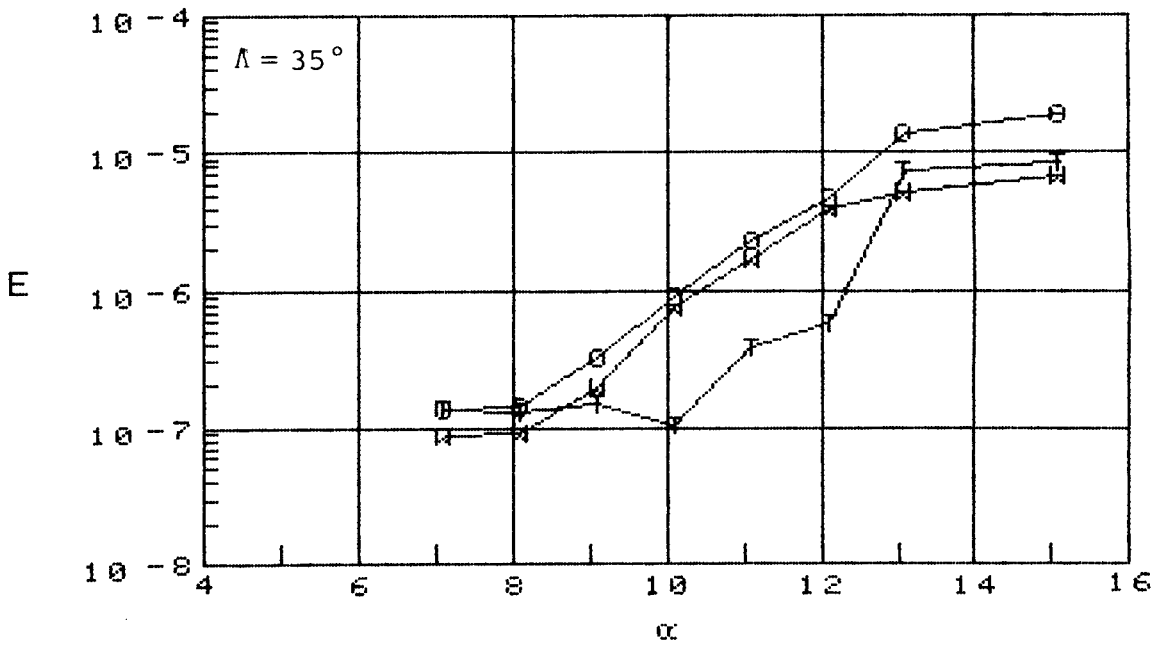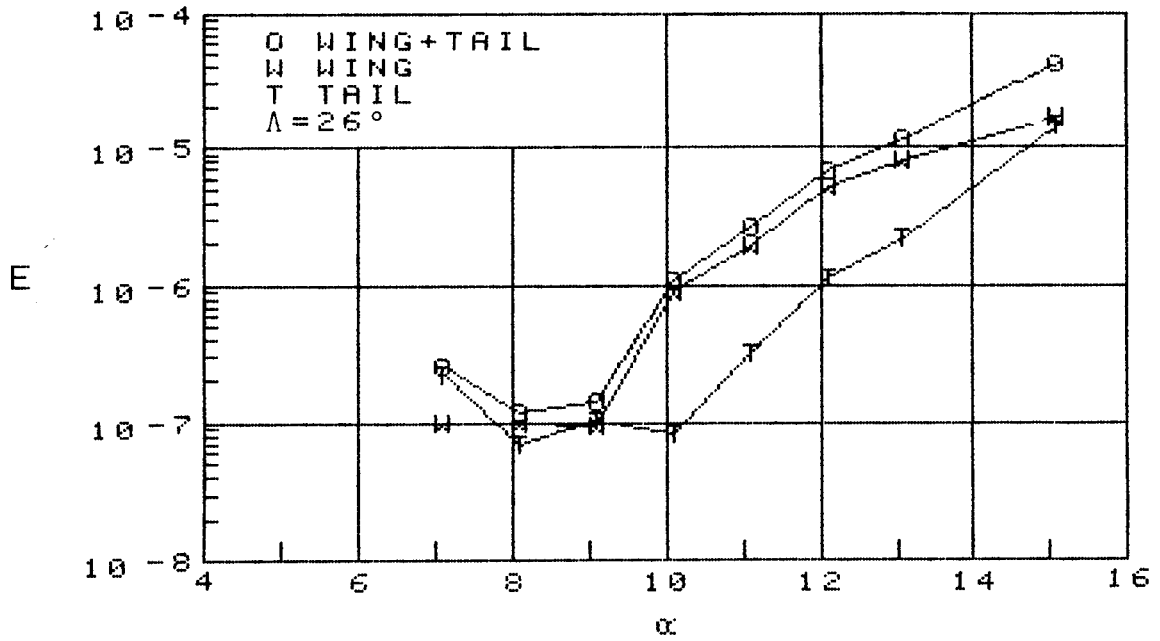
(b) Fuselage vertical bending mode, FVB

Figure 25. Continued.
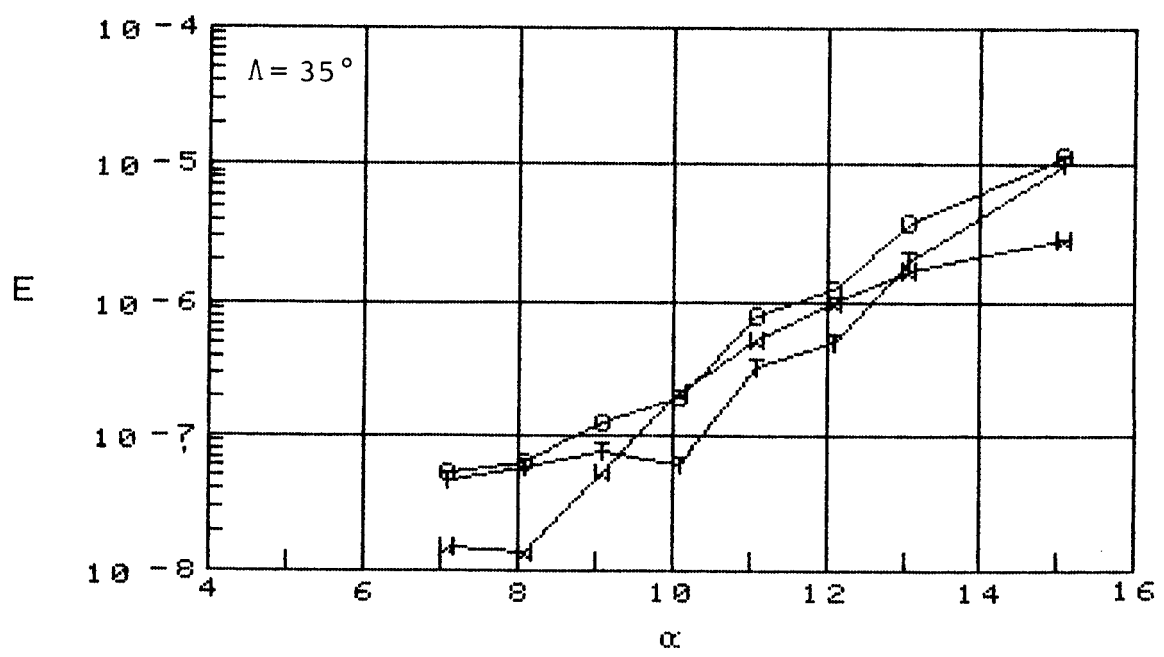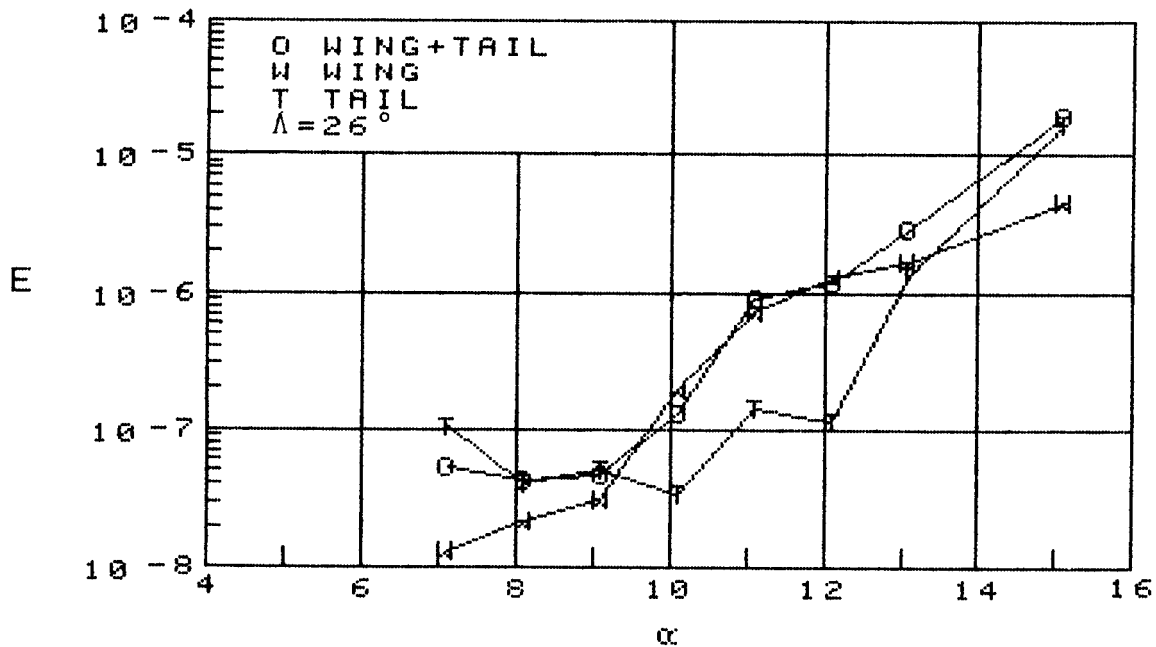
(c) Wing antisymmetrical bending mode, WASB

Figure 25. Continued.
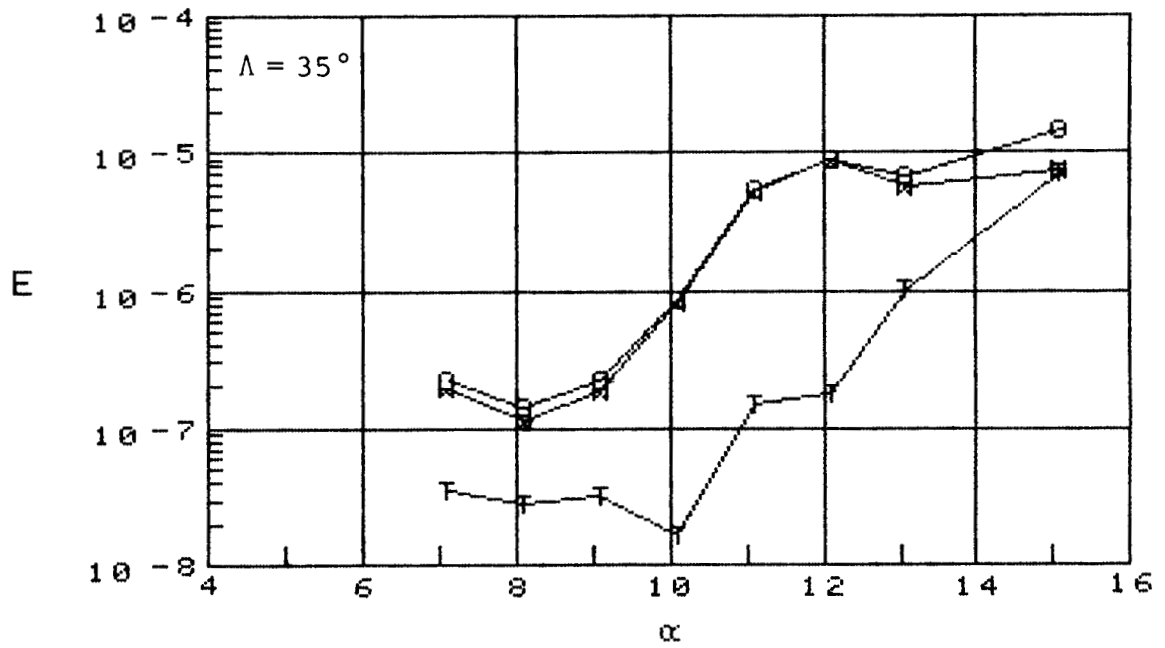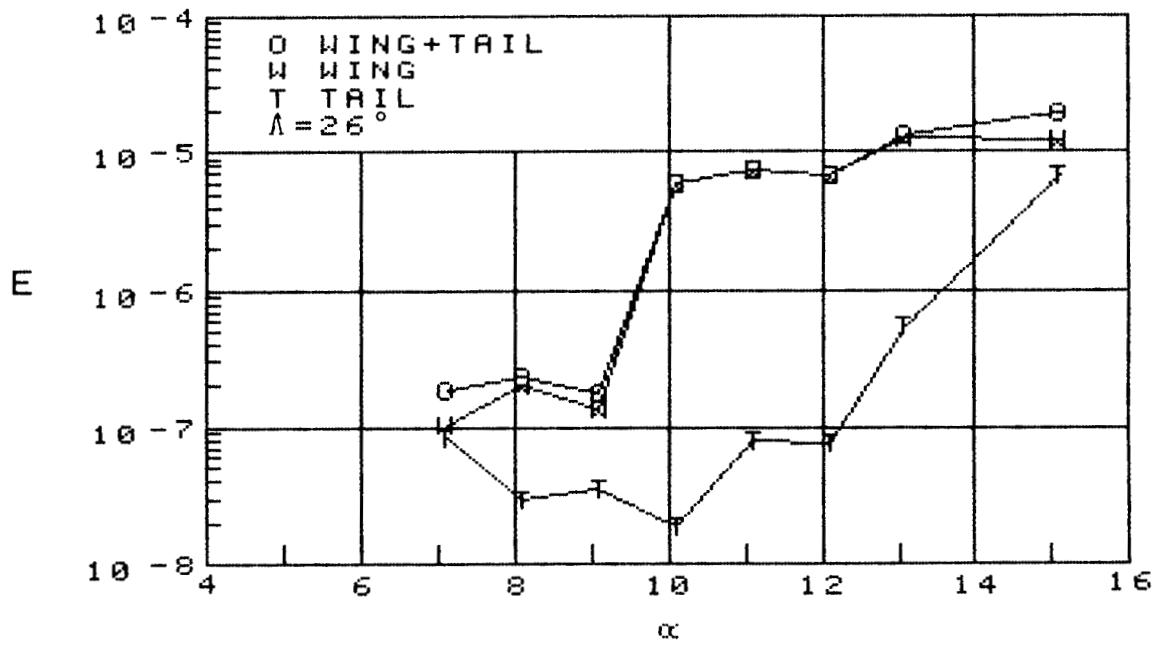
(d) Right wing torsion mode, RWT

Figure 25. Continued.
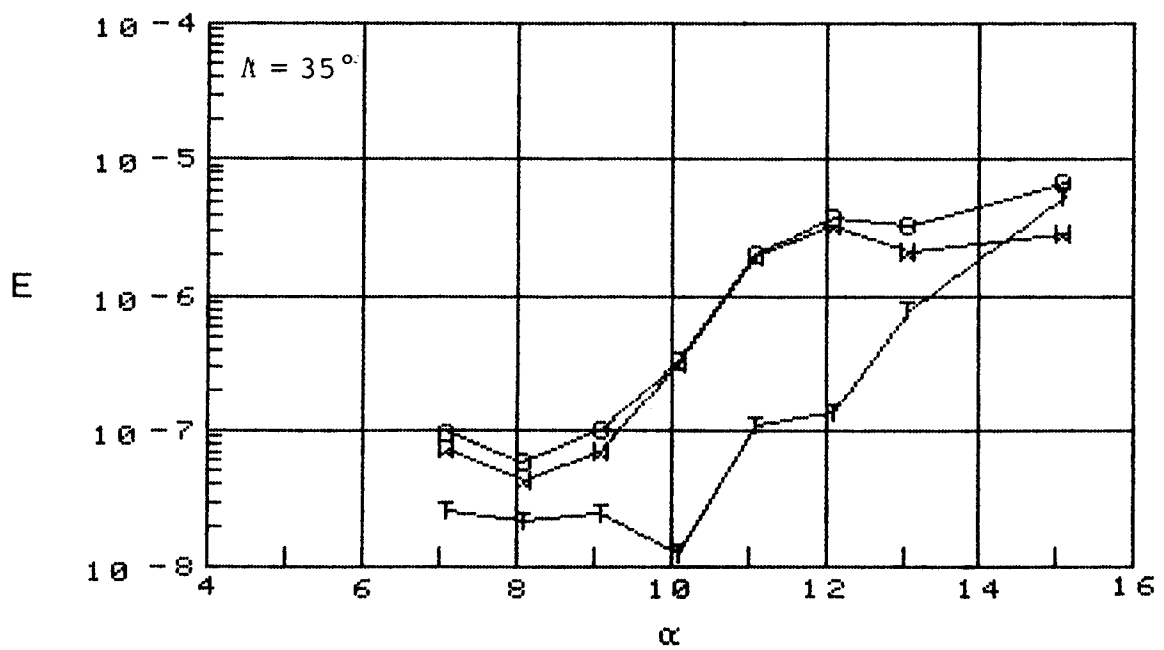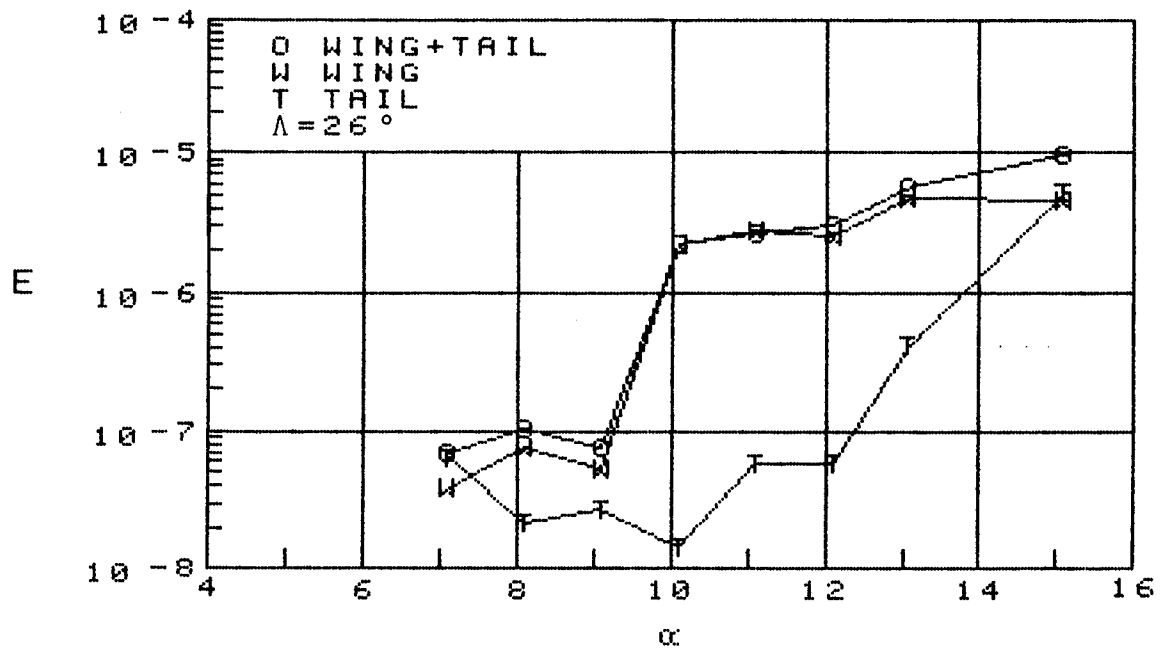
(e) Left wing torsion mode, LWT

Figure 25. Continued.
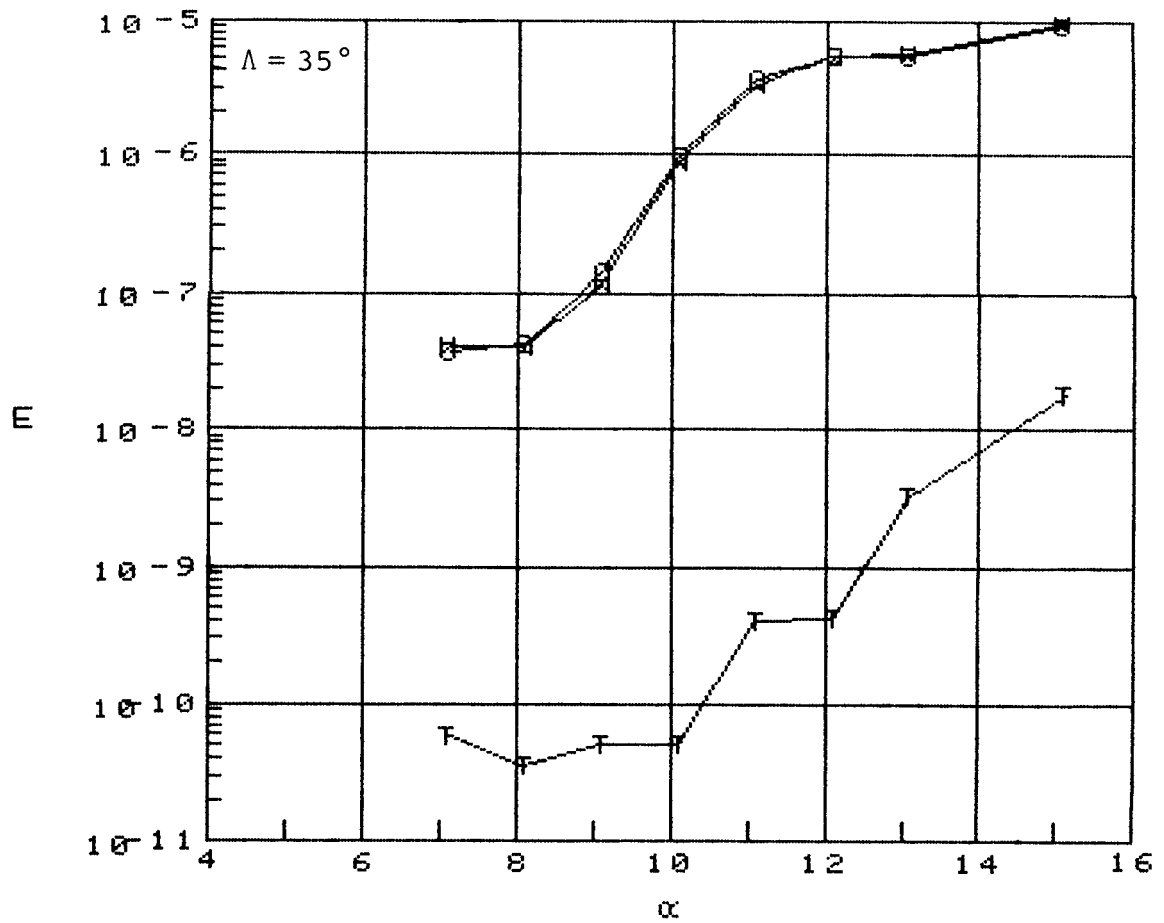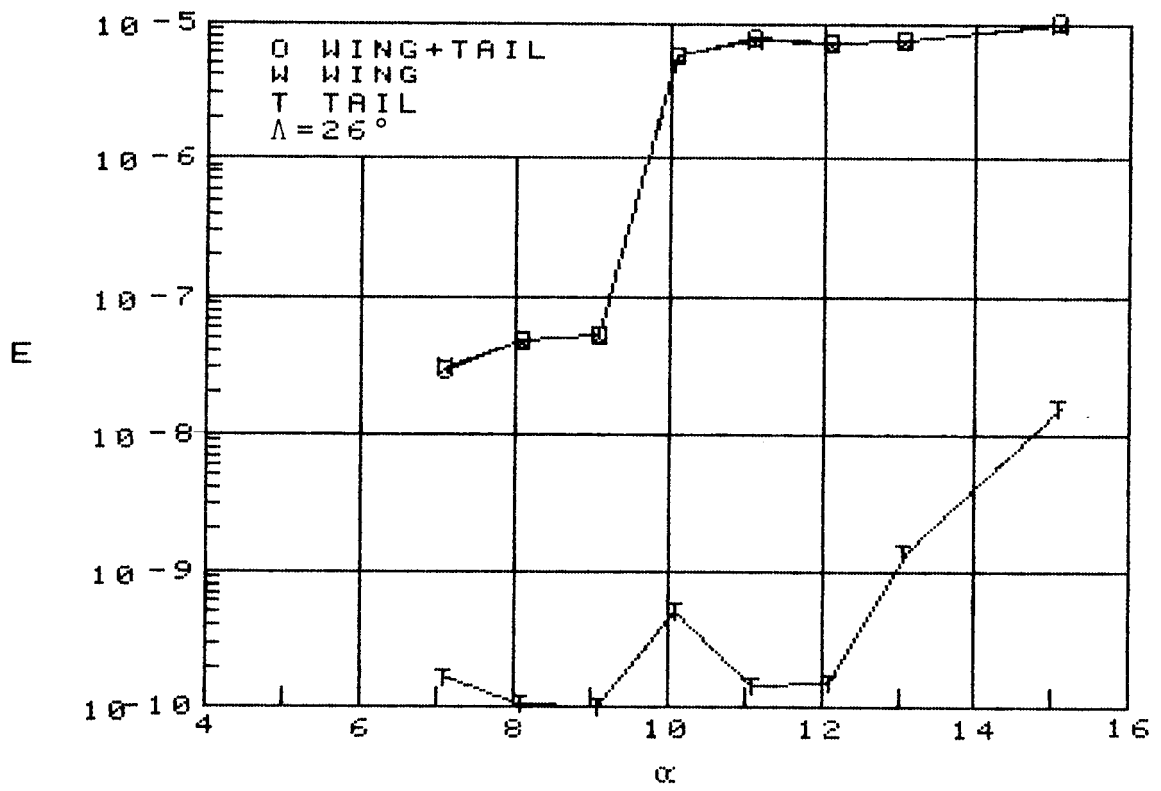
(f) Wing symmetrical torsion mode, WST

Figure 25. Concluded.
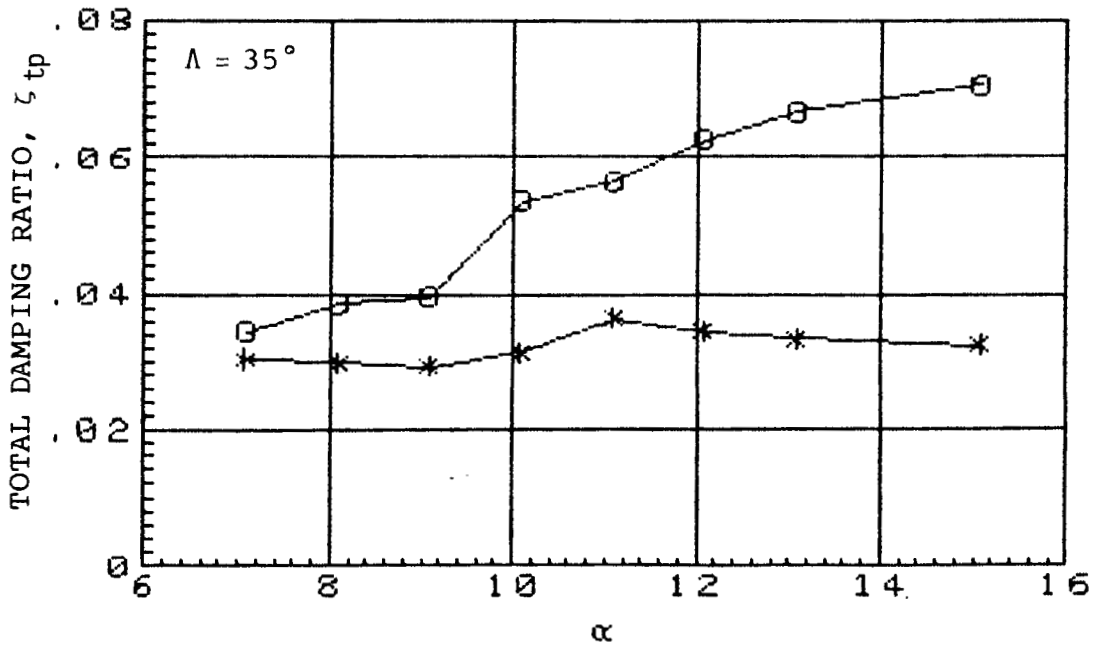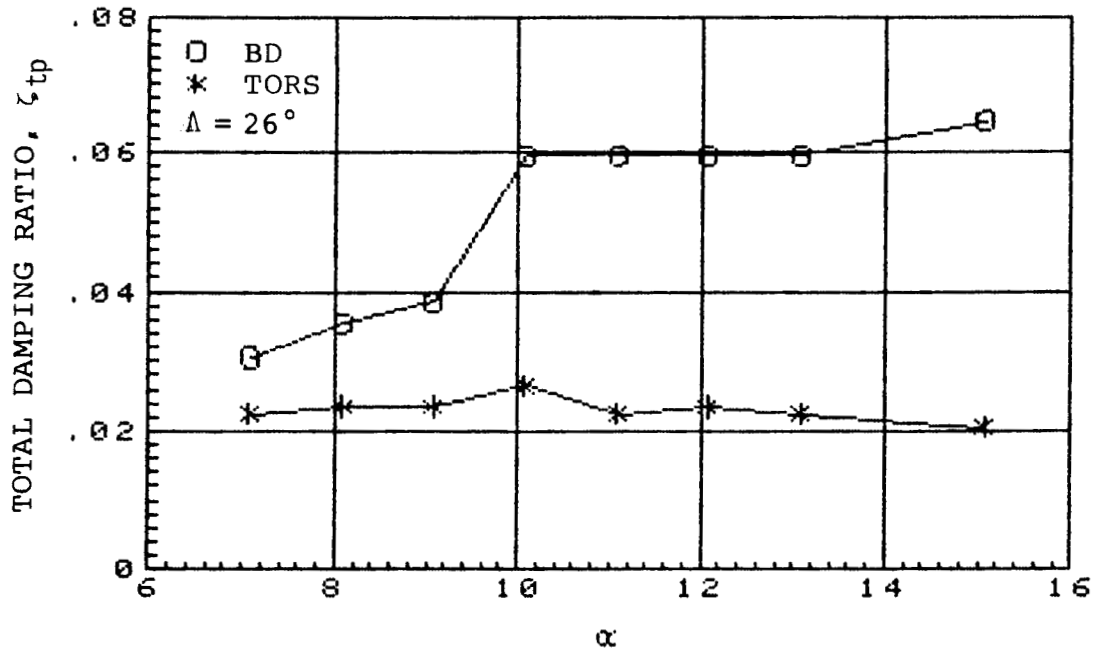
Figure 26. Total damping ratios measured from model buffeting, $M = 0.80$, $\zeta_{sp} = 0.005$.
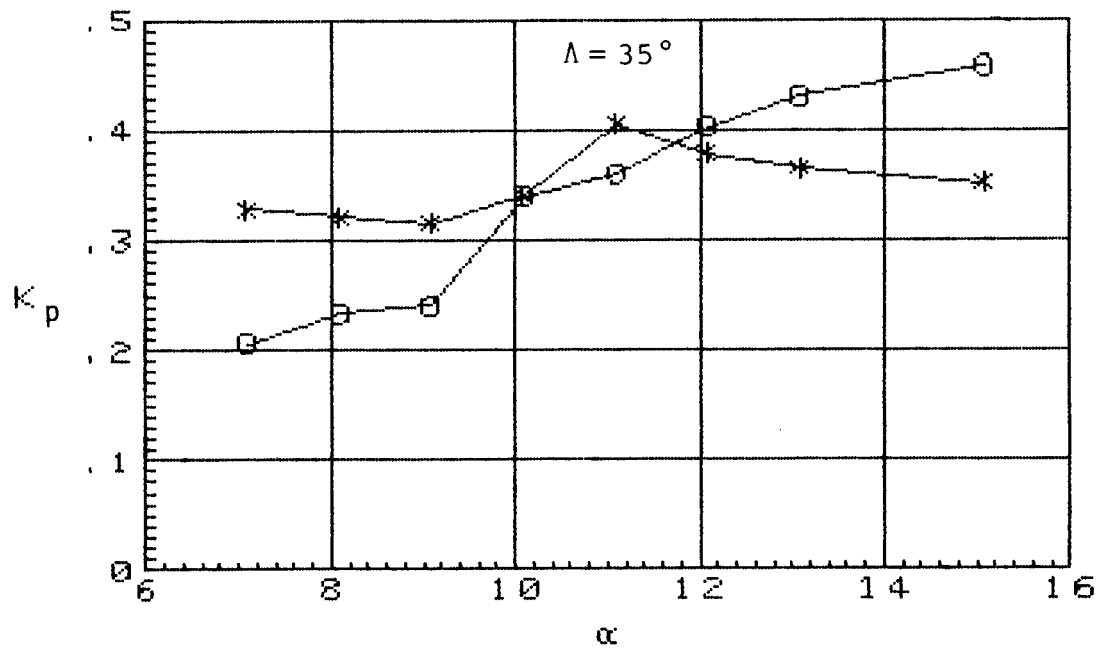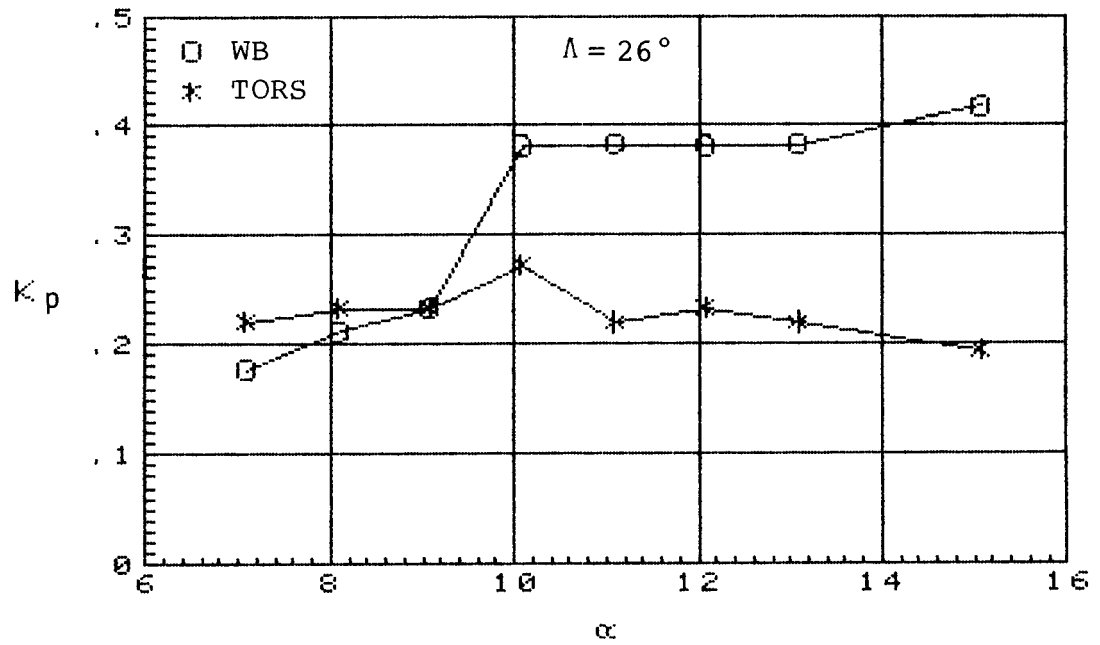
Figure 27. Variation of damping parameter with angle of attack for pivotal vibration modes of TACT aircraft, M = 0.80.

RIGHT WING
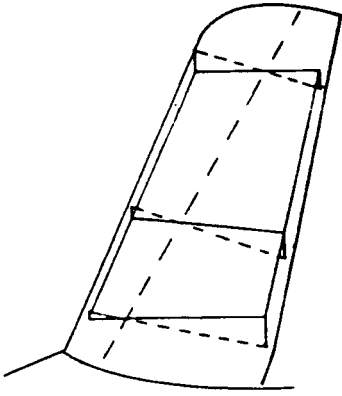
LEFT WING
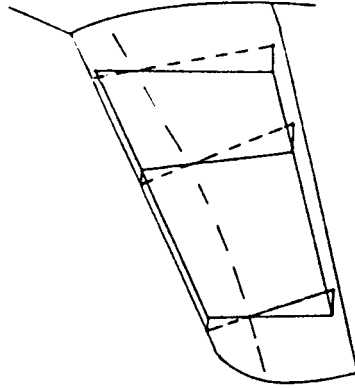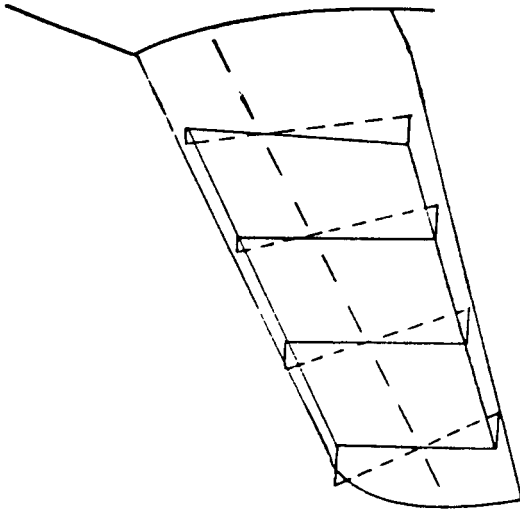
AIRCRAFT COMPOSITE MODE
FIRST WING TORSION
(LEAST SQUARES APPROXIMATION)

M_c = 1041.6 LBS

f_c = 14.92 HZ

MODEL FIRST
WING TORSION

Figure 28. Composite first wing torsion mode for the F-111 TACT aircraft and comparison with first wing torsion mode for the 1/6-scale aluminum model.

87
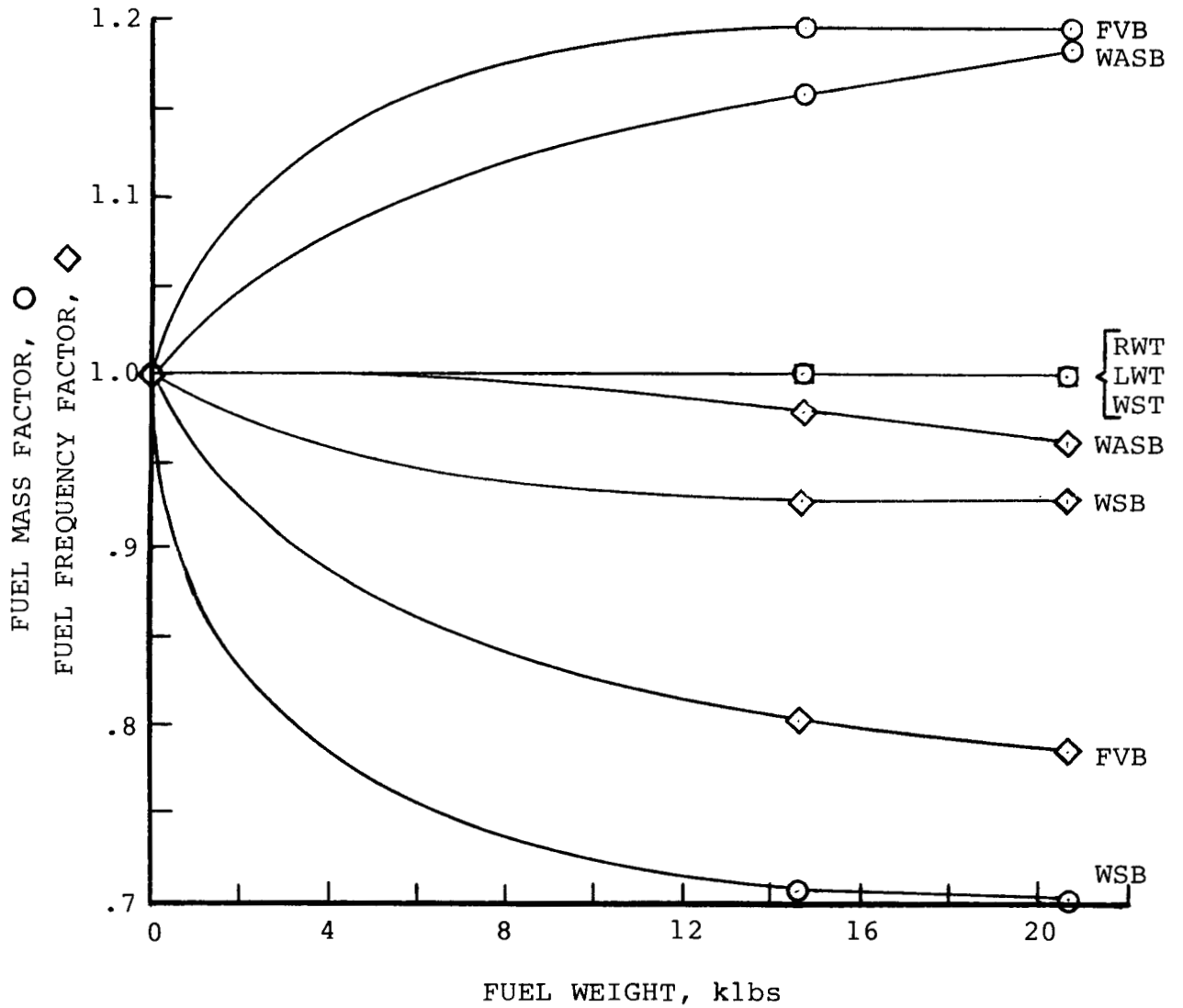
Figure 29. Mass and frequency factors due to fuel weight.
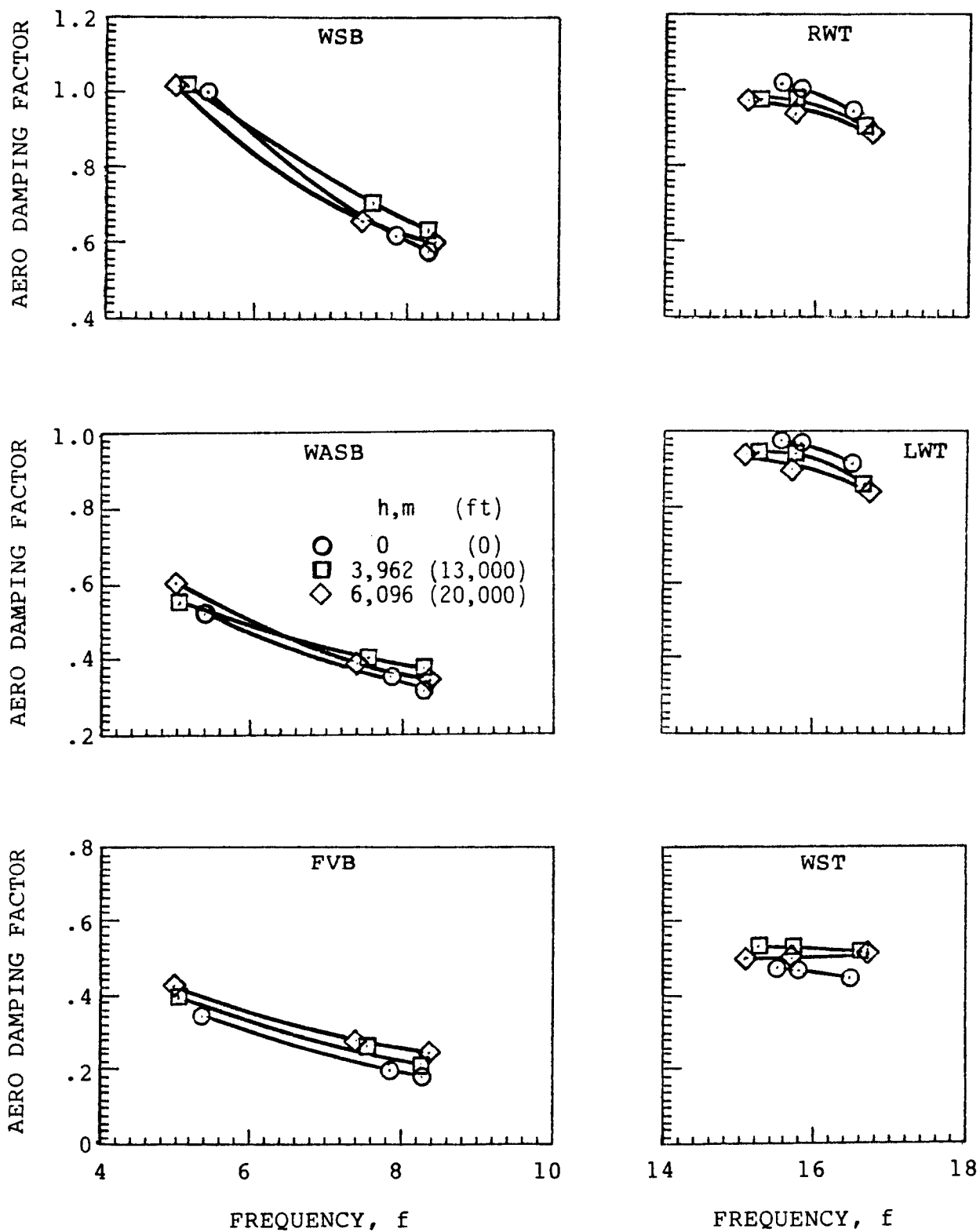
Figure 30.   Variations of aerodynamic damping with frequency and altitude.
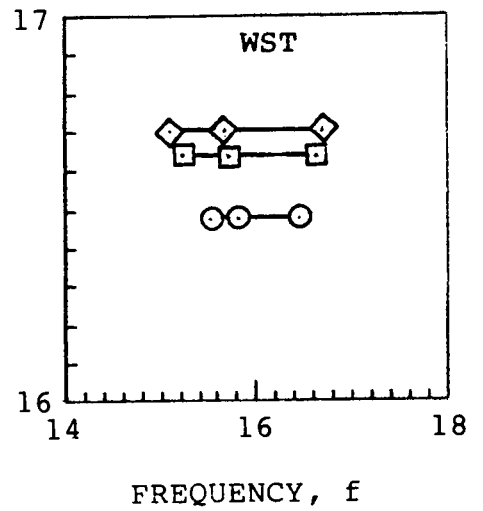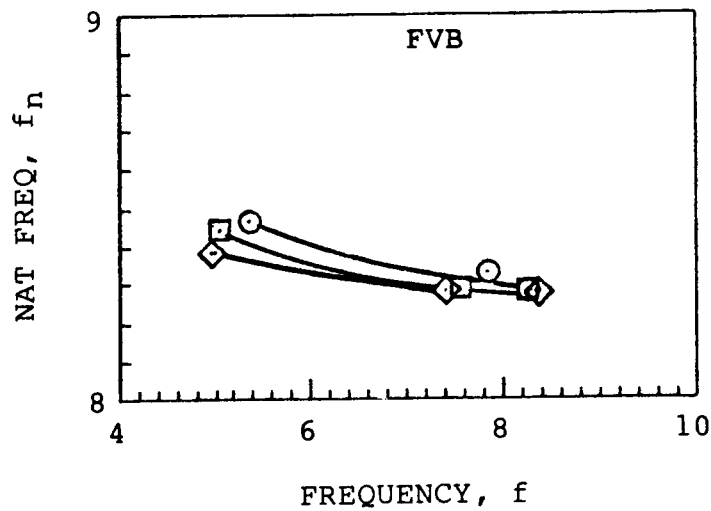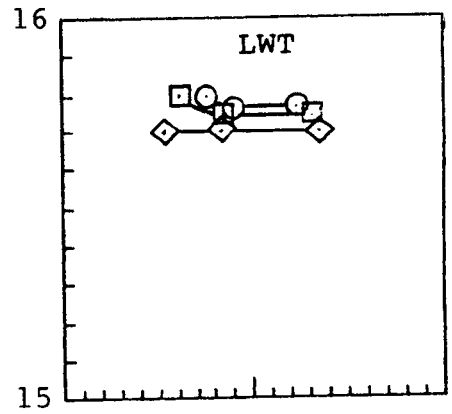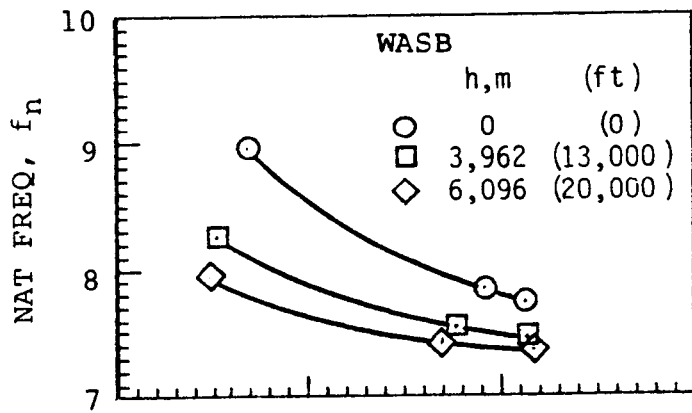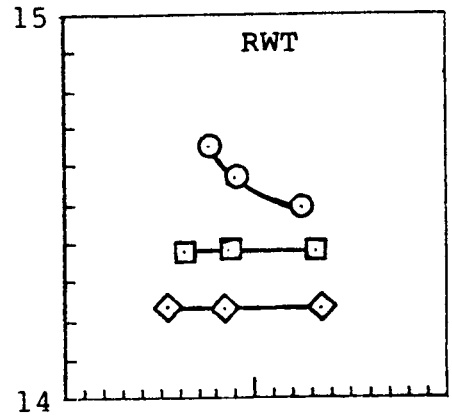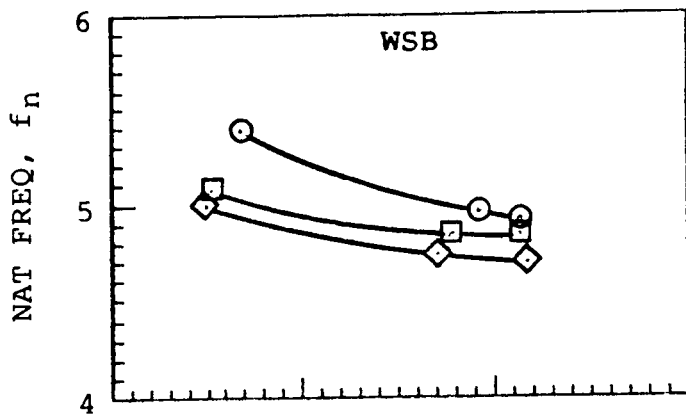
Figure 31. Variations of natural frequency with frequency and altitude.
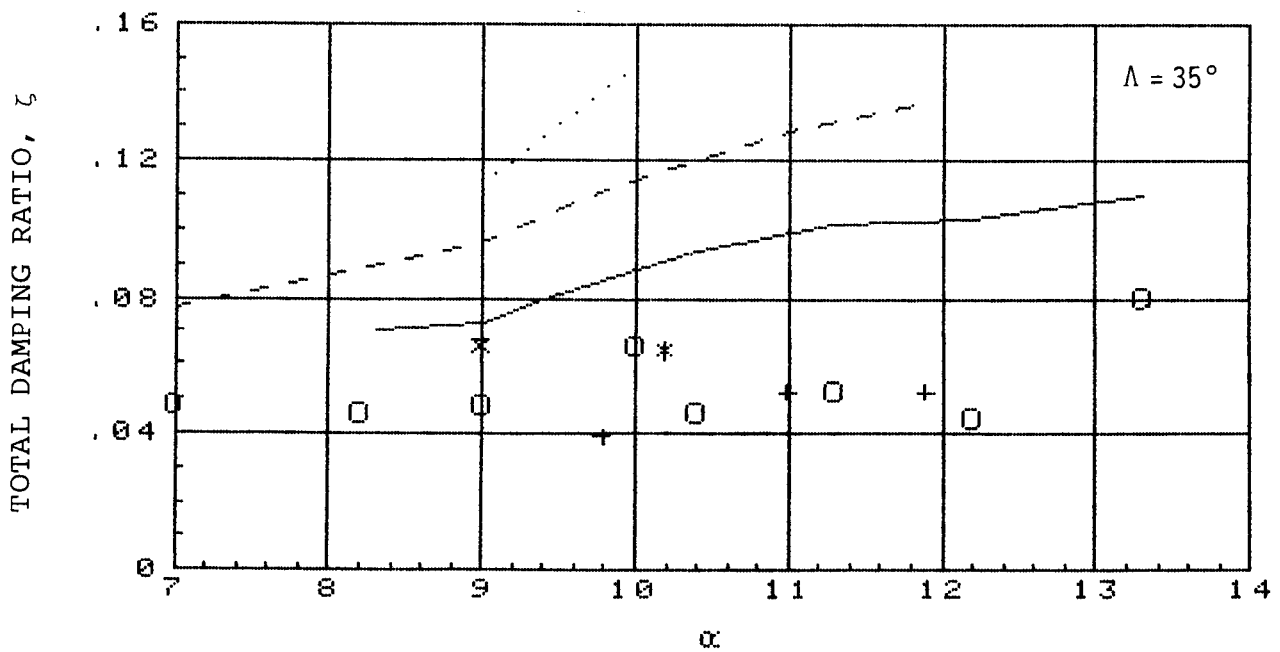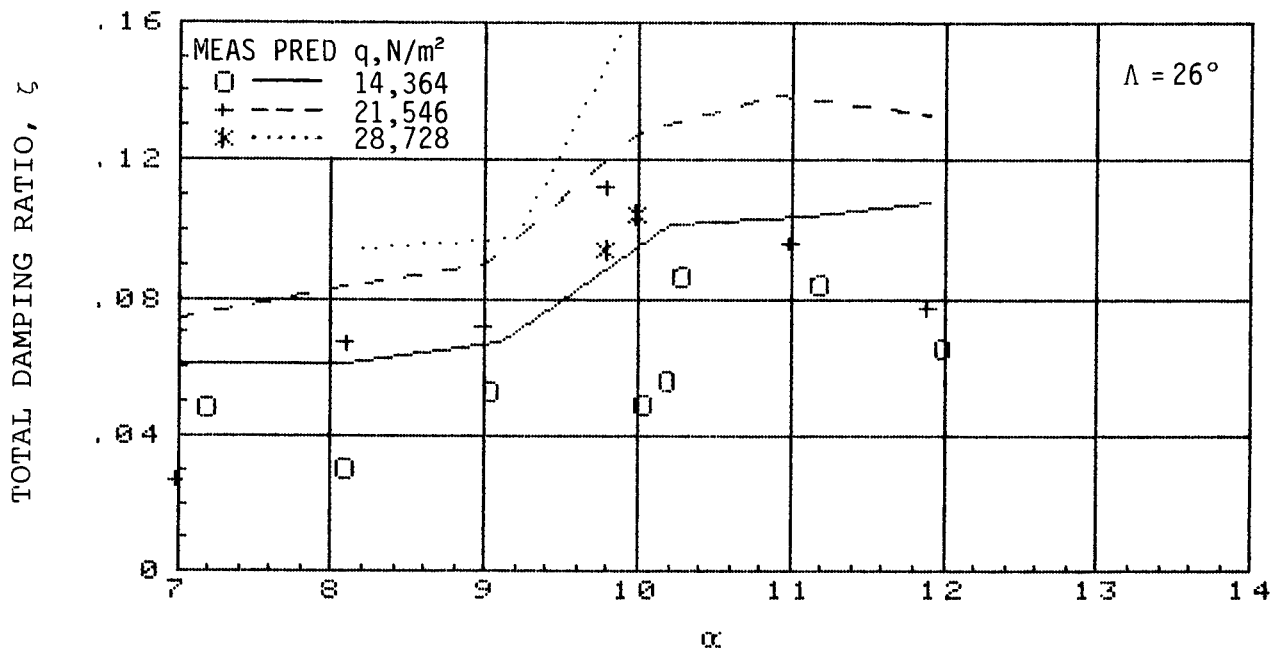
(a) Wing symmetrical bending mode, WSB

Figure 32. Predicted and measured total damping ratios of TACT aircraft, M = 0.80.
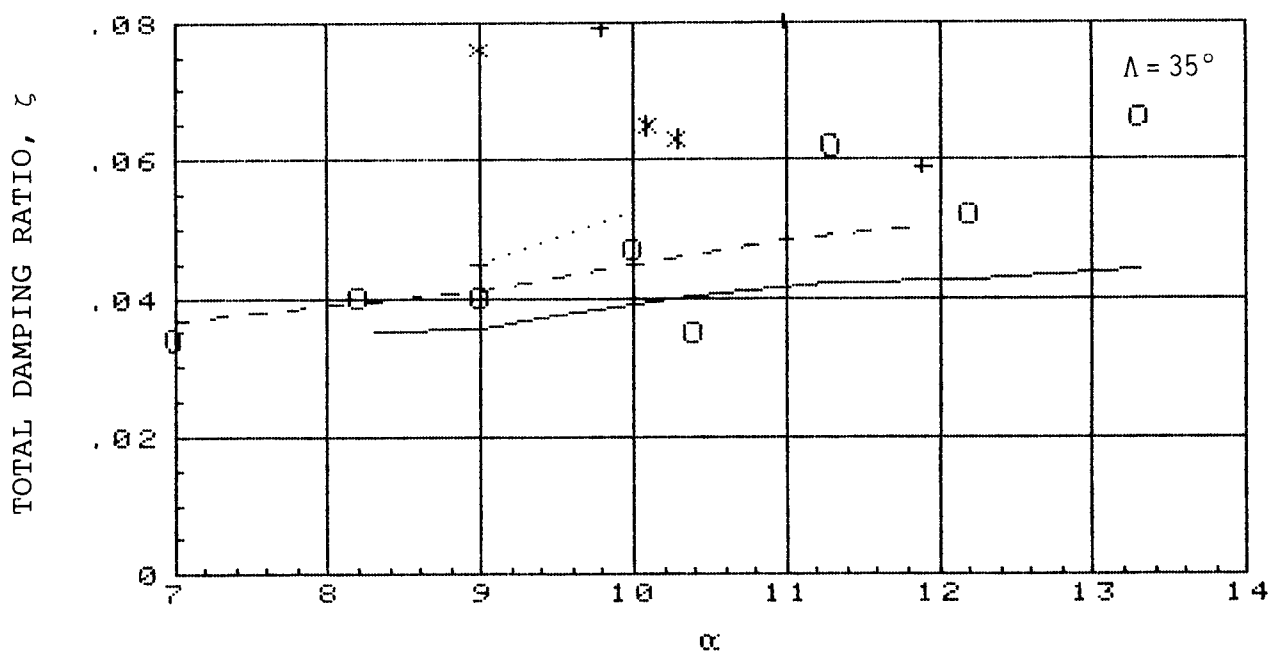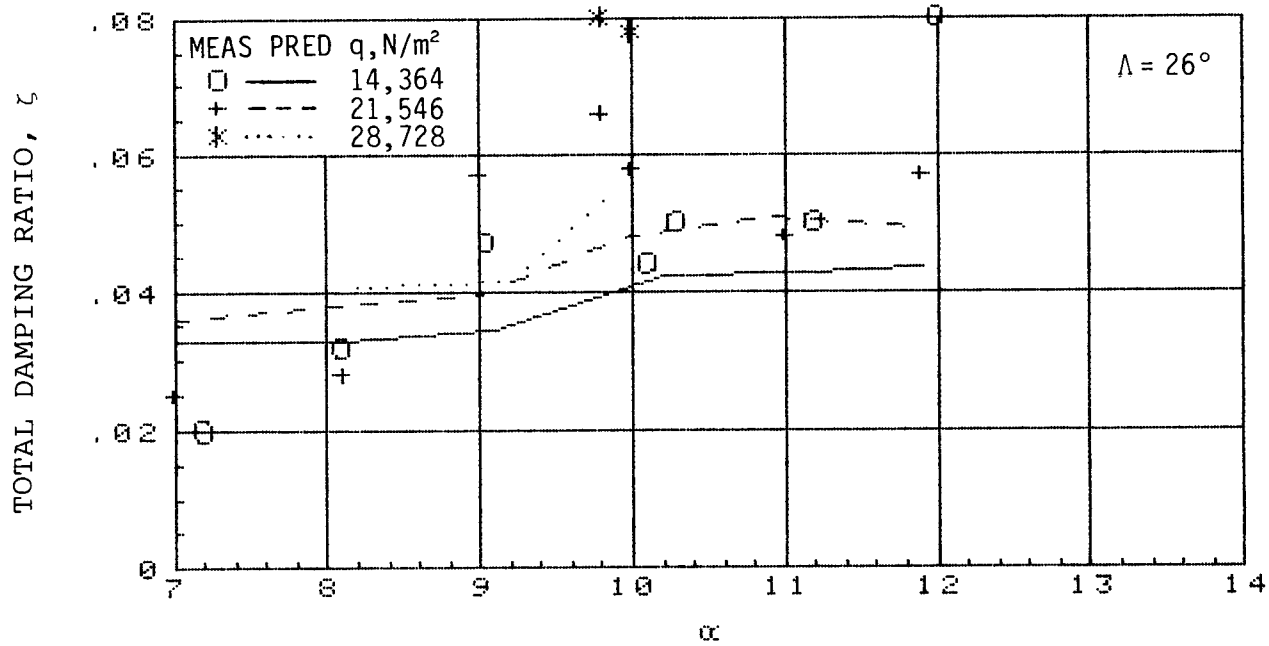
(b) Fuselage vertical bending mode, FVB

Figure 32. Continued.
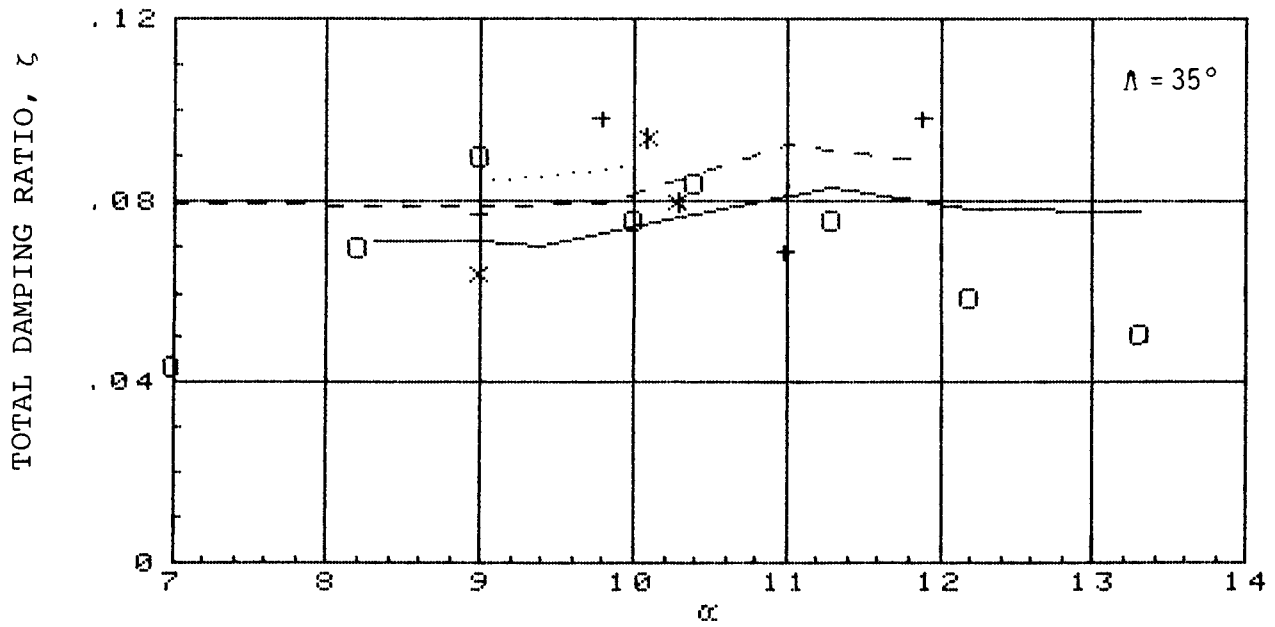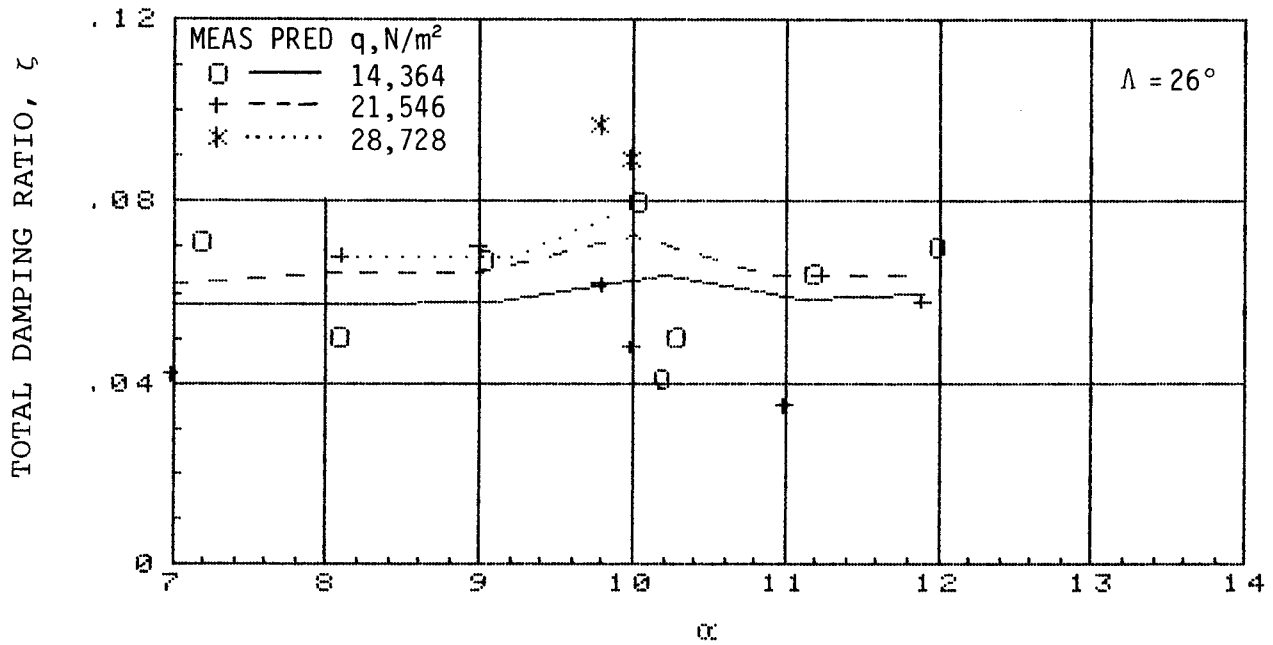
(c) Right wing torsion mode, RWT

Figure 32.   Concluded.
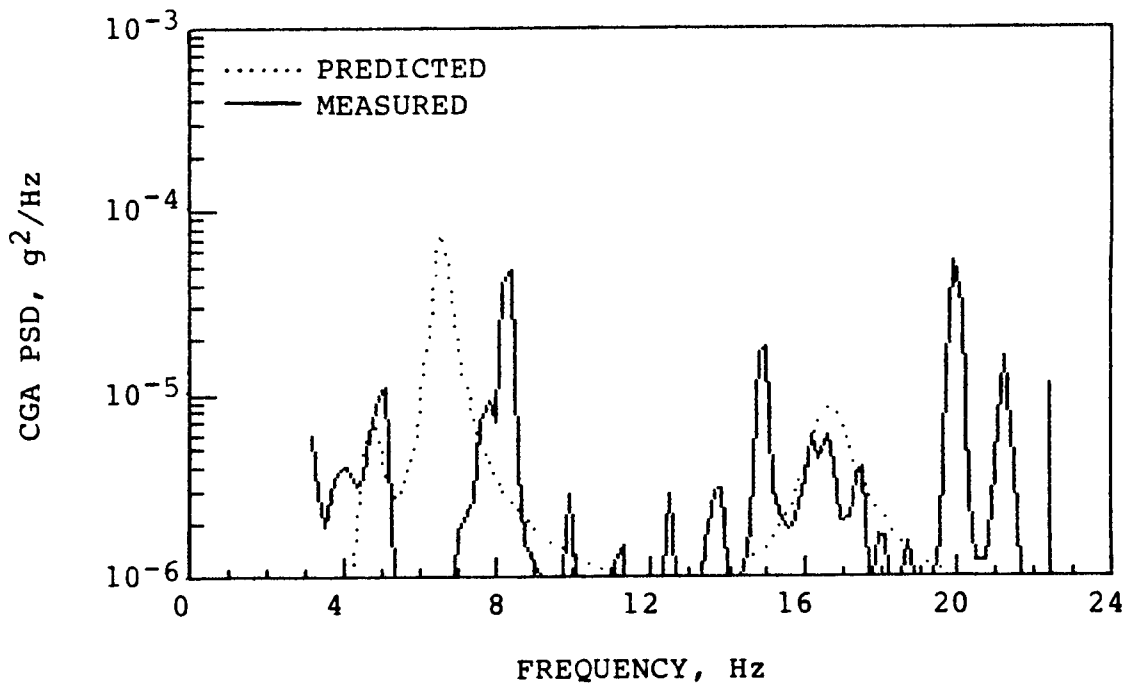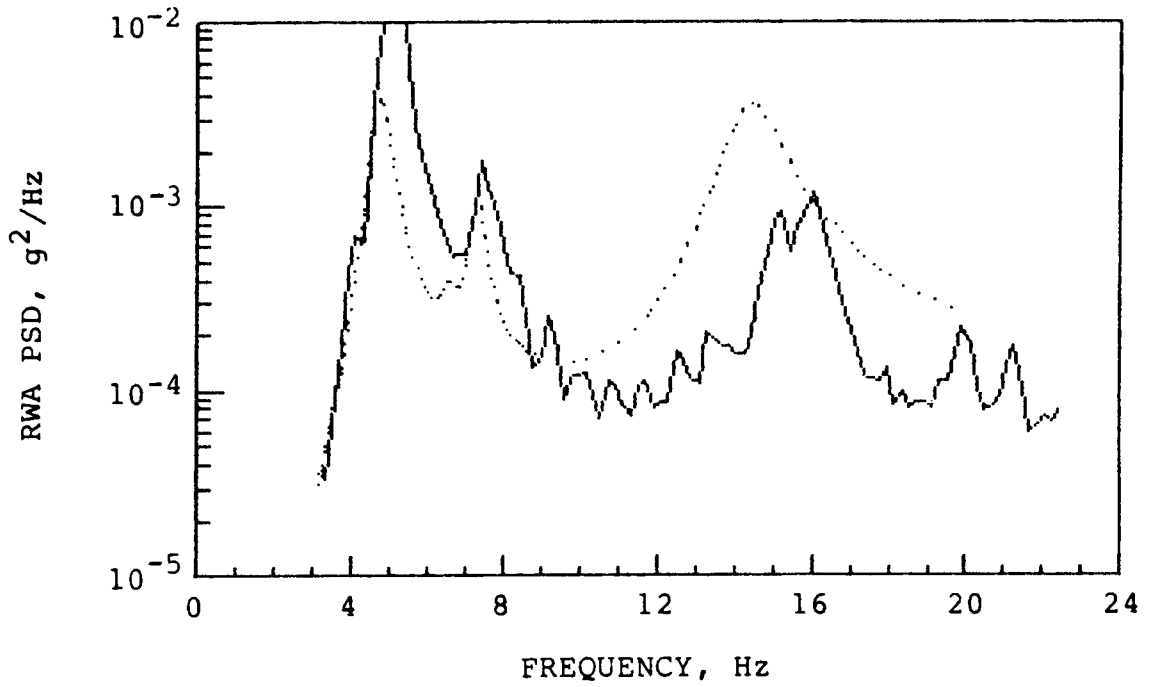
(a) $\alpha = 7.0°$, $q = 15,417$ N/m² (322 lbs/ft²), $T = 113$ sec.

Figure 33. Predicted and measured PSDs of wing-tip and center-of-gravity accelerations of TACT aircraft for $\Lambda = 26°$, $M = 0.80$.

C-2
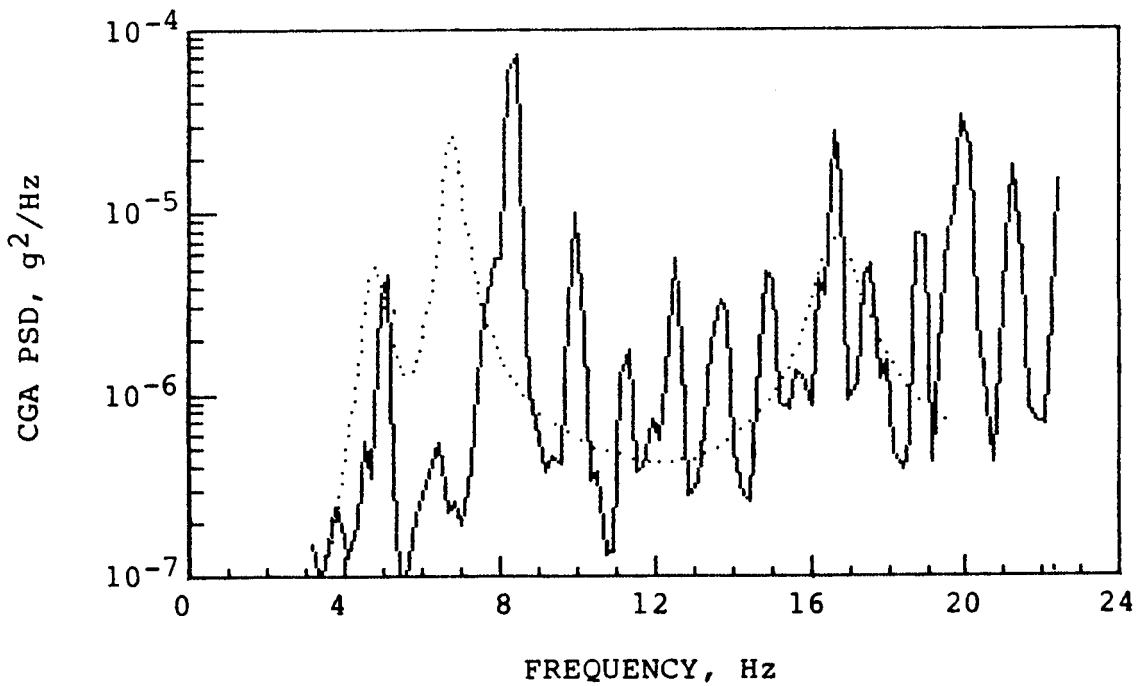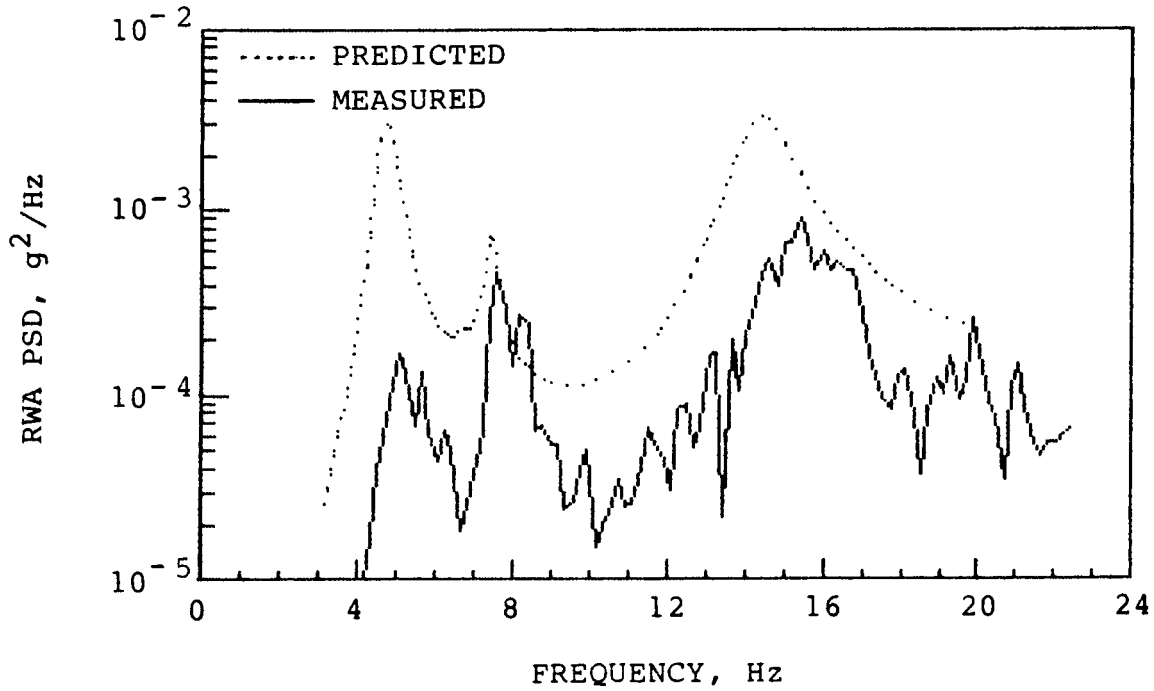
(b) $\alpha = 8.1°$, $q = 13{,}167$ N/m² (275 lbs/ft²), T = 42 sec.

Figure 33. $\Lambda = 26°$ Continued.
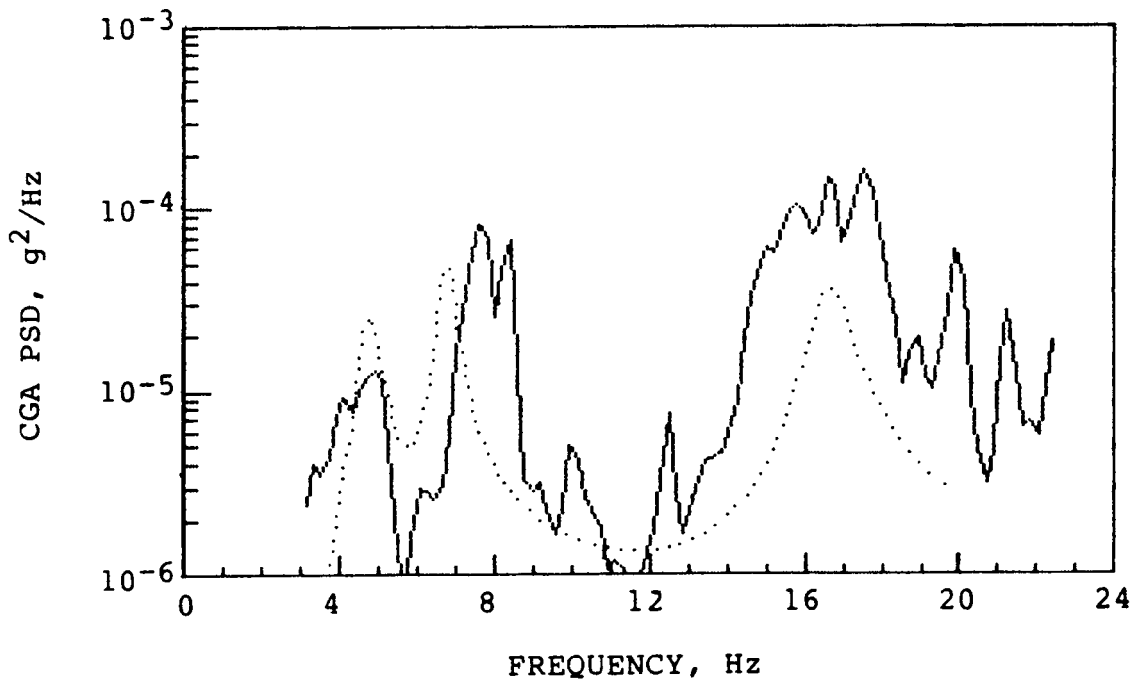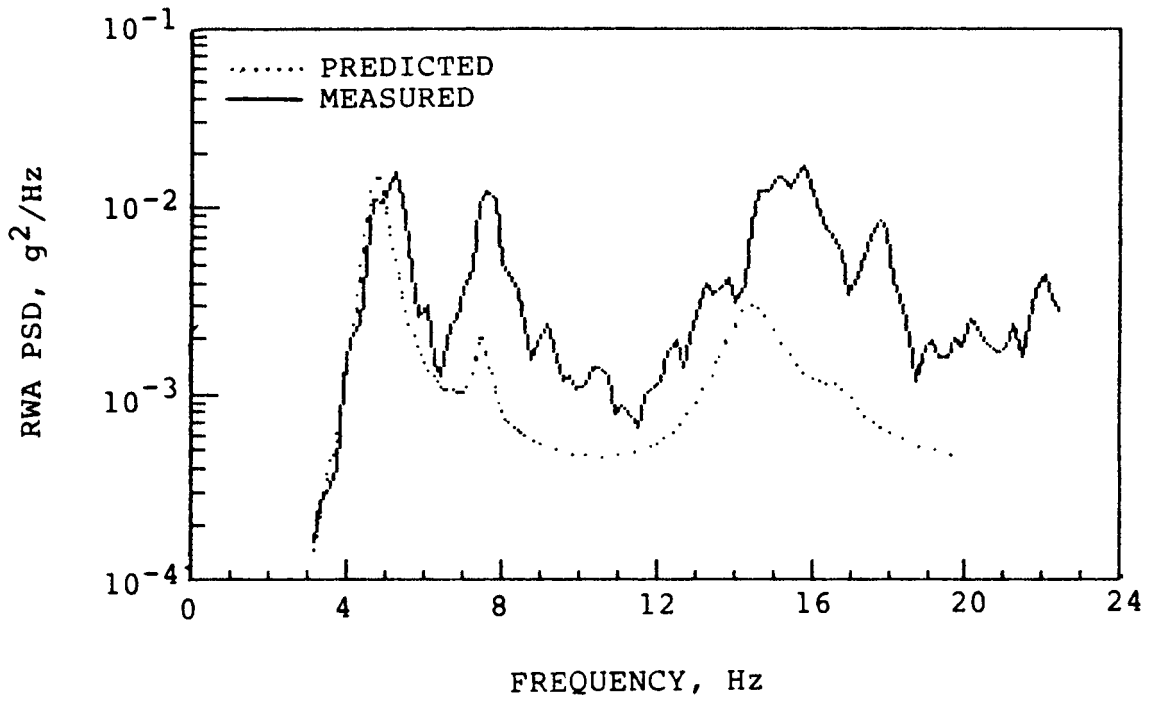
(c) $\alpha = 9.1°$, $q = 13{,}742$ N/m² (287 lbs/ft²), $T = 84$ sec.

Figure 33. $\Lambda = 26°$ Continued.
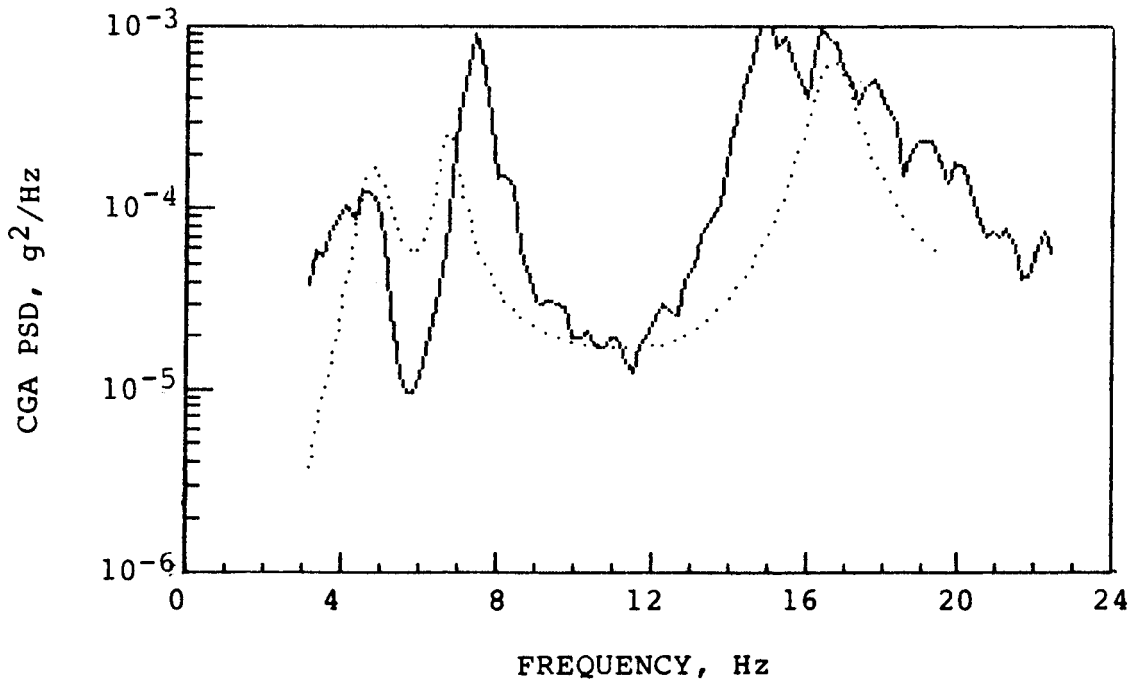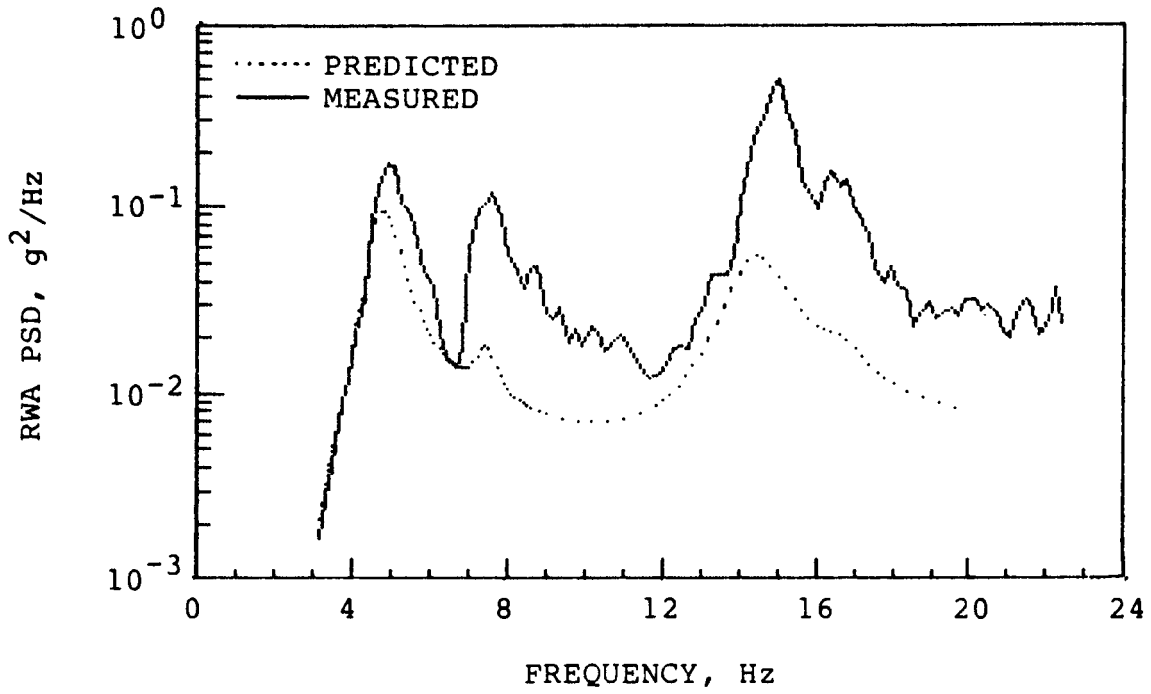
(d) $\alpha = 10.2°$, $q = 14,939$ N/m² (312 lbs/ft²), T = 161 sec.

Figure 33. $\Lambda = 26°$ Continued.
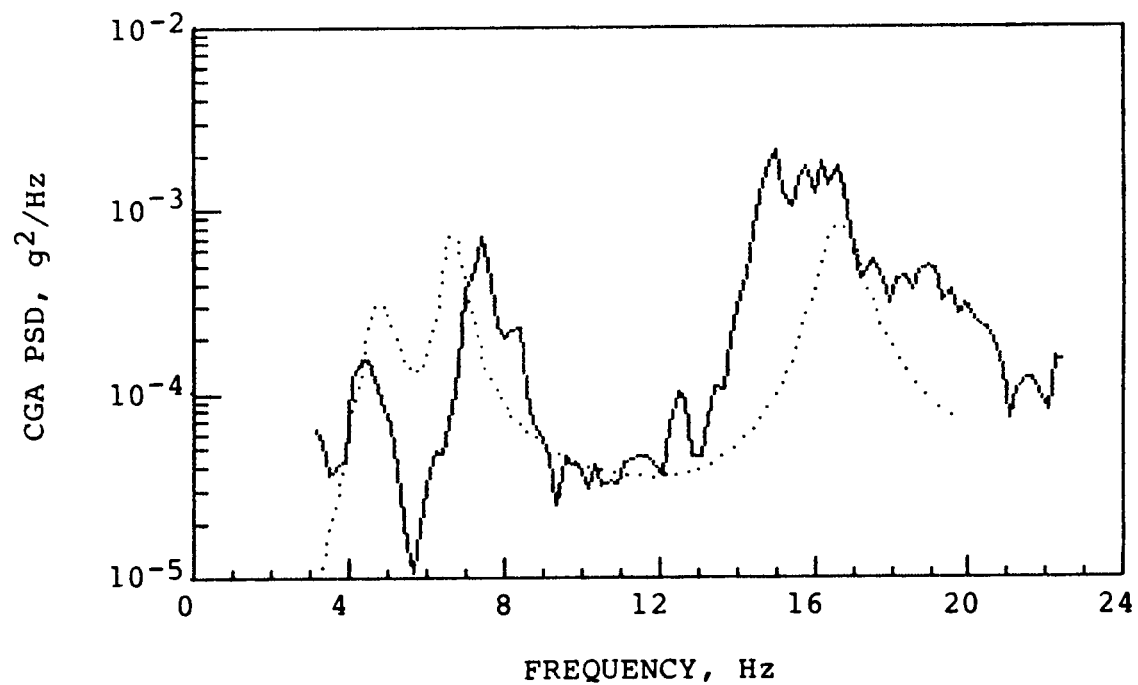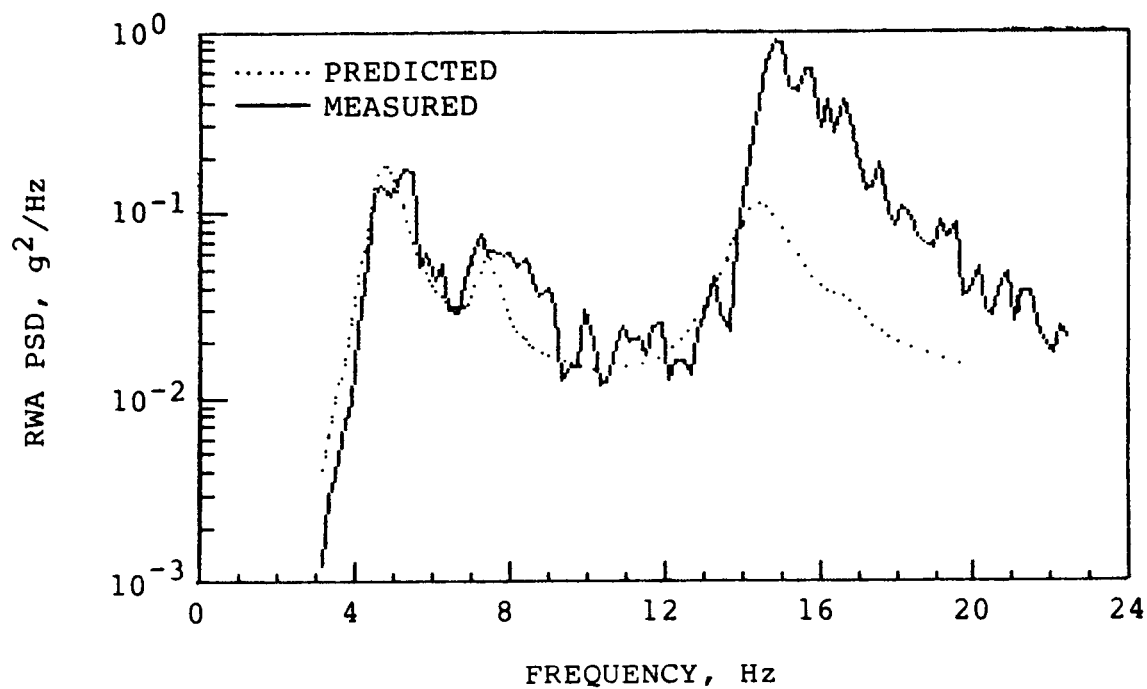
(e) $\alpha = 11.1°$, $q = 15,130$ N/m^2 (316 lbs/ft^2), T = 72 sec.

Figure 33. $\Lambda = 26°$ Continued.
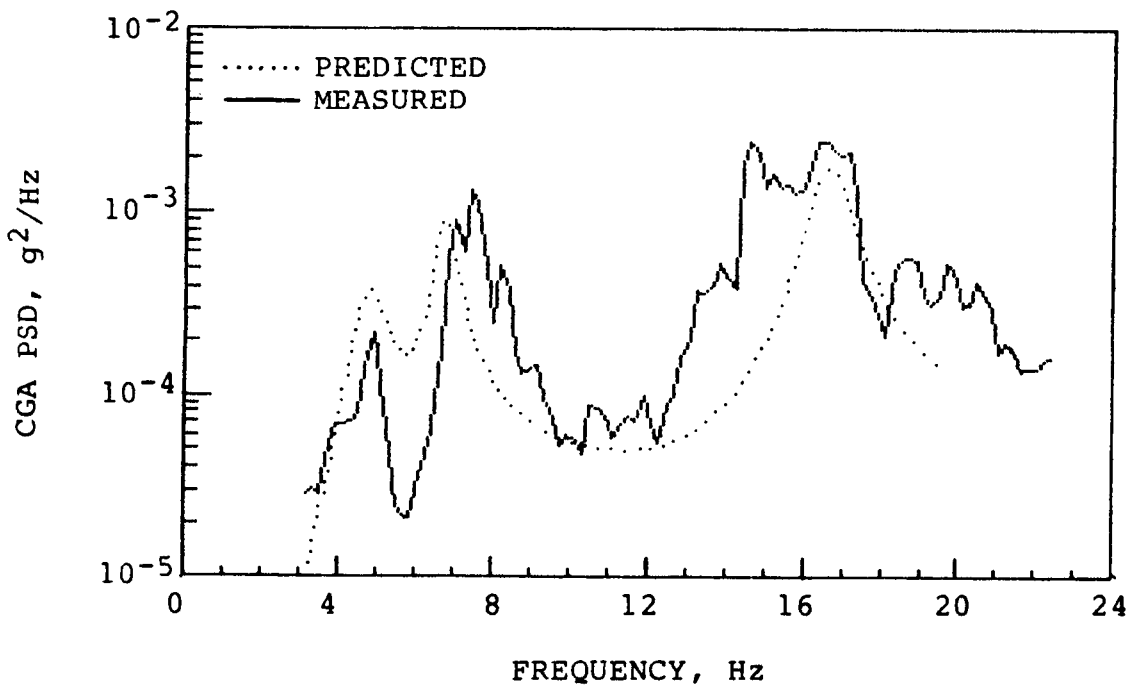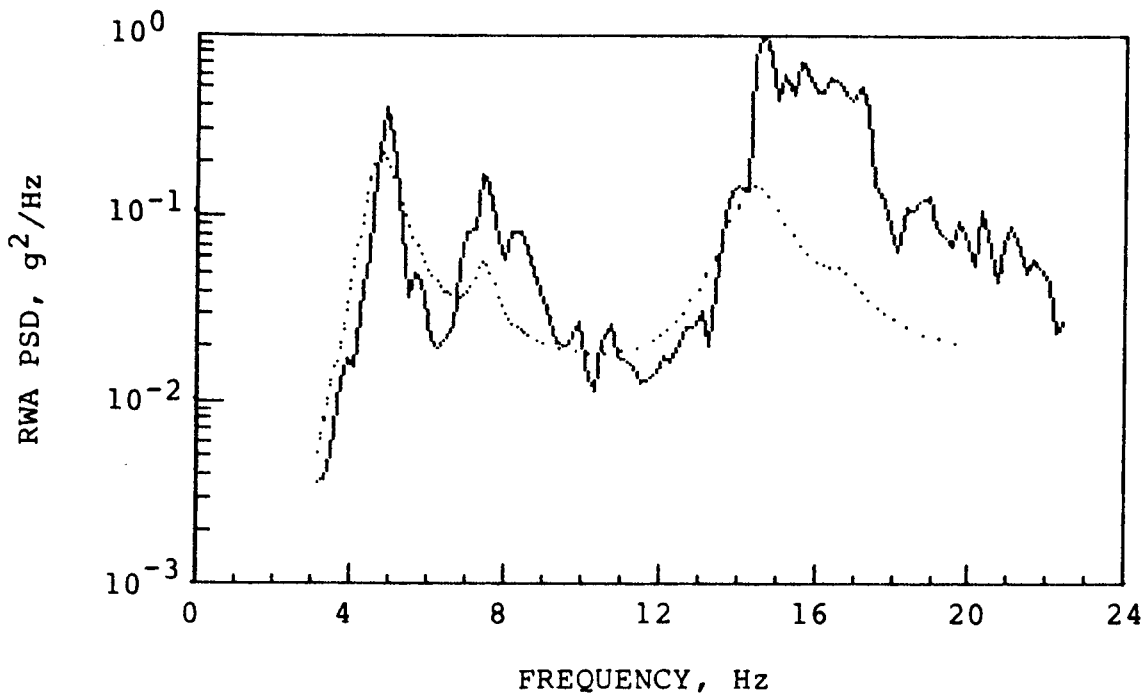
(f) $\alpha = 11.9°$, $q = 16,136$ N/m² (337 lbs/ft²), T = 57 sec.

Figure 33. $\Lambda = 26°$ Continued.
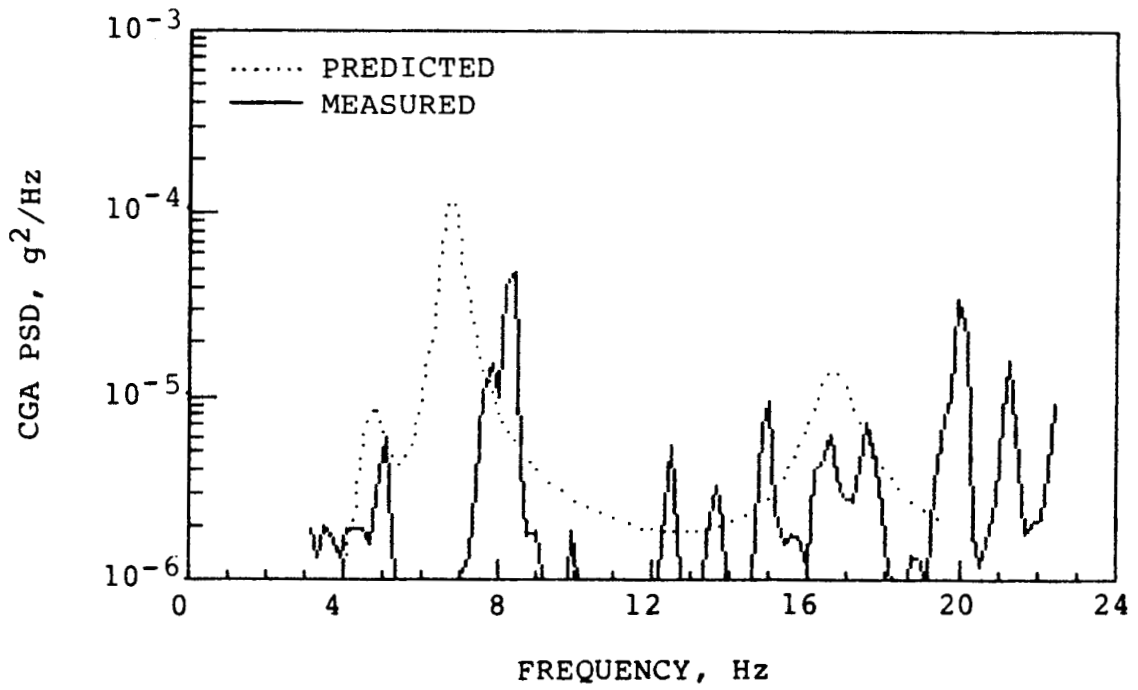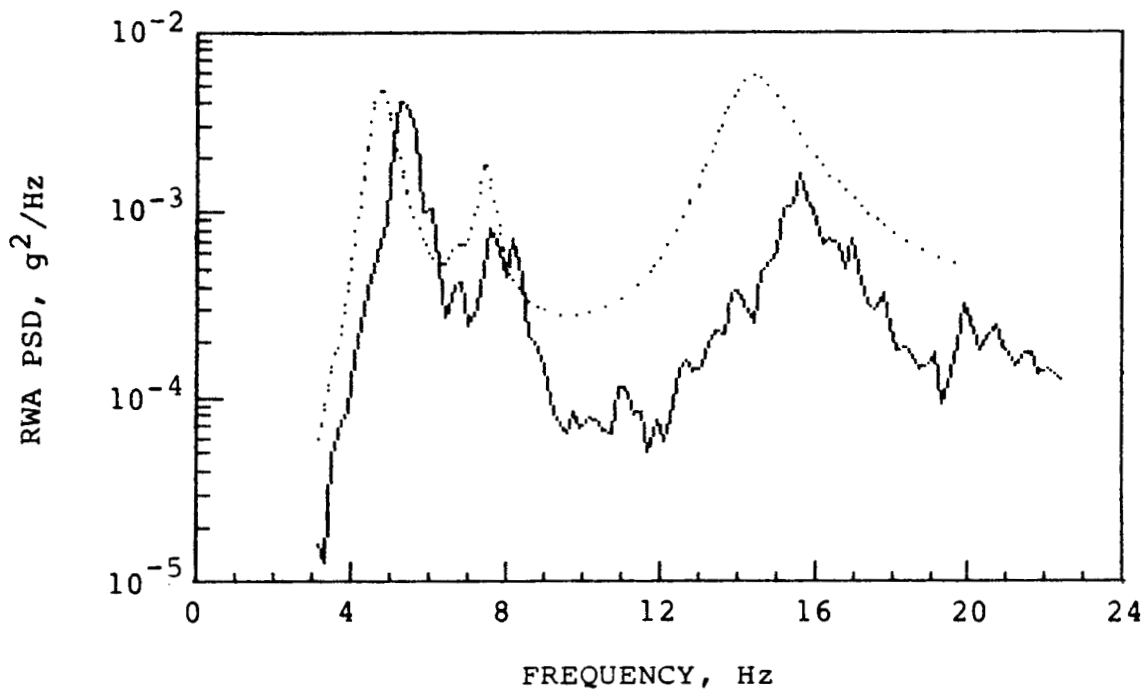
(g) $\alpha = 7.0°$, $q = 21{,}594$ N/m² (451 lbs/ft²), T = 98 sec.

Figure 33. $\Lambda = 26°$ Continued.
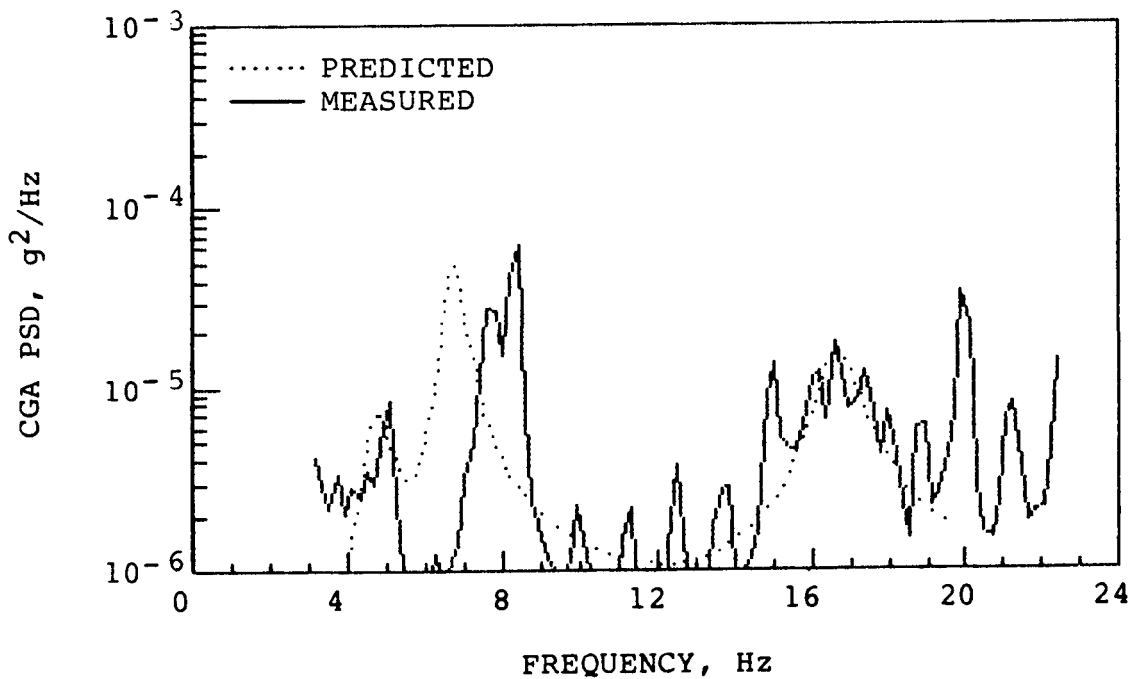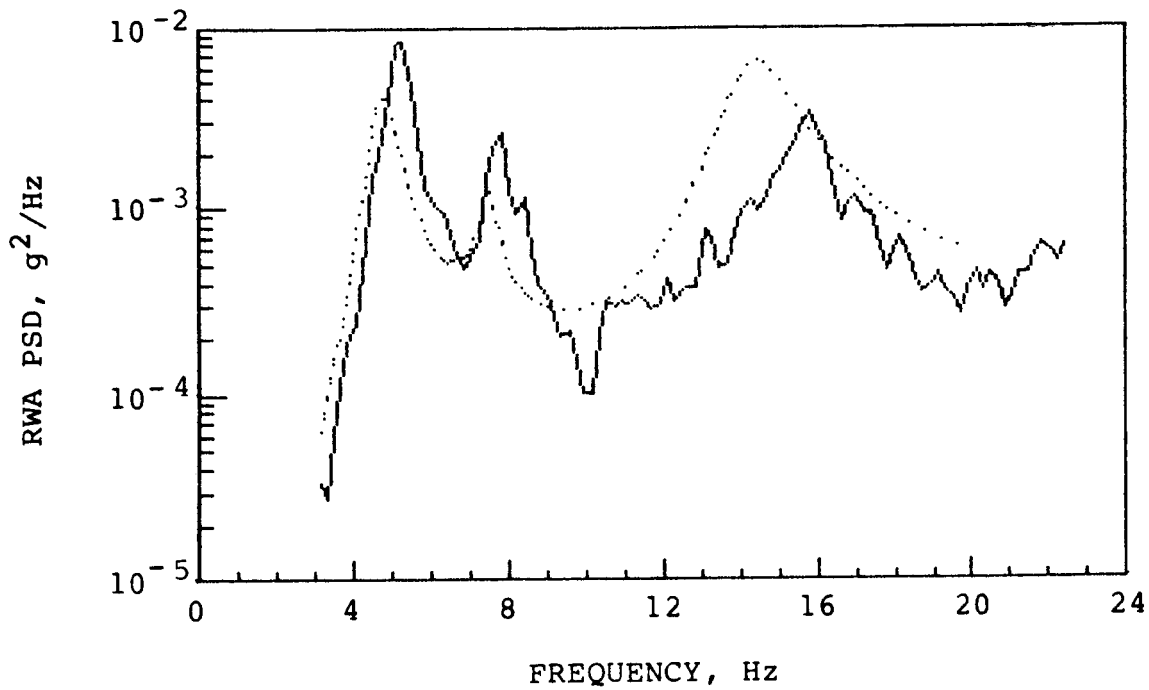
(h) $\alpha = 8.1°$, $q = 21,450$ N/m² (448 lbs/ft²), T = 122 sec.

Figure 33. $\Lambda = 26°$ Continued.
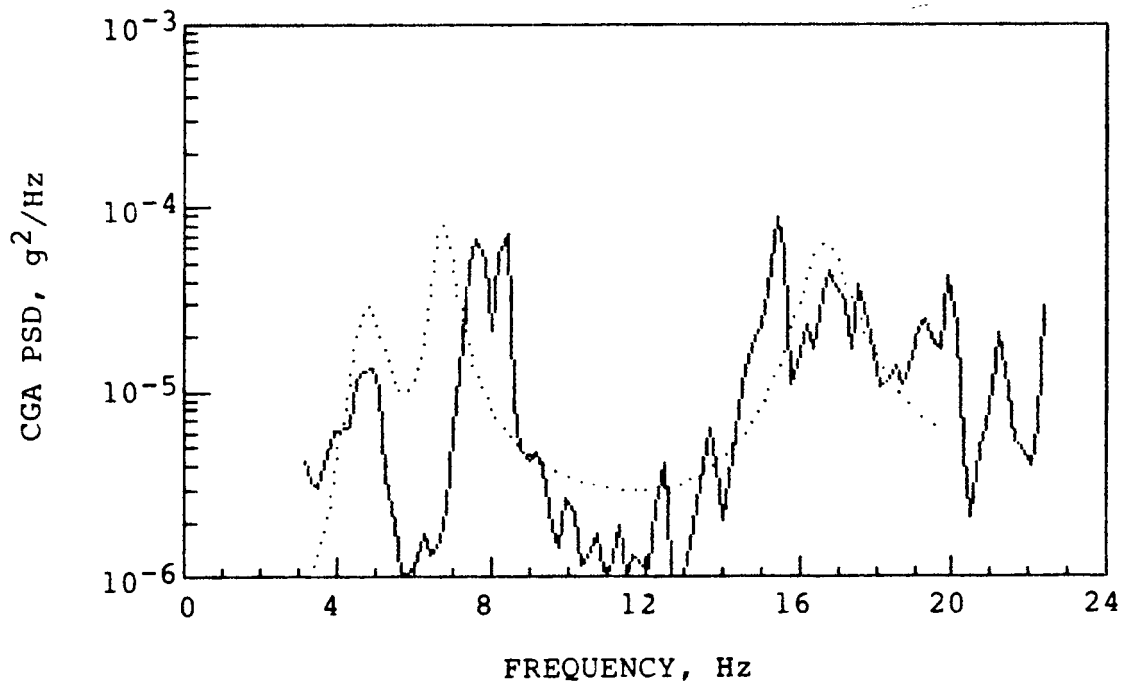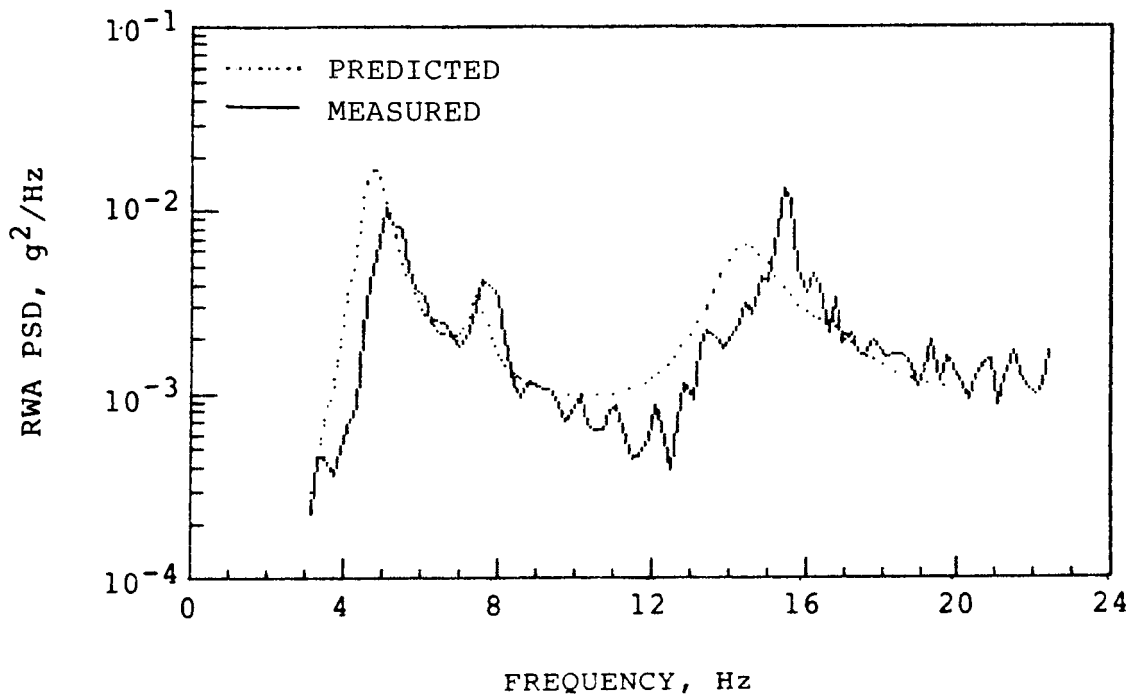
(i) $\alpha = 9.0°$, $q = 21,929$ N/m² (458 lbs/ft²), T = 164 sec.

Figure 33. $\Lambda = 26°$ Continued.
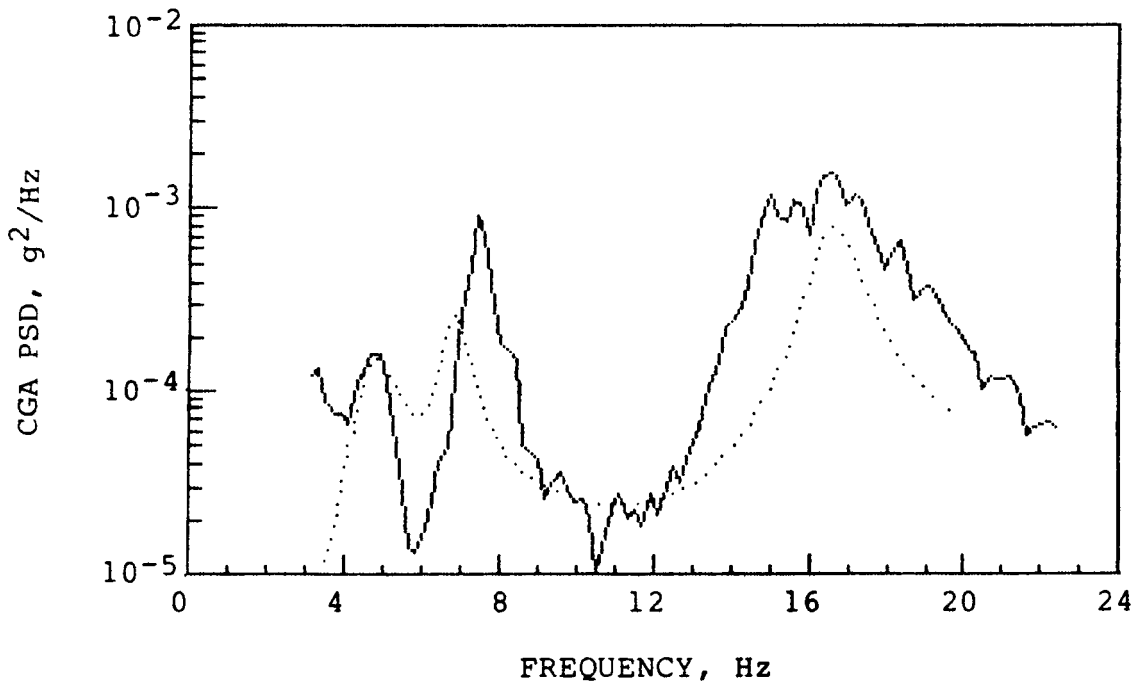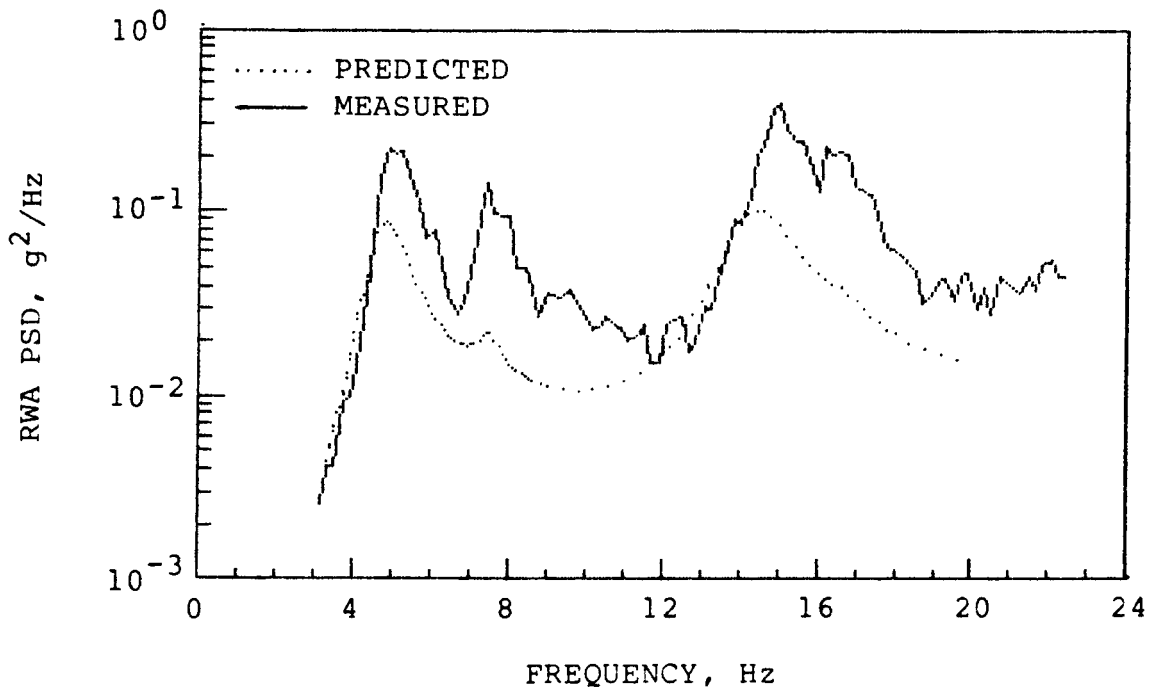
(j) $\alpha = 10.0$, $q = 21,642$ N/m^2 (452 lbs/ft^2), T = 150 sec.

Figure 33. $\Lambda = 26°$ Continued.
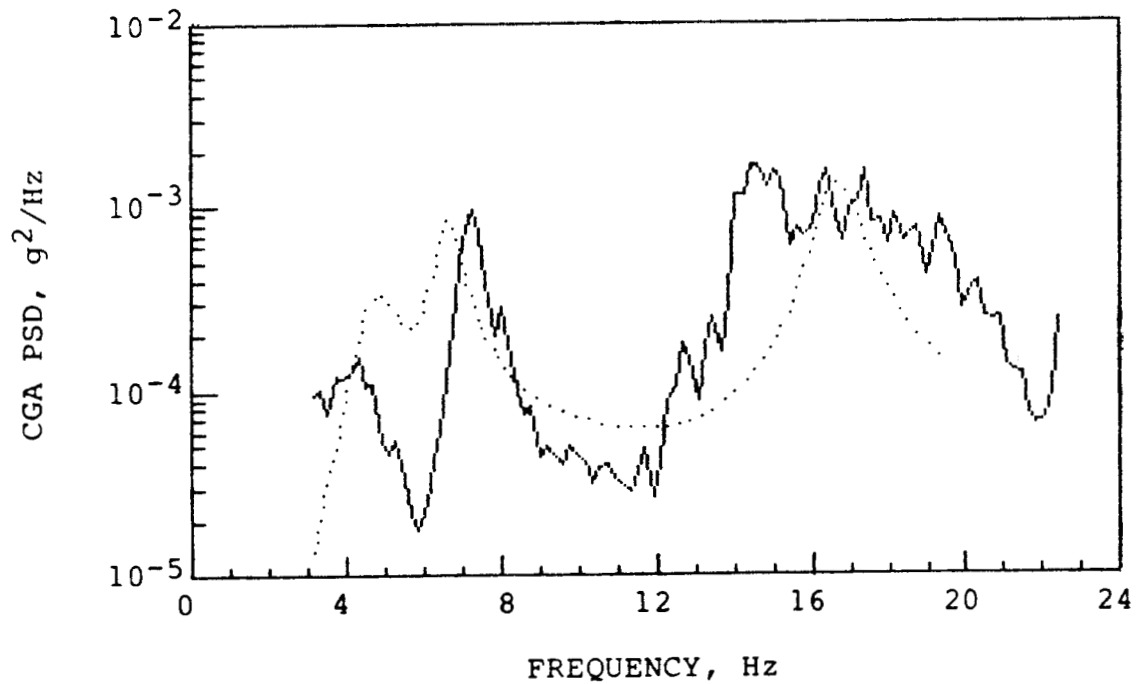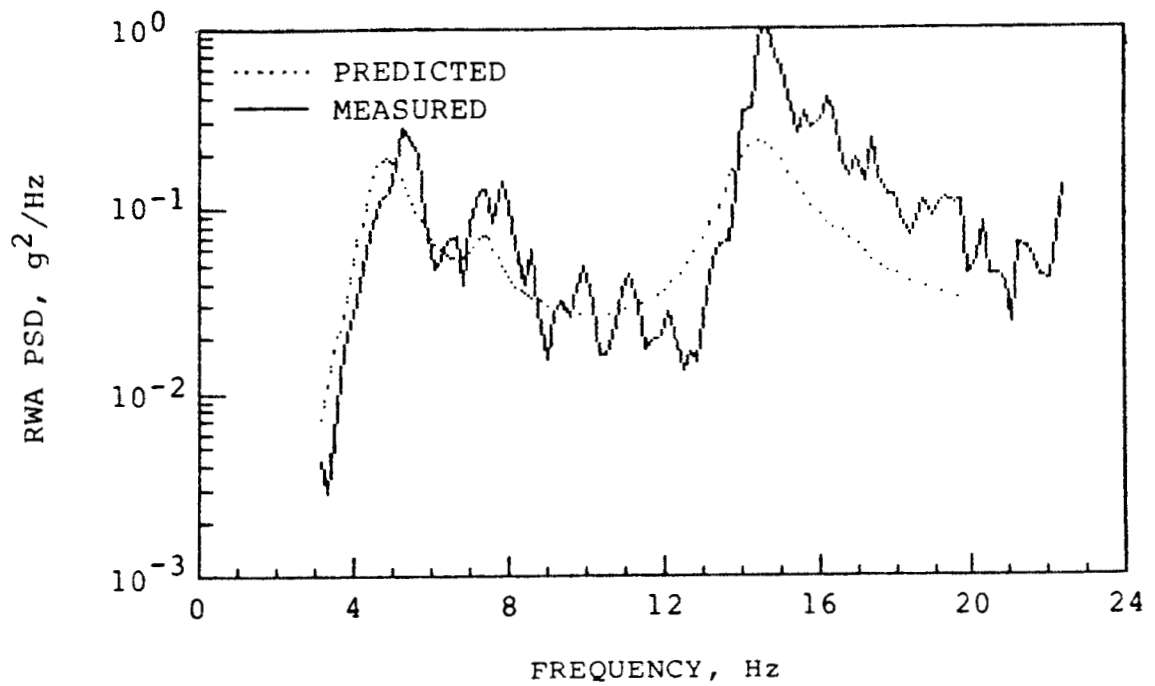
(k) $\alpha = 10.9°$, $q = 22{,}264$ N/m² (465 lbs/ft²), T = 50 sec.

Figure 33. $\Lambda = 26°$ Continued.
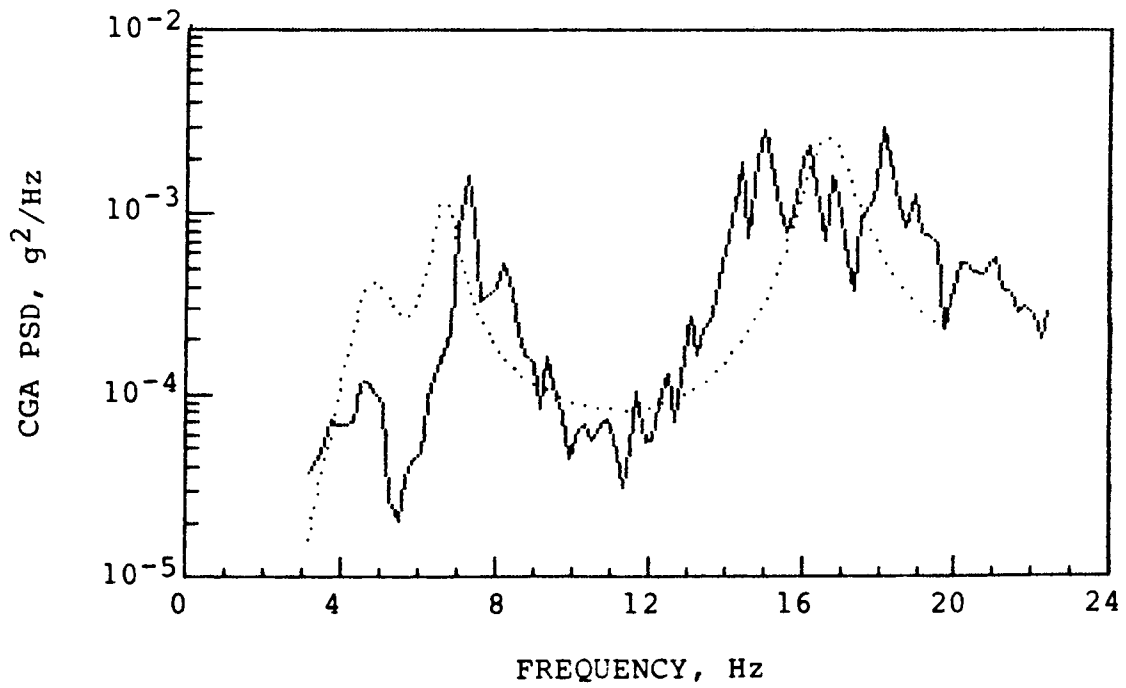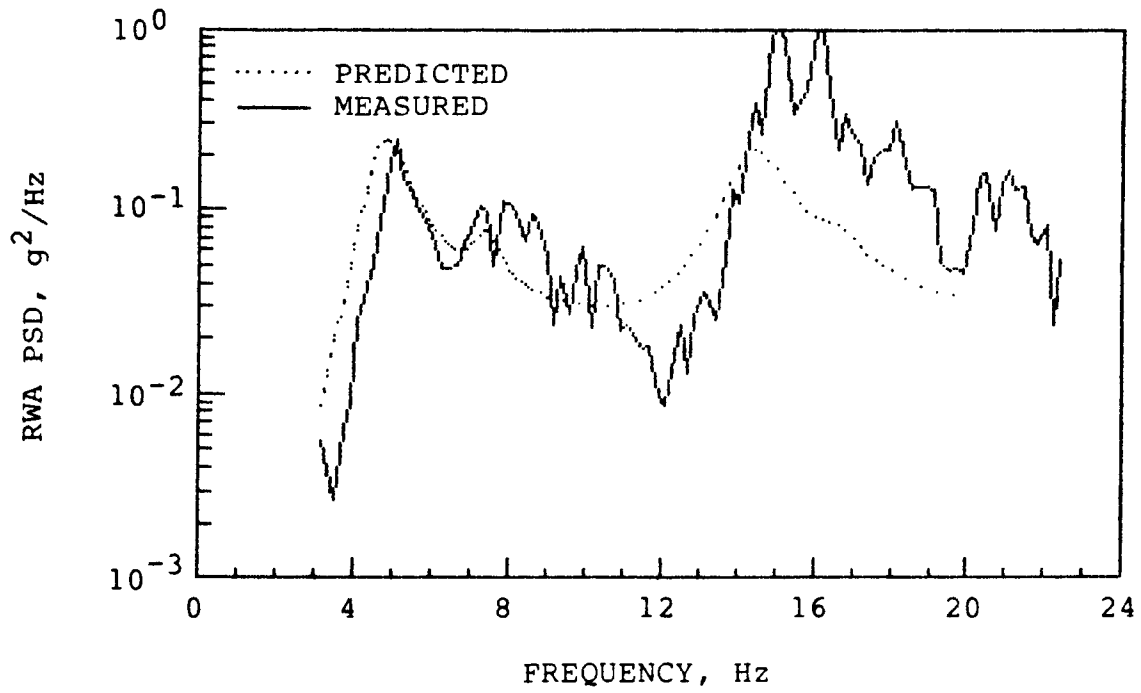
(1) $\alpha = 11.9°$, $q = 21,115$ N/m² (441 lbs/ft²), $T = 45$ sec.

Figure 33. $\Lambda = 26°$ Continued.
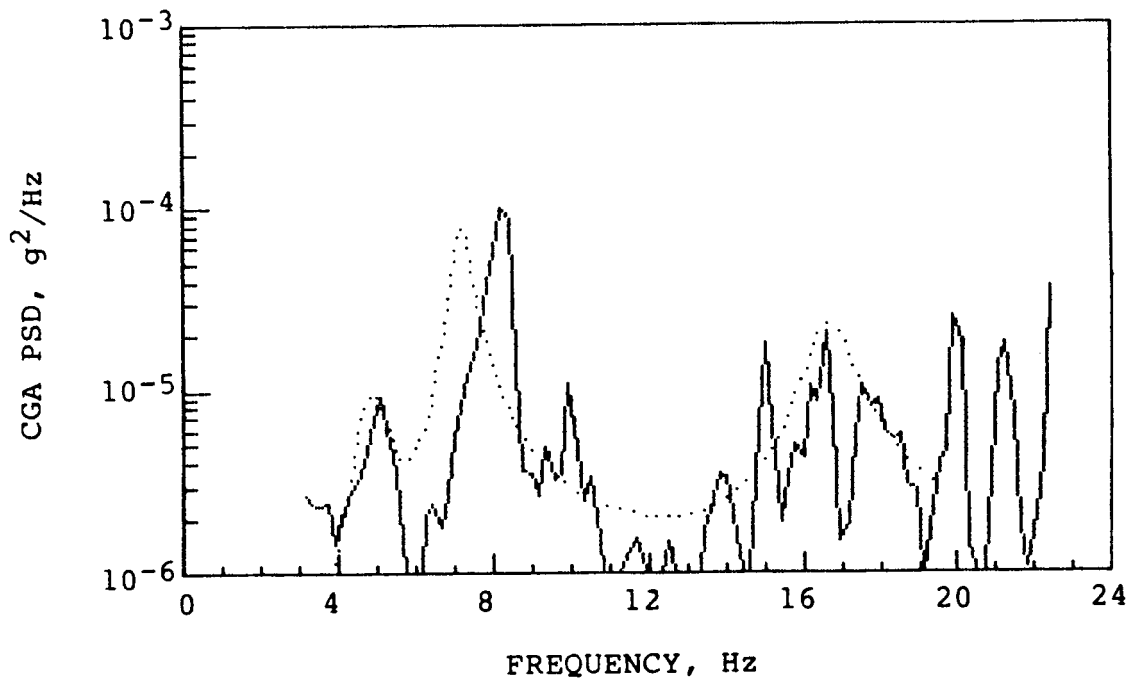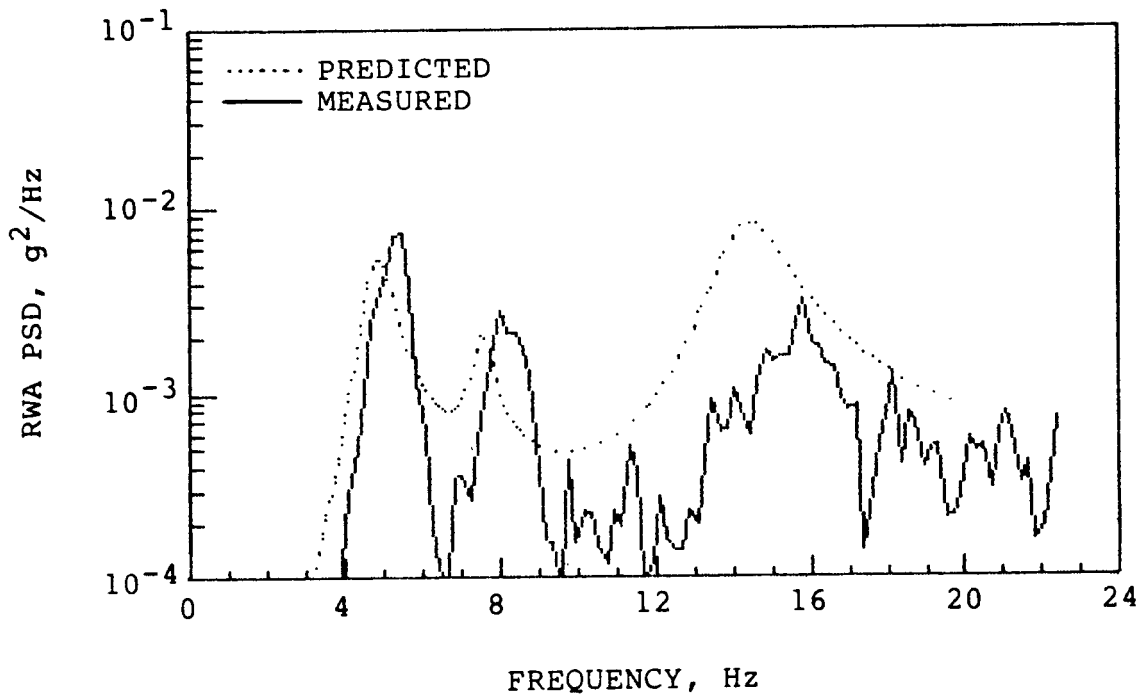
(m) $\alpha = 8.2°$, $q = 26,765$ N/m^2 (559 lbs/ft^2), T = 24 sec.

Figure 33. $\Lambda = 26°$ Continued.
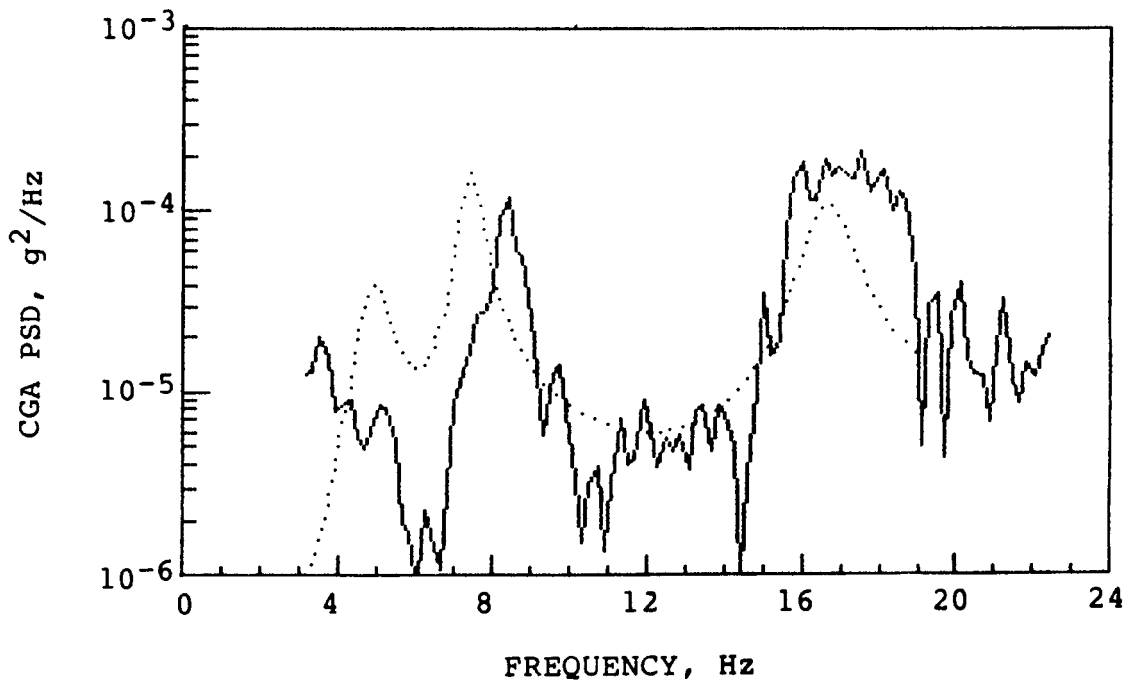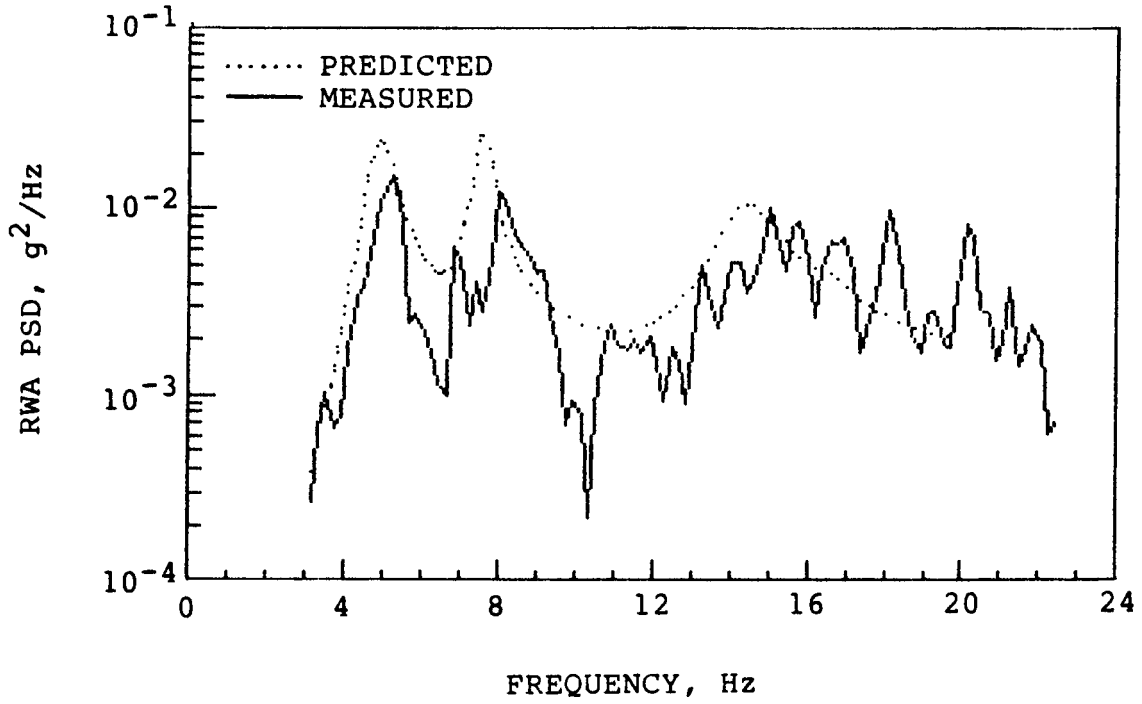
(n) $\alpha = 9.2°$, $q = 25,951$ N/m² (542 lbs/ft²), T = 24 sec.

Figure 33. $\Lambda = 26°$ Continued.
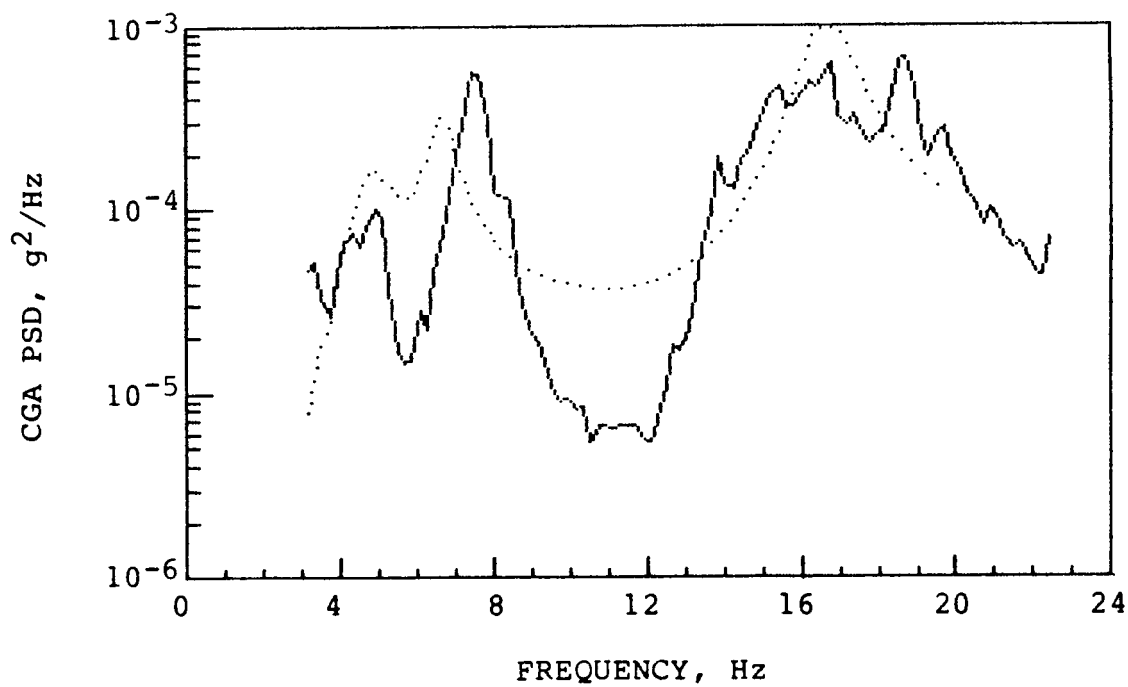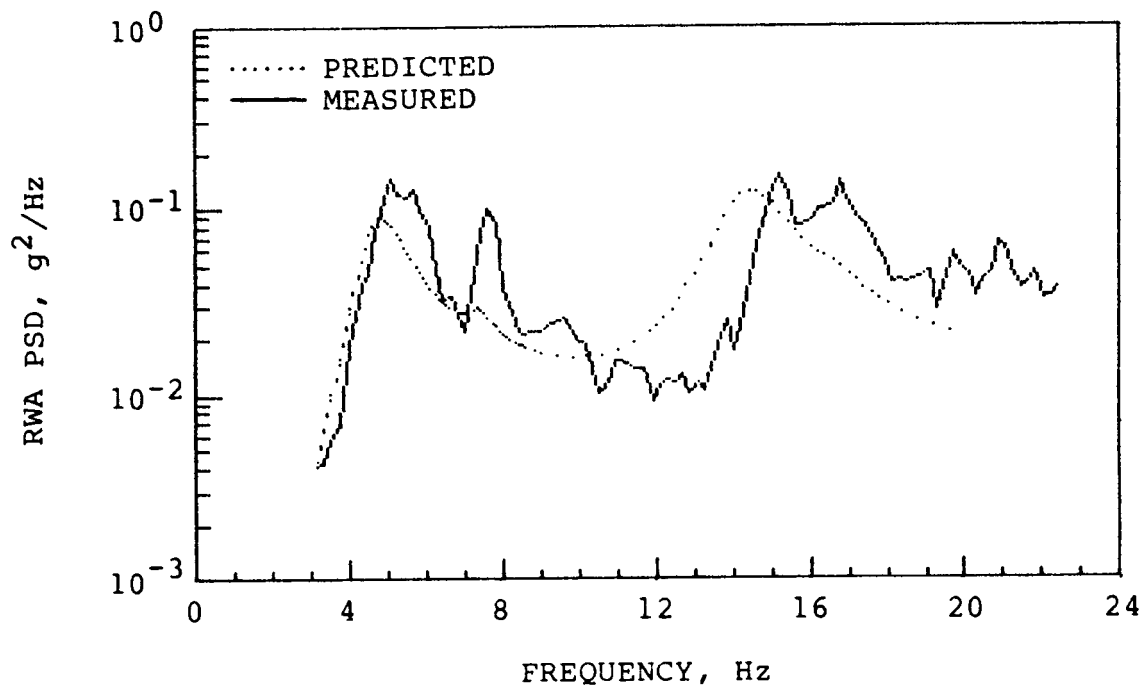
(o) $\alpha = 9.9°$, $q = 28,728$ N/m² (600 lbs/ft²), T = 126 sec.

Figure 33. $\Lambda = 26°$ Concluded.
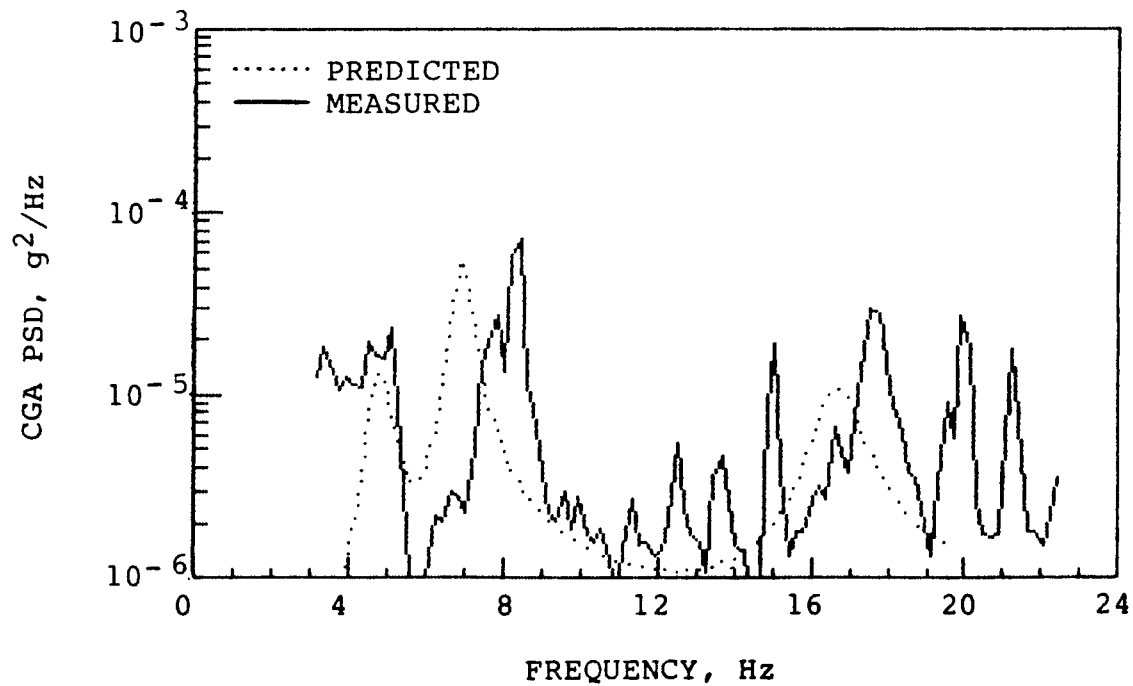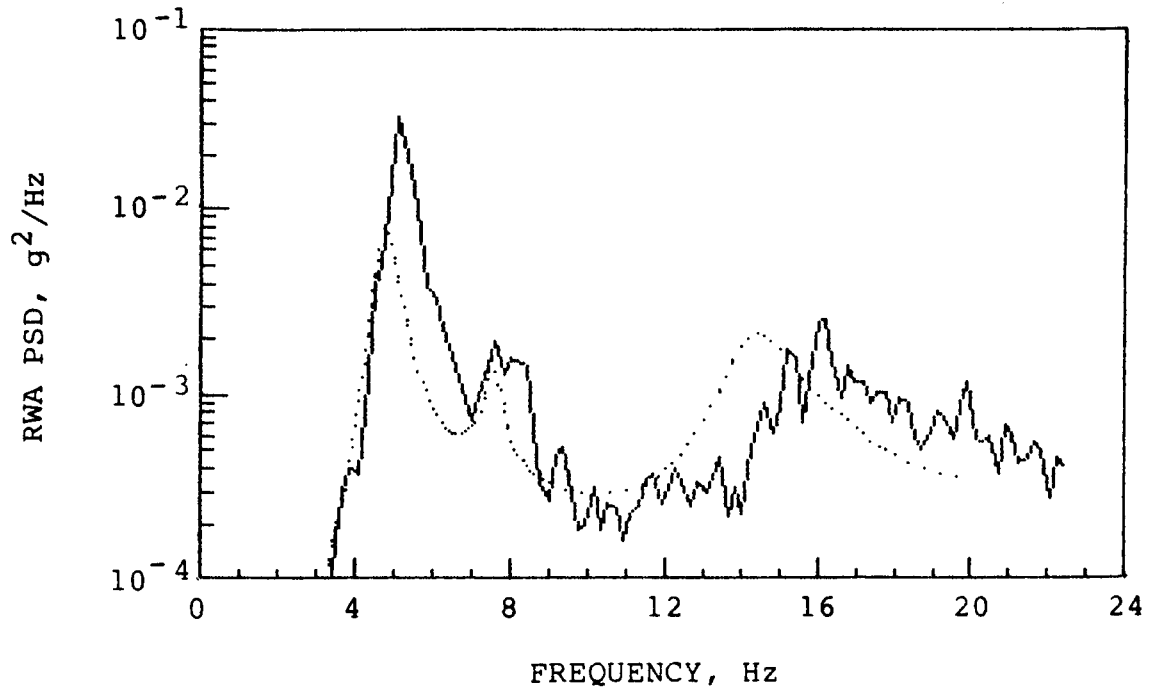
(a) $\alpha = 8.3°$, $q = 15{,}034$ N/m^2 (314 lbs/ft^2), $T = 74$ sec.

Figure 34.   Predicted and measured PSDs of wing-tip and center-of-gravity
accelerations of TACT aircraft for $\Lambda = 35°$, M = 0.80.
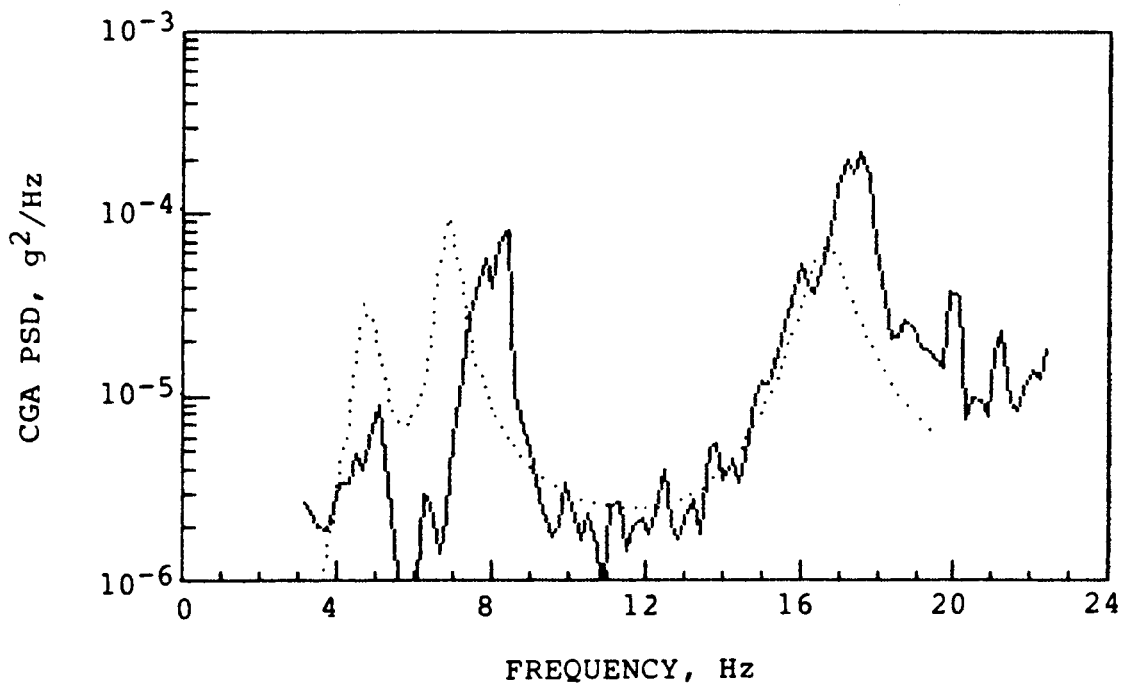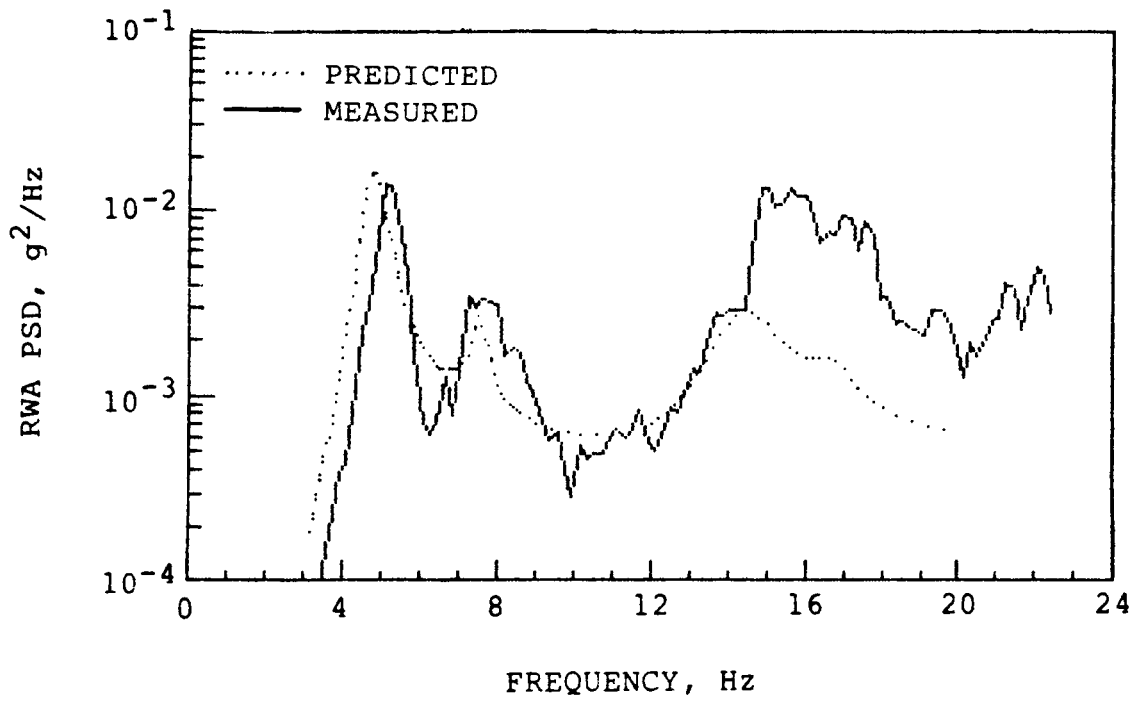
(b) $\alpha = 9.0°$, $q = 15,369$ N/m² (321 lbs/ft²), $T = 80$ sec.

Figure 34. $\Lambda = 35°$ Continued.
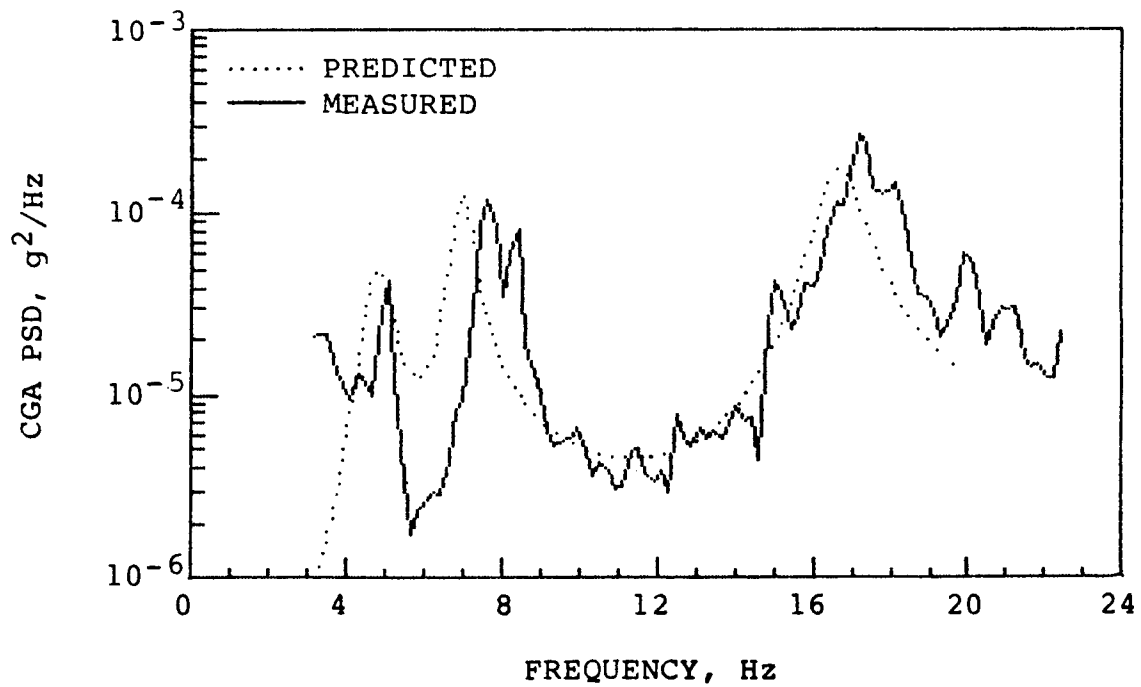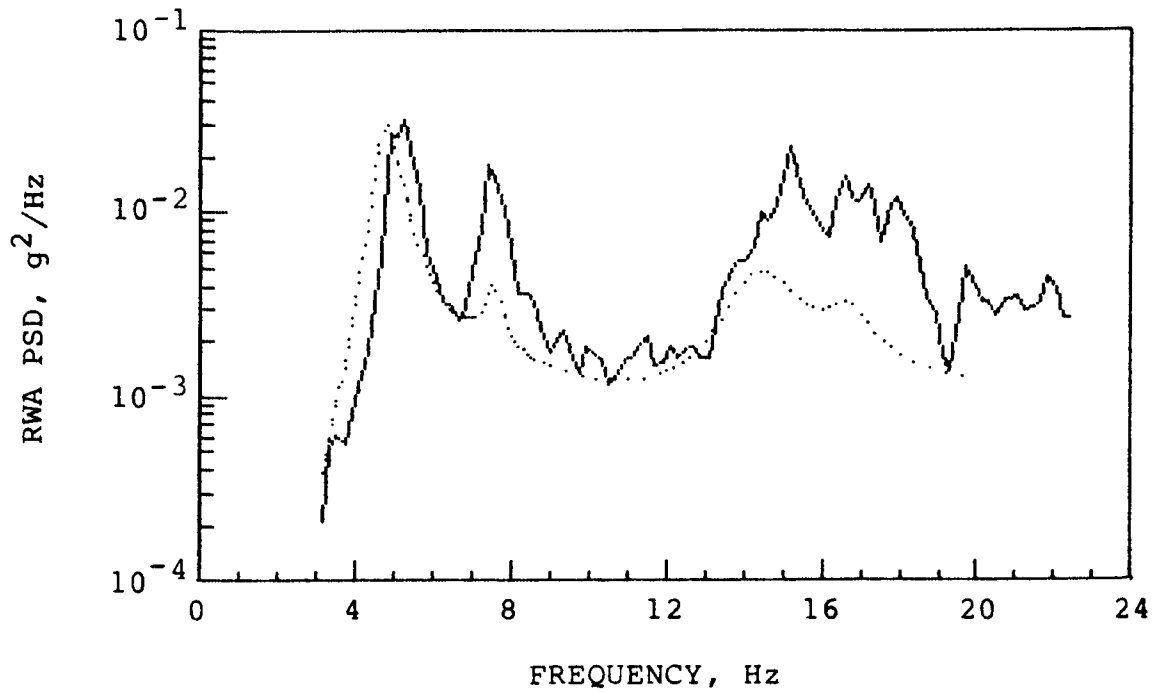
(c) $\alpha = 9.4°$, $q = 15,226$ N/m² (318 lbs/ft²), T = 115 sec.

Figure 34. $\Lambda = 35°$ Continued.
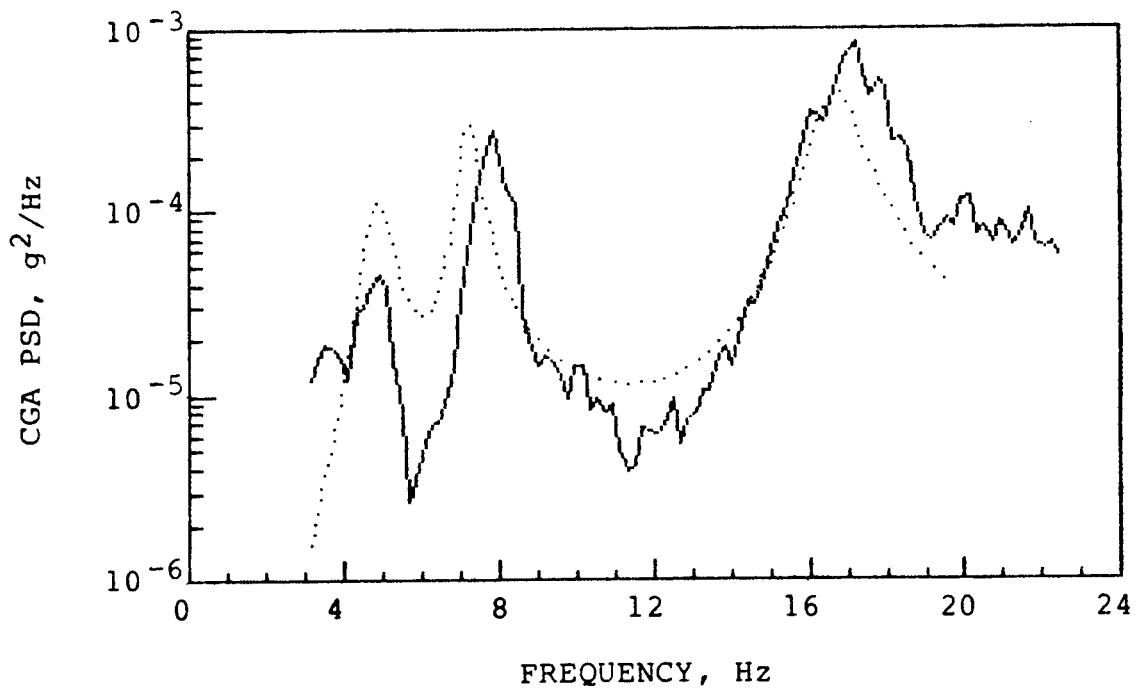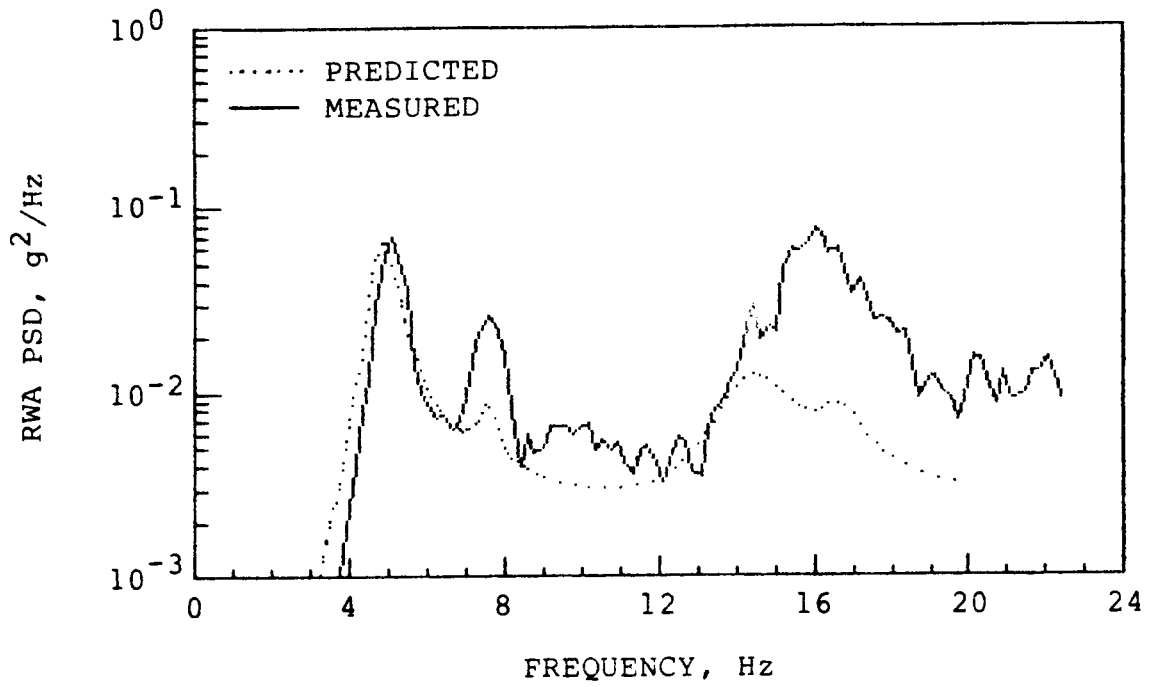
(d) $\alpha = 10.1°$, $q = 15{,}178$ N/m^2 (317 lbs/ft^2), $T = 122$ sec.

Figure 34. $\Lambda = 35°$ Continued.
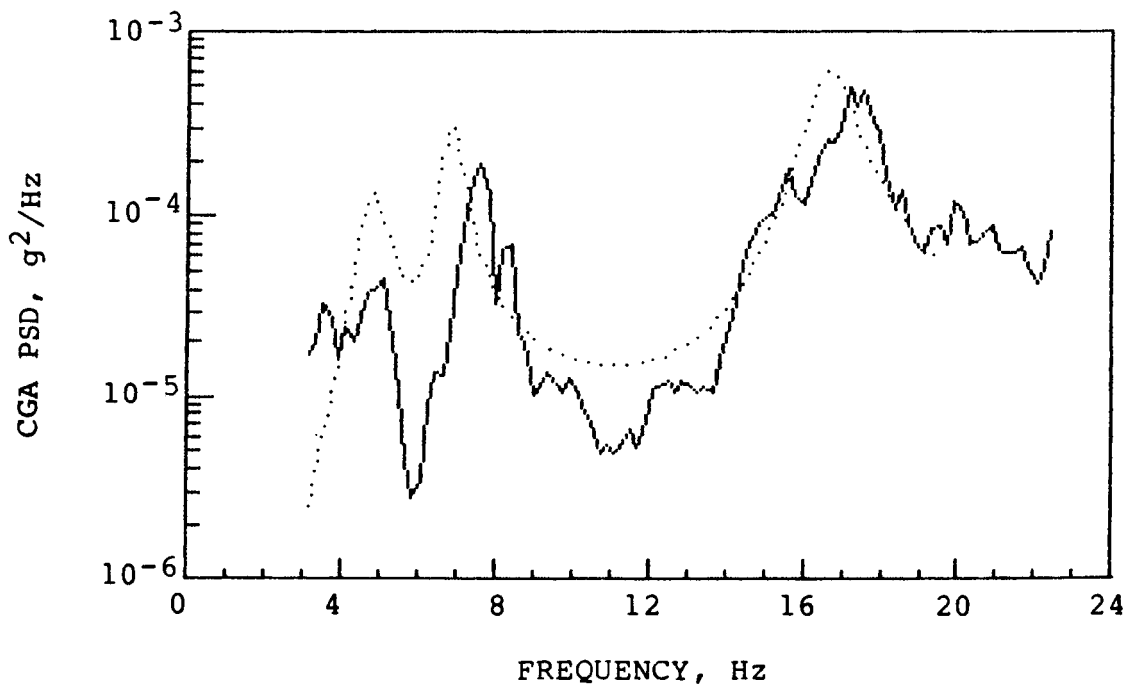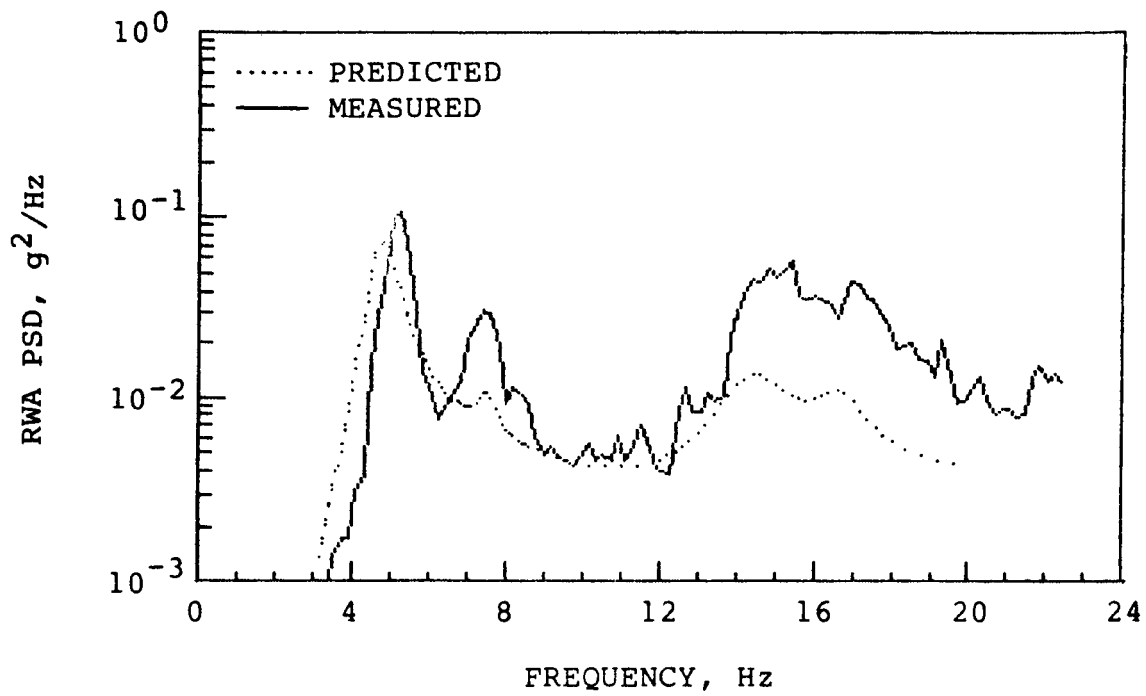
(e) $\alpha = 10.4°$, $q = 15,178$ N/m² (317 lbs/ft²), T = 120 sec.

Figure 34. $\Lambda = 35°$ Continued.
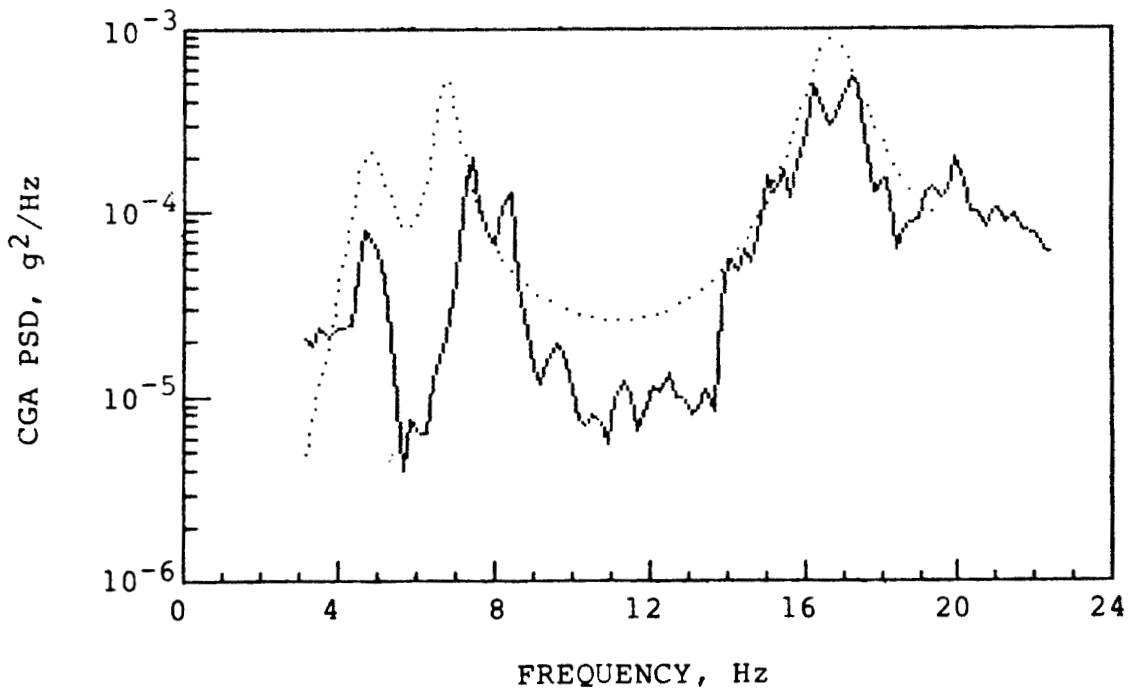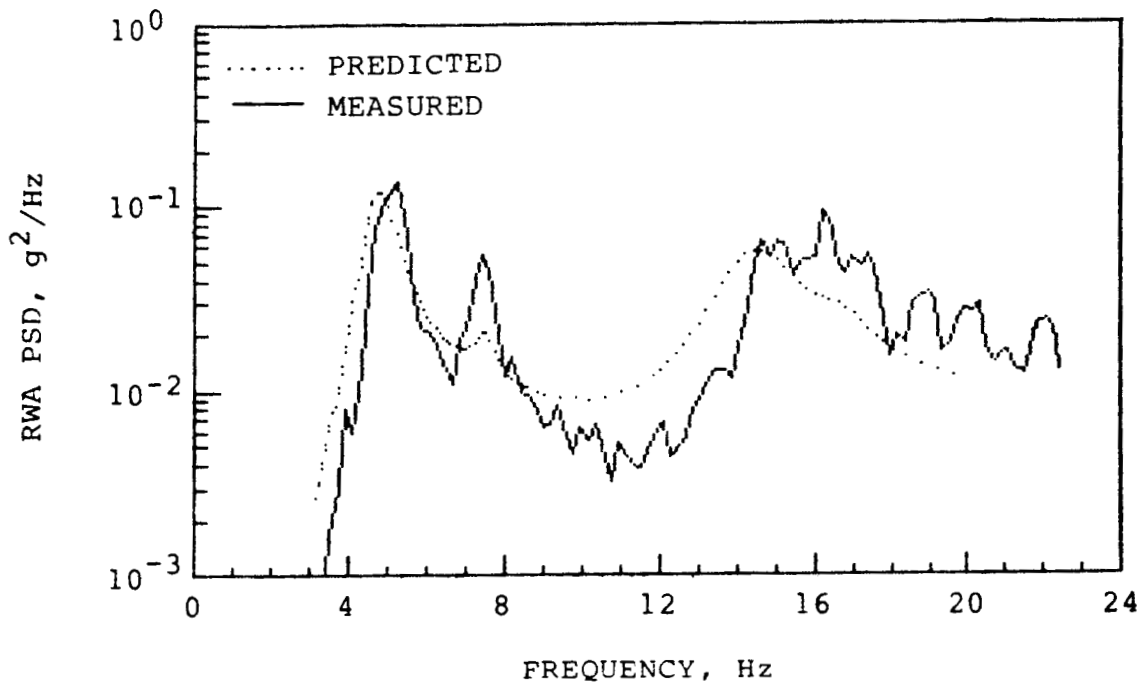
(f) $\alpha = 11.3°$, $q = 14,795$ n/m² (309 lbs/ft²), T = 73 sec.

Figure 34. $\Lambda = 35°$ Continued.
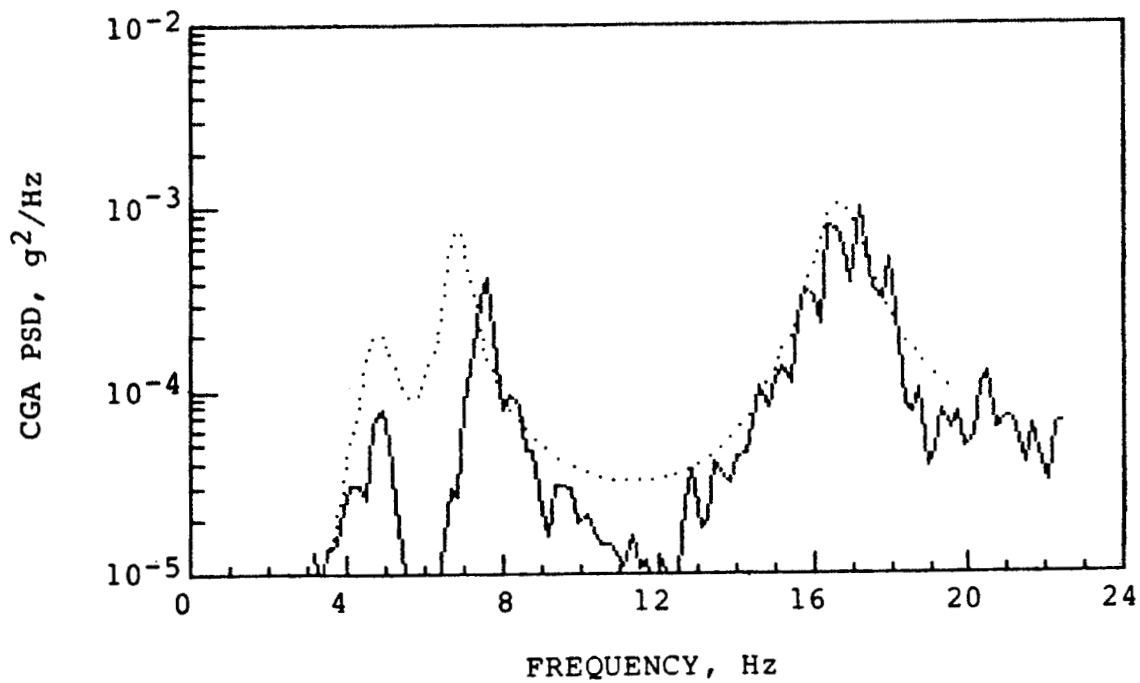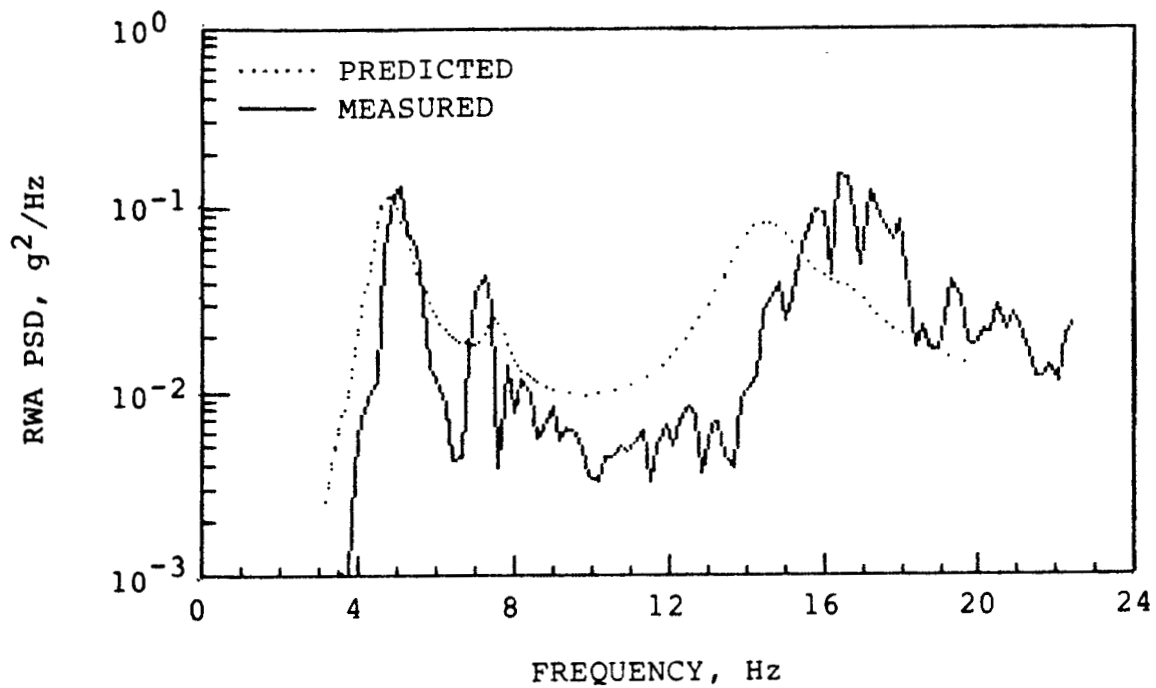
(g) $\alpha = 12.2°$, $q = 14,125$ N/m² (295 lbs/ft²), T = 38 sec.

Figure 34. $\Lambda = 35°$ Continued.

115
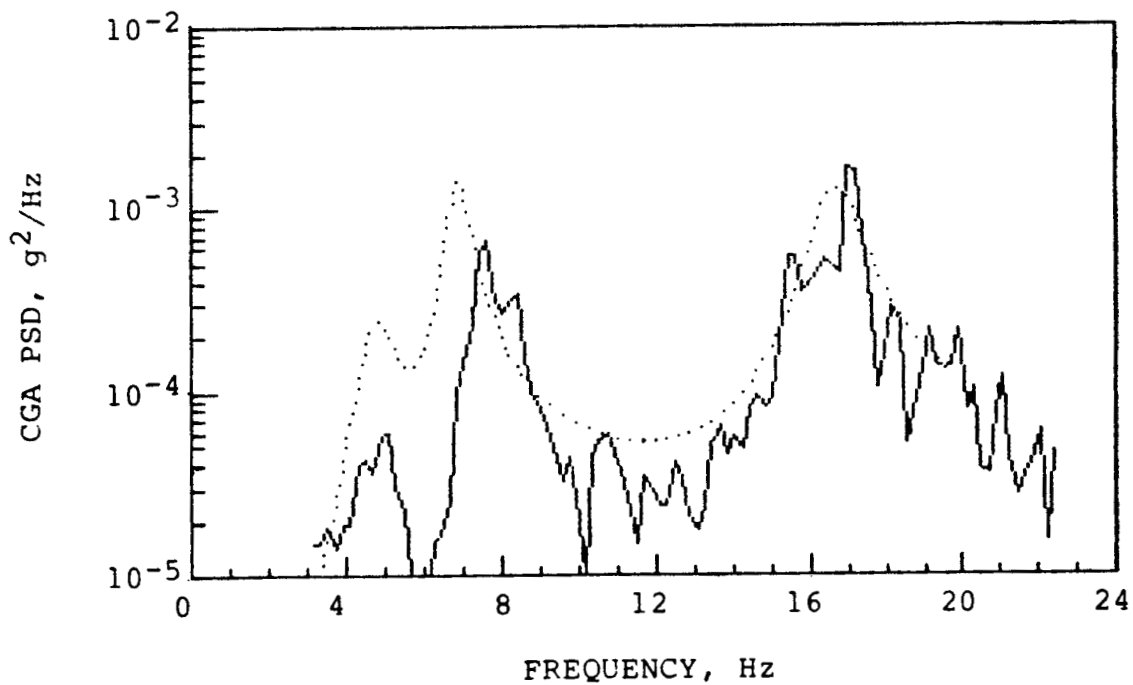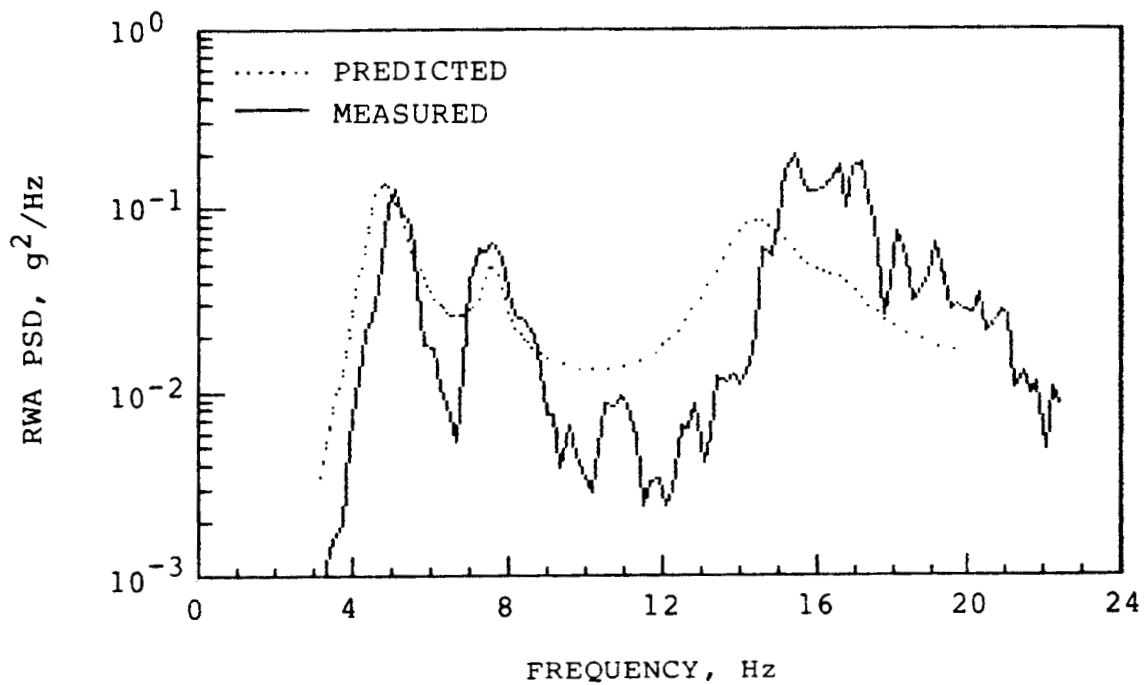
(h) $\alpha = 13.3°$, $q = 14,843$ N/m² (310 lbs/ft²), T = 37 sec.

Figure 34. $\Lambda = 35°$ Continued.
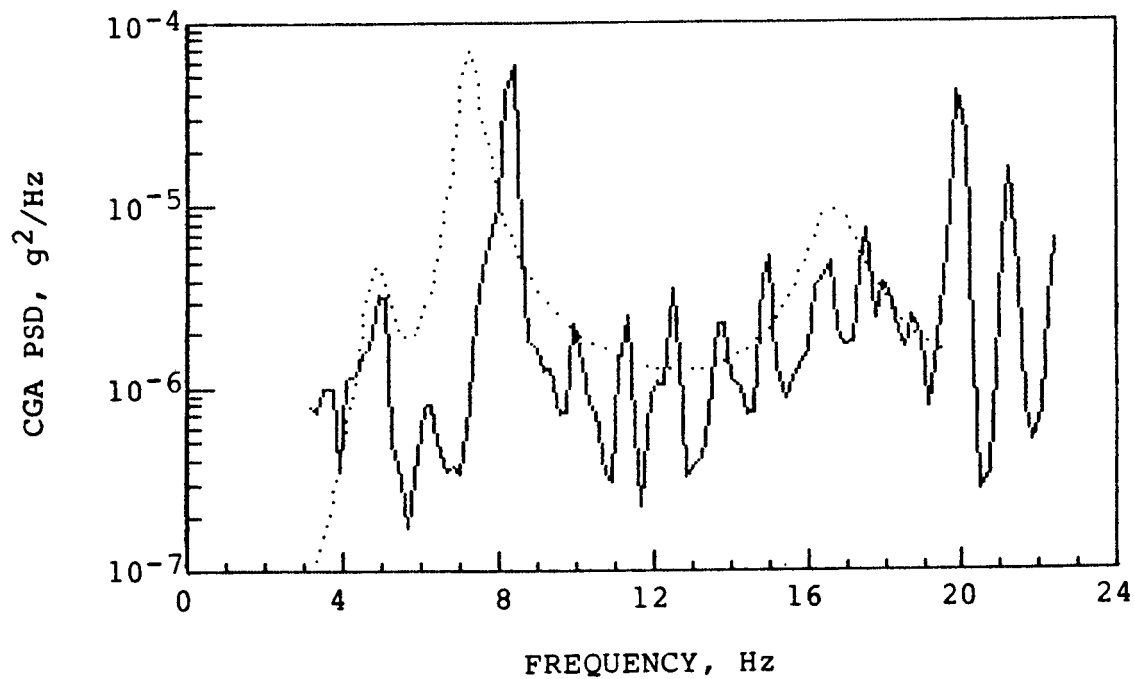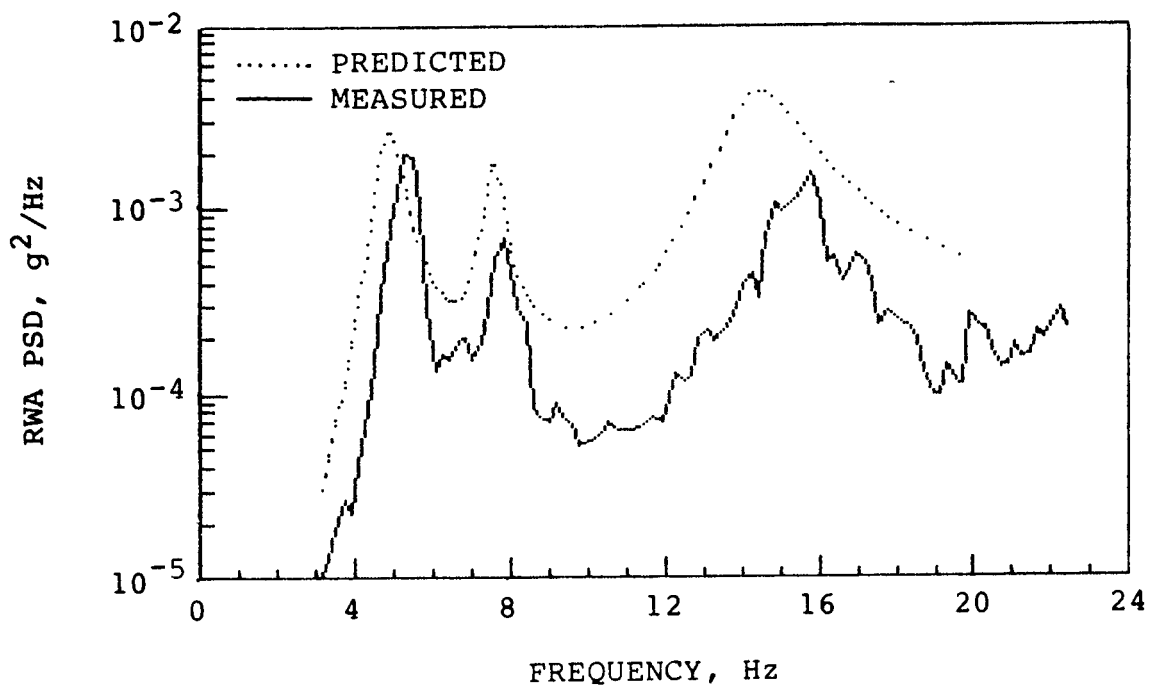
(i) $\alpha = 7.0°$, $q = 21{,}546$ N/m² (450 lbs/ft²), T = 104 sec.

Figure 34. $\Lambda = 35°$ Continued.

117
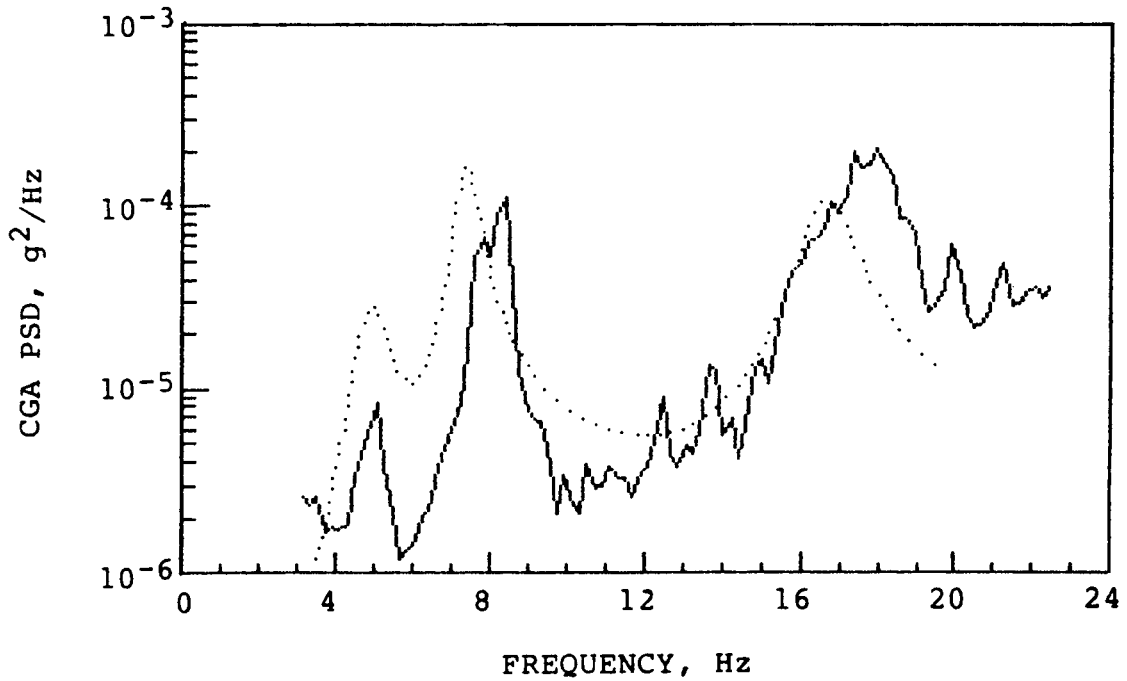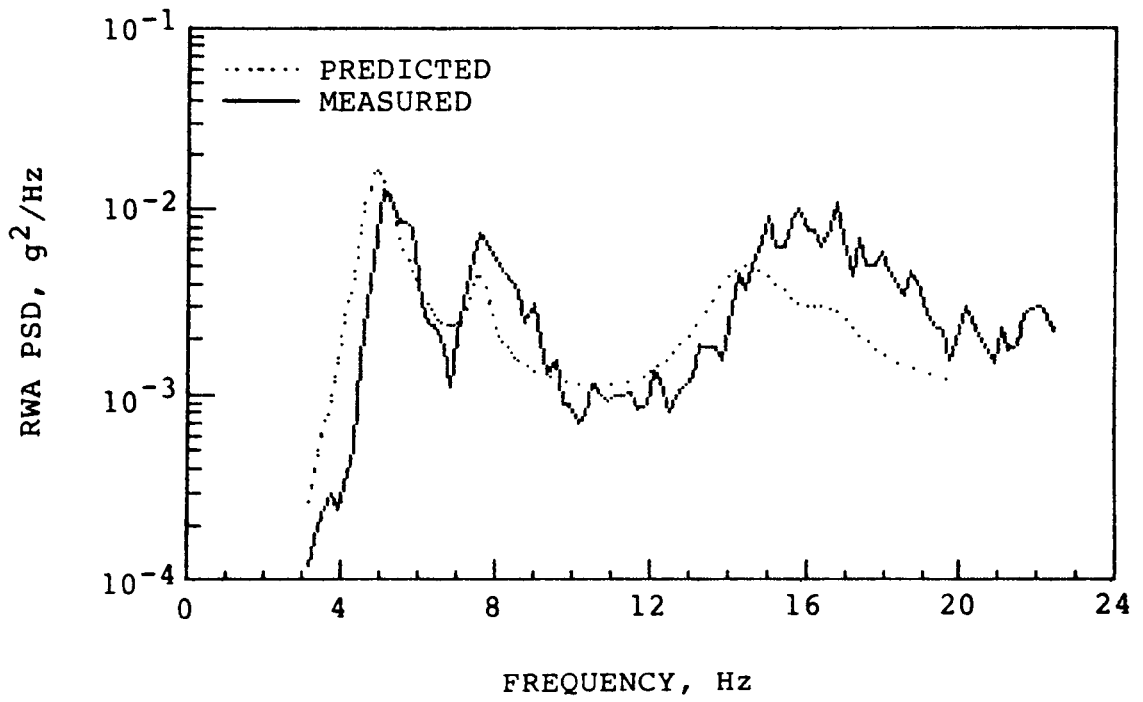
(j) $\alpha = 9.0°$, $q = 22,647$ N/m² (473 lbs/ft²), $T = 102$ sec.

Figure 34. $\Lambda = 35°$ Continued.
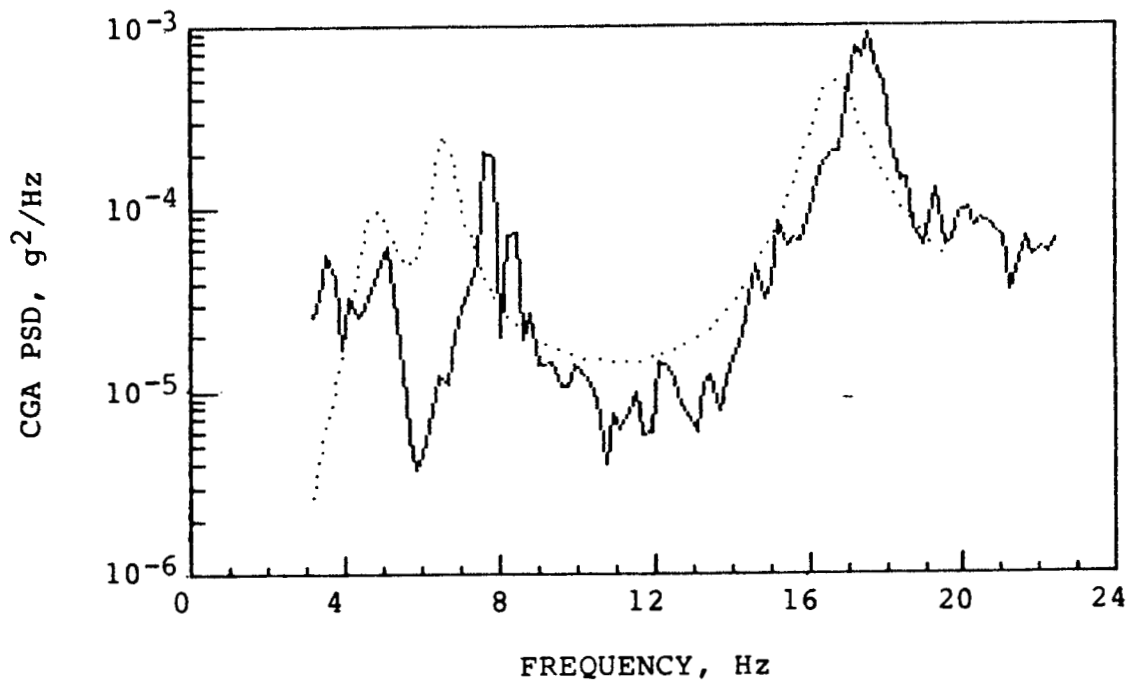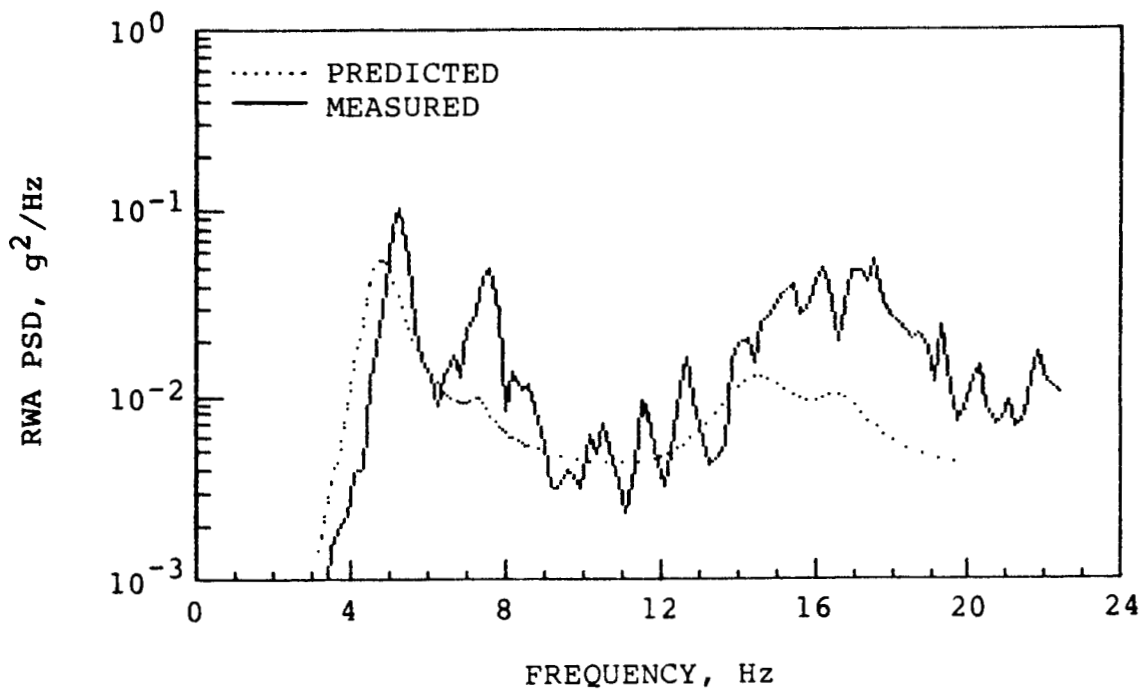
(k) $\alpha = 9.8°$, $q = 21,019$ N/m² (439 lbs/ft²), T = 37 sec.

Figure 34. $\Lambda = 35°$ Continued.
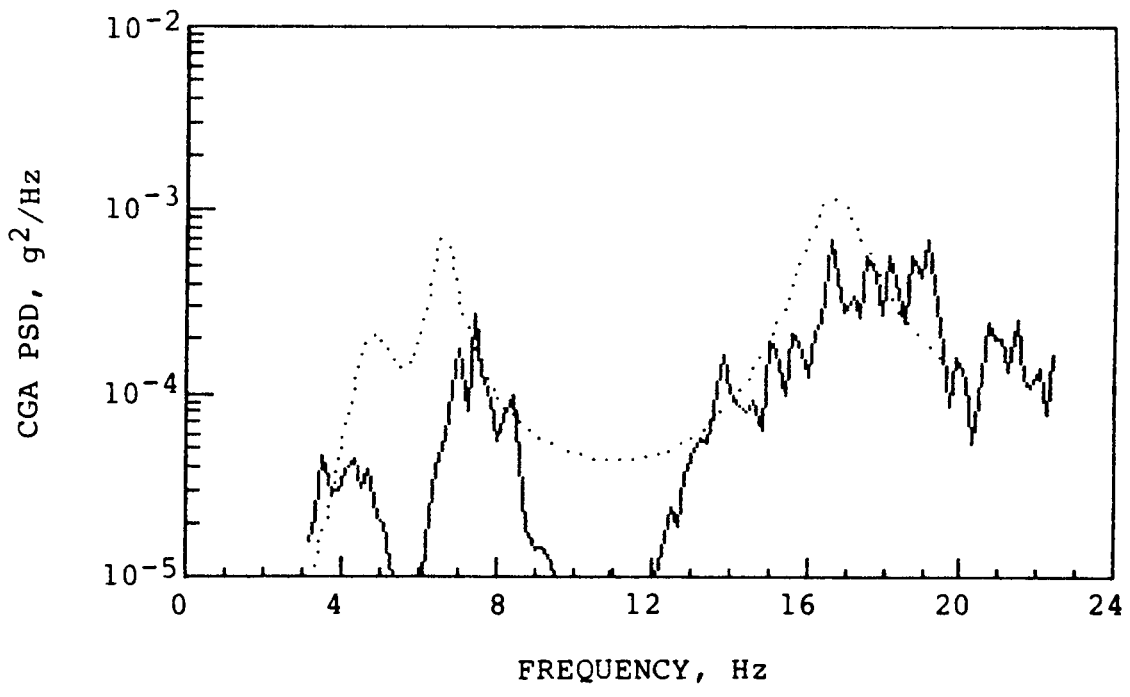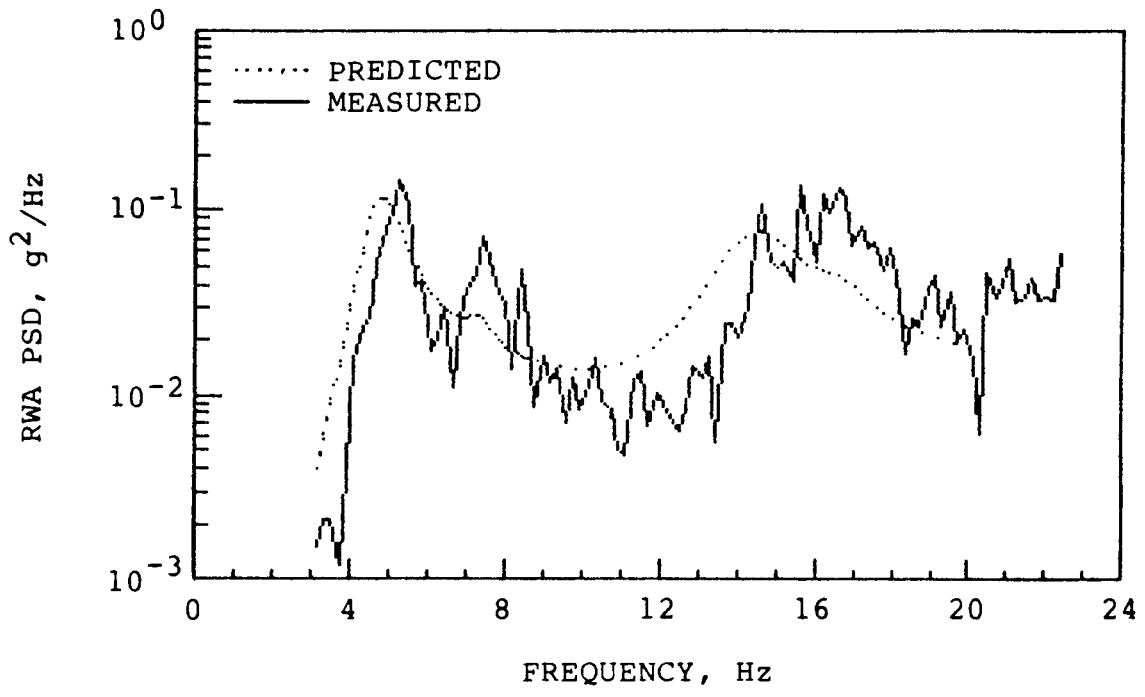
(1) $\alpha = 11.0°$, $q = 21,546$ N/m² (450 lbs/ft²), T = 31 sec.

Figure 34. $\Lambda = 35°$ Continued.
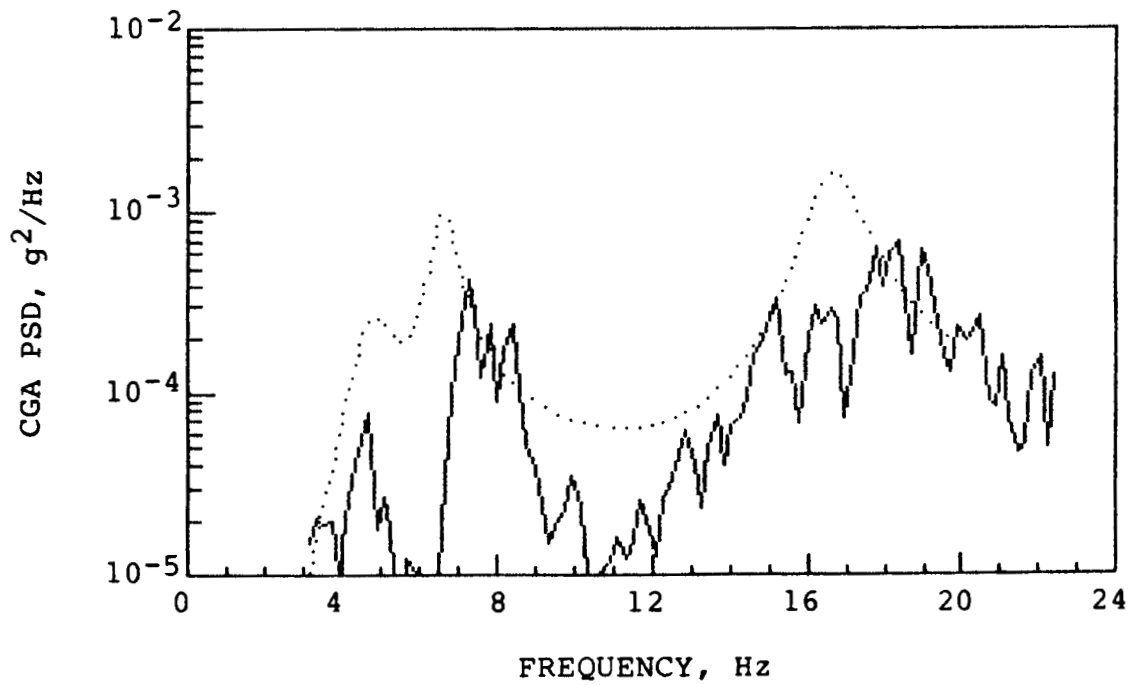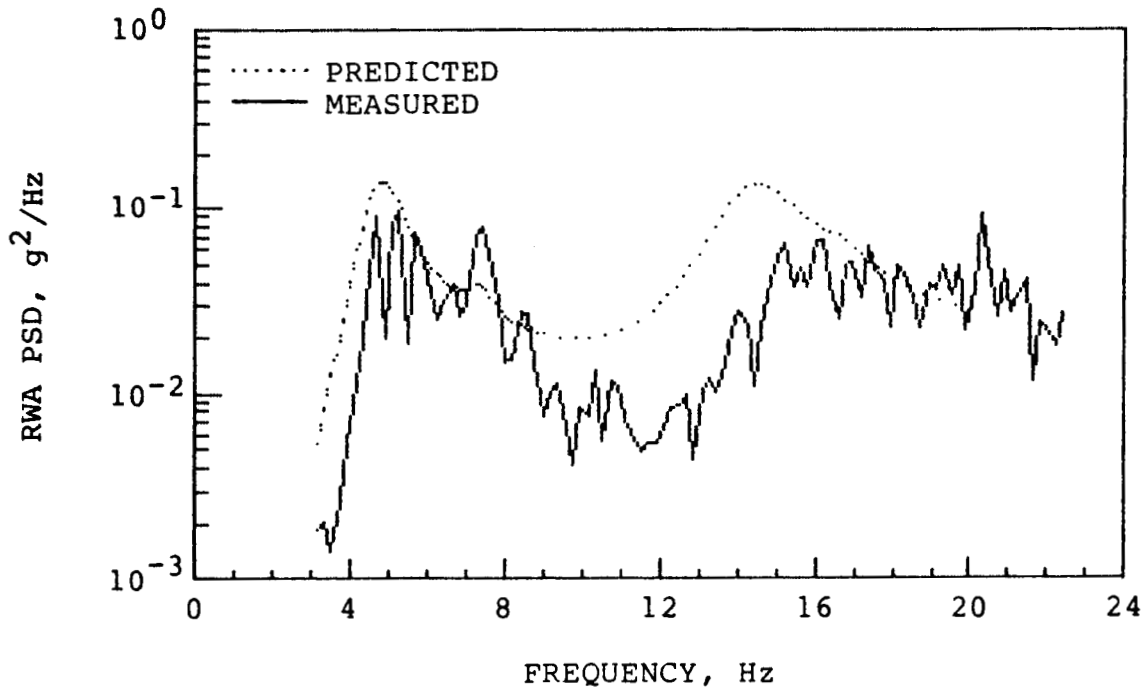
(m) $\alpha = 11.9°$, $q = 21,211$ N/m^2 (443 lbs/ft^2), T = 28 sec.

Figure 34. $\Lambda = 35°$ Continued.
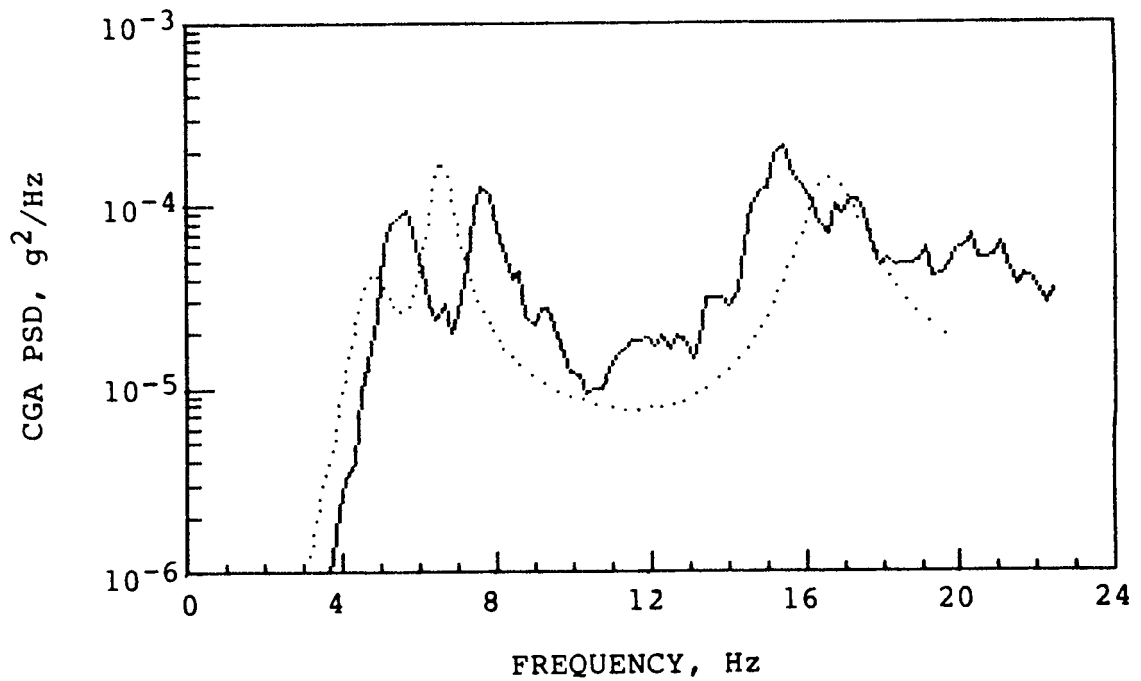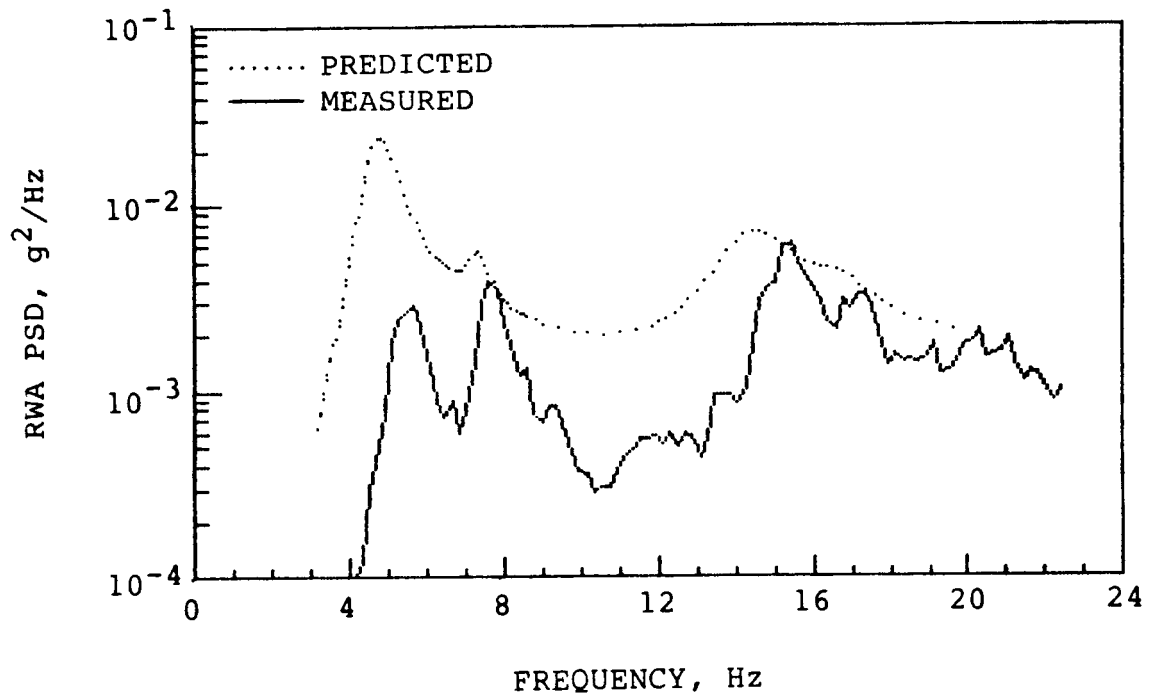
(n) $\alpha = 9.0°$, $q = 28,489$ N/m^2 (595 lbs/ft^2), T = 122 sec.

Figure 34. $\Lambda = 35°$ Continued.
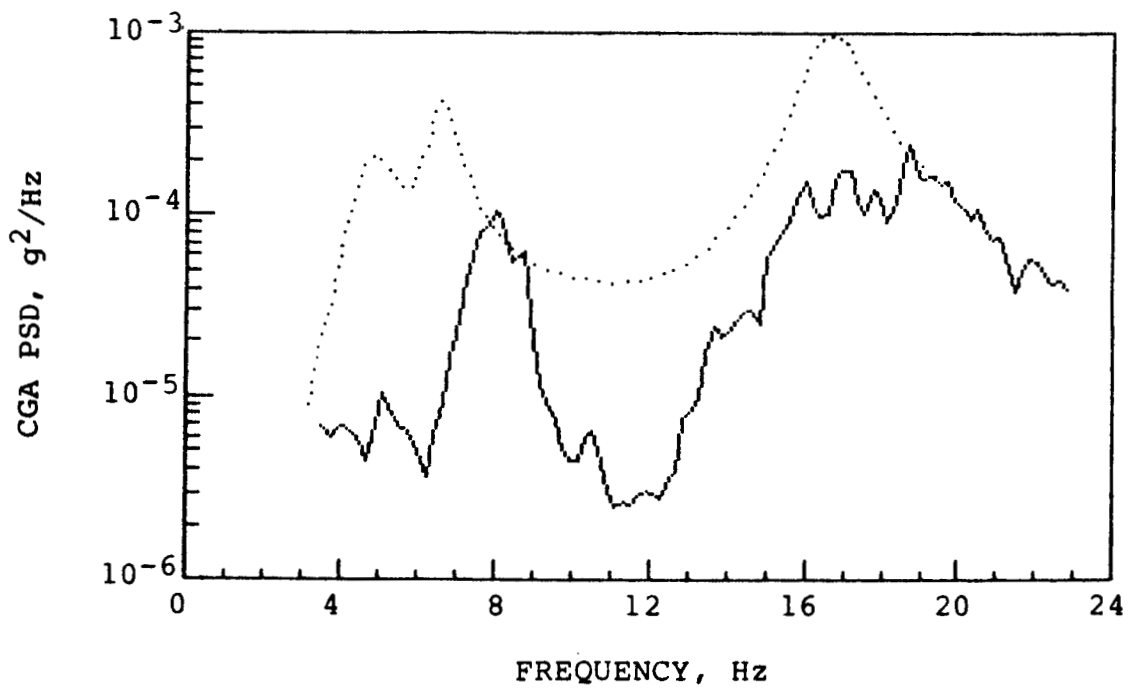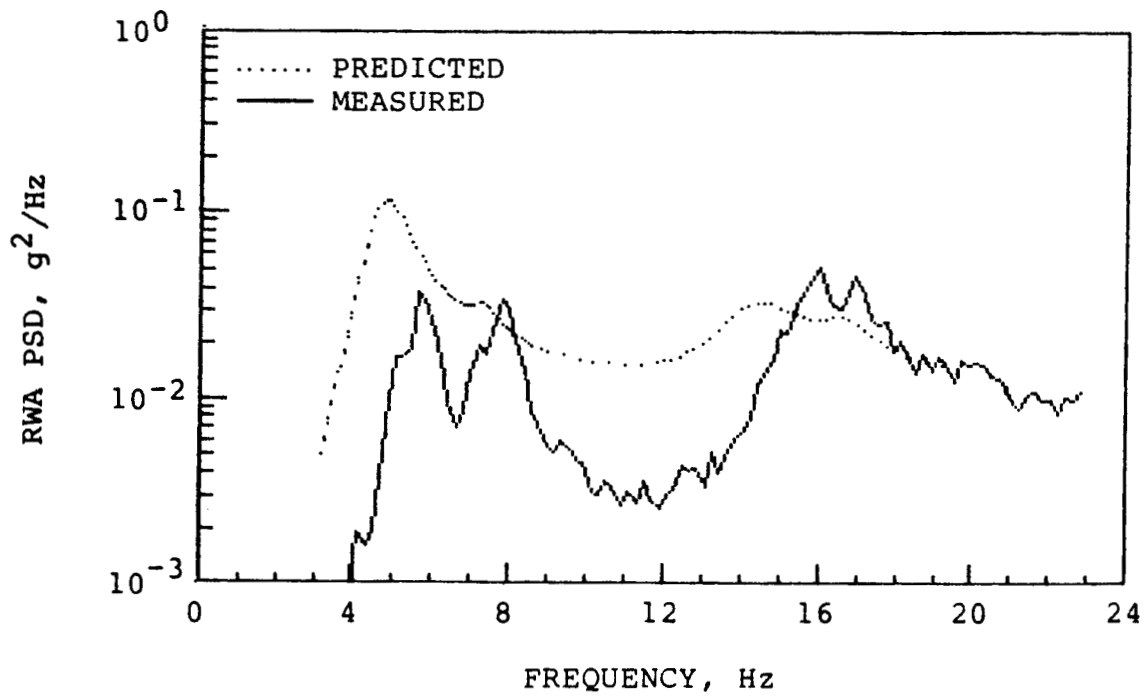
(o) $\alpha = 10.0°$, $q = 28,249$ N/m² (590 lbs/ft²), $T = 151$ sec.

Figure 34. $\Lambda = 35°$ Concluded.
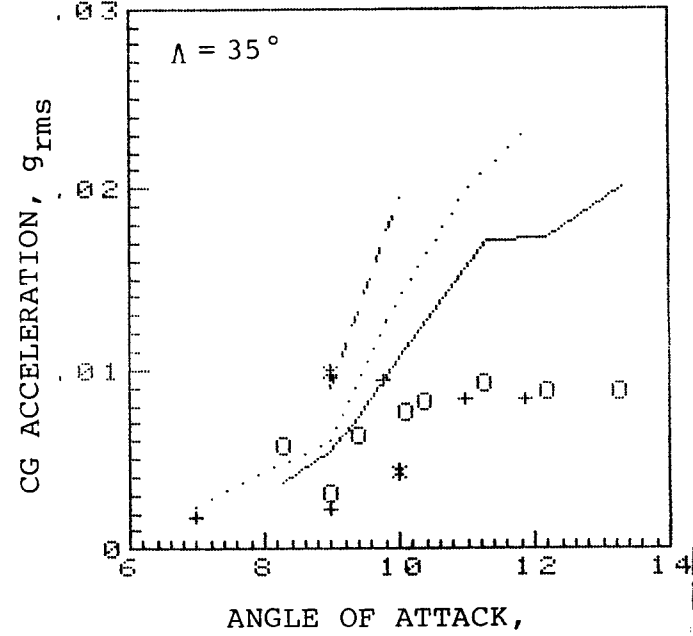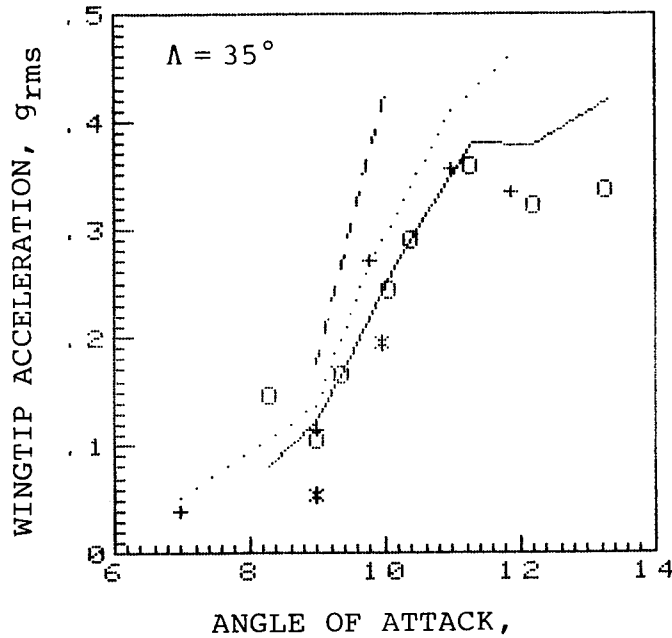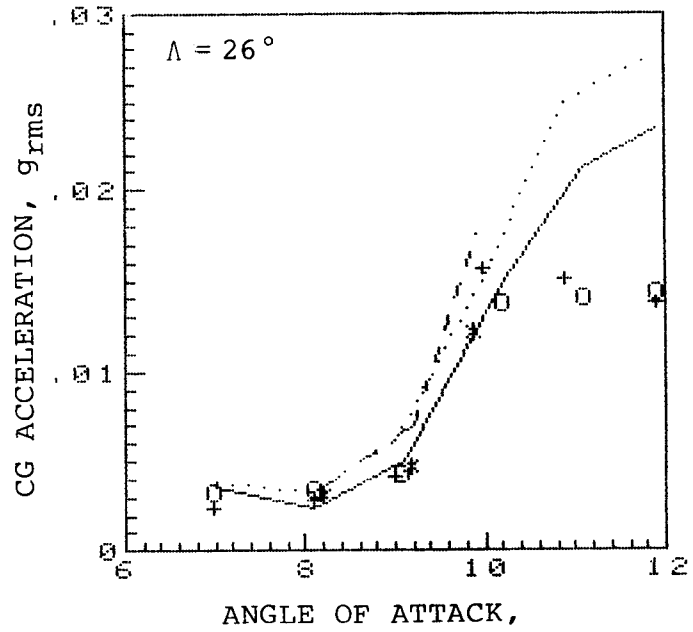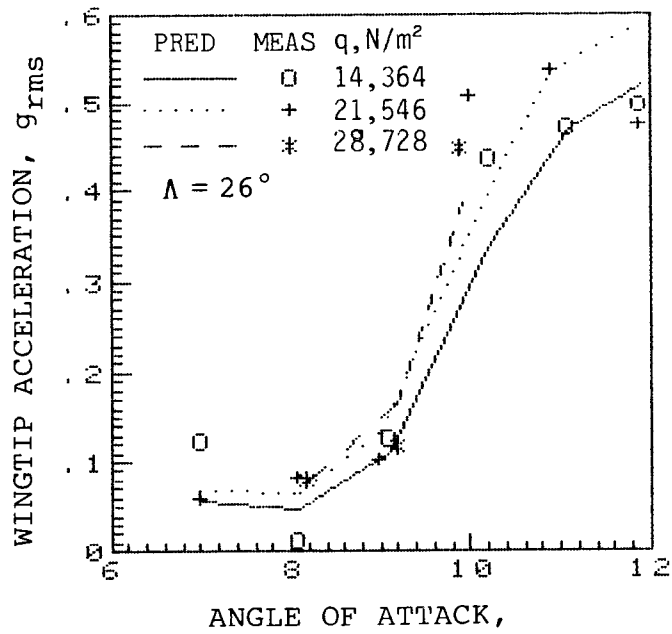
(a) WSB mode

Figure 35. Predicted and measured RMS accelerations of wing tip and center of gravity versus angle of attack of TACT aircraft, M = 0.80.
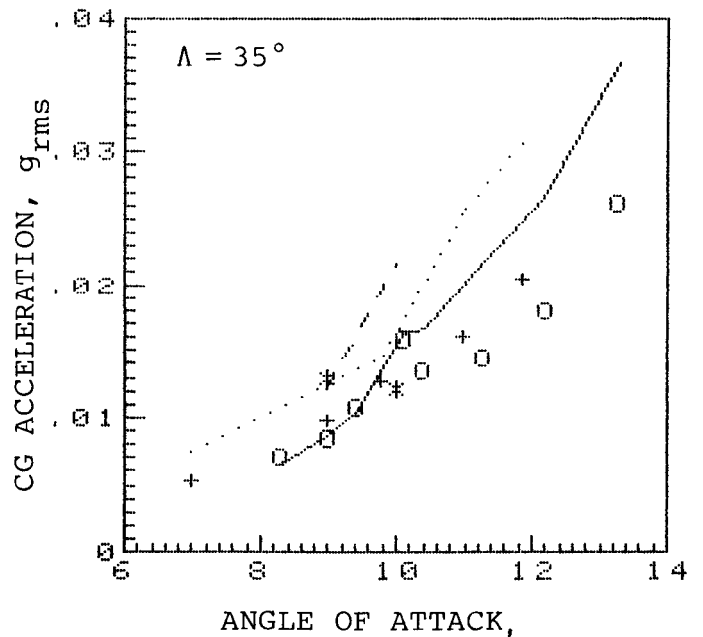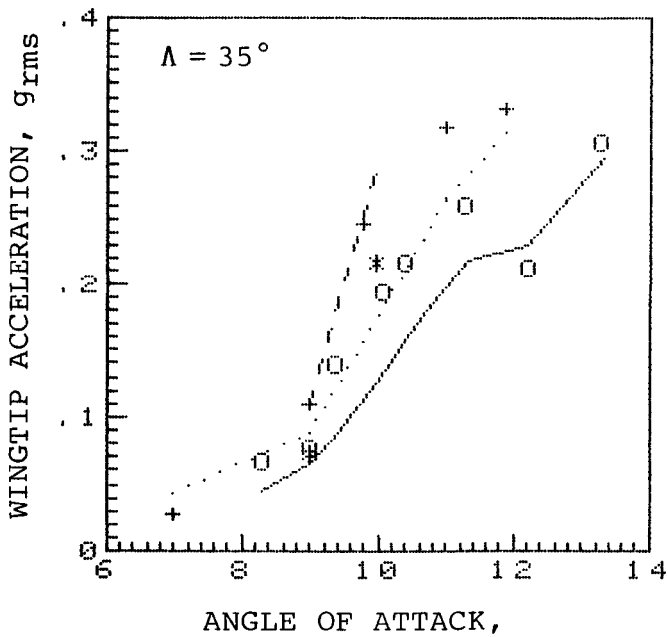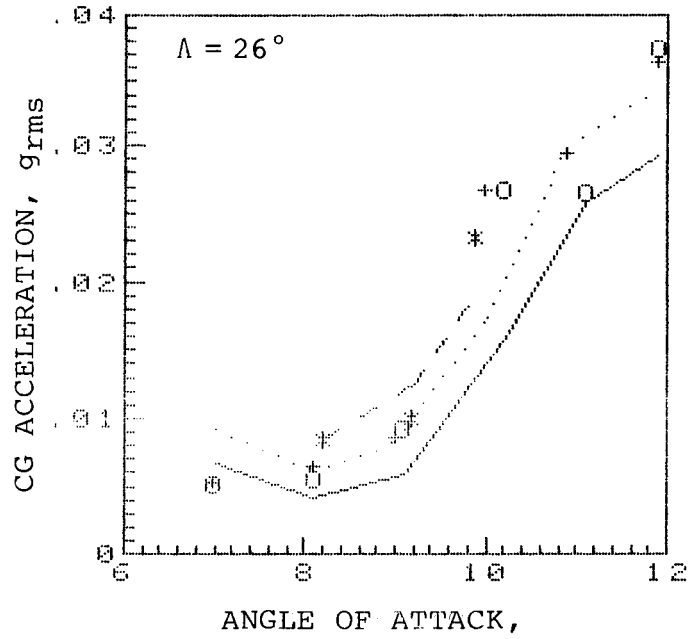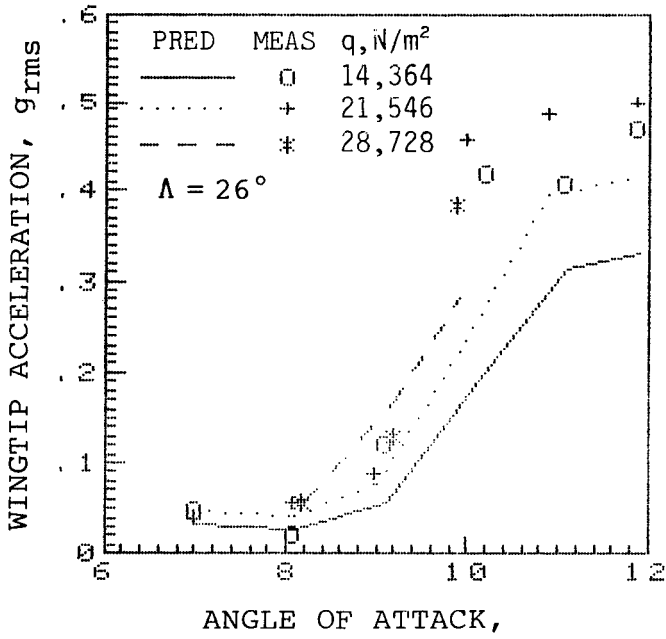
(b) FVB & WASB modes

Figure 35. Continued.
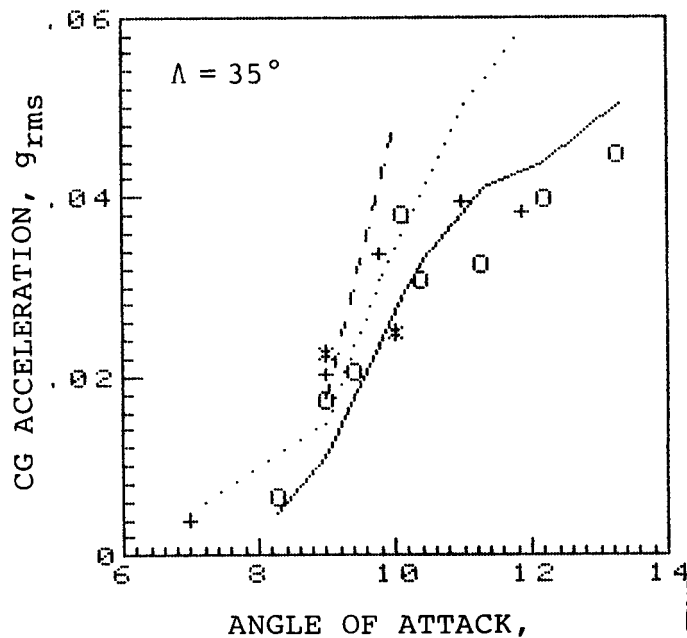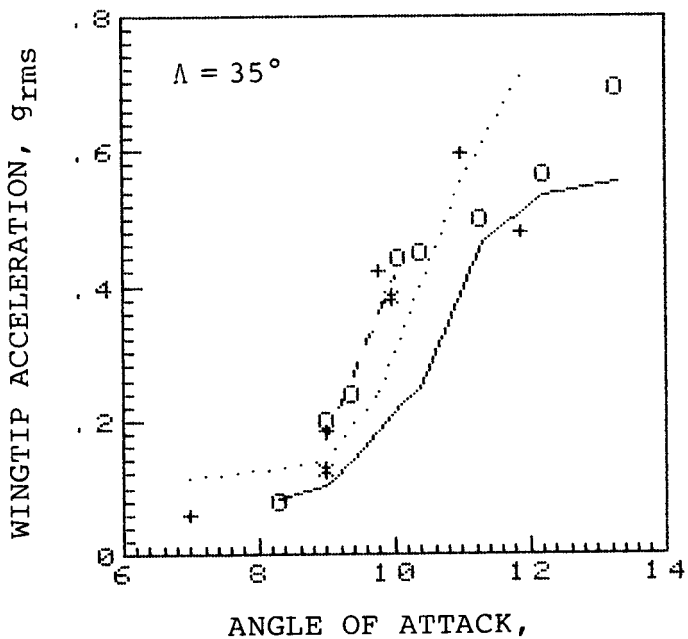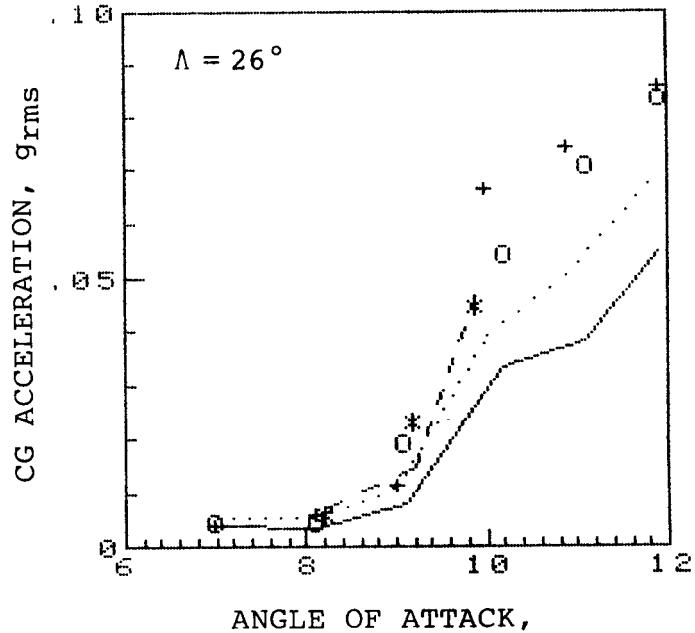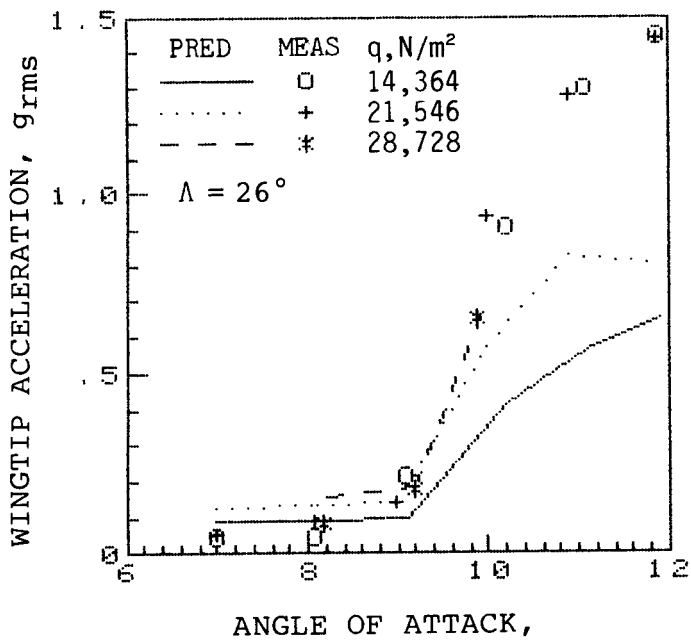
(c) RWT, LWT & WST modes

Figure 35. Continued.
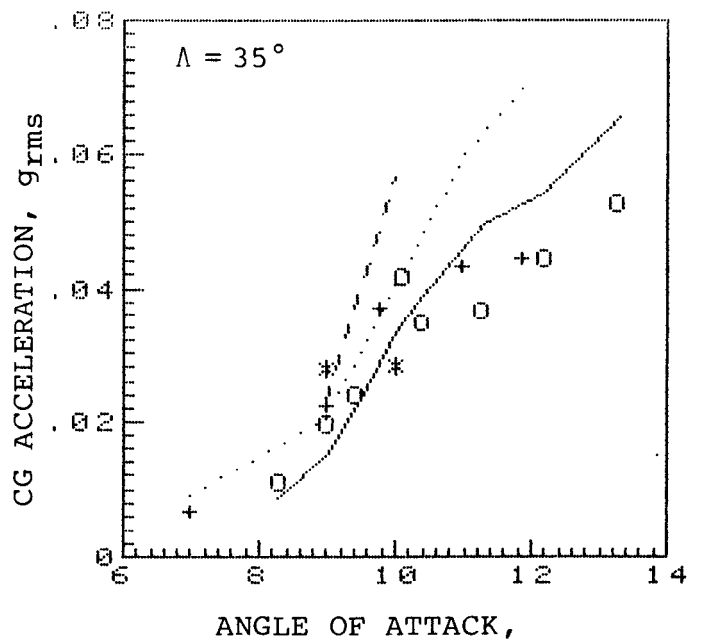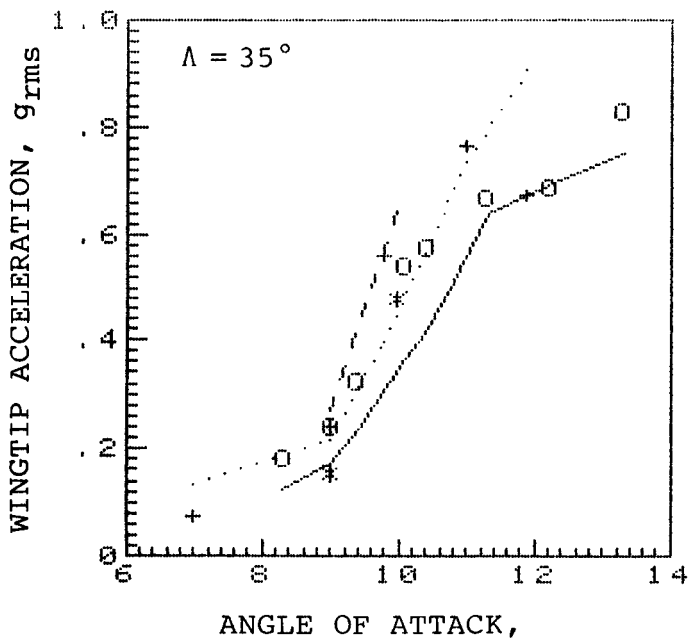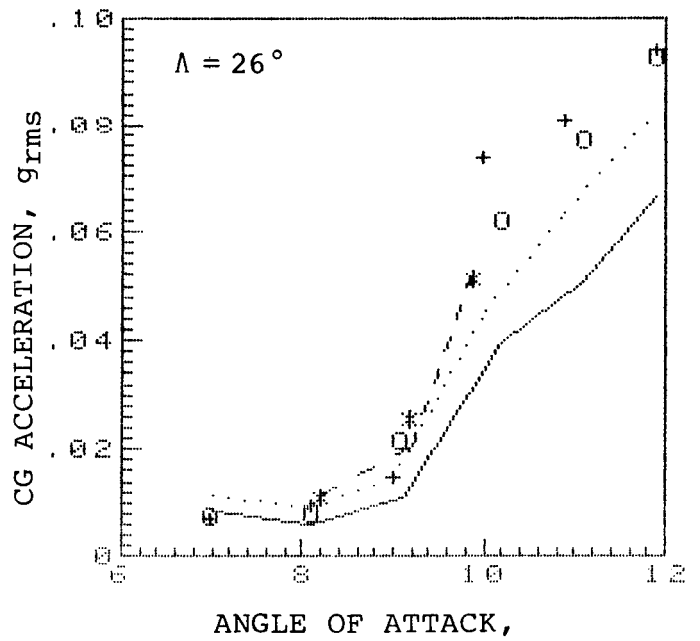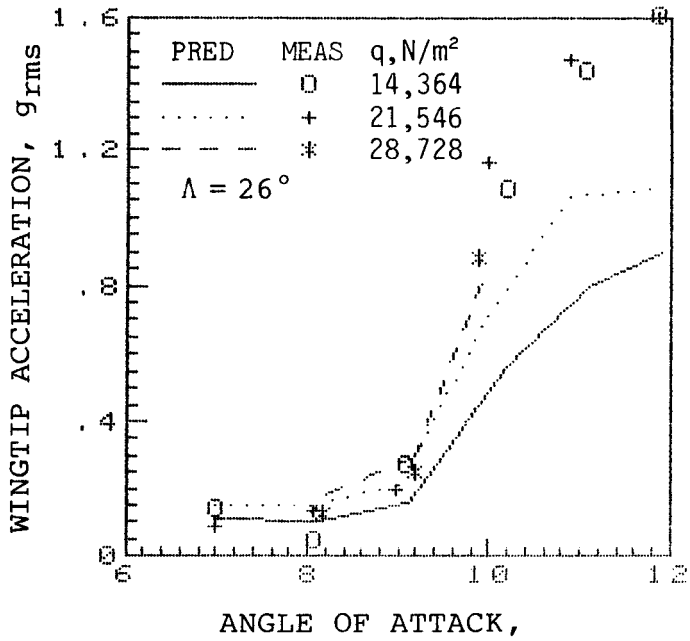
(d) WSB, FVB, WASB, RWT, LWT & WST modes

Figure 35. Concluded.
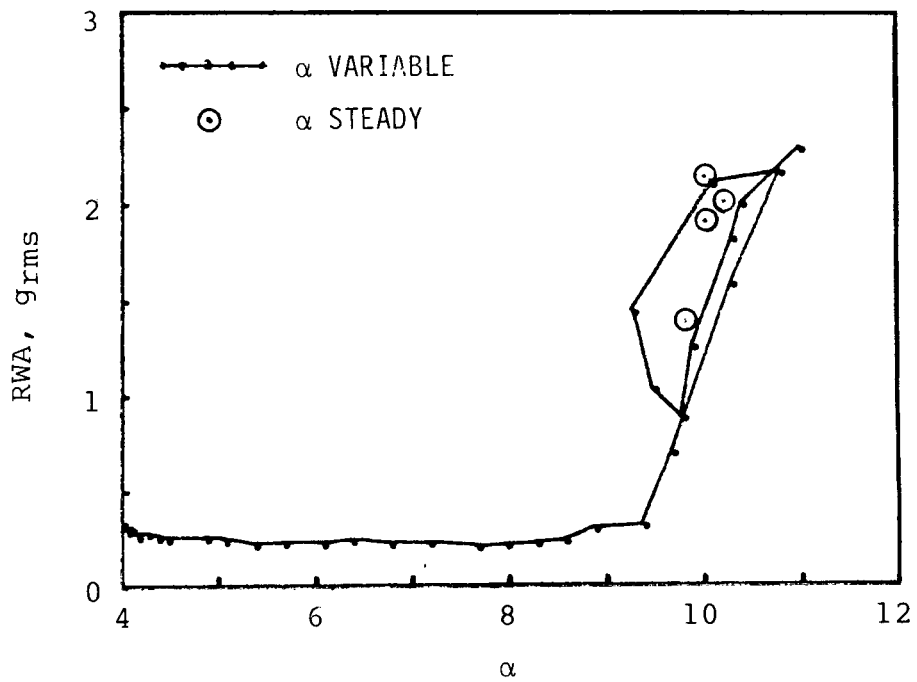
Figure 36. Effect of pitch rate on accelerations of wing tip, M = 0.80,
$\Lambda = 26°$, q = 26,300 N/m² (α VARIABLE points at 1 per second).

APPENDIX A

THEORETICAL VIBRATION MODES OF F-111 TACT

The six natural modes of vibration used for this investigation were developed by General Dynamics, Fort Worth Division, for the F-111 TACT aircraft using a finite element NASTRAN model of the complete airplane. The aircraft was modeled from wing tip to wing tip in this case because the instrumentation placement caused an asymmetry of the mass distribution. In spite of asymmetry the modes obtained were generally symmetric or antisymmetric; however, some modes, particularly those involving torsion, were asymmetric.

The six modes selected for the F-111 TACT buffet prediction are presented in Figures A1 through A6. The modes are as follows:

1. First wing symmetrical bending (WSB)
2. First fuselage vertical bending (FVB)
3. First wing antisymmetric bending (WASB)
4. First right wing torsion (RWT)
5. First left wing torsion (LWT)
6. First wing symmetric torsion (WST)

The natural frequencies and generalized masses of the modes are given in Table 1.
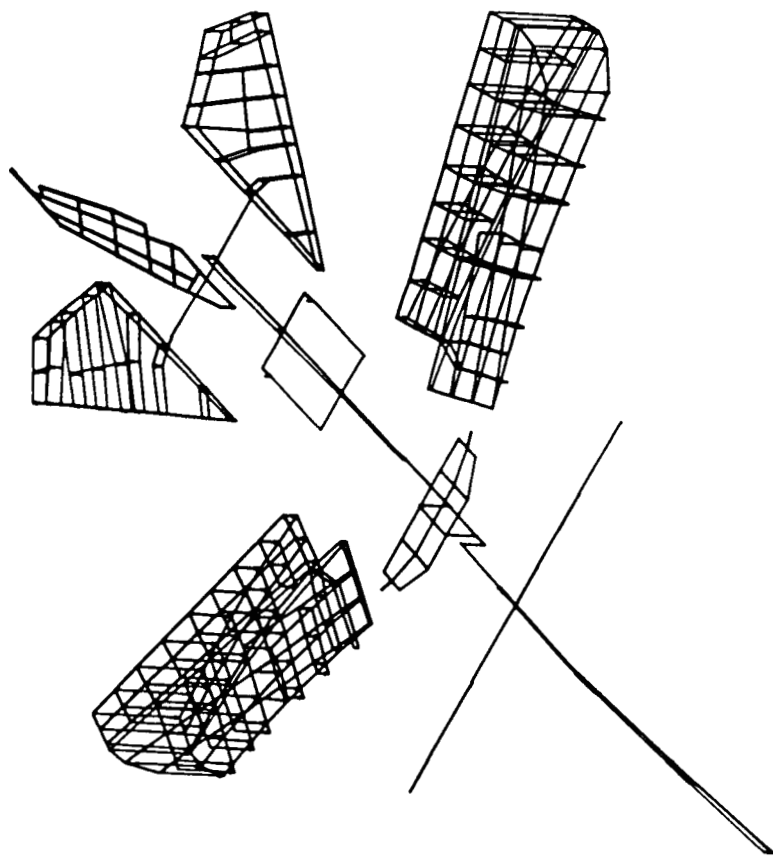
Figure A1. First wing symmetric bending (WSB) mode, f = 4.418 Hz.
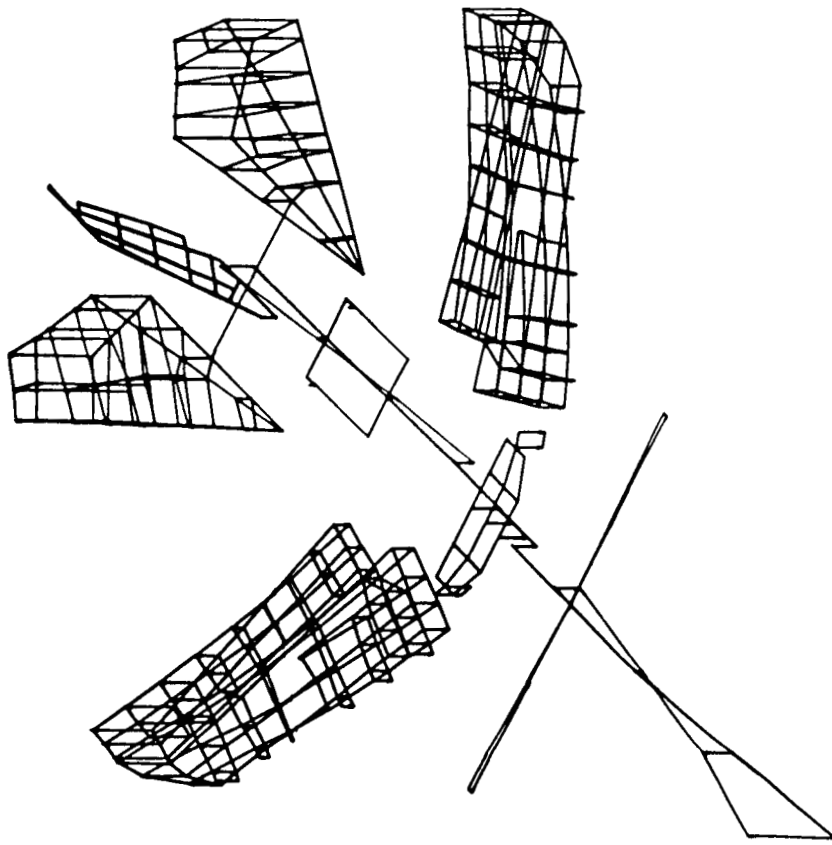
Figure A2. First fuselage vertical bending (FVB) mode, f = 7.296 Hz.
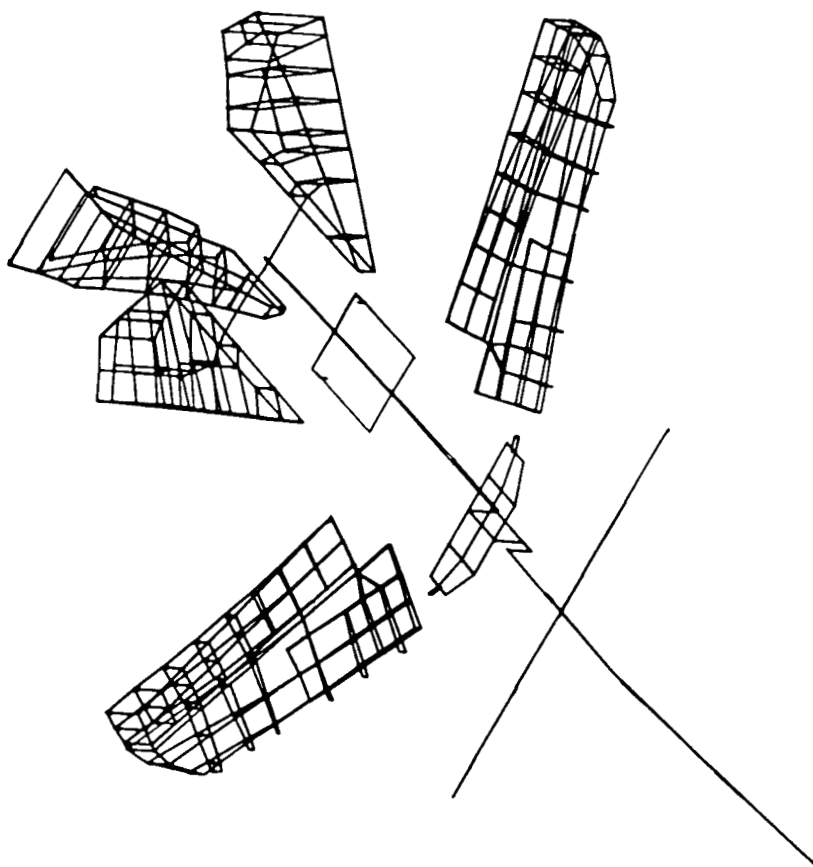
Figure A3. First wing antisymmetric bending (WASB) mode, f = 7.684 Hz.
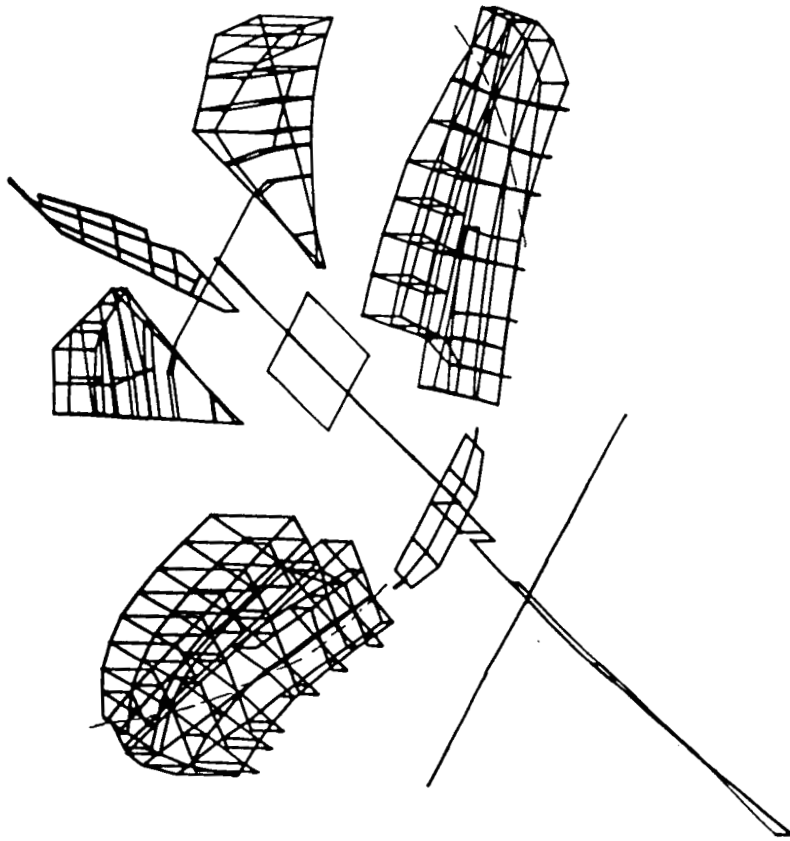
Figure A4. First right wing torsion (RWT) mode, f = 14.093 Hz.
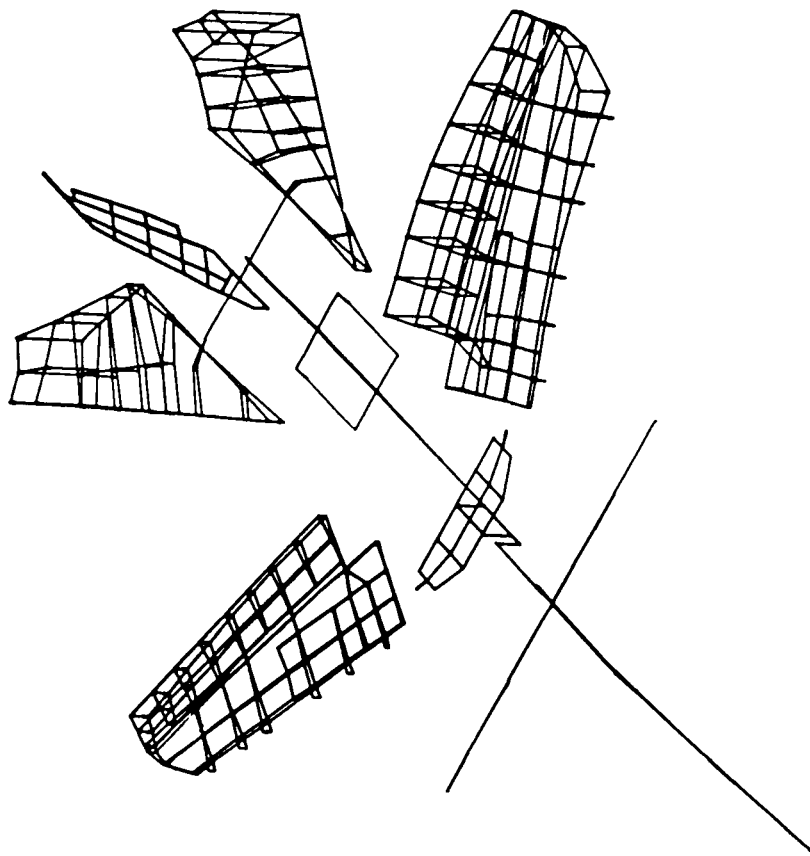
Figure A5. First left wing torsion (LWT) mode, f = 15.204 Hz.
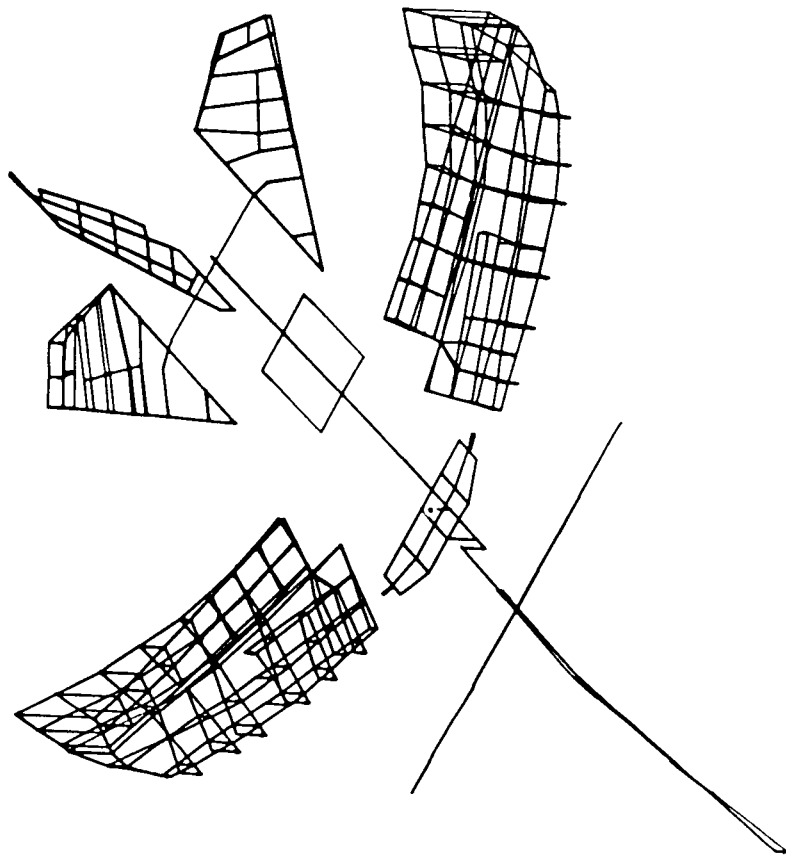
Figure A6. First wing symmetric torsion (WST) mode, f = 17.139 Hz.

APPENDIX B

DETERMINATION OF $\tilde{\omega}_i$ AND $\tilde{\omega}_i$ AS FUNCTIONS OF EXCITATION FREQUENCY

The presence of aerodynamic forces in the equations of motion (Eq. 9) results in eigenvalues, of $\tilde{\omega}_i$ and $\tilde{\zeta}_i$, that are functions of the excitation frequency, ω. Idealy, Eq. 1 should be solved directly as was done in Ref. 12:

$$\{r_i\} = \left(\left[M_i(\omega^2 - \omega_i^2 - i2\omega\omega_i\zeta_i)\right] + \left[Q_{ij}\right]\right)^{-1}\{Q_{iB}\}$$

However, an alternate source of the $\tilde{\omega}_i$ and $\tilde{\zeta}_i$ is the eigenvalue solution to the matrix as obtained from routine flutter analyses that make use of velocity-damping-frequency curves to determime structural stability. These damping values unfortu nately are based on attached flow aerodynamic forces, and do not reflect the effects of transonic and/or separated flow fields. However, damping information that does include transonic and/or separation effects is available from model tests using a scaling technique implemented by Butler and Spavins (Ref. 8). A limitation of this technique is that the vibration modes exhibited by solid metal models rarely simulate those of a full-scale flexible aircraft except for the first symmetric wing bending and possibly the first symmetric wing torsion modes.

As mentioned above, each of the available sources of $\tilde{\omega}_i$ and $\tilde{\zeta}_i$ are deficient, either by not including transonic and separation effects of by not including data for all modes of interest. A technique is therefore proposed in this section which combines the data from the two sources to eliminate the deficiencies. The basic idea is to use wind-tunnel model data as described by Butler and Spavins (Ref. 8) to obtain damping-parameter values (Eq. 1) for "pivot modes" (i.e., first symmetric wing bending and wing symmetric wing torsion modes), and then to use the flutter solution roots to scale the damping to other modes (Eq. 7). The primary assumption is that the real flow fields affect modes similar to the "pivot modes" in a similar manner. This technique is described in the following example.

Consider the velocity-damping-frequency (V-g-ω) curves shown in Figure B1. The form shown on the left-hand side is that customarily used for determining flutter speeds. The velocity at the point of crossing to positive damping of root 3 is demoted as the flutter velocity, V_f. However, when the same data are plotted as a function of exciting frequency ω, as shown on the right-hand-side of Figure B1, it is readily apparent how mode damping and frequency vary with ω. The hypothetical modes noted are the first wing symmetric and antisymmetric bending modes (1 and 2) and the first wing symmetric and antisymmetric torsion modes (3 and 4). For this example, the symmetric bending and torsion modes are very similar to the model bending and torsion modes and hence would be considered as "pivot" modes. By scaling $\tilde{\zeta}_1$, and $\tilde{\zeta}_3$ from wind-tunnel data using the scaling technique at the modal frequency for each mode, the values of $\tilde{\zeta}_2$ and $\tilde{\zeta}_4$ are obtained from the plot through the ratios

$$\left(\frac{\tilde{\zeta}_2}{\tilde{\zeta}_1}\right)_T \quad \text{and} \quad \left(\frac{\tilde{\zeta}_4}{\tilde{\zeta}_3}\right)_T$$

where the subscribt "T" refers to theoretical values. Thus,

$$\tilde{\zeta}_2 = \tilde{\zeta}_1 \left(\frac{\tilde{\zeta}_2}{\tilde{\zeta}_1} \right)_T \quad \text{and} \quad \tilde{\zeta}_4 = \tilde{\zeta}_3 \left(\frac{\tilde{\zeta}_4}{\tilde{\zeta}_3} \right)_T$$

The values of $\tilde{\zeta}_1$, and $\tilde{\zeta}_3$ for frequencies other than the respective modal frequencies are also determined from the plot.

The frequency shifts due to aerodynamic stiffness are assumed to be incremental corrections, $\Delta\tilde{\omega}_i$, added to the undamped natural frequency, ω_i as

$$\tilde{\omega}_i = \omega_i + \Delta\tilde{\omega}_i$$

As as example, $\Delta\tilde{\omega}_i$, is noted in the right-hand-side plot.

The scaling technique as well as the theoretical root plots are sensitive to altitude, Mach number and airplane gross weight. In addition, the scaling technique is sensitive to angle of attack. Thus, the data necessary to fully determine $\tilde{\omega}_i$ and $\tilde{\zeta}_i$ for a particular aircraft and flight conditions include plots similar to that in the right-hand-side of Figure B1 for sufficient gross weight, Mach and altitude conditions to cover the buffet prediction regime. Also necessary are the wind-tunnel damping data at sufficient Mach number and angle-of-attack conditions for scaling to the flight conditions. The wind-tunnel data must cover enough "pivot modes" so that the desired airplane modes will be available for use in the equations of motion.

Figure B1.   Hypothetical example of flutter eigenvalues.

APPENDIX C

DEVELOPMENT OF A COMPOSITE MODE

In the development, of a new mode that is a combination of several (base) normal modes, the idea of diagonalized equations of motion allows the establishment of a relationship between the $\tilde{\omega}$ and $\tilde{\zeta}$ of the new mode with $\tilde{\omega}_i$ and $\tilde{\zeta}_i$ of the base normal modes from which the new mode is formed. However, before addressing the relationship of the eigenvalues, the calculation of generalized mass for the composite mode will be discussed.

Let it be assumed that three base modes are to be combined to produce a final composite mode subject to some constraints on the mode shape. Let the modal deflections of the composite mode $\{h_c\}$ be defined as

$$\{h_c\} = p_1\{h_1\} + p_2\{h_2\} + p_3\{h_3\}$$

$$\{h_c\} = \{p_1 h_1 + p_2 h_2 + p_3 h_3\} \qquad \text{C1}$$

where p_i are the real weighting numbers assigned to mode i as determined by shape constraints on $\{h_c\}$, and $\{h_i\}$ are the modal deflections for base mode i. Since the h_i vectors are orthogonal, i.e.,

$$\lfloor h_i \rfloor \{h_j\} = 0, \quad i \neq j$$

$$= \Sigma h_i^2 \neq 0, \quad i = j \qquad \text{C2}$$

then it can shown that the composite generalized mass is a simple sum of the generalized masses of the three base modes. Calculating M_c in the usual manner,

$$M_c = \lfloor h_c \rfloor \lceil m \rfloor \{h_c\}$$

$$= \lfloor p_1 h_1 + p_2 h_2 + p_3 h_3 \rfloor \lceil m \rfloor \{p_1 h_1 + p_2 h_2 + p_3 h_3\}$$

$$= \sum_k (p_1 h_1 + p_2 h_2 + p_3 h_3)_k m_k p_1 h_{1_k}$$

$$+ \sum_k (p_1 h_1 + p_2 h_2 + p_3 h_3)_k m_k p_2 h_{2_k}$$

$$+ \sum_k (p_1 h_1 + p_2 h_2 + p_3 h_3)_k m_k p_3 h_{3_k}$$

leads to

$$M_c = p_1^2 \sum_k m_k h_{1_k}^2 + p_2^2 \sum_k m_k h_{2_k}^2 + p_3^2 \sum_k m_k h_{3_k}^2$$

$$+ 2p_1 p_2 \sum_k m_k h_{1_k} h_{2_k} + \cdots + 2p_2 p_3 \sum_k m_k h_{2_k} h_{3_k}$$

But

$$M_i = \sum_k m_k h_{i_k}^2$$

139

and from equation C2,

$$\sum_k m_k h_{i_k} h_{j_k} = 0, \quad i \neq j$$

hence

$$M_c = p_1^2 M_1 + p_2^2 M_2 + p_3^2 M_3 \qquad\qquad C3$$

Thus, once the weighting numbers, p_i, are obtained, M_c is readily calculated from M_i. This property (Eq. C3) will also play an important role in establishing the damping and frequency relationships.

Starting with Equations 10, 16, and 17, the relationships between eigenvalues of the composite mode and its base modes can now be developed. Combining Equations 10, 16 and 17 yields

$$\left[\frac{\omega_i^2}{\omega^2}\right] + \left[\frac{Q_{ij}}{M_i \omega^2}\right] \approx \left[\frac{1}{\omega^2}(\widetilde{\omega}_i^2 + i2\omega\,\widetilde{\omega}_i \zeta_i)\right]$$

which can be rearranged to become

$$[Q_{ij}] \approx [M_i]\left[(\widetilde{\omega}_i^2 - \omega_i^2) + i2\widetilde{\omega}_i \omega \zeta_i\right] \qquad\qquad C4$$

For a composite mode,

$$Q_c = \lfloor p_i \rfloor [Q_{ij}]\{p_j\}$$

thus

$$Q_c \approx \lfloor p_i \rfloor [M_i]\left[(\widetilde{\omega}_i^2 - \omega_i^2) + i2\widetilde{\omega}_i \omega \zeta_i\right]\{p_j\}$$

But because the right-hand side matrices are diagonal,

$$Q_c \approx [p_i^2 M_i]\left[(\widetilde{\omega}_i^2 - \omega_i^2) + i2\widetilde{\omega}_i \omega \zeta_i\right]$$

$$Q_c \approx \sum_i p_i^2 M_i (\widetilde{\omega}_i^2 - \omega_i^2 + i2\widetilde{\omega}_i \omega \zeta_i) \qquad\qquad C5$$

By virtue of Equation C4, we may also write

$$Q_c \approx M_c(\widetilde{\omega}_c^2 - \omega_c^2 + i2\widetilde{\omega}_c \omega \zeta_c)$$

which may be combined with Equation C5 to yield

$$M_c(\widetilde{\omega}_c^2 - \omega_c^2 + i2\widetilde{\omega}_c \omega \zeta_c) \approx \sum_i p_i^2 M_i(\widetilde{\omega}_i^2 - \omega_i^2 + i2\widetilde{\omega}_i \omega \zeta_i) \qquad C6$$

Equation C6 is the basic complex equation from which the eigenvalue relationships will be derived.

In the absence of aerodynamic forces, the generalized stiffness of the equivalent mode must be equal to the weighted sum of the generalized stiffnesses of the base modes. Hence, the following must be true:

$$M_c \omega_c^2 = \sum_i p_i^2 M_i \omega_i^2 \qquad\qquad\qquad C7$$

where, it will be noted, the approximation sign has been changed to an equal sign. This is true because the aerodynamic forces are the only source of off-diagonal terms. Equating the real and imaginary parts of Equation C6 yields

$$M_c (\tilde{\omega}_c^2 - \omega_c^2) \approx \sum_i p_i M_i (\tilde{\omega}_i^2 - \omega_i^2)$$

and

$$M_c (2\tilde{\omega}_c \omega \tilde{\zeta}_c) \approx \sum_i p_i^2 M_i (2\tilde{\omega}_i \omega \tilde{\zeta}_i)$$

which, with Equation C7 and further simplification become

$$M_c \tilde{\omega}_c^2 \approx \sum_i p_i^2 M_i \tilde{\omega}_i^2 \qquad\qquad\qquad C8$$

and

$$M_c \tilde{\omega}_c \tilde{\zeta}_c \approx \sum_i p_i^2 M_i \tilde{\omega}_i \tilde{\zeta}_i \qquad\qquad\qquad C9$$

Thus, Equations C7, C8 and C9 provide a full set of equations to determine ω_c, $\tilde{\omega}_c$ and $\tilde{\zeta}_c$ from ω_i, $\tilde{\omega}_i$ and $\tilde{\zeta}_i$. However, in our case, because the composite modes are being used for scaling wind-tunnel data, one more step is necessary before this technique is complete.

The added equations necessary to determine the base-mode damping values from the scaled composite-mode damping values are available from the $\tilde{\zeta}_i$ data generated by the theoretical solution. The ratios described in Appendix B provide the following relationships from the theoretical damping data:

$$\zeta_i = \zeta_k \left(\frac{\tilde{\zeta}_i}{\tilde{\zeta}_k} \right)_T \qquad\qquad\qquad C10$$

where $\tilde{\zeta}_k$ is some reference damping value, usually that for one of the base modes. Substituting Equation C10 into C9 yields

$$M_c \tilde{\omega}_c \tilde{\zeta}_c \approx \tilde{\zeta}_k \sum_i p_i^2 M_i \tilde{\omega}_i \left(\frac{\tilde{\zeta}_i}{\tilde{\zeta}_i} \right)_T \qquad\qquad\qquad C11$$

which will now provide a value for $\tilde{\zeta}_k$ from the scaled value of $\tilde{\zeta}_c$ for the composite mode.

In summary, the above technique for using composite modes to improve the accuracy of damping estimates for full-scale aircraft modes consists of the following eight steps:

1. Pick a set of base aircraft modes that can be combined to better simulate the mode of interest on the model. (As an example, the F-111 TACT has three asymmetric wing torsion modes that will combine to produce a symmetric torsion mode with a node line very similar to that of the model).

2. Calculate p_i for the constraints imposed by the model mode shape.

3. Calculate M_c for airplane gross weight from

$$M_c = \sum_i p_i^2 M_i$$

4. Calculate ω_c and $\tilde{\omega}_c$ for flight conditions from

$$\omega_c^2 = \frac{1}{M_c} \sum_i p_i^2 \omega_i^2 M_i$$

$$\tilde{\omega}_c^2 = \frac{1}{M_c} \sum_i p_i^2 \tilde{\omega}_i^2 M_i$$

5. Calculate $\tilde{\zeta}_c$ with the Ref. 8 scaling technique for the flight conditions.

6. Calculate the $(\tilde{\zeta}_i/\tilde{\zeta}_k)_T$ ratios from the theoretical flutter solution roots for the flight conditions.

7. Calculate $\tilde{\zeta}_k$ from

$$\tilde{\zeta}_k = \frac{M_c \tilde{\omega}_c \tilde{\zeta}_c}{\sum_i p_i^2 M_i \tilde{\omega}_i (\tilde{\zeta}_i/\tilde{\zeta}_k)_T}$$

8. Finally, calculate $\tilde{\zeta}_i$ from $\tilde{\zeta}_i$ and $(\tilde{\zeta}_i/\tilde{\zeta}_k)_T$.

This technique is a generalized damping scaling method which permits miss-matching between model and full scale aircraft modes. The only requirement for implementing the technique is that the aircraft modes be similar enough to the model mode so that a reasonable number of base modes (at most 3 or 4) will be sufficient to construct the composite mode.

APPENDIX D

COUPLING BETWEEN WING MODES
AND FLUCTUATING PRESSURES

The apparent coupling that exists between wing vibration modes and fluctuating pressures under certain conditions was demonstrated earlier in this report in Figures 17 and 18. It was also suspected, but could not be proven, that such a coupling existed for the F-111 at similar conditions. For the F-111 TACT, the wing torsion and second wing bending modes were thought to be coupling where as for the F-111 case, the first wing torsion mode was suspect. Demonstration of the possible existence of such coupling is important, however, it does not explain the mechanism.

A clue to a possible means for the coupling can be deduced from the static pressures in Figures 14. The occurance of trailing-edge pressure divergence at about $\alpha = 10°$ also corresponds to a large forward movement of the upper surface main shock as shown by comparing Figures 14(a) at $\alpha = 9°$ and 14(b) at $\alpha = 10°$. It will also be noted that the forward shock movement for the aircraft is much larger than that for the model. The condition of this transistion is the occurrence of Shock-Induced Trailing Edge Separation (SITES) which was extensively discussed by Cunningham, et al in Ref. 27. Dynamic oscillatory investigations of this flow regime were also conducted by Triebstein (Ref. 28) in two-dimensional flow. In either investigation, it was shown that this transition was accompanied by a step change in pitching moment with either increasing of decreasing angle-of-attack. With increasing angle-of-attack, the forward shock movement produced a loss of lift toward the leading edge and the trailing-edge divergence produced a gain of lift toward the trailing edge. The net result was to provide a step change in pitching moment that was nose down for increasing angle-of-attack. For decreasing angle-of-attack, the opposite occurred and produced a step change in pitching moment that was nose up. Such a step change in effect resulted in a nonlinear spring that would provide an increased resistance to wing motion past the point of SITES for either increasing or decreasing angle-of-attack.

The nonlinear spring described above can potentially produce a limit amplitude, self-sustaining oscillation, the existence of which could explain the higher torsion mode response exhibited by the full scale aircraft. How this is possible can be described by considering an airfoil with a torsion spring. Slowly increasing incidence at angles below that of SITES allows the torsion spring to attain a continuous state of equilibrium with aerodynamic pitching moment. When SITES is reached, a sudden nose-down increment is imposed on the aerodynamic pitching moment which will tend to reduce wing incidence. This will be a dynamic negative-pitch rate which will delay re-attachment and permit the nose-down moment to put work into the system. At some point, re-attachment does take place and the nose-down moment disappears. Accelerations become negative and the wing experiences a reducing pitch rate until it reaches zero and begins nose-up motion. Positive pitch rate now takes over which will produce a delay in SITES and allow an overshoot of the initial starting point due to stored elastic energy during the down stroke. When SITES does occur, the cycle then repeats itself.

It is possible to cast the concept just described in mathematical form with a simple one-degree-of-freedom spring mass system. The appropriate equation of motion for say the RWT mode is

$$M_{RWT} \, \ddot{r} + 2M_{RWT} \, \omega_{RWT} \, \zeta_{RWT} \, \dot{r} + M_{RWT} \, \omega^2_{RWT} \, r = F(r)$$

where

$M_{RWT}, \omega_{RWT}, \zeta_{RWT}$ = mass, frequency, and total damping for the RWT mode

r = response of the RWT mode

$F(r)$ = nonlinear generalized force due to the step change in the static pressure distribution

The nonlinear right-hand side term $F(r)$ is obtained by integrating the RWT mode deflections with the step change in the C_p values that occur during the transition to SITES. The function of r is expressed as

$$F(r) = 0, \quad r < r_{TRANS}$$

$$F(r) = F, \quad r \geq r_{TRANS}$$

In order to include the hysteresis effects, pitch rate must be taken into account so that

$$r_{TRANS}(\dot{r}) > r_{TRANS}(0), \quad \dot{r} > 0$$

$$r_{TRANS}(\dot{r}) < r_{TRANS}(0), \quad \dot{r} < 0$$

which simply parallels the idea that positive pitch rate delays separation and negative pitch rate delays re-attachment. This equivalence is possible when the mode of interest is a torsion mode or has a significant streamwise angular deflection. The relationship of the step change, F, and hysteresis is shown in Figure D1 where the coordinate system has been referenced to $r = 0$ at the occurance of SITES.

By writing the derivatives in finite difference form,

$$r = r_n$$

$$\dot{r} = \frac{r_{n+1} - r_{n-1}}{2 \Delta t}$$

$$\ddot{r} = \frac{r_{n+1} - 2r_n + r_{n-1}}{\Delta t^2}$$

a finite difference solution to the above equation of motion can be cast in the form

$$r_{n+1} = \frac{1}{1 + \lambda \zeta} \left[-\lambda^2 \epsilon + (2 - \lambda^2) \, r_n - (1 - \lambda \zeta) \, r_{n-1} \right], \quad r_n \geq r_{TRANS}(\dot{r})$$

144

and

$$r_{n+1} = \frac{1}{1 + \lambda \zeta} \left[(2-\lambda^2) \, r_n - (1-\lambda \zeta) \, r_{n-1} \right], \quad r_n < r_{TRANS} \, (\dot{r})$$

where

$$\lambda = \Delta t \omega_{RWT}$$

$$\zeta = \zeta_{RWT}$$

$$\varepsilon = \frac{F}{M_{RWT} \, \omega_{RWT}^2}$$

The initial conditions are

$$\left. \begin{array}{l} r = 0 \\ \\ \dot{r} = 0 \end{array} \right\} \quad t = 0$$

which are satisfied in the finite difference form as

$$r_0 = 0$$

$$r_1 = 0$$

$$r_2 = - \frac{\lambda^2 \varepsilon}{1 + \lambda \zeta}$$

By denoting Δr as the half width of the hysteresis (shown in Figure D1),

$$\Delta r = \tfrac{1}{2} (r_{TRANS} (\dot{r} > 0) - (r_{TRANS} (\dot{r} < 0))$$

the solution to the equation of motion can be presented as a function of the parameters ε and Δr for the system M_{RWT}, ζ_{RWT} and ω_{RWT}.

The algorithm described above was programmed and estimates were made for the appropriate ε value to be used for the RWT mode. The estimate of ε was obtained by using the C_p distributions shown in Figures 14(a) at $\alpha = 9°$ and 14(b) at $\alpha = 10°$ in the following form:

$$\varepsilon = \frac{\tfrac{1}{2} \rho V^2}{M_{RWT} \, \omega_{RWT}^2} \int_A h_{RWT} \, (x,y) \left[C_{p_{10}} (x,y) - C_{p_9} (x,y) \right] dx \, dy$$

where

$h_{RWT} (x,y)$ = deflection of the RWT mode at point x,y

$C_{p_{10}} (x,y)$ = C_p value at $\alpha = 10°$ and point x,y

$C_{p_9} (x,y)$ = C_p value at $\alpha = 9°$ and point x,y

A = area of the wing

145

In actuality, the above integral was evaluated in the same manner as were the buffet excitation forces by summing the product of C_p values, mode deflections, and panel areas over the exposed wing area. The value obtained was

$$\epsilon_{10-9} = 0.00387 \text{ m} \quad (0.0127 \text{ ft})$$

at the intermediate altitude of 6.1 Km (20K ft). Other parameters were

$$M_{RWT} = 809.4 \text{ lbs}, \quad f_{RWT} = 14.17 \text{ Hz and } \zeta_{RWT} = 0.07$$

where ζ_{RWT} was estimated from Figure 32(c).

Estimates for Δr were not possible based on the available data, hence, a parameter study was conducted by letting Δr vary as a fraction of ϵ. A sample plot shown in Figure D2 for $\Delta r = \epsilon$ illustrates how the transient solution quickly approaches a limit amplitude oscillatory motion. It is also interesting to note that the apparent frequency is slightly higher than that of the RWT mode. Since the number of time steps in the plot represents ten cycles, it is easy to calculate the apparent frequency. The results for varying Δr are listed below for the wing-tip accelerometer (RWAC) response in g's:

$$\epsilon = 0.00387 \text{ m} \quad (0.0127 \text{ ft})$$

$\Delta r/\epsilon$	Δr, m	RWT Apparent f, Hz	RWAC g's Response
0.2	0.00077	18.4	0.71
0.4	0.00155	17.0	1.42
0.6	0.00232	16.4	1.79
0.8	0.00310	15.1	2.05
1.0	0.00387	14.9	2.34

where the modal deflection at the right wing-tip accelerometer was taken as 0.525 for the RWT mode as has been used throughout this report.

The response results presented above are in excellent order-of-magnitude agreement with the torsion mode RMS responses at $\alpha = 10°$ shown in Figure 35(c). The slightly higher frequency also agrees with observations in the flight test PSD's in Figures 33 and 34 for $\Lambda = 26°$ and 6.1 Km altitude. Since the estimate for ϵ was considered to be conservative, the above results are especially encouraging. It is also interesting to note that the reduced pressure levels shown by Kinsey (Ref. 13) with increasing dynamic pressure would also explain the peculiar tendency to maintain constant response levels nearly independent of altitidue as shown in Figure 35(c). Reducing or increasing the C_p values used to evaluate ϵ would tend to offset the variation in ϵ due to dynamic pressure. This effect would be primarily due to static aeroelasticity.

This concept also helps explain why the high torsion-mode response did not appear on the 1/6-scale wind-tunnel model. As estimate for ϵ was made using the pressure data shown in Figuues 14(a) and 14(b). The result was 0.000077 m (0.000253 ft) which is far less than 1/6 of the full scale result of 0.00387. For similar deflections between model and aircraft, the ratio should be the same

as the scale factor. Hence, because amplitude of model motion on the basis of ε is more like 0.12 relative to the aircraft motion, this concept would predict very little influence of the coupling mechanism on the wind-tunnel model excitation forces. Another very important aspect is the mismatch of scaled torsion-mode frequencies as was discussed earlier, so that even if the coupling occurred on the model, it would not appear in the correct range of full-scale frequencies.

With regard to a more realistic math model for the limit amplitude oscillations, it is expected that the nonlinear spring would be slightly more complicated. A calculation of ε for the incidence change from 10° to 11° produced a higher ε value of 0.00651 m (0.0232 ft), which indicates an increasing nonlinear-spring constant beyond SITES. Similar results could be produced with such a spring and would explain the high response measured in the torsion modes at angles of attack beyond the transition to SITES ($\alpha > 10°$ for this case).

In view of the promising results obtained with the simple math model, further research on this approach should be very beneficial. A better definition of ε and Δr as functions of both static and dynamic motions is the most obvious first step. In addition, the math model would need refinement to reflect the knowledge gained through the experimental work. The result of this effort should be a simplified method for predicting the occurance and magnitude of limit amplitude oscillations in which wing motions couple with separated flow fields.
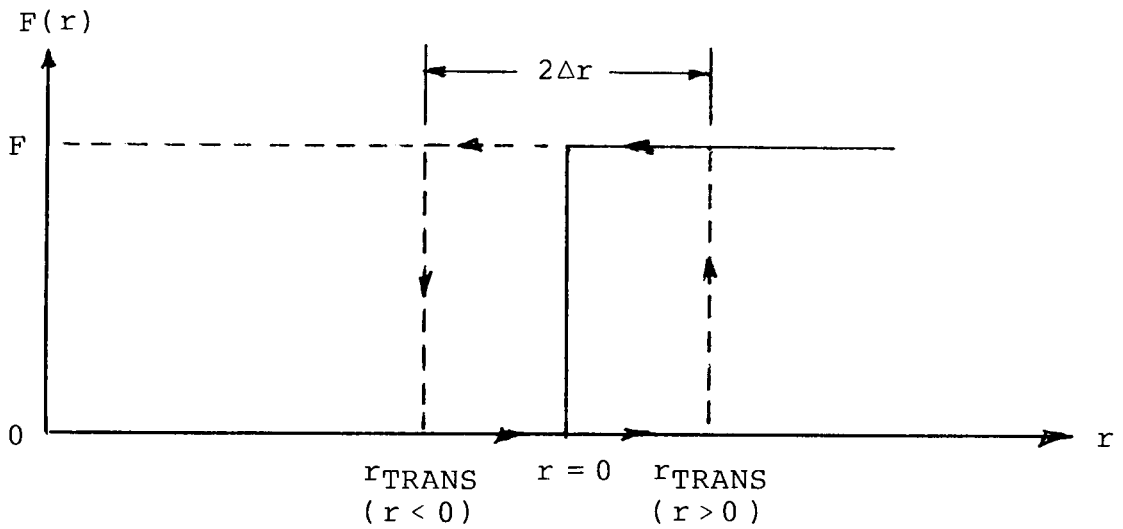
Figure D1. Schematic diagram of the variation of the nonlinear generalized force step function due to shock induced trailing edge separation.


Nt—Number of Time Steps
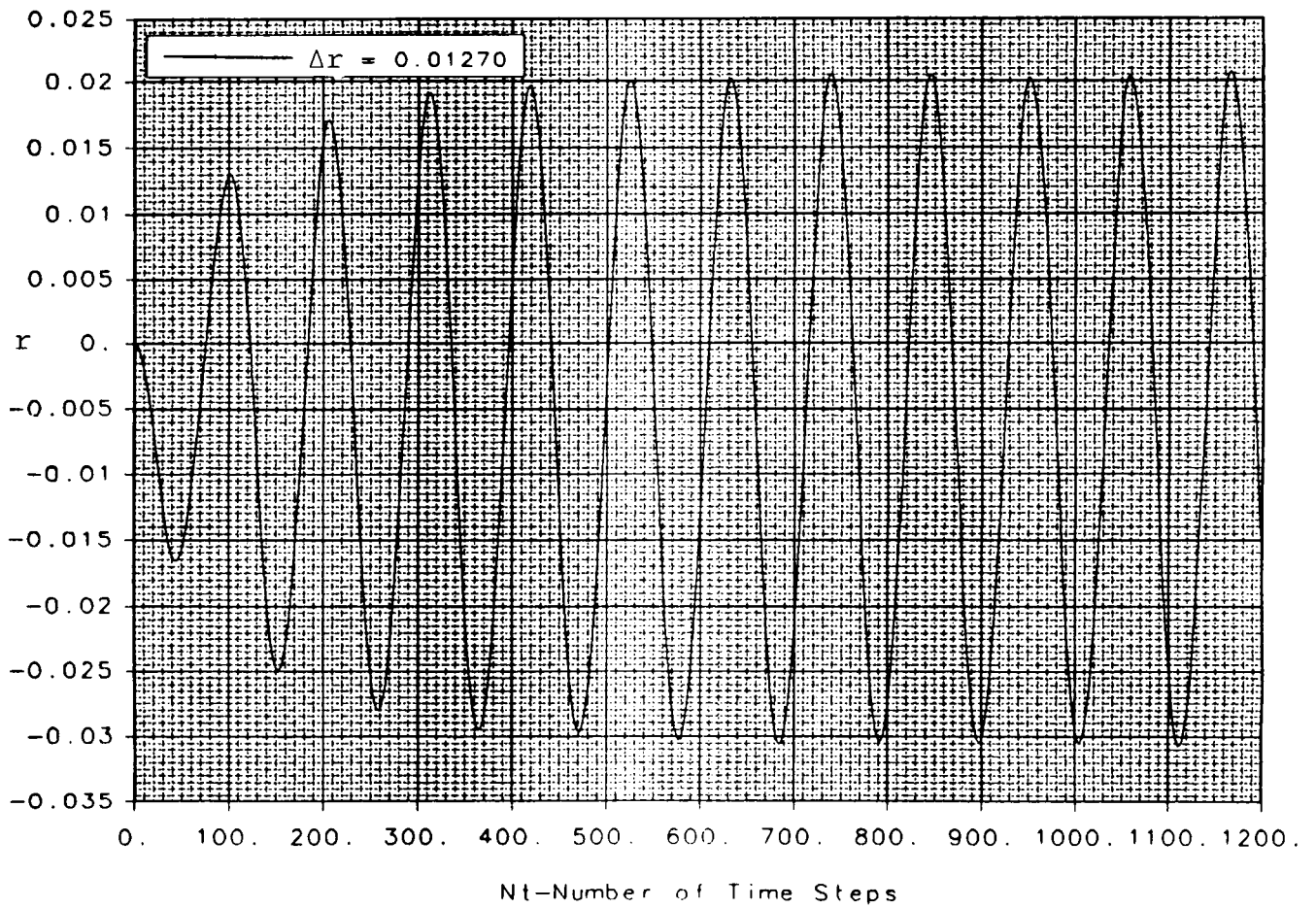
Figure D2. Sample of limited amplitude oscillations produced by the shock induced trailing edge separation model.

148

1. Report No. NASA CR-4069	2. Government Accession No.	3. Recipient's Catalog No.
4. Title and Subtitle Predictions of F-111 TACT Aircraft Buffet Response and Correlations of Fluctuating Pressures Measured on Aluminum and Steel Models and the Aircraft		5. Report Date MAY 1987
		6. Performing Organization Code
7. Author(s) Charles F. Coe and Atlee M. Cunningham, Jr.		8. Performing Organization Report No. H-1388
		10. Work Unit No. RTOP 506-43-31
9. Performing Organization Name and Address Coe Engineering, Inc. 610 Cuesta Drive Los Altos, California 94022		11. Contract or Grant No. NAS2-11420
		13. Type of Report and Period Covered Contractor Report - Final
12. Sponsoring Agency Name and Address National Aeronautics and Space Administration Washington, D.C. 20546		14. Sponsoring Agency Code

15. Supplementary Notes

16. Abstract

Results of buffet research that was conducted as part of the joint USAF/NASA F-111 TACT Research Program are presented. Presented separately are: (1) the correlation of wind-tunnel and flight measurements of buffet excitation and (2) a method for predicting buffet response based on fluctuating pressure measurements and the correlation of predicted and measured buffeting of the F-111 TACT aircraft.

The correlation of wind-tunnel and flight measurements of buffet excitation showed that there generally was good agreement between measurements of pressure fluctuations on the models and aircraft in regions of separated flow. At shock-wave boundaries of the separated flow, correlations of pressure fluctuations were not so good, due to Reynolds number and static elastic effects.

The buffet prediction method, which applies a forcing function that is obtained by real-time integration of pressure time histories with the natural modes, is described in detail. The generalized forces, including the effects of wing and tail, correlations of predicted and measured damping, and correlations of predicted and measured buffet response are presented. All presented data are for a Mach number of 0.8 with wing-sweep angles of 26° and 35° for a range of angles-of-attack that includes buffet onset to high intensity buffeting. Generally, the buffet predictions were considered to be quite good particularly in light of past buffet-prediction experience.

17. Key Words (Suggested by Author(s)) Aerodynamic Damping Buffeting Fluctuating Pressures Structural Dynamics	18. Distribution Statement Unclassified — Unlimited Subject category 02

19. Security Classif. (of this report) Unclassified	20. Security Classif. (of this page) Unclassified	21. No. of Pages 152	22. Price* A08

For sale by the National Technical Information Service, Springfield, Virginia 22161.